

Journal of
Mechanics of
Materials and Structures

Volume 2, N° 4

April 2007

 mathematical sciences publishers

JOURNAL OF MECHANICS OF MATERIALS AND STRUCTURES

<http://www.jomms.org>

EDITOR-IN-CHIEF Charles R. Steele
ASSOCIATE EDITOR Marie-Louise Steele
Division of Mechanics and Computation
Stanford University
Stanford, CA 94305
USA

BOARD OF EDITORS

D. BIGONI University of Trento, Italy
H. D. BUI École Polytechnique, France
J. P. CARTER University of Sydney, Australia
R. M. CHRISTENSEN Stanford University, U.S.A.
G. M. L. GLADWELL University of Waterloo, Canada
D. H. HODGES Georgia Institute of Technology, U.S.A.
J. HUTCHINSON Harvard University, U.S.A.
C. HWU National Cheng Kung University, R.O. China
IWONA JASIUK University of Illinois at Urbana-Champaign
B. L. KARIHALOO University of Wales, U.K.
Y. Y. KIM Seoul National University, Republic of Korea
Z. MROZ Academy of Science, Poland
D. PAMPLONA Universidade Católica do Rio de Janeiro, Brazil
M. B. RUBIN Technion, Haifa, Israel
Y. SHINDO Tohoku University, Japan
A. N. SHUPIKOV Ukrainian Academy of Sciences, Ukraine
T. TARNAI University Budapest, Hungary
F. Y. M. WAN University of California, Irvine, U.S.A.
P. WRIGGERS Universität Hannover, Germany
W. YANG Tsinghua University, P.R. China
F. ZIEGLER Technische Universität Wien, Austria

PRODUCTION


PAULO NEY DE SOUZA Production Manager
SHEILA NEWBERY Senior Production Editor
SILVIO LEVY Scientific Editor

See inside back cover or <http://www.jomms.org> for submission guidelines.

Regular subscription rate: \$500 a year.

Subscriptions, requests for back issues, and changes of address should be sent to Mathematical Sciences Publishers, 798 Evans Hall, Department of Mathematics, University of California, Berkeley, CA 94720-3840.

©Copyright 2008. Journal of Mechanics of Materials and Structures. All rights reserved.

 mathematical sciences publishers

ASYMPTOTIC ANALYSIS AND REFLECTION PHOTOELASTICITY FOR THE STUDY OF TRANSIENT CRACK PROPAGATION IN GRADED MATERIALS

NITESH JAIN AND ARUN SHUKLA

The behavior of a rapidly moving transient crack in functionally graded materials (FGMs) is investigated theoretically and experimentally. First, a systematic theoretical analysis is presented for the development of the transient elastodynamic local stress, strain, and displacement field expansions near a growing mixed mode crack tip in FGMs. The crack propagation direction is assumed to be inclined to the direction of the property variation. The displacement potential approach in conjunction with asymptotic analysis is utilized to derive explicit expressions for stress, strain, and in-plane displacement fields. The transient crack growth is assumed to include processes in which both the crack tip speed and the dynamic stress intensity factor are differentiable functions of time. These stress fields are used to generate the contours of constant maximum shear stress (isochromatics fringes) and the effect of transient crack growth on these contours is discussed. To further understand the transient crack growth behavior, a series of dynamic fracture experiments are performed with functionally graded material fabricated in-house. The phenomenon of transition from a static crack to a dynamic mode I crack is examined in these experiments. The full-field stress data around the crack is recorded using dynamic photoelasticity and high-speed digital photography. Due to opaqueness of FGMs, birefringent coatings are employed to obtain the full-field isochromatics around the crack tip. The stress field expansions developed in the first part of the study are used to interpret the experimental observations. The results of the experiments showed that the higher order transient expansion provides an accurate representation of crack tip fields under severe transient conditions.

1. Introduction

Increasing multifunctional performance requirements in aerospace, power generation, microelectronics, and bioengineering applications often demand properties that are unattainable with any single material. Correspondingly, composite and layered materials are developed to invoke the desirable characteristic of each constituent phase in order to meet such requirements. However, the internal stresses caused by the elastic and the thermal property mismatch at an interface between two differing bulk materials can mitigate the successful implementation of such composites. To address this problem, functionally gradient materials (FGMs) have been developed. FGMs accommodate a gradual transition of the properties of different materials from one location to the other, such that the mismatch in mechanical and thermal properties is minimized [Surendranath et al. 2003; Suresh and Mortensen 1998].

Keywords: functionally graded material, dynamic fracture, transient crack, asymptotic analysis, photoelasticity, high-speed imaging.

This work was supported by the National Science Foundation under grant CMS-0244330 and by the Air Force Office of Scientific Research under grant FA-95500610162.

A fundamental understanding of the mechanics of crack formation, initiation, and growth is essential for efficient design of critical components fabricated using FGMs. Several researchers have investigated the behavior of embedded and edge cracks in graded materials subjected to quasistatic loading [Jin and Noda 1994; Erdogan 1995; Gu and Asaro 1997; Chalivendra et al. 2003; Jain et al. 2004]. All these studies concluded that the inverse square-root singularity at the crack tip is not affected by material nonhomogeneities as long as the elastic modulus and Poisson's ratio are sufficiently smooth functions of spatial position. Although the stationary crack problem in FGMs has received considerable attention, less is known about the behavior of a rapidly propagating crack in these materials. The problem of a crack moving with a constant velocity in FGMs has been presented by [Atkinson and List 1978; Wang and Meguid 1994; Nakagaki et al. 1998; Parameswaran and Shukla 1998; Marur and Tippur 2000; Rousseau and Tippur 2001; Li and Weng 2002; Jain and Shukla 2004; Jain and Shukla 2006]. Recently, there has been some work on the fracture mechanics of anisotropic functionally graded materials. Sladek et al. [2005] proposed a meshless method based on the local Petrov–Galerkin approach for crack analysis in anisotropic FGMs. Kim and Paulino [2004] presented an interaction integral formulation for evaluating the elastic T-stress for a mixed mode crack in orthotropic nonhomogeneous materials. In most of these investigations, it is presumed that the crack tip stress field depends upon the instantaneous crack velocity and the instantaneous stress intensity factor. However, in many situations, reflecting stress waves pass through the specimen constructively and destructively interfering with one another, and thus result in a highly complex time-dependent stress intensity factor. Due to the nonhomogeneous nature of FGM and resulting mathematical complexities, very few investigations on the transient dynamic response of cracked FGMs have been reported in the literature [Zhang et al. 2003; Shukla and Jain 2004; Chalivendra et al. 2003]. In all these investigations the crack is subjected to a single mode of loading, that is, either an opening or a tearing mode. But from a practical viewpoint, strength-controlling flaws in load bearing structures, in general, are expected to be inclined at random orientations to the applied principal stress. Also, it has been reported in experimental and numerical studies that propagating cracks in FGMs can follow inclined paths under various loading conditions due to spatial variation of properties in graded materials [Li et al. 2000; Tilbrook et al. 2005; Abanto-Bueno and Lambros 2006]. The transient elastodynamic solution for a crack growing in an arbitrary direction in FGMs is still not known. However, the solution for a homogeneous material is presented in the work of [Freund and Rosakis 1992].

This paper provides a theoretical analysis for the derivation of transient, asymptotic, elastodynamic near-tip fields for a crack growing in an arbitrary direction in an FGM. The transient elastodynamic problem is formulated in terms of two displacement potentials, and an asymptotic analysis is performed to develop explicit expressions for stress, strain, and in-plane displacement fields. In this context, transient crack growth is understood to include processes in which both the crack tip speed and the dynamic stress intensity factor are differentiable functions of time. These crack tip fields are needed to analyze the full-field experimental data obtained from various experimental techniques such as photoelasticity, Moiré interferometry, holographic interferometry, and coherent gradient sensing (CGS). The stress fields developed in this paper are used to generate the contours of constant maximum shear stress (isochromatic fringes) and the effect of the transient crack growth on these contours is discussed. This is followed by a series of experiments to get further insight into the behavior of mode-I transient cracks in FGMs. The full-field stress data around the propagating crack is recorded using dynamic photoelasticity and high speed digital photography. Due to the opaqueness of FGMs, birefringent coatings are employed to obtain

the full-field isochromatic fringes around the moving crack tip. A high speed camera capable of taking 200 million frames per second is used to record these isochromatic fringes. The stress field expansion developed in the first part of the study is used to interpret these experimental observations, with the conclusion that the higher order expansion provides an accurate representation of crack tip fields under severe transient conditions.

2. Elastodynamic transient crack tip fields

2.1. Theoretical consideration. The variation of elastic and physical properties in FGMs is in general limited to a single direction. At any given point in the material, the properties can be assumed to be the same in all directions and hence, at a continuum level FGMs are isotropic nonhomogeneous solids. The transient elastodynamic problem is formulated in terms of two displacement potentials and an asymptotic analysis is performed to develop the stress, strain, and displacement fields around a propagating crack in an FGM. The direction of transient crack propagation is assumed to be inclined to the direction of property variation. The properties are assumed to vary exponentially with distance. When the crack is inclined to the property gradation direction, the stress state near the crack tip is mixed mode, irrespective of the far field loading.

2.2. Theoretical formulation. Consider a crack moving nonuniformly in an FGM as shown in Figure 1. The original coordinate system is a spatially fixed Cartesian coordinate system $X - Y$. A moving coordinate system $x - y$ at the crack tip is now defined such that the crack velocity is in the x -direction. Suppose that the crack propagates with a nonuniform speed, $c(t)$, and the crack faces satisfy the traction free boundary condition. Localized crack tip plasticity and three-dimensional effects are neglected in this formulation. The shear modulus and mass density are assumed to vary exponentially in the X_1 direction as given in (1) and the Poisson's ratio ν is assumed to be constant. The property gradation direction forms an angle φ with the $Y = 0$ axis. We have

$$\mu = \mu_0 \exp(\delta X_1), \quad \rho = \rho_0 \exp(\delta X_1), \quad S = \frac{\lambda}{\mu}, \tag{1}$$

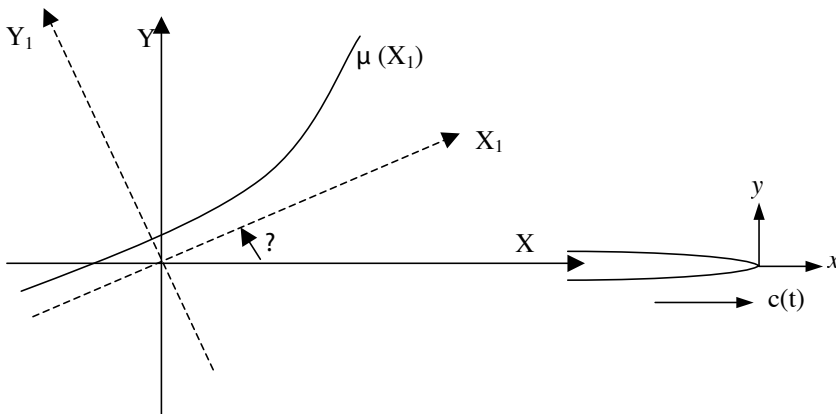


Figure 1. Propagating crack orientation with respect to the direction of property variation in a FGM.

where μ and λ are the shear modulus and Lamé's constant, μ_0 and ρ_0 are the shear modulus and mass density at $X = X_1 = 0$, and δ is the nonhomogeneity parameter, having the dimension of inverse length. Equation (1) can be written in terms of (X, Y) coordinates by using a simple transformation

$$\mu(X, Y) = \mu_0 \exp(\alpha X + \beta Y), \quad \rho(X, Y) = \rho_0 \exp(\alpha X + \beta Y), \quad (2)$$

$$\alpha = \delta \cos \varphi, \quad \beta = \delta \sin \varphi. \quad (3)$$

The equations of motion for a plane problem in the absence of body forces in the fixed coordinate system can be written as

$$\sigma_{XX,X} + \sigma_{XY,Y} = \rho u_{,tt}, \quad \sigma_{XY,X} + \sigma_{YY,Y} = \rho v_{,tt}, \quad (4)$$

where σ_{ij} are in-plane stress components and u, v are in-plane displacements. The Hooke's law for plane elasticity problem can be written as

$$\sigma_{XX} = ((\lambda_0 + 2\mu_0)u_{,X} + \lambda_0 v_{,Y}) \exp(\alpha X + \beta Y),$$

$$\sigma_{YY} = ((\lambda_0 + 2\mu_0)v_{,Y} + \lambda_0 u_{,X}) \exp(\alpha X + \beta Y), \quad (5)$$

$$\sigma_{XY} = (u_{,Y} + v_{,X}) \mu_0 \exp(\alpha X + \beta Y).$$

Introducing the displacement potentials (Φ and Ψ) as

$$u = \Phi_{,X} + \Psi_{,Y}, \quad v = \Phi_{,Y} - \Psi_{,X}, \quad (6)$$

substituting (6) into (5), and substituting the resulting equality into (4), the equation of motion can be expressed in terms of displacement potentials Φ and Ψ as

$$\begin{aligned} \frac{\partial}{\partial X} \left((S+2) \nabla^2 \Phi - \frac{\rho_0}{\mu_0} \frac{\partial^2 \Phi}{\partial t^2} \right) + \frac{\partial}{\partial Y} \left(\nabla^2 \Psi - \frac{\rho_0}{\mu_0} \frac{\partial^2 \Psi}{\partial t^2} \right) \\ + \alpha \left(S \nabla^2 \Phi + 2 \frac{\partial^2 \Phi}{\partial X^2} + 2 \frac{\partial^2 \Psi}{\partial X \partial Y} \right) + \beta \left(2 \frac{\partial^2 \Phi}{\partial X \partial Y} + \frac{\partial^2 \Psi}{\partial Y^2} - \frac{\partial^2 \Psi}{\partial X^2} \right) = 0, \\ \frac{\partial}{\partial Y} \left((S+2) \nabla^2 \Phi - \frac{\rho_0}{\mu_0} \frac{\partial^2 \Phi}{\partial t^2} \right) - \frac{\partial}{\partial X} \left(\nabla^2 \Psi - \frac{\rho_0}{\mu_0} \frac{\partial^2 \Psi}{\partial t^2} \right) \\ + \alpha \left(\frac{\partial^2 \Psi}{\partial Y^2} - \frac{\partial^2 \Psi}{\partial X^2} + 2 \frac{\partial^2 \Phi}{\partial X \partial Y} \right) + \beta \left((S+2) \frac{\partial^2 \Phi}{\partial Y^2} - 2 \frac{\partial^2 \Psi}{\partial X \partial Y} + \lambda_0 \frac{\partial^2 \Phi}{\partial X^2} \right) = 0. \end{aligned} \quad (7)$$

Equations (7) can only be satisfied when (see [Jain and Shukla 2004])

$$\begin{aligned} (S+2) \nabla^2 \Phi - \frac{\rho_0}{\mu_0} \frac{\partial^2 \Phi}{\partial t^2} + (S+2) \left(\alpha \frac{\partial \Phi}{\partial X} + \beta \frac{\partial \Phi}{\partial Y} \right) + \left(\alpha \frac{\partial \Psi}{\partial Y} - \beta \frac{\partial \Psi}{\partial X} \right) = 0, \\ \nabla^2 \Psi - \frac{\rho_0}{\mu_0} \frac{\partial^2 \Psi}{\partial t^2} + S \left(\alpha \frac{\partial \Phi}{\partial Y} - \beta \frac{\partial \Phi}{\partial X} \right) + \left(\alpha \frac{\partial \Psi}{\partial X} + \beta \frac{\partial \Psi}{\partial Y} \right) = 0. \end{aligned} \quad (8)$$

Now we introduce the moving crack tip coordinates $x = X - ct$ and $y = Y$. The coordinate change implies the substitutions

$$\frac{\partial^2}{\partial X^2} = \frac{\partial^2}{\partial x^2} \quad \text{and} \quad \frac{\partial^2}{\partial t^2} = c^2 \frac{\partial^2}{\partial x^2} + \frac{\partial^2}{\partial t^2} - \dot{c} \frac{\partial}{\partial x} - 2c \frac{\partial^2}{\partial x \partial t}, \quad \text{where } \dot{c} = \frac{\partial c}{\partial t}. \quad (9)$$

Using these transformations, Equation (8) becomes

$$\begin{aligned} \alpha_l^2 \frac{\partial^2 \Phi}{\partial x^2} + \frac{\partial^2 \Phi}{\partial y^2} + \left(\alpha \frac{\partial \Phi}{\partial x} + \beta \frac{\partial \Phi}{\partial y} \right) - \frac{1}{S+2} \left(\alpha \frac{\partial \Psi}{\partial y} - \beta \frac{\partial \Psi}{\partial x} \right) + \frac{\rho_0}{\mu_0(S+2)} \left(\dot{c} \frac{\partial \Phi}{\partial x} + 2c \frac{\partial^2 \Phi}{\partial x \partial t} - \frac{\partial^2 \Phi}{\partial t^2} \right) &= 0, \\ \alpha_s^2 \frac{\partial^2 \Psi}{\partial x^2} + \frac{\partial^2 \Psi}{\partial y^2} + \left(\alpha \frac{\partial \Psi}{\partial x} + \beta \frac{\partial \Psi}{\partial y} \right) + S \left(\alpha \frac{\partial \Phi}{\partial y} - \beta \frac{\partial \Phi}{\partial x} \right) + \frac{\rho_0}{\mu_0(S+2)} \left(\dot{c} \frac{\partial \Psi}{\partial x} + 2c \frac{\partial^2 \Psi}{\partial x \partial t} - \frac{\partial^2 \Psi}{\partial t^2} \right) &= 0, \end{aligned} \tag{10}$$

where

$$\alpha_l = \left(1 - \frac{\rho_0 c^2}{\mu_0(S+2)} \right)^{1/2}, \quad \alpha_s = \left(1 - \frac{\rho_0 c^2}{\mu_0} \right)^{1/2}.$$

These equations reduce to the classical two-dimensional wave equations of motion if α and β equal zero. In the case of nonhomogeneity, the equations lose their classical form and remain coupled in Φ and Ψ , through the nonhomogeneity parameters α and β .

2.3. Asymptotic expansion of crack tip fields. At this point, we employ the standard asymptotic analysis proposed in [Freund 1990]. We introduce coordinates $\eta_1 = x/\varepsilon$, $\eta_2 = y/\varepsilon$, where ε is a small arbitrary positive parameter ($0 < \varepsilon < 1$), used so that the region around the crack tip is expanded to fill the entire region of observation. As ε becomes infinitely small, all the points in the x - y plane, except those very near the crack tip, are pushed out of the field of observation in the η_1 - η_2 plane, and the crack line occupies the whole negative η_1 -axis. We assume that Φ and Ψ can be expressed in powers of ε as

$$\begin{aligned} \Phi(x, y) = \Phi(\varepsilon\eta_1, \varepsilon\eta_2) &= \sum_{m=0}^{\infty} \varepsilon^{(m+3)/2} \phi_m(\eta_1, \eta_2), \\ \Psi(x, y) = \Psi(\varepsilon\eta_1, \varepsilon\eta_2) &= \sum_{m=0}^{\infty} \varepsilon^{(m+3)/2} \psi_m(\eta_1, \eta_2). \end{aligned} \tag{11}$$

The first term of series ($m = 0$) corresponds to the expected square root singular contribution proportional to $r^{-1/2}$ in the asymptotic near-tip stress field.

Substituting the assumed asymptotic form (11) into the governing Equation (10), we obtain two equations, in each of which the left-hand side is an infinite power series in ε and the right-hand side vanishes. Since ε is an arbitrary number, the coefficient of each power of ε should vanish identically to satisfy these resulting equations. Therefore, the governing equation reduces to a system of coupled differential equations in Φ and Ψ . These equations have the general form

$$\begin{aligned} \alpha_l^2 \frac{\partial^2 \phi_m}{\partial \eta_1^2} + \frac{\partial^2 \phi_m}{\partial \eta_2^2} + \left(\alpha \frac{\partial \phi_{m-2}}{\partial \eta_1} + \beta \frac{\partial \phi_{m-2}}{\partial \eta_2} \right) + \frac{1}{S+2} \left(\alpha \frac{\partial \psi_{m-2}}{\partial \eta_2} - \beta \frac{\partial \psi_{m-2}}{\partial \eta_1} \right) \\ + \frac{\rho_0 c^{1/2}}{\mu_0(S+2)} \frac{\partial}{\partial t} \left(c^{1/2} \frac{\partial \phi_{m-2}}{\partial \eta_1} \right) - \frac{\rho_0}{\mu_0(S+2)} \frac{\partial^2 \phi_{m-4}}{\partial t^2} &= 0, \\ \alpha_s^2 \frac{\partial^2 \psi_m}{\partial \eta_1^2} + \frac{\partial^2 \psi_m}{\partial \eta_2^2} + \left(\alpha \frac{\partial \psi_{m-2}}{\partial \eta_1} + \beta \frac{\partial \psi_{m-2}}{\partial \eta_2} \right) + S \left(\alpha \frac{\partial \phi_{m-2}}{\partial \eta_2} - \beta \frac{\partial \phi_{m-2}}{\partial \eta_1} \right) \\ + \frac{\rho_0 c^{1/2}}{\mu_0} \frac{\partial}{\partial t} \left(c^{1/2} \frac{\partial \psi_{m-2}}{\partial \eta_1} \right) - \frac{\rho_0}{\mu_0(S+2)} \frac{\partial^2 \psi_{m-4}}{\partial t^2} &= 0, \end{aligned} \tag{12}$$

where

$$\phi_k, \psi_k = \begin{cases} \phi_k, \psi_k & \text{for } k \geq 0, \\ 0 & \text{for } k < 0. \end{cases}$$

For $m = 0$ and $m = 1$, Equations (12) are not coupled in Φ and Ψ and reduce to Laplace’s equation in the coordinates $\eta_1, \alpha_l \eta_2$ or $\eta_1, \alpha_s \eta_2$ (similar to that for a homogeneous material having elastic properties equal to the elastic properties of the FGM at the crack tip). Indeed, as will be seen, ϕ_0 and ψ_0 have the same spatial structure in both transient and steady state cases. This is not so, however, for ϕ_m, ψ_m if $m > 1$.

Since the crack is propagating at an angle to the direction of property gradation, the stress field near the crack tip is a combination of both opening and shear modes (mixed mode). For the elastic solution, the stress field related to the opening mode and the shear modes can be superposed to obtain the mixed mode solution. The solutions for $m = 0$ and 1 are the same as for homogeneous material and can be written as

$$\begin{aligned} \phi_m(\rho_l, \theta_l, t) &= A_m(t)\rho_l^{(m+3)/2} \cos \frac{1}{2}(m+3)\theta_l + C_m(t)\rho_l^{(m+3)/2} \sin \frac{1}{2}(m+3)\theta_l, \\ \psi_m(\rho_s, \theta_s, t) &= B_m(t)\rho_s^{(m+3)/2} \sin \frac{1}{2}(m+3)\theta_s + D_m(t)\rho_s^{(m+3)/2} \cos \frac{1}{2}(m+3)\theta_s \end{aligned} \tag{13}$$

for $m = 0, 1$, where

$$\rho_l = (\eta_1^2 + \alpha_l^2 \eta_2^2)^{1/2}, \quad \tan \theta_l = \frac{\alpha_l \eta_2}{\eta_1}, \quad \rho_s = (\eta_1^2 + \alpha_s^2 \eta_2^2)^{1/2}, \quad \tan \theta_s = \frac{\alpha_s \eta_2}{\eta_1}.$$

The solution (13) appears to be the same as for steady state crack growth. However, the two solutions differ fundamentally in that the coordinates (ρ_l, θ_l) now depend upon time. It is the crack speed that determines the degree of distortion of these coordinates, and the crack speed is now a function of time. Also one should note that the coefficients of the series solution given in (13) are time dependent.

Using the definitions of dynamic stress intensity factors K_{ID} and K_{IID} for the opening and the shear modes [Shukla and Chona 1987] and considering the crack face boundary conditions we get

$$\begin{aligned} A_0(t) &= \frac{4(1 + \alpha_s^2)}{3(4\alpha_s \alpha_l - (1 + \alpha_s^2)^2)} \frac{K_{ID}(t)}{\mu_c \sqrt{2\pi}}, & B_0(t) &= -\frac{2\alpha_l}{1 + \alpha_s^2} A_0(t), \\ C_0(t) &= \frac{8\alpha_s}{3(4\alpha_s \alpha_l - (1 + \alpha_s^2)^2)} \frac{K_{IID}(t)}{\mu_c \sqrt{2\pi}}, & D_0(t) &= \frac{1 + \alpha_s^2}{2\alpha_l} C_0(t). \end{aligned} \tag{14}$$

The solution for higher orders of m can be obtained recursively (see [Jain and Shukla 2004]):

$$\begin{aligned} \phi_2 &= A_2(t)\rho_l^{5/2} \cos \frac{5}{2}\theta_l - \frac{1}{4}\alpha_l^{-2}\rho_l^{5/2}(\cos \frac{1}{2}\theta_l(\alpha A_0(t) + \beta C_0(t)) + \sin \frac{1}{2}\theta_l(\alpha C_0(t) - \beta A_0(t))) \\ &\quad - \frac{2}{5} \frac{\alpha_s}{(k+2)(\alpha_l^2 - \alpha_s^2)} \rho_s^{5/2}(\cos \frac{5}{2}\theta_s(\alpha B_0(t) - \beta D_0(t)) - \sin \frac{5}{2}\theta_s(\alpha B_0(t) + \beta D_0(t))) \\ &\quad + \rho_l^{5/2} \left(\frac{1}{6}(D_l(A_0(t)) + \frac{1}{2}B_l^A(t)) \cos \frac{1}{2}\theta_l - \frac{1}{8}B_l^A(t) \cos \frac{3}{2}\theta_l \right. \\ &\quad \left. + \frac{1}{6}(D_l(C_0(t)) + \frac{1}{2}B_l^C(t)) \sin \frac{1}{2}\theta_l + \frac{1}{8}B_l^C(t) \sin \frac{3}{2}\theta_l \right), \end{aligned}$$

$$\begin{aligned}
 \psi_2 = & B_2(t)\rho_s^{5/2} \sin \frac{5}{2}\theta_s - \frac{1}{4}\alpha_s^{-2}\rho_s^{5/2}(\cos \frac{1}{2}\theta_s(\alpha B_0(t) + \beta D_0(t)) + \sin \frac{1}{2}\theta_s(\alpha B_0(t) - \beta D_0(t))) \\
 & + \frac{2}{5} \frac{k\alpha_l}{(\alpha_l^2 - \alpha_s^2)} \rho_l^{5/2} (\cos \frac{5}{2}\theta_l(\alpha C_0(t) - \beta A_0(t)) - \sin \frac{5}{2}\theta_l(\alpha A_0(t) + \beta C_0(t))) \\
 & + \rho_s^{5/2} \left(\frac{1}{6} (D_s(B_0(t)) + \frac{1}{2} B_s^B(t)) \sin \frac{1}{2}\theta_s + \frac{1}{8} B_s^B(t) \sin \frac{3}{2}\theta_s \right. \\
 & \left. + \frac{1}{6} (D_s(D_0(t)) + \frac{1}{2} B_s^D(t)) \cos \frac{1}{2}\theta_s - \frac{1}{8} B_s^D(t) \cos \frac{3}{2}\theta_s \right). \quad (15)
 \end{aligned}$$

The coefficients appearing in this solution are defined in the [Appendix](#).

2.4. Stress, strain, and displacement fields. The stress, strain, and displacement fields around the crack tip can now be obtained using displacement potentials (Φ and Ψ) found in the previous section. Detailed expressions for the stress, strain, and displacements are not included here for brevity, but they are provided in an [online supplement to this paper](#). The authors can supply these expressions in machine readable form upon request.

2.5. Discussions of solutions. To get an insight into the effects of transient terms on the dynamic fracture process, contours of constant maximum shear stress (isochromatics) and contours of constant first stress invariant (isopachics) are generated for mixed mode loading conditions. The asymptotic representation of crack tip stress and displacement fields contain coefficients $A_n(t)$, $B_n(t)$, $C_n(t)$, and $D_n(t)$, which can be related to fracture parameters such as stress intensity factor and nonsingular stress components as in (14). The contours are generated for assumed values of the dynamic stress intensity factors (coefficient A_0 and C_0), whereas the higher order coefficients A_1 , A_2 , C_1 , C_2 , B_1 , B_2 , D_1 and D_2 are assumed to be zero. However, the nonhomogeneity and transient specific parts of the higher order terms, that have A_0 , B_0 , C_0 and D_0 as the coefficients, are retained. The typical values of material properties and material thickness used in generating contours are as follows: Poisson's ratio = 0.3, shear modulus at the crack tip $\mu_c = 1.5$ GPa, density at the crack tip $\rho_c = 1200$ kg/m³, and thickness $t = 0.01$ m. The nonhomogeneity parameter α for plotting these contours is obtained by fitting an exponential curve to the property variation profile of the laboratory-fabricated FGMs [Jain and Shukla 2006]. The nonhomogeneity parameter α for FGM fabricated in this study is 0.57. The crack velocity used in generating all the contours is 650 ms⁻¹. This choice of velocity is made on the basis of available experimental data on velocities that are typically observed for this FGM [Jain and Shukla 2006].

2.5.1. Isochromatic fringe patterns. Isochromatic fringe patterns obtained in photoelasticity represent contours of constant maximum shear stress and their generation is governed by the stress-optic law

$$\frac{Nf_\sigma}{2h} = \tau_{\max} = \frac{\sigma_1 - \sigma_2}{2} = \sqrt{\left(\frac{\sigma_x - \sigma_y}{2}\right)^2 + \tau_{xy}^2}, \quad (16)$$

where f_σ is the material fringe value, N is the isochromatic fringe order and h is the thickness of the specimen. Equation (16) is used to generate the isochromatic fringe patterns around the crack tip in FGMs. In generating these contours the crack is assumed to be on the negative x -axis and the crack tip is located at (0, 0). Also, the direction of crack propagation is assumed to be towards the positive x -axis. Figure 2 shows the effect of the rate of change of mode- I stress intensity factor ($dK_{ID}(t)/dt$) on contours of constant maximum shear stress for mixed mode loading around the crack tip corresponding

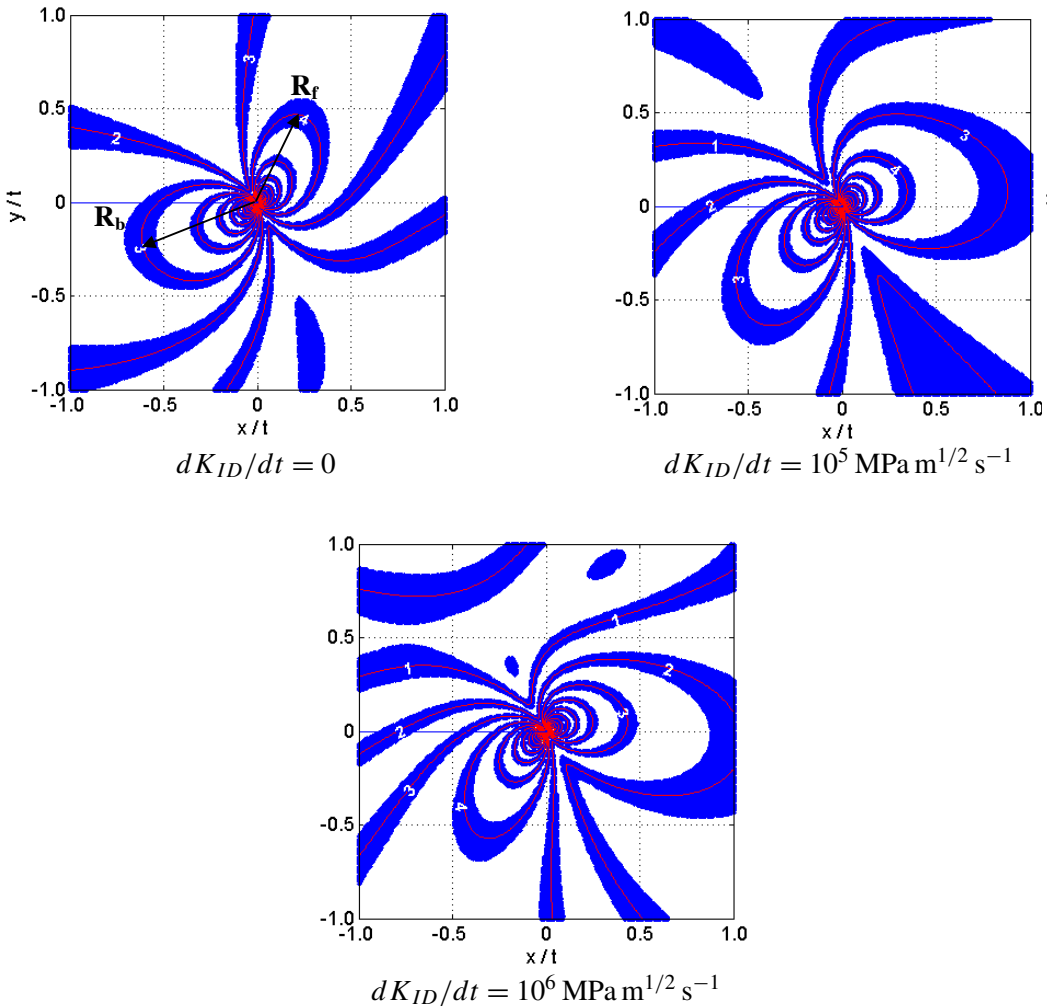


Figure 2. Effect of the rate of change of mode-I stress intensity factor on the contours of constant maximum shear stress around the crack tip in an FGM ($\alpha = 0.57$, $K_{ID}(t) = 1 \text{ MPa m}^{1/2}$, $K_{IID}(t) = 1 \text{ MPa m}^{1/2}$, $c = 650 \text{ ms}^{-1}$, $dc/dt = 0$). The front and rear apogee radii are marked in part (a) with R_f and R_b , respectively.

to $\alpha = 0.57$, $K_{ID} = K_{IID} = 1.0 \text{ MPa m}^{1/2}$, and $c = 650 \text{ ms}^{-1}$. As observed in [Dally and Shukla 1979] the rate of change of K_{ID} at crack initiation could be of the order of $10^5 \text{ MPa m}^{1/2} \text{ sec}^{-1}$, the values of $dK_{ID}(t)/dt$ are varied over six orders of magnitude for generating the contours. The fringe order increases as the crack tip is approached, with very high fringe orders in the close vicinity of the crack tip. This is a direct consequence of the stress singularity that exists at the crack tip. As $dK_{ID}(t)/dt$ increases, the fringes in front of the crack tip decrease in size and number, and the reverse happens for fringes behind the crack tip. This effect can be quantified in terms of increase in apogee radius (see Figure 2a) of a given fringe.

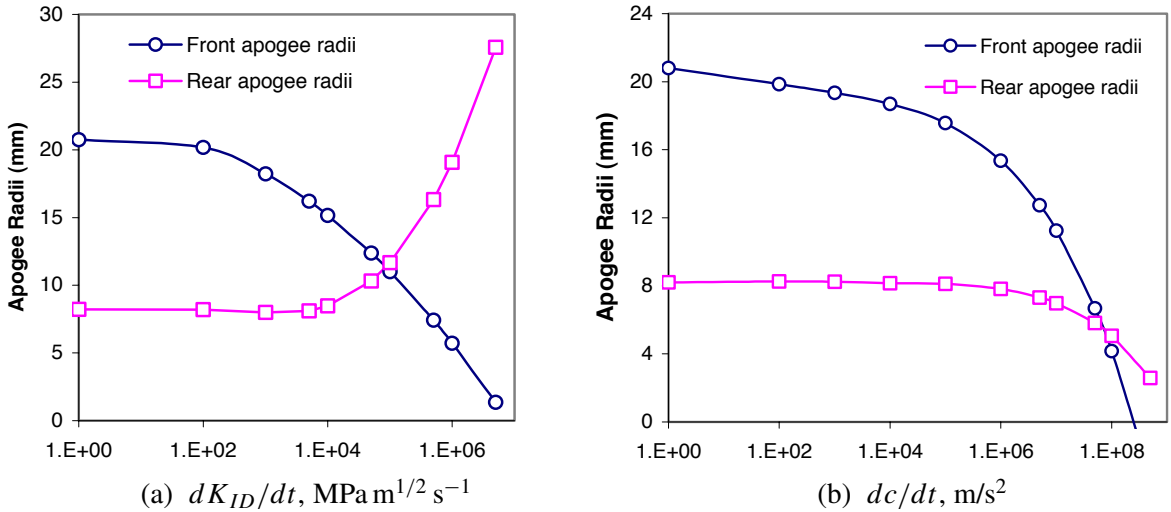


Figure 3. Variation of apogee radii of the third order isochromatic fringe as a function of (a) rate of change of mode-I stress intensity factor, and (b) crack tip acceleration.

The front and rear apogee radii of the third fringe order are determined from isochromatic fringe patterns and are plotted in Figure 3a as functions of $dK_{ID}(t)/dt$. The front apogee radius decreases from 20.7 mm to 5.7 mm as $dK_{ID}(t)/dt$ increases from 0 to 10^6 MPa $m^{1/2} s^{-1}$. The corresponding increase in the rear apogee radius is from 8.2 mm to 19.1 mm. The dependence of the fringe radius on the rate of change of mode-I stress intensity factor is nonlinear; a rapid change in the front and rear apogee radii are observed at higher values of $dK_{ID}(t)/dt$.

An additional consequence of the variation of the rate of change of mode I stress intensity factor is its effect on the tilt and shape of the isochromatic fringe contours surrounding the crack tip, as observed in Figure 2. As $dK_{ID}(t)/dt$ increases the fringes on the front side of the crack tip bend towards the direction of crack propagation and the fringes on the rear side bend away from the crack faces.

Figure 3b and Figure 4 show data obtained for a crack propagating in an FGM under different values of crack acceleration. The value of dc/dt is varied over eight orders of magnitude. (Dally and Shukla [1979] showed that the rate of change of velocity at crack initiation could be of the order of 10^7 ms^{-2} in their work with homogeneous materials.) Figure 4 shows isochromatic fringes for $dc/dt = 10^6, 10^7$ and 10^8 ms^{-2} . The changes in fringe size and shape until crack tip accelerations of 10^6 ms^{-2} are reached are negligible. For dc/dt above 10^6 ms^{-2} , as the crack acceleration increases, the front and rear fringe loops decrease in size. Figure 3b shows the variation of the front and the rear apogee radii of the third order fringe as a function of crack tip acceleration. It can be seen that the effect of dc/dt is more pronounced at higher crack tip accelerations.

3. Experiments

To investigate the expediency of the analysis presented in this work, a sequence of dynamic fracture experiments under mode-I conditions has been performed. In doing so, the phenomenon of transition from

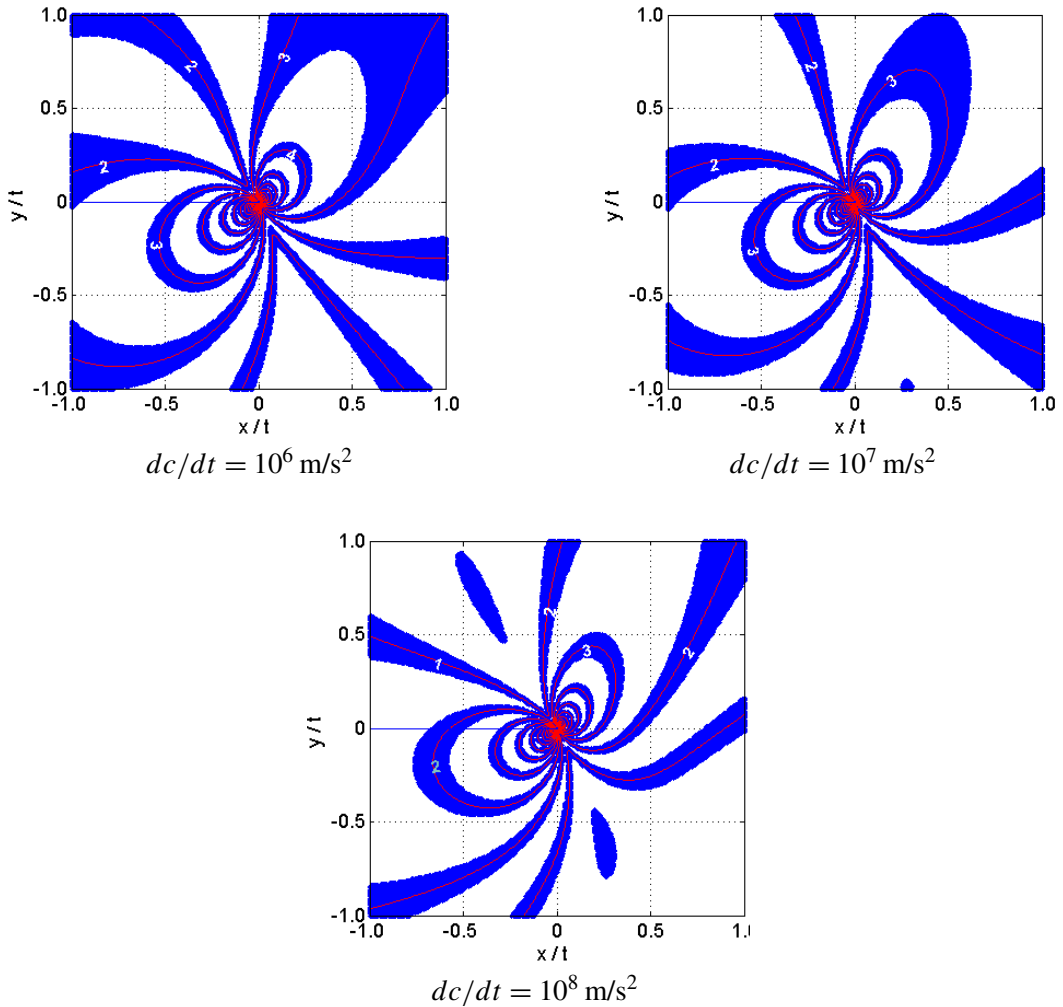


Figure 4. Effect of the crack tip acceleration on contours of the constant maximum shear stress around the crack tip in an FGM ($\alpha = 0.57$, $K_{ID}(t) = 1 \text{ MPa m}^{1/2}$, $K_{IID}(t) = 1 \text{ MPa m}^{1/2} dK_{ID}(t)/dt = 0$, $c = 650 \text{ ms}^{-1}$).

a static crack to a dynamic crack is studied. Dynamic photoelasticity along with high-speed photography is utilized to get the full field data around the crack tip during the transition.

3.1. Materials. The FGMs for this study were prepared as a particulate composite with continuously varying particle volume fraction along a single dimension. An unsaturated polyester resin (MR 17090, Ashland Chemical Company) was used as the matrix material. This highly cross-linked thermosetting polymer is ideal for fracture studies due to its relatively brittle nature. Cenospheres (LV01-SG, Sphere Services Inc.) particles with an average diameter of $127 \mu\text{m}$ were used as the filler material in the fabrication of the FGMs. These cenospheres, obtained from the fly ash of thermal power plants, are hollow spheres made of aluminum silicates.

FGM specimens were fabricated using a procedure developed in [Parameswaran and Shukla 2000]. The cenospheres have a low specific gravity of 0.67, compared to 1.18 for the resin. When the resin-cenosphere mixture is poured into the mold, the top layer of the mixture which is rich in cenospheres gets poured first and fills the bottom layer of the mold. Subsequently, the cenospheres diffuse towards the top of the mold due to buoyancy. The resin takes approximately 4 to 5 hours for gelation and once it gels and starts curing, further movement of spheres is arrested by the increased viscosity. This results in a casting with a resin rich region in the bottom, a cenosphere rich region at the top, and an intermediate region with continuously varying cenosphere content.

Detailed mechanical and physical characterization of the FGMs fabricated by the above procedure can be found in [Jain and Shukla 2004].

3.2. Specimen geometry and loading. A modified single edge notch tension (M-SENT) specimen as shown in Figure 5 is employed in this study. A first crack tip (starter crack) was made such that the subsequent crack propagation is increasing fracture toughness direction. An INSTRON 5585 apparatus is used to load the M-SENT specimens to a predetermined K_Q (static stress intensity factor) before the first crack tip is initiated by drawing a sharp knife-edge across the tip. After initiation the crack propagates across the ligament, breaking a crack detection gauge before coming to rest temporarily at the second crack tip. Breaking the crack detection gauge triggers an electronic circuit that causes the high-speed camera to commence taking a sequence of photographs of the isochromatics associated with the moving crack. At the second crack tip, the value of the stress intensity factor begins to increase

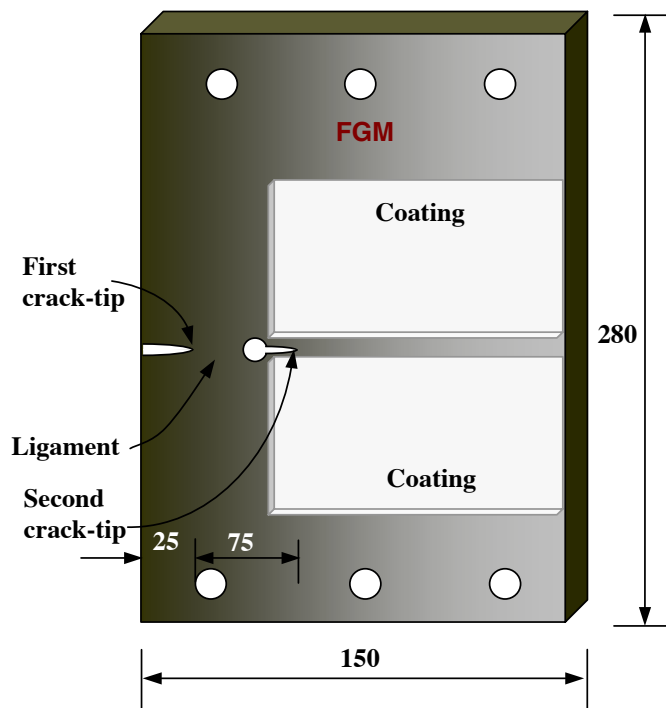


Figure 5. Specimen geometry for investigation of the transient nature of the crack tip. All dimensions are in mm.

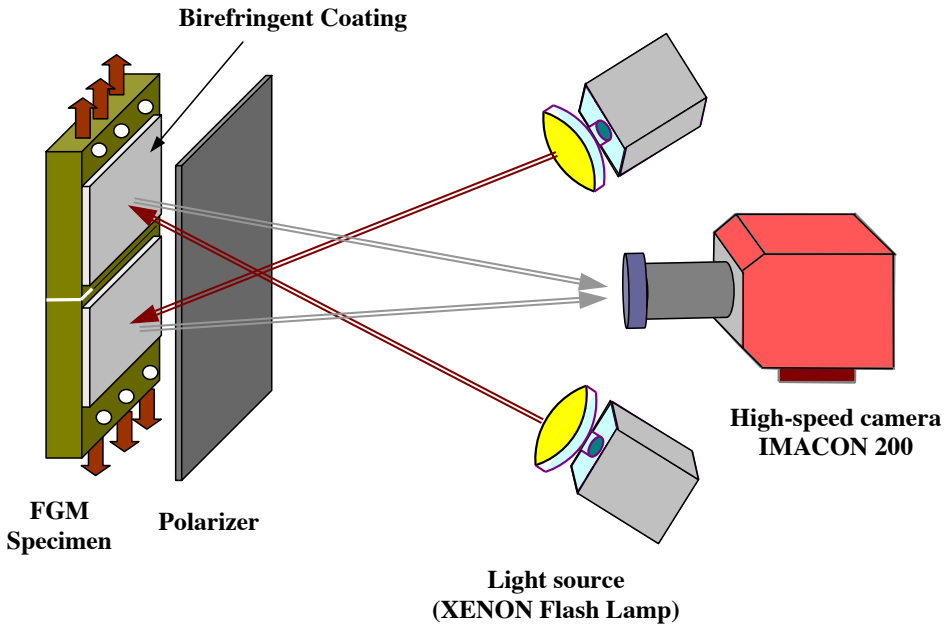


Figure 6. Photoelastic configuration for testing FGM specimens.

until it becomes sufficiently large to produce reinitiation of the crack. The bluntness of the second crack tip is controlled so that the crack remains at rest for a relatively long time (approximately $200 \mu\text{s}$) and reinitiation occurs at high values of K_Q .

3.3. Birefringent coatings. In this study we use a split birefringent coating technique [Der and Barker 1978], in which the coating is placed on both sides of the specimen, and a small distance (2 mm) away from the anticipated crack path. Birefringent coatings consisted of 3 mm thick polycarbonate sheets with vacuum deposited aluminum on the back surface. The sheets are cut to desired dimensions while using liberal amounts of cooling fluid to ensure minimum development of residual stresses. Extra fast-setting epoxy adhesive is used to bond the sheets to the specimens. Details on the validation of this technique can be found in [Jain and Shukla 2004].

3.4. High speed real time imaging of the transition from a static to a dynamic crack. A schematic of the experimental setup for testing M-SENT FGM specimens is shown in Figure 6. High speed digital imaging is employed along with dynamic photoelasticity to obtain real time, full field quantification of the transition from a static to a dynamic crack. A circular polarizer is placed in front of the split birefringent coatings to form a dark field circular polariscope. Power Light 2500DR xenon flash lamps were used as light sources to illuminate the specimen. The xenon flash lamps are a broadband source of light and therefore a monochromatic filter was placed just before the camera to ensure that the imaged isochromatic fringe patterns correspond to a single wavelength of light (546 nm). Due to stress-induced birefringence in the photoelastic coatings, this arrangement results in the formation of isochromatic fringe patterns during the failure process.

Images of the isochromatic fringes are captured using an Imacon 200 ultra-high speed digital camera. This CCD based camera provides 16 independently programmable digital images of dynamic events up to a maximum framing rate of 200×10^6 frames/s. The camera is operated with interframe times of $6 \mu\text{sec}$ (170,000 frames/sec) so as to record the increase in K at the stationary crack prior to initiation, and the dynamic value of $K(t)$ immediately after the initiation.

3.5. Photoelastic analysis. When the load is applied, the surface displacements of the specimen at the specimen-coating interface are transmitted to the coating. Observing the coating in a reflection polariscope generates a fringe pattern, which is related to the surface strains in the specimen. The method to determine the stress intensity factor is based on strain optic law applied to photoelastic coating, and on the fact that there is perfect strain transfer between specimen and coating (that is, $\varepsilon_1^S - \varepsilon_2^S = \varepsilon_1^C - \varepsilon_2^C$). We have

$$\varepsilon_1^S - \varepsilon_2^S = \varepsilon_1^C - \varepsilon_2^C = F_{CR} \frac{Nf_\varepsilon}{2hC} = F_{CR} \frac{1 + \nu^C}{E^C} \frac{Nf_\sigma}{2hC}, \quad (17)$$

where f_σ is the material fringe constant associated with the incident light wave length, N is the isochromatic fringe order, h is the thickness of the coating, ν is Poisson's ratio, and superscripts S and C refer to specimen and coating, respectively.

F_{CR} is a reinforcement correction factor that accounts for the fact that the coating carries a portion of the load, causing the strain on the specimen to be reduced by a certain amount. F_{CR} essentially depends upon the relative thickness and properties of the coating and specimen [Dally and Riley 2005].

In the derivation of the crack tip fields, the FGM is assumed to be an isotropic nonhomogeneous solid, which is justified because the size of the three-dimensional zone at the crack tip (thickness/2 = 6.3 mm) is orders of magnitude larger than the cenosphere diameter (127 μm). The strain expressions obtained in Section 2.4 are substituted in (17) and the resulting equation is solved using an over-deterministic nonlinear least squares method to obtain the fracture parameters. This involves fitting of a six parameter theoretical solution, which includes K_I , K_{II} , and σ_{ox} (T -stress) and so on, to field data taken from the isochromatic loops.

4. Experimental results

A series of experiments were conducted with K_Q ranging from 1.0 to 1.25 $\text{MPa m}^{1/2}$. Figure 7 shows a set of six frames recorded during the transition from a static to a dynamic crack. Isochromatics from each of the frames are analyzed using the aforementioned photoelastic procedure to obtain the stress intensity factor history. The crack remains stationary until frame 6 and starts moving afterwards. The size of the isochromatics decreases substantially as soon as the second crack starts to move, indicating the reduction in the value of stress intensity factor around the crack tip. These isochromatics are analyzed using the procedure described in the previous sections to obtain the dynamic stress intensity factor. The photoelastic fringes were regenerated using the calculated fracture parameters from data analysis. A good agreement between the regenerated fringes and the experimental fringes were observed.

Figure 8 shows the extension of the second crack with time. Measurements were repeated five times and the 95% confidence interval obtained using the Student's t-distribution is also shown. As the crack starts to move, the velocity of the crack continuously increases until it reaches a certain value and then stays constant. The crack initiation time is estimated to be 26.1 μsec , from curve fitting.

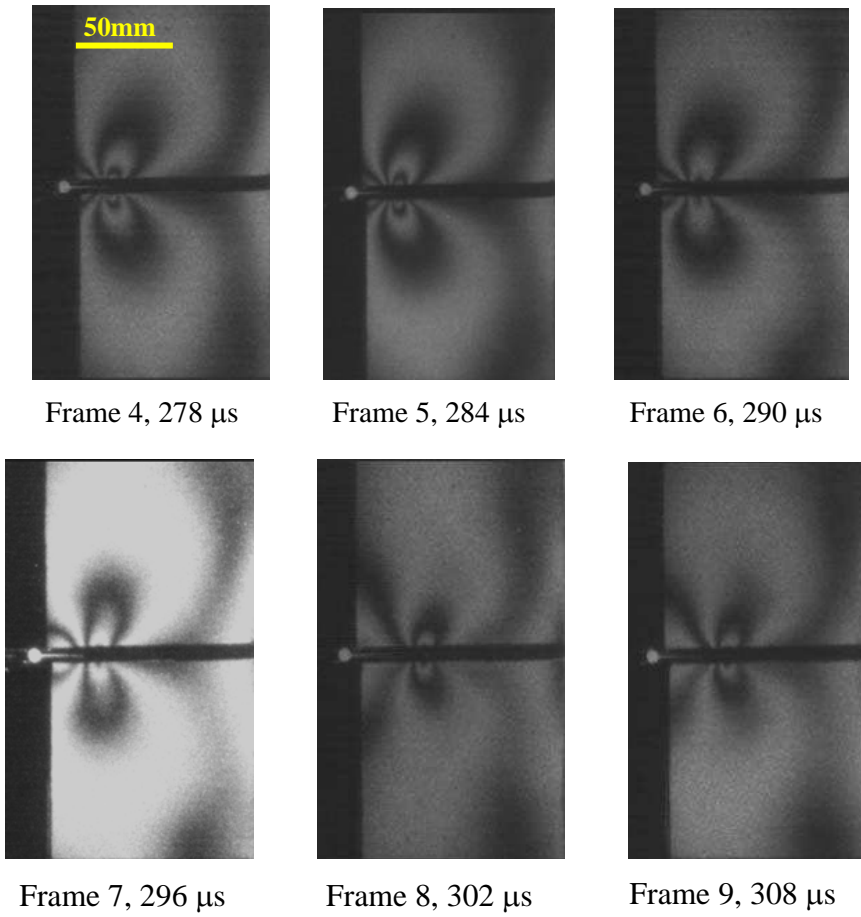


Figure 7. Isochromatic fringe patterns during crack initiation at a second crack tip.

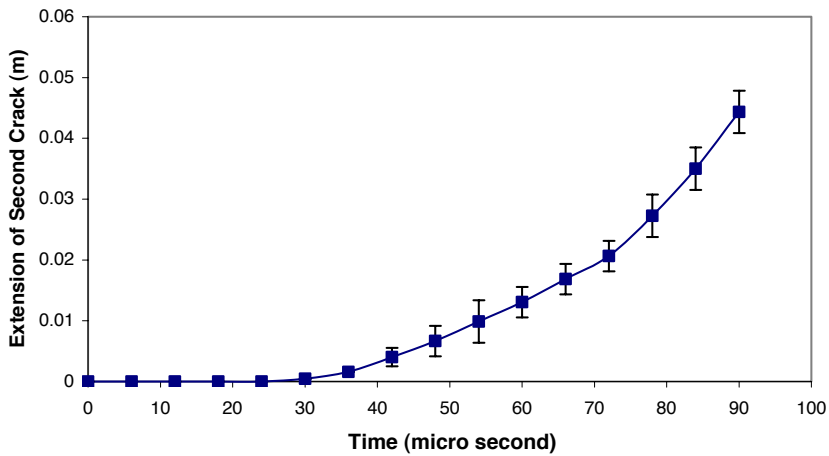


Figure 8. Crack tip position as a function of time.

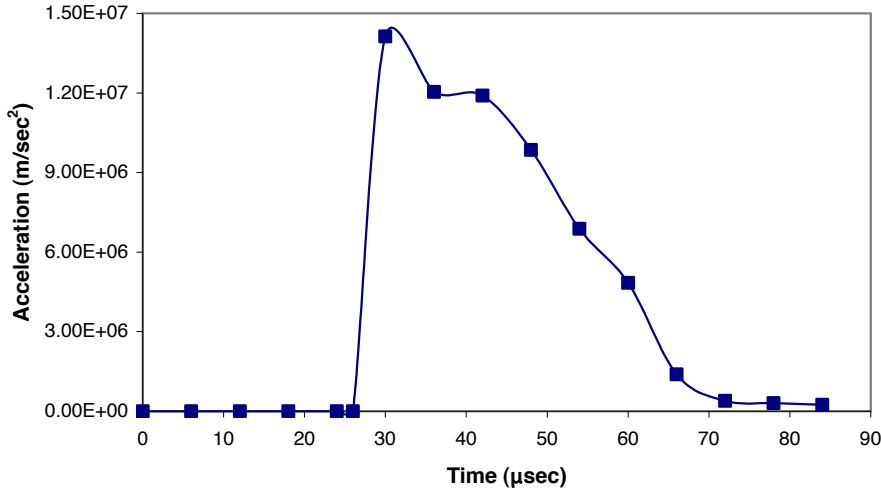


Figure 9. Crack tip acceleration as a function of time.

The crack propagation profile and time of initiation are subsequently used for calculating crack acceleration. The acceleration profile is plotted in Figure 9 and shows that crack acceleration is $1.4 \times 10^7 \text{ m/sec}^2$ just after initiation and decreases afterwards. It is plausible that crack acceleration is even higher as crack extension occurs by void coalescence and the crack jumps from zero to finite velocity.

Figure 10 shows the variation of the stress intensity factor with time. The stress intensity factor increases monotonically at the arrested crack until K_Q becomes large enough to produce initiation at the second crack tip. The first frame was captured after $4 \mu\text{sec}$, which is approximately the time for the shear wave to clear the near field region ($r = 5 \text{ mm}$). It can be seen that the stress intensity factor decreases rapidly from $K_Q = 1.38 \text{ MPa m}^{1/2}$ to $K(t) = 0.97 \text{ MPa m}^{1/2}$ in $4 \mu\text{sec}$. The stress intensity factor decreases further to $0.88 \text{ MPa m}^{1/2}$ after which it shows monotonic increase.

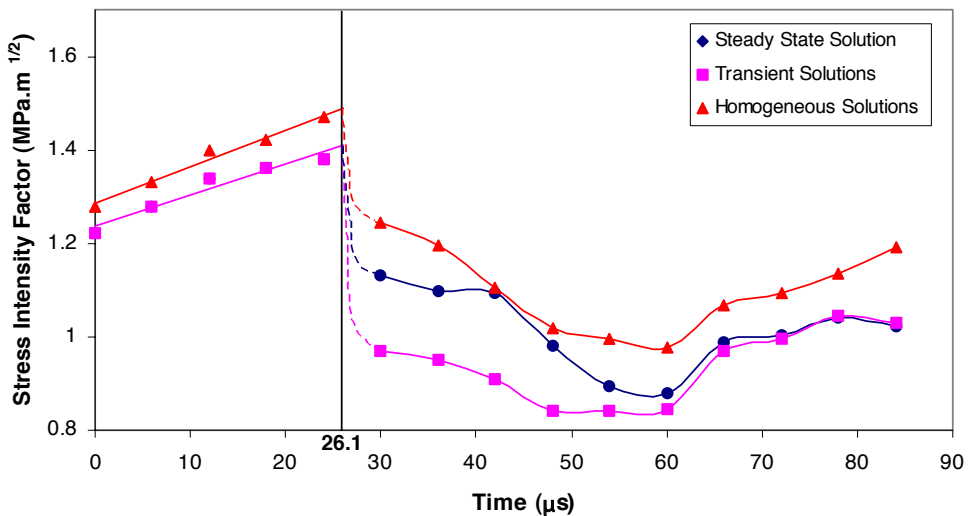


Figure 10. Stress intensity factor as a function of time.

To investigate the effect of transient higher order terms, analysis is also performed neglecting the transient higher order terms. The stress intensity factor history thus obtained using the steady state solution is also shown in [Figure 10](#). The average error introduced by neglecting transient higher order terms is as high as 20%. It is also observed that after 60 μsec , when the crack tip acceleration decreases considerably, the instantaneous stress intensity factor obtained with transient fields and steady state fields are in good agreement. This suggests that it is essential to include transient higher order terms in the stress field expansion in order to obtain an accurate value of the instantaneous stress intensity factor during highly transient phenomena.

[Figure 10](#) also shows the stress intensity factor history obtained using just the homogeneous stress field expansion. As expected, the error induced by just using homogeneous terms for analyzing the isochromatics in FGMs can be as high as 30% in the estimation of the stress intensity factor.

5. Concluding remarks

Motivated by the transient nature of the elastic fields in the vicinity of a growing crack tip, an approximation of the near-tip field in the form of an asymptotic expansion has been introduced. The analysis is performed for a crack growing in an arbitrary direction in an FGM. The higher order terms in the expansions take into account the recent history of the stress intensity factor and crack motion. The solution thus obtained is used to examine the effect of the transient terms on the near-tip stress fields. This is accomplished by discussing the effect of crack tip acceleration and rate of change of the stress intensity factor on synthetically generated contours of constant maximum shear stress and constant first stress invariant. To investigate the expediency of the analysis presented in this work, a sequence of dynamic fracture experiments has been performed. In doing so, the phenomenon of transition from a static crack to a dynamic crack is utilized. It is found that during this transition the crack tip accelerations can be as high as 10^8 m/sec^2 . The full field data obtained from these transition experiments were analyzed using the analytically derived equations. It is found that not including the transient higher order terms in the stress field expansion during highly transient phenomena might give rise to errors as high as 20% in the estimation of the stress intensity factor.

Appendix: Coefficients occurring in the expressions of ϕ_2 and ψ_2 , pages 600–601.

$$\begin{aligned}
 D_I(A_0(t)) &= -\frac{3c^{1/2}\rho_0}{\alpha_I^2\mu_0(k+2)}\frac{d}{dt}(c^{1/2}A_0(t)) & B_I^A(t) &= \frac{3c^2}{2\alpha_I^4}\left(\frac{\rho_0}{\mu_0(k+2)}\right)^2 A_0(t)\frac{dc}{dt} \\
 D_I(C_0(t)) &= -\frac{3c^{1/2}\rho_0}{\alpha_I^2\mu_0(k+2)}\frac{d}{dt}(c^{1/2}C_0(t)) & B_I^C(t) &= \frac{3c^2}{2\alpha_I^4}\left(\frac{\rho_0}{\mu_0(k+2)}\right)^2 C_0(t)\frac{dc}{dt} \\
 D_S(B_0(t)) &= -\frac{3c^{1/2}\rho_0}{\alpha_S^2\mu_0}\frac{d}{dt}(c^{1/2}B_0(t)) & B_S^B(t) &= \frac{3c^2}{2\alpha_S^4}\left(\frac{\rho_0}{\mu_0}\right)^2 B_0(t)\frac{dc}{dt} \\
 D_S(D_0(t)) &= -\frac{3c^{1/2}\rho_0}{\alpha_S^2\mu_0}\frac{d}{dt}(c^{1/2}D_0(t)) & B_S^D(t) &= \frac{3c^2}{2\alpha_S^4}\left(\frac{\rho_0}{\mu_0}\right)^2 D_0(t)\frac{dc}{dt}
 \end{aligned}$$

References

- [Abanto-Bueno and Lambros 2006] J. Abanto-Bueno and J. Lambros, “An experimental study of mixed mode crack initiation and growth in functionally graded materials”, *Exp. Mech.* **46**:2 (2006), 179–196.
- [Atkinson and List 1978] C. Atkinson and R. D. List, “Steady state crack propagation into media with spatially varying elastic properties”, *Int. J. Eng. Sci.* **16**:10 (1978), 717–730.
- [Chalivendra et al. 2003] V. B. Chalivendra, A. Shukla, and V. Parameswaran, “Quasi-static stress fields for a crack inclined to the property gradation in functionally graded materials”, *Acta Mech.* **162**:1-4 (2003), 167–184.
- [Dally and Riley 2005] J. W. Dally and W. F. Riley, *Experimental stress analysis*, College House Enterprises, 2005.
- [Dally and Shukla 1979] J. W. Dally and A. Shukla, “Dynamic crack behavior at initiation”, *Mech. Res. Commun.* **6**:4 (1979), 239–244.
- [Der and Barker 1978] V. K. Der and D. C. Barker, D. B. and Holloway, “A split birefringent coating technique to determine dynamic stress intensity factors”, *Mech. Res. Commun.* **5**:6 (1978), 313–318.
- [Erdogan 1995] F. Erdogan, “Fracture mechanics of functionally graded materials”, *Compos. Eng.* **5**:7 (1995), 753–770.
- [Freund 1990] L. B. Freund, *Dynamic fracture mechanics*, Cambridge University Press, Cambridge, 1990.
- [Freund and Rosakis 1992] L. B. Freund and A. J. Rosakis, “The structure of the near-tip field during transient elastodynamic crack growth”, *J. Mech. Phys. Solids* **40**:3 (1992), 699–719.
- [Gu and Asaro 1997] P. Gu and R. J. Asaro, “Cracks in functionally graded materials”, *Int. J. Solids Struct.* **34**:1 (1997), 1–17.
- [Jain and Shukla 2004] N. Jain and A. Shukla, “Displacements, strains and stresses associated with propagating cracks in materials with continuously varying properties”, *Acta Mech.* **171**:1-2 (2004), 75–103.
- [Jain and Shukla 2006] N. Jain and A. Shukla, “Mixed mode dynamic fracture in particulate reinforced functionally graded materials”, *Exp. Mech.* **46**:2 (2006), 137–154.
- [Jain et al. 2004] N. Jain, C. E. Rousseau, and A. Shukla, “Crack-tip stress fields in functionally graded materials with linearly varying properties”, *Theor. Appl. Fract. Mech.* **42**:2 (2004), 155–170.
- [Jin and Noda 1994] Z. H. Jin and N. Noda, “Crack-tip singular field in nonhomogeneous materials”, *J. Appl. Mech. (Trans. ASME)* **61** (1994), 738–739.
- [Kim and Paulino 2004] J. H. Kim and G. H. Paulino, “*T*-stress in orthotropic functionally graded materials: Lekhnitskii and Stroh formalisms”, *Int. J. Fract.* **126**:4 (2004), 345–384.
- [Li and Weng 2002] C. Y. Li and G. J. Weng, “Yoffe-type moving crack in a functionally graded piezoelectric material”, *P. Roy. Soc. Lond. A Mat.* **A458**:2018 (2002), 381–399.
- [Li et al. 2000] H. Li, J. Lambros, B. A. Cheeseman, and M. H. Santare, “Experimental investigation of the quasi-static fracture of functionally graded materials”, *Int. J. Solids Struct.* **37**:27 (2000), 3715–3732.
- [Marur and Tippur 2000] P. R. Marur and H. V. Tippur, “Numerical analysis of crack tip fields in functionally graded materials with a crack normal to the elastic gradient”, *Int. J. Solids Struct.* **37**:38 (2000), 5353–5370.
- [Nakagaki et al. 1998] M. Nakagaki, H. Sasaki, and S. Hagihara, “A study of crack in functionally graded material under dynamic loading”, *Dynamic Fracture, Failure and Deformation, ASME* **300** (1998), 1–6.
- [Parameswaran and Shukla 1998] V. Parameswaran and A. Shukla, “Dynamic fracture of a functionally gradient material having discrete property variation”, *J. Mater. Sci.* **33**:13 (1998), 3303–3311.
- [Parameswaran and Shukla 2000] V. Parameswaran and A. Shukla, “Processing and characterization of a model functionally gradient materials”, *J. Mater. Sci.* **35**:1 (2000), 21–29.
- [Rousseau and Tippur 2001] C.-E. Rousseau and H. V. Tippur, “Dynamic fracture of compositionally graded materials with cracks along the elastic gradient: experiments and analysis”, *Mech. Mater.* **33**:7 (2001), 403–421.
- [Shukla and Chona 1987] A. Shukla and R. Chona, “The stress field surrounding a rapidly propagating curving crack”, pp. 86–99 in *Fracture Mechanics: Eighteenth Symposium, ASTM STP 945*, edited by D. T. Read and R. P. Reed, 1987.
- [Shukla and Jain 2004] A. Shukla and N. Jain, “Dynamic damage growth in particle reinforced graded materials”, *Int. J. Impact Eng.* **30**:7 (2004), 777–803.

- [Sladek et al. 2005] J. Sladek, V. Sladek, and C. Zhang, “The MLPG method for crack analysis in anisotropic functionally graded materials”, *Structure Integrity and Durability* **1** (2005), 131–144.
- [Surendranath et al. 2003] H. Surendranath, H. A. Bruck, and S. Gowrisankaran, “Enhancing the optimization of material distributions in composite structures using gradient architectures”, *Int. J. Solids Struct.* **40**:12 (2003), 2999–3020.
- [Suresh and Mortensen 1998] S. Suresh and A. Mortensen, *Functionally graded materials*, The Institute of Materials, IOM Communications Ltd., London, 1998.
- [Tilbrook et al. 2005] M. T. Tilbrook, R. J. Moon, and M. Hoffman, “Curved crack propagation in homogeneous and graded materials”, *Fatigue Fract. Eng. Mater. Struct.* **28**:11 (2005), 939–950.
- [Wang and Meguid 1994] X. D. Wang and S. A. Meguid, “On the dynamic crack propagation in an interface with spatially varying elastic properties”, *Int. J. Fract.* **69**:1 (1994), 87–99.
- [Zhang et al. 2003] C. Zhang, J. Sladek, and V. Sladek, “Effects of material gradients on transient dynamic mode-III stress intensity factors in a FGM”, *Int. J. Solids Struct.* **40**:20 (2003), 5251–5270.

Received 27 Jul 2006. Accepted 23 Sep 2006.

NITESH JAIN: nitesh_jain@goodyear.com

Corporate Research, The Goodyear Tire and Rubber Company, 142 Goodyear Blvd., Akron, OH 44305, United States

ARUN SHUKLA: shuklaa@egr.uri.edu

Dynamic Photomechanics Laboratory, Department of Mechanical Engineering and Applied Mechanics, University of Rhode Island, 110 Wales Hall, 92 Upper College Rd., Kingston, RI 02881, United States

ASYMPTOTIC HOMOGENIZATION MODEL FOR THREE-DIMENSIONAL NETWORK REINFORCED COMPOSITE STRUCTURES

KRISHNA S. CHALLAGULLA, ANASTASIS GEORGIADES AND ALEXANDER L. KALAMKAROV

The method of asymptotic homogenization is used to develop a comprehensive micromechanical model pertaining to three-dimensional composite structures with an embedded periodic network of isotropic reinforcements, the spatial arrangement of which renders the behavior of the given structures macroscopically anisotropic. The model developed in this paper allows the transformation of the original boundary value problem into a simpler one that is characterized by some effective elastic coefficients. These coefficients are calculated from a so-called *unit cell* or periodicity problem, and are shown to depend solely on the geometric and material characteristics of the unit cell and are completely independent of the global formulation of the boundary-value problem. As such, the effective elastic coefficients are universal in nature and can be used to study a wide variety of boundary value problems. The model is illustrated by means of several examples of a practical importance and it is shown that the effective properties of a given composite structure can be tailored to satisfy the requirements of a particular application by changing certain geometric parameters such as the size or relative orientation of the reinforcements. For the special case in which the reinforcements form only a two-dimensional (in-plane) network, the results converge to those of previous models obtained either by means of asymptotic homogenization or by stress-strain relationships in the reinforcements.

1. Introduction

Recent trends have seen the integration of composite materials into new engineering platforms where they replace or strategically compliment other traditional structural materials. Presently, composites can be found in a wide range of applications ranging from sporting and recreational goods, to large-scale structures in the mechanical, aerospace, transportation and civil engineering fields. The continued incorporation of composite materials into new applications can be facilitated if their macroscopic behavior can be predicted at the design stage. To meet this objective, comprehensive micromechanical models must be developed. The effectiveness of such models largely depends on the acknowledgment of the fact that composites have to be approached from two different angles; microscopic and macroscopic. The microscopic view-point addresses the unique behavior and individual characteristics of the various constituents such as the reinforcing fibers and the matrix material, whereas the macroscopic perspective treats the overall composite structure as a single entity. A successful micromechanical model is one which takes both the local and the global aspects of the composite into consideration; it is sophisticated enough to consider the geometrical orientation and mechanical interaction of the various constituents at

Keywords: asymptotic homogenization, composite structures, 3D spatial network, unit cell, effective elastic coefficients.
This work has been supported by the Natural Sciences and Engineering Research Council of Canada (NSERC)..

the local level, but not too convoluted to be readily amenable to analytic and numerical treatments at the macroscopic stress/strain level.

The problem of micromechanical modeling of composites made up of inclusions embedded in a matrix has been the subject of investigation for many years. Among the earlier models developed were the composite spheres model [Hashin 1962] pertinent to macroscopically isotropic composites, and the composite cylinders model proposed by Hashin and Rosen [1964]. In the former model, the inclusions are treated as spherical particles of radius a embedded in a region of matrix of radius b . The absolute size of the particles is allowed to vary, but the ratio of a/b is kept constant. The model was used to estimate the shear and bulk moduli of macroscopically isotropic composites. For the macroscopically anisotropic (in particular, transversely isotropic) composite material, the composite cylinders model treats the reinforcing fibers as cylindrical inclusions of radius a associated with a region of matrix of radius b . As with the composite spheres model, the absolute size of the reinforcements is allowed to vary in order to cover all the available continuous material, but the ratio a/b is kept constant.

Other early work includes the self-consistent scheme [Hill 1965; Budiansky 1965] where a composite is modeled by rigid inclusions embedded in an incompressible matrix, and the Hashin and Shtrikman model [Hashin and Shtrikman 1963a; 1963b]. In their work, Hashin and Shtrikman employed a variational approach to determine upper and lower limits for the effective elastic properties [Hashin and Shtrikman 1963a] as well as electric and thermal conductivities [Hashin and Shtrikman 1963b] of multiphase materials (with quasiisotropic global characteristics). It was discovered that the upper and lower bounds were close to one another (thus representing a reasonably accurate estimate of the properties of the multiphase material) when the properties of the individual constituents were of comparable magnitude. Later on, Milton [1981; 1982] obtained higher-order bounds for the elastic, electromagnetic, and transport properties of two-component composites. Eshelby [1957] studied the case of an ellipsoidal inclusion or inhomogeneity within an infinite matrix and showed that knowing the uniform strain inside the inclusion or homogeneity is sufficient to determine such quantities as the strain fields both near and far from the inclusion/inhomogeneity, the total strain energy in the matrix, etc. Hill [1963] studied the problem of two isotropic media forming perfect bond and having arbitrary volume fractions. Irrespective of the geometry of either component, Hill obtained a complete solution for the special case when these components have equal rigidities but different compressibilities. Russel [1973] studied the problem of slender elastic illusions (of arbitrary cross-section) embedded in a preferred direction within an infinite elastic medium strained uniformly at infinity. His model permitted the calculation of the longitudinal tensile modulus and Poisson's ratio, as well as the bulk modulus of the composite. The author then applied the model to the special case of slender spheroidal inclusions. In the same work, Russel also examined the effect of the inclusion's volume fraction on the elastic properties of the composite. Other work can be found, among others, in [Mori and Tanaka 1973; Sendekyj 1974; Christensen 1990].

More recently, Drugan and Willis [1996] used the Hashin–Shtrikman variational principle generalized by the second author for random microstructures to derive constitutive equations for two-phase composites of arbitrary isotropy; Kalamkarov and Liu [1998] developed a multiphase fiber-matrix composite material model using a work conjugate approach to derive a so-called mesostructure; Zeman and Šejnoha [2001] used the finite element method to determine effective elastic coefficients of graphite epoxy composites having a random distribution of fibers in a transverse plane section of the composite by extracting an approximate periodicity from the fiber distribution.

Phenomena occurring in composite materials can often be described by means of partial differential equations which are characterized by two vastly different scales: a microscopic scale which reflects the periodicity of the regular composite and a macroscopic scale which is a manifestation of the global formulation of the boundary value problem. The microscopic scale is of the same order of magnitude as the size or spacing of the reinforcements, whereas the macroscopic scale has an order of magnitude similar to a characteristic dimension of the composite structure. The coupling of these two scales in the original problem renders the solution of the pertinent differential equations a very difficult task. To overcome this difficulty, the method of asymptotic homogenization can be used to decouple the microscopic and the macroscopic variations, so that each can be solved independently or sequentially. The mathematical framework of asymptotic homogenization can be found in [Bensoussan et al. 1978; Sanchez-Palencia 1980; Kalamkarov 1992; Cioranescu and Donato 1999; Cioranescu and Paulin 1999] and others. In recent years, asymptotic homogenization methods have been used to analyze periodic composite and smart structures, see, for example, the pioneering work of Duvaut [1976] on inhomogeneous plates; Caillerie [1984] applied a two-scale formalism directly to the three-dimensional problem of a thin non-homogeneous layer. Accordingly, Caillerie introduced two sets of rapid coordinates. One of these, in the tangential directions, is associated with rapid periodic oscillations in the composite properties. The other is associated with the small thickness of the layer and takes into consideration that there is no periodicity in this transverse direction; Kohn and Vogelius [1984], Kohn and Vogelius [1985] adopted this approach in their study of the pure bending of a thin, linearly elastic homogeneous plate; Guedes and Kikuchi [1990] used a finite element approach to compute effective elastic properties (including error estimates) of composite materials. In his monograph, Kalamkarov [1992], studied a wide variety of elastic and thermoelastic boundary-value problems using the asymptotic homogenization and derived expressions for the effective properties of different structures such as laminated and reinforced plates and shells, infinite cylinders with wavy surfaces, etc; Kalamkarov and Kolpakov [2001] used asymptotic homogenization techniques to derive effective elastic and piezoelectric coefficients for a smart plate; Kalamkarov and Georgiades [2002] applied the asymptotic homogenization method to general 3-dimensional smart composites with nonhomogeneous boundary conditions (which generate boundary-layer like solutions) and obtained effective elastic, piezoelectric, thermal expansion and hygroscopic expansion coefficients. The same authors, Kalamkarov and Georgiades [2004] and Georgiades and Kalamkarov [2004], obtained effective elastic, piezoelectric and thermal expansion coefficients pertinent to wafer- and rib-reinforced smart plates; Georgiades et al. [2006] obtained effective coefficients for thin smart network-reinforced plates.

The present paper develops a novel asymptotic homogenization model for three-dimensional network reinforced composite structures; see Figure 1. In this model, the composite structure is made of periodically arranged unit cells and different elements of unit cell can be made of different materials.

The rest of the paper is organized as follows. The basic problem formulation and model development is presented in Section 2. Section 3 derives the general model for three-dimensional network reinforced composite structures and Section 4 uses it to analyze and discuss various examples. Finally Section 5 concludes the paper.

2. Homogenization model for three-dimensional structures

2.1. General model. Consider a general composite structure representing an inhomogeneous solid occupying domain G with boundary ∂G that contains a large number of periodically arranged reinforcements as shown in [Figure 2](#).

The elastic deformation of this structure can be described by means of the following set of equations:

$$\frac{\partial \sigma_{ij}^\varepsilon}{\partial x_j} = f_i \quad \text{in } G, \quad \mathbf{u}^\varepsilon(\mathbf{x}) = 0 \quad \text{on } \partial G, \quad (1)$$

where,

$$\sigma_{ij}^\varepsilon\left(\mathbf{x}, \frac{\mathbf{x}}{\varepsilon}\right) = C_{ijkl}\left(\frac{\mathbf{x}}{\varepsilon}\right) e_{kl}^\varepsilon\left(\mathbf{x}, \frac{\mathbf{x}}{\varepsilon}\right) \quad (2)$$

$$e_{ij}^\varepsilon\left(\mathbf{x}, \frac{\mathbf{x}}{\varepsilon}\right) = \frac{1}{2} \left[\frac{\partial u_i}{\partial x_j}\left(\mathbf{x}, \frac{\mathbf{x}}{\varepsilon}\right) + \frac{\partial u_j}{\partial x_i}\left(\mathbf{x}, \frac{\mathbf{x}}{\varepsilon}\right) \right]. \quad (3)$$

Here, C_{ijkl} is the tensor of elastic coefficients, e_{kl} is the strain tensor and \mathbf{u} is the displacement field. Finally, f_i represent body forces. The elastic coefficients satisfy the familiar symmetry relationships $C_{ijkl} = C_{jikl} = C_{klij}$ and we assume that they also satisfy the strong convexity relation $C_{ijkl}\chi_{ij}\chi_{kl} > 0$ for any 3×3 real matrix χ_{ij} . It is also assumed in [Equation \(2\)](#) that the C_{ijkl} coefficients are all periodic with a unit cell Y of characteristic dimension ε . It is assumed that ε is made nondimensional by dividing length of unit cell by a certain characteristic dimension of the overall structure. Furthermore, it is assumed that the other two dimensions of the unit cell are of the same order of magnitude as the length. Consequently, the periodic composite structure in [Figure 2](#) is seen to be made up of a large number of unit-cells periodically arranged within the domain G . Let us also note at this point that if the boundary conditions in [Equation \(1\)](#) were made nonhomogeneous, then the resulting field expansions (displacement, strain, etc) would be characterized by boundary-layer type solutions [[Kalamkarov and Georgiades 2002](#)]. However, the effective coefficients would not be affected in any way. Thus, for simplicity, homogeneous displacement boundary conditions are chosen here.

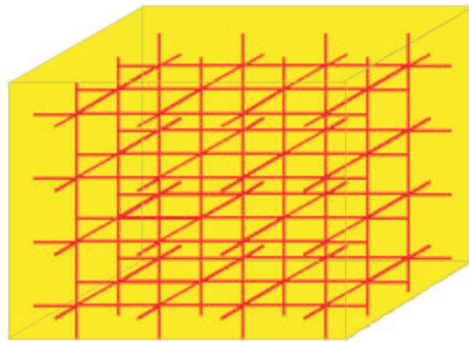


Figure 1. Three-dimensional network reinforced composite structure.

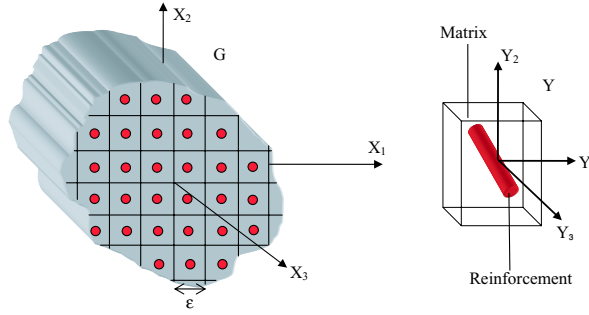


Figure 2. Three-dimensional composite structure with its periodicity (unit) cell.

2.2. Asymptotic expansion, governing equation, and unit cell problem. Kalamkarov and Georgiades [2002] develops the asymptotic homogenization model for the three-dimensional smart composite structures. In this section, only a brief overview of the steps involved in the development of the model are given in so far as it represents the starting point of our current work. The first step is to define the so-called fast or microscopic variables, as well as new rules of differentiation according to

$$y_i = \frac{x_i}{\varepsilon}, \quad \frac{\partial}{\partial x_i} \rightarrow \frac{\partial}{\partial x_i} + \frac{1}{\varepsilon} \frac{\partial}{\partial y_i}. \quad (4)$$

The introduction of these variables transforms the boundary value problem, by separating variables x_i and y_i , and corresponding stress field in Equations (1) and (2) into

$$\frac{\partial \sigma_{ij}^\varepsilon}{\partial x_j} + \frac{1}{\varepsilon} \frac{\partial \sigma_{ij}^\varepsilon}{\partial y_j} = f_i \quad \text{in } G, \quad u^\varepsilon = 0 \quad \text{on } \partial G, \quad (5)$$

$$\sigma_{ij}^\varepsilon(\mathbf{x}, \mathbf{y}) = C_{ijkl}(\mathbf{y}) \frac{\partial u_k}{\partial x_l}(\mathbf{x}, \mathbf{y}). \quad (6)$$

The displacement and stress fields are subsequently expressed as infinite power series in terms of the small parameter ε :

$$\begin{aligned} \mathbf{u}^\varepsilon(\mathbf{x}, \mathbf{y}) &= \mathbf{u}^{(0)}(\mathbf{x}, \mathbf{y}) + \varepsilon \mathbf{u}^{(1)}(\mathbf{x}, \mathbf{y}) + \varepsilon^2 \mathbf{u}^{(2)}(\mathbf{x}, \mathbf{y}) + \dots, \\ \sigma_{ij}^\varepsilon(\mathbf{x}, \mathbf{y}) &= \sigma_{ij}^{(0)}(\mathbf{x}, \mathbf{y}) + \varepsilon \sigma_{ij}^{(1)}(\mathbf{x}, \mathbf{y}) + \varepsilon^2 \sigma_{ij}^{(2)}(\mathbf{x}, \mathbf{y}) + \dots. \end{aligned} \quad (7)$$

Here all functions in \mathbf{y} are periodic with the unit cell Y (see Figure 2). By substituting Equations (4) and (6) into Equation (5) while considering at the same time the periodicity of $\mathbf{u}^{(i)}$ in y_j one can readily show that $\mathbf{u}^{(0)}$ is independent of the microscopic variable \mathbf{y} . Subsequently, by substituting Equation (7) into Equation (5) and equating like powers of ε one obtains a sequence of differential equations the first

two of which are

$$\frac{\partial \sigma_{ij}^{(0)}}{\partial y_j} = 0, \quad (8)$$

$$\frac{\partial \sigma_{ij}^{(1)}}{\partial y_j} + \frac{\partial \sigma_{ij}^{(0)}}{\partial x_j} = f_i, \quad (9)$$

where,

$$\sigma_{ij}^{(0)} = C_{ijkl} \left(\frac{\partial u_k^{(0)}}{\partial x_l} + \frac{\partial u_k^{(1)}}{\partial y_l} \right), \quad (10)$$

$$\sigma_{ij}^{(1)} = C_{ijkl} \left(\frac{\partial u_k^{(1)}}{\partial x_l} + \frac{\partial u_k^{(2)}}{\partial y_l} \right). \quad (11)$$

Combination of Equations (8) and (10) yields the following expression:

$$\frac{\partial}{\partial y_j} \left(C_{ijkl} \frac{\partial u_k^{(1)}(\mathbf{x}, \mathbf{y})}{\partial y_l} \right) = - \frac{\partial C_{ijkl}(\mathbf{y})}{\partial y_j} \frac{\partial u_k^{(0)}(\mathbf{x})}{\partial x_l}. \quad (12)$$

The separation of variables on the right-hand-side of Equation (12) allows to write down the solution as

$$u_n^{(1)}(\mathbf{x}, \mathbf{y}) = V_n(\mathbf{x}) + \frac{\partial u_k^{(0)}(\mathbf{x})}{\partial x_l} N_n^{kl}(\mathbf{y}), \quad (13)$$

where functions N_m^{kl} are periodic in \mathbf{y} and satisfy

$$\frac{\partial}{\partial y_j} \left(C_{ijmn}(\mathbf{y}) \frac{\partial N_m^{kl}(\mathbf{y})}{\partial y_n} \right) = - \frac{\partial C_{ijkl}}{\partial y_j}. \quad (14)$$

It is seen that Equation (14) depends entirely on the fast variable \mathbf{y} and is thus solved on the domain Y of the unit cell remembering at the same time the periodicity of C_{ijkl} , N_m^{kl} in y_i . Consequently, Equation (14) is appropriately referred to as the *unit-cell problem*.

The next important step in the model development is the homogenization process. This is achieved by first substituting Equation (13) into Equation (10) and combining the result with Equation (9). The resulting expression is finally integrated over the domain Y of the unit cell (with volume $|Y|$) remembering to treat x_i as a parameter as far as integration with respect to \mathbf{y} is concerned. This gives

$$\frac{1}{|Y|} \int_Y \frac{\partial \sigma_{ij}^{(1)}(\mathbf{x}, \mathbf{y})}{\partial y_j} dv + \tilde{C}_{ijkl} \frac{\partial^2 u_k^{(0)}(\mathbf{x})}{\partial x_j \partial x_l} = f_i,$$

where we have defined \tilde{C}_{ijkl} as the effective or homogenized elastic coefficients

$$\tilde{C}_{ijkl} = \frac{1}{|Y|} \int_Y \left(C_{ijkl}(\mathbf{y}) + C_{ijmn}(\mathbf{y}) \frac{\partial N_m^{kl}}{\partial y_n} \right) dv. \quad (15)$$

One observes that the effective coefficients are free from the periodicity complications that characterize their actual rapidly varying material counterparts, C_{ijkl} , and as such, are more amenable to analytical

and numerical treatment. The effective coefficients shown above are universal in nature and can be used to study a wide variety of boundary value problems associated with a given composite structure.

3. Three-dimensional network reinforced composite structures

For the problem at hand, we turn our attention to a general macroscopically anisotropic three-dimensional composite structure reinforced with N families of reinforcements or bars, see, for example, [Figure 1](#), where a particular case of 3 families of reinforcements is shown. The members of each family are made of generally different isotropic materials and are oriented at angles $\phi_1^n, \phi_2^n, \phi_3^n$, for $n = 1, 2, \dots, N$, with the y_1, y_2, y_3 axes respectively. Furthermore, they are assumed to be much stiffer than the surrounding matrix so that we are justified in neglecting the contribution of the latter in the ensuing analysis. For the particular case of framework or lattice network structures the surrounding matrix is absent and this is modeled by assuming zero matrix rigidity. The nature of the network structure of [Figure 1](#) is such that it would be more efficient if we first considered a simpler type of unit cell made of only a single reinforcement as shown in [Figure 3](#). Having solved this, the effective elastic coefficients of more general structures with several families of reinforcements can readily be determined by superposition of solution for each of them found separately. In doing so, we accept of course the error incurred at the regions of intersection between the reinforcements, but this error is highly localized and will not add significantly to the integral over the unit cell. A mathematical justification for this kind of argument in the form of the so-called principle of the split homogenized operator has been provided by [Bakhvalov and Panasenko \[1984\]](#). In order to calculate the effective coefficients for the simpler structure of [Figure 3](#), one must first solve the unit cell problem [Equation \(14\)](#) and then apply the formula in [Equation \(15\)](#).

3.1. Problem formulation. We begin the problem formulation for the structure of [Figure 3](#) by introducing the following notation:

$$b_{ij}^{kl} = C_{ijmn}(\mathbf{y}) \frac{\partial N_m^{kl}(\mathbf{y})}{\partial y_n} + C_{ijkl}. \quad (16)$$

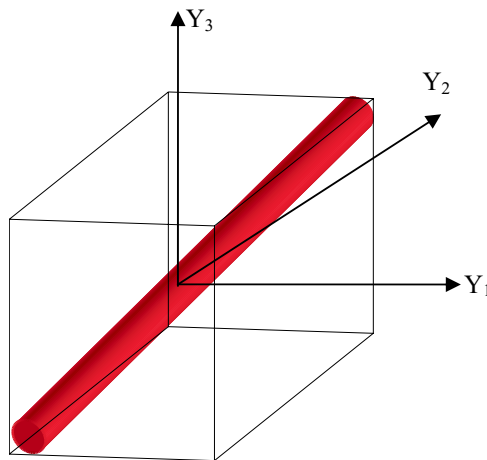


Figure 3. Unit cell of composite network reinforced with a single reinforcement family.

With this definition in mind, the unit cell problem of Equation (14) becomes $\partial\{b_{ij}^{kl}\}/\partial y_j = 0$.

Because of the multiconstituent nature of the network structures under consideration, it is prudent to also consider the interfacial conditions that exist between the matrix and the reinforcements. The first such condition is a direct consequence of the continuity of the $N_m^{kl}(y)$ functions and may be stated as:

$$N_n^{kl}(r)|_s = N_n^{kl}(m)|_s. \quad (17)$$

Furthermore, continuity of the displacement field leads to:

$$b_{ij}^{kl}n_j(r)|_s = b_{ij}^{kl}n_j(m)|_s. \quad (18)$$

In Equations (17) and (18) the suffixes s, r, m stand for *interface, reinforcement* and *matrix*, respectively. n_j are the components of the unit normal vector to the interface. As mentioned earlier on, we will further assume that the structure of interest is made of high modulus reinforcements and “soft” matrix. As such, we may take $b_{ij}^{kl}(m) \approx 0$ and thus, condition in Equation (18) becomes $b_{ij}^{kl}n_j(r)|_s = 0$.

In summary, the final problem that must be solved in conjunction with Equation (17) for the three-dimensional network structure reinforced with a single family of isotropic bars is:

$$\frac{\partial}{\partial y_j} \{b_{ij}^{kl}\} = 0, \quad b_{ij}^{kl}n_j(r)|_s = 0. \quad (19)$$

3.2. Coordinate transformation. Before proceeding to the solution of the unit cell problem given in Equation (19) we perform a coordinate transformation of the microscopic coordinates $\{y_1, y_2, y_3\}$ onto $\{\eta_1, \eta_2, \eta_3\}$ as shown in Figure 4. The coordinate transformation is carried out in such a way that the η_1 coordinate axis coincides with the direction of the reinforcement and η_2, η_3 are perpendicular to it.

Thus, derivatives transform according to

$$\frac{\partial}{\partial y_i} = q_{ji} \frac{\partial}{\partial \eta_j},$$

where q_{ij} are the components of the matrix of direction cosines characterizing the axis rotation.

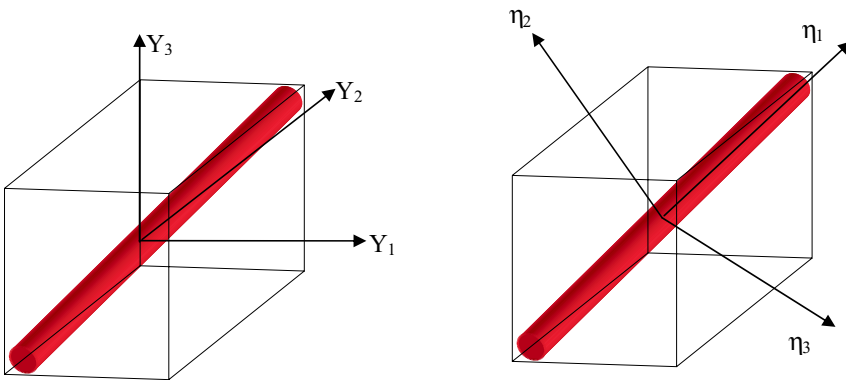


Figure 4. Unit cell in original and rotated macroscopic coordinates.

With this choice of coordinate system, it is evident that problems in Equation (19) will be independent of η_1 and will only depend on η_2 and η_3 . Consequently, derivatives with respect to η_1 in the pertinent differential equations vanish and the analysis of the problem is simplified.

3.3. Determination of elastic coefficients. With reference to Figure 4 we begin by rewriting Equation (19) in terms of the η_i coordinates to get

$$b_{ij}^{kl} = C_{ijmn}q_{pn} \frac{\partial N_m^{kl}}{\partial \eta_p} + C_{ijkl}, \quad (20)$$

$$b_{ij}^{kl}q_{2i}n'_2 + b_{ij}^{kl}q_{3i}n'_3|_s = 0. \quad (21)$$

Here n'_i represent the components of the unit normal vector expressed in terms of the new coordinates. Expanding Equation (20) remembering at the same time the independence of the problem on η_1 gives:

$$b_{ij}^{kl} = C_{ijkl} + C_{ijm1}q_{21} \frac{\partial N_m^{kl}}{\partial \eta_2} + C_{ijm2}q_{22} \frac{\partial N_m^{kl}}{\partial \eta_2} + C_{ijm3}q_{23} \frac{\partial N_m^{kl}}{\partial \eta_2} \\ + C_{ijm1}q_{31} \frac{\partial N_m^{kl}}{\partial \eta_3} + C_{ijm2}q_{32} \frac{\partial N_m^{kl}}{\partial \eta_3} + C_{ijm3}q_{33} \frac{\partial N_m^{kl}}{\partial \eta_3}. \quad (22)$$

It is possible to solve the system of Equations (20) and (21) by assuming a linear variation of the N_i^{kl} functions in η_2 and η_3 , that is,

$$N_1^{kl} = \lambda_1\eta_2 + \lambda_2\eta_3, \quad N_2^{kl} = \lambda_3\eta_2 + \lambda_4\eta_3, \quad N_3^{kl} = \lambda_5\eta_2 + \lambda_6\eta_3, \quad (23)$$

where λ_i are constants to be determined from the boundary conditions. It should be noted that the values of the constants λ_i are different for the different combinations of the suffixes k, l in Equation (23) and in the sequel. From Equations (22) and (23), the elastic b_{ij}^{kl} coefficients may be written as follows

$$b_{11}^{kl} = C_{11kl} + C_{11}q_{21}\lambda_1 + C_{11}q_{31}\lambda_2 + C_{12}q_{22}\lambda_3 + C_{12}q_{32}\lambda_4 + C_{13}q_{23}\lambda_5 + C_{13}q_{33}\lambda_6, \\ b_{22}^{kl} = C_{22kl} + C_{12}q_{21}\lambda_1 + C_{12}q_{31}\lambda_2 + C_{22}q_{22}\lambda_3 + C_{22}q_{32}\lambda_4 + C_{23}q_{23}\lambda_5 + C_{23}q_{33}\lambda_6, \\ b_{33}^{kl} = C_{33kl} + C_{13}q_{21}\lambda_1 + C_{13}q_{31}\lambda_2 + C_{23}q_{22}\lambda_3 + C_{23}q_{32}\lambda_4 + C_{33}q_{23}\lambda_5 + C_{33}q_{33}\lambda_6, \\ b_{23}^{kl} = C_{23kl} + C_{44}q_{23}\lambda_3 + C_{44}q_{33}\lambda_4 + C_{44}q_{22}\lambda_5 + C_{44}q_{32}\lambda_6, \\ b_{13}^{kl} = C_{13kl} + C_{55}q_{23}\lambda_1 + C_{55}q_{33}\lambda_2 + C_{55}q_{21}\lambda_5 + C_{55}q_{31}\lambda_6, \\ b_{12}^{kl} = C_{12kl} + C_{66}q_{22}\lambda_1 + C_{66}q_{32}\lambda_2 + C_{66}q_{21}\lambda_3 + C_{66}q_{31}\lambda_4. \quad (24)$$

Here C_{ij} are the elastic coefficients of the isotropic reinforcements in the contracted notation (see, for example, [Reddy 1997]). Substituting Equation (24) in Equation (21) and letting j take on the values 1,

2, 3 results in 6 linear algebraic equations in λ_i for $i = 1, 2, \dots, 6$

$$\begin{aligned}
 A_1\lambda_1 + A_2\lambda_2 + A_3\lambda_3 + A_4\lambda_4 + A_5\lambda_5 + A_6\lambda_6 + A_7 &= 0, \\
 A_8\lambda_1 + A_9\lambda_2 + A_{10}\lambda_3 + A_{11}\lambda_4 + A_{12}\lambda_5 + A_{13}\lambda_6 + A_{14} &= 0, \\
 A_{15}\lambda_1 + A_{16}\lambda_2 + A_{17}\lambda_3 + A_{18}\lambda_4 + A_{19}\lambda_5 + A_{20}\lambda_6 + A_{21} &= 0, \\
 A_{22}\lambda_1 + A_{23}\lambda_2 + A_{24}\lambda_3 + A_{25}\lambda_4 + A_{26}\lambda_5 + A_{27}\lambda_6 + A_{28} &= 0, \\
 A_{29}\lambda_1 + A_{30}\lambda_2 + A_{31}\lambda_3 + A_{32}\lambda_4 + A_{33}\lambda_5 + A_{34}\lambda_6 + A_{35} &= 0, \\
 A_{36}\lambda_1 + A_{37}\lambda_2 + A_{38}\lambda_3 + A_{39}\lambda_4 + A_{40}\lambda_5 + A_{41}\lambda_6 + A_{42} &= 0,
 \end{aligned} \tag{25}$$

where A_i are constants which depend on the direction of the reinforcement as well as its mechanical properties. The explicit expressions for these constants are given in [Appendix A](#). Once the system of [Equation \(25\)](#) is solved, the determined λ_i coefficients are substituted back into [Equation \(24\)](#) to solve for the b_{ij}^{kl} coefficients. In turn, these are used to calculate the effective elastic coefficients of the structure of [Figure 3](#) by integrating over the volume of the unit cell as explained below in [Section 3.4](#). Before closing this section, it would not be amiss to mention that if [Equation \(23\)](#) were assumed to be polynomials of a higher order, then after following the procedure outlined here and comparing terms of equal powers of η_2 and n_3 , all of the terms would vanish except the linear ones.

3.4. Effective elastic coefficients. The effective elastic coefficients of the network composite structure of [Figure 3](#) are obtained by means of the rule of homogenization in [Equation \(15\)](#), which, on account of notation in [Equation \(16\)](#) becomes

$$\tilde{C}_{ijkl} = \frac{1}{|Y|} \int_Y b_{ij}^{kl} dv.$$

Assuming that the length (within unit cell), cross-sectional area of the reinforcement and volume of the unit cell in coordinates y_1, y_2, y_3 are L, A, V , respectively, then the effective elastic coefficients are,

$$\tilde{C}_{ijkl} = \frac{AL}{V} b_{ij}^{kl} = V_f b_{ij}^{kl},$$

where b_{ij}^{kl} is constant and V_f is the volume fraction of the reinforcement within the unit cell. It can be proved that the effective elastic coefficients \tilde{C}_{ijkl} satisfy the same symmetry and convexity relationships as their actual material counterparts C_{ijkl} [[Bakhvalov and Panasenko 1984](#)].

For network structures with more than a single family of reinforcements, the effective coefficients can be determined by superposition ignoring stress concentration and other local complications at the regions of intersections. For example, for a network composite structure with N families of isotropic reinforcements, the effective elastic coefficients will be given by

$$\tilde{C}_{ijkl} = \sum_{n=1}^N V_f^{(n)} b_{ij}^{(n)kl}, \tag{26}$$

where the superscript (n) represents the n -th reinforcement family.

4. Examples of network structures

Let us now apply above developed general theory to the analysis of some examples of practical importance.

Example 1 (Convergence of model for the case of 2D composite network). For the purposes of the first example, we will verify the validity of our model for the case of 2D network structures whereby the reinforcements lie entirely in the Y_2 - Y_3 plane. [Figure 5](#) shows the pertinent unit cell for such a structure.

Solving [Equation \(25\)](#) for λ_i and substituting the results into [Equation \(24\)](#) gives the following expressions for the all nonzero elastic coefficients:

$$\begin{aligned} b_{11}^{11} &= E \cos^4 \theta, & b_{11}^{12} &= E \cos^3 \theta \sin \theta, & b_{11}^{22} &= b_{12}^{12} = E \cos^2 \theta \sin^2 \theta, \\ b_{22}^{12} &= E \cos \theta \sin^3 \theta, & b_{22}^{22} &= E \sin^4 \theta, & b_{ij}^{kl} &= b_{kl}^{ij}, \end{aligned}$$

while the effective coefficients of the composite structure are

$$\begin{aligned} \tilde{C}_{11} &= \frac{AL}{V} E \cos^4 \theta, & \tilde{C}_{22} &= \frac{AL}{V} E \sin^4 \theta, & \tilde{C}_{12} &= \tilde{C}_{66} = \frac{AL}{V} E \cos^2 \theta \sin^2 \theta, \\ \tilde{C}_{16} &= \frac{AL}{V} E \cos^3 \theta \sin \theta, & \tilde{C}_{26} &= \frac{AL}{V} E \cos \theta \sin^3 \theta, & \tilde{C}_{ij} &= \tilde{C}_{ji}. \end{aligned}$$

where we have denoted by E Young's modulus of the reinforcing material. These results are the same as those earlier obtained by [Kalamkarov \[1992\]](#) who developed an asymptotic homogenization model for a thin network-reinforced composite shell and [Pshenichnov \[1982\]](#) who used a different approach based on stress-strain relationships in the reinforcements.

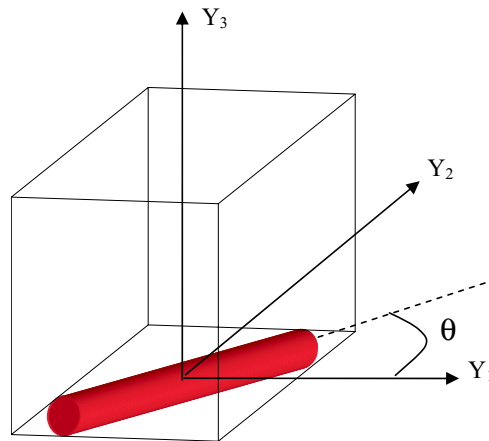


Figure 5. Unit cell for (2D) structure with reinforcements in the Y_1 - Y_2 plane.

Example 2. The second example pertains to the cubic structure of [Figure 6](#). This composite structure has three families of reinforcements, each family oriented along one of the coordinate axes.

Noting that $q_{ij} = \delta_{ij}$, where δ_{ij} is the Kronecker symbol, the values of λ_i for the reinforcement in the Y_1 direction are readily obtained from Equation (25) to be as follows

$$\begin{aligned}\lambda_1 &= \frac{-C_{12kl}}{C_{66}}, & \lambda_2 &= \frac{-C_{13kl}}{C_{55}}, & \lambda_3 &= \frac{C_{33}C_{22kl} - C_{23}C_{33kl}}{C_{23}^2 - C_{22}C_{33}}, \\ \lambda_4 + \lambda_5 &= \frac{-C_{23kl}}{C_{44}}, & \lambda_6 &= \frac{C_{22}C_{33kl} - C_{23}C_{22kl}}{C_{23}^2 - C_{22}C_{33}}.\end{aligned}$$

It is observed here that because the transformation tensor q equals the second-order identity sensor, the number of equations is reduced from 6 to 5 and the unknowns λ_4 and λ_5 occur everywhere as the linear combination of $\lambda_4 + \lambda_5$. The same result will occur with reinforcements oriented entirely along either the Y_2 or the Y_3 directions. In both of these cases, a pair of the unknown λ_i occurs as a linear combination and the number of equations is reduced to 5 (with correspondingly 5 unknowns). From Equation (24) the b_{ij}^{kl} coefficients are given by

$$b_{11}^{kl} = C_{11kl} + \frac{[C_{12}C_{33} - C_{13}C_{23}]C_{22kl} + [C_{13}C_{22} - C_{12}C_{23}]C_{33kl}}{C_{23}^2 - C_{22}C_{33}}.$$

After substituting expressions for elastic coefficients we obtain

$$b_{11}^{11} = E, \quad b_{11}^{22} = b_{11}^{33} = b_{11}^{23} = b_{11}^{13} = b_{11}^{12} = 0, \quad b_{22}^{kl} = b_{33}^{kl} = b_{23}^{kl} = b_{13}^{kl} = b_{12}^{kl} = 0. \quad (27)$$

Repeating the procedure for the reinforcement in the Y_2 direction yields $b_{22}^{22} = E$ with the remaining coefficients equal to zero, and for the reinforcement in the Y_3 direction the only nonzero coefficient is $b_{33}^{33} = E$.

We are now ready to compute the effective elastic coefficients of the cubic network structures shown in Figure 6. Let the length (within unit cell) and cross-sectional area of the i -th reinforcement in the Y_i direction be L_i and A_i respectively (in coordinates y_1, y_2, y_3). Also let us assume that E_i is the Young's modulus of the reinforcement in the Y_i direction. Then, for a unit cell of volume V , the corresponding volume fraction v_i is given by $v_i = A_i L_i / V$. Thus, from Equations (26) and (27) the nonzero effective elastic coefficients for the composite network structure of Figure 6 are

$$\tilde{C}_{11} = \frac{A_1 L_1}{V} E_{(1)} = v_1 E_{(1)}, \quad \tilde{C}_{22} = \frac{A_2 L_2}{V} E_{(2)} = v_2 E_{(2)}, \quad \tilde{C}_{33} = \frac{A_3 L_3}{V} E_{(3)} = v_3 E_{(3)}, \quad (28)$$

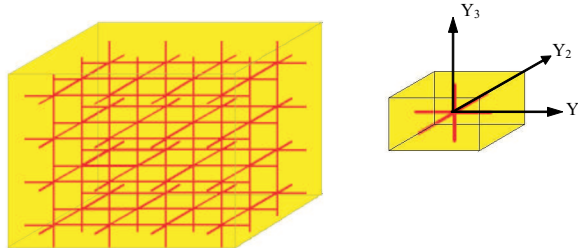


Figure 6. Cubic network structure with reinforcements in Y_1, Y_2, Y_3 directions.

where $E_{(i)}$ is the young's modulus of the i -th reinforcement. In the case where the reinforcements have the same material properties (namely Young's modulus E) the expressions in Equation (28) become

$$\tilde{C}_{11} = \frac{A_1}{V} E = v_1 E, \quad \tilde{C}_{22} = \frac{A_2}{V} E = v_2 E, \quad \tilde{C}_{33} = \frac{A_3}{V} E = v_3 E.$$

It is observed that all the off-diagonal terms in the stiffness matrix are zero. This is partly because the reinforcements in a particular direction have no effect on the stiffness of the structure in the directions perpendicular to it and partly due to the fact that the matrix stiffness is neglected in this model.

Example 3. This example pertains to a composite network structure with a conical arrangement of isotropic reinforcements. In this example (to be referred to as structure S_1) the unit cell is made of three reinforcements oriented as shown in Figure 7. The expressions for the effective coefficients are readily determined from Equations (24)–(26). Although the expressions are too lengthy to be reproduced here, some of these coefficients will be presented graphically in the next section.

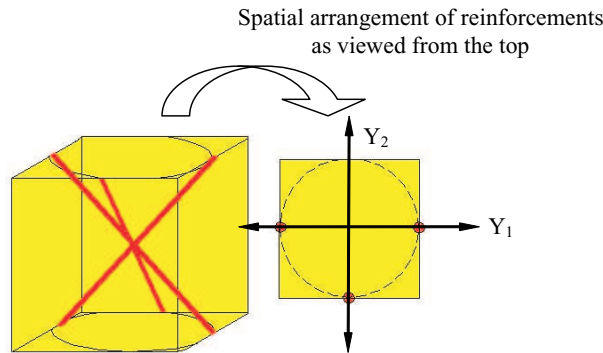


Figure 7. Unit cell for composite network structure with conical arrangement of isotropic reinforcements (structure S_1).

Example 4. In this example let us consider a general unit cell (S_2) as shown in Figure 8. The general unit cell consists of three reinforcements two of which span from different corners of the unit cell to the diametrically opposite ones and the third reinforcement is oriented from the middle of the bottom edge to the middle of the top edge on the opposite face.

The effective coefficients for this structure are calculated as for the ones in the previous examples. The resulting expressions are too lengthy to be reproduced here. However as an illustration some of the effective coefficients are plotted vs. the height of the unit-cell in the following section.

4.1. Plots of effective properties and discussion. The mathematical model and methodology presented in Sections 3.1–3.4 can be used in analysis and design to tailor the effective elastic coefficients of any three-dimensional composite network structure by changing the material, number, orientation and/or cross-sectional area and material selection of the reinforcements. In this section typical effective coefficients will be computed and plotted. For illustration purposes, we will assume that the reinforcements have a Young's modulus and Poisson's ratio equal to 200 GPa and 0.3, respectively.

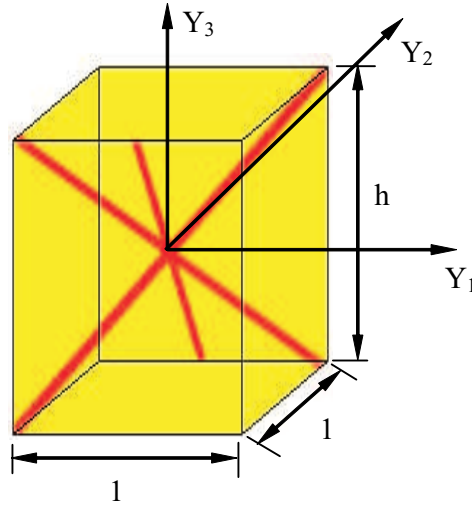


Figure 8. Structure S_2 .

We will begin with the plot of some of the effective coefficients for the structure shown in Figure 7. The effective coefficients will be plotted vs. the total volume fraction of the reinforcements within the unit cell. As expected, the effective coefficients increase with an increase in the overall reinforcement volume fraction, see for example Figures 9 and 10.

It would also be of interest to plot the variation of some of the effective coefficients of structure S_1 with the angle of inclination of the reinforcements to the Y_3 axis. As this angle increases, the reinforcements are oriented progressively closer to the Y_1 and Y_2 axis and the stiffness in these directions is expected to increase. Indeed a reference to Figures 11 and 12 shows precisely that. On the contrary, (see Figure 13) at the same time as the stiffness in the Y_1 and Y_2 directions increases the corresponding value in the Y_3 direction decreases because the reinforcements are oriented further away from the Y_3 axis.

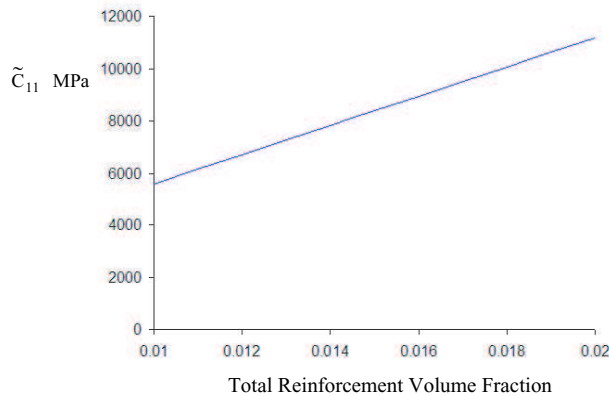


Figure 9. Plot of \tilde{C}_{11} vs. reinforcement volume fraction for structure S_1 .

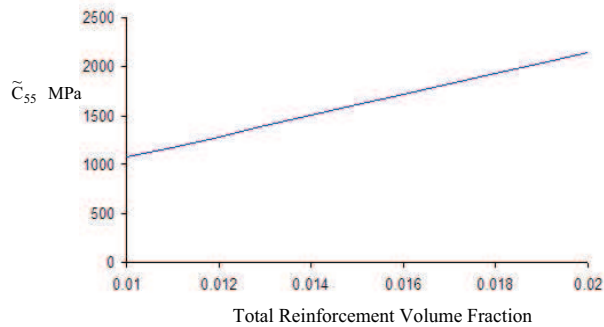


Figure 10. Plot of \tilde{C}_{55} vs. reinforcement volume fraction for structure S_1 .

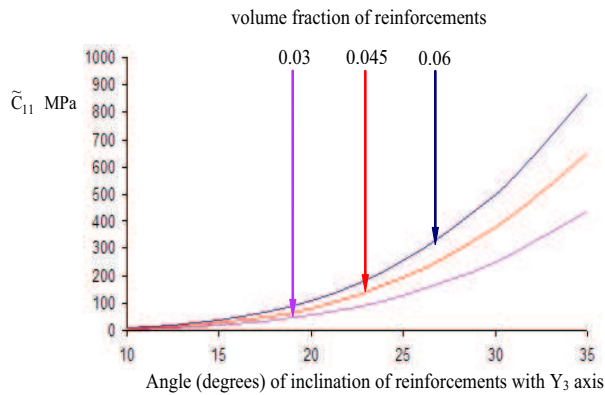


Figure 11. Plot of the \tilde{C}_{11} effective coefficient vs. inclination of reinforcements with the Y_3 axis pertaining to structure S_1 for reinforcement volume fractions equal to 0.03, 0.045, and 0.06.

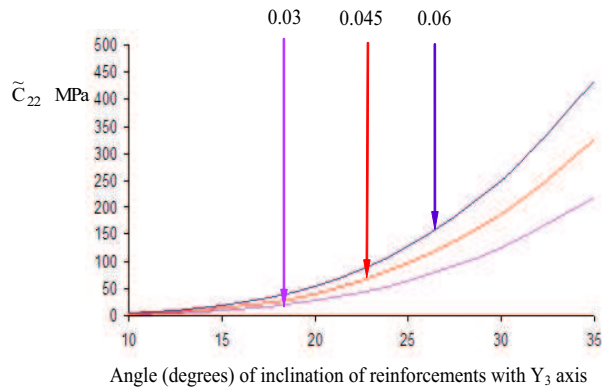


Figure 12. Plot of the \tilde{C}_{22} effective coefficient vs. inclination of reinforcements with the Y_3 axis pertaining to structure S_1 for reinforcement volume fractions equal to 0.03, 0.045, and 0.06.

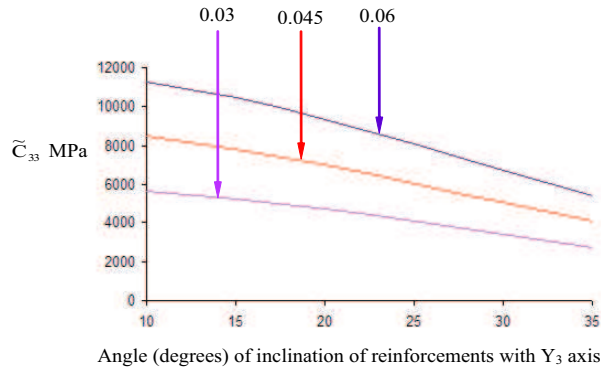


Figure 13. Plot of the \tilde{C}_{33} effective coefficient vs. inclination of reinforcements with the Y_3 axis pertaining to structure S_1 for reinforcement volume fractions equal to 0.03, 0.045, and 0.06.

We now turn our attention to the S_2 composite structure (Figure 8) and plot some of the effective coefficients by varying the relative height of the unit cell (height divided by length) but keeping the other dimensions as well as the cross-sectional area of the reinforcements constant. It is noted that as the relative height of the unit cell is varied, the lengths and orientations of reinforcements change.

Figure 14 shows a plot of effective coefficients \tilde{C}_{11} , \tilde{C}_{22} , \tilde{C}_{33} , and \tilde{C}_{55} vs. the relative height of the unit cell. As the relative height of the unit-cell increases, the volume fraction of the reinforcements decreases and at the same time the reinforcements are oriented closer to the Y_3 axis and further away from Y_1 , and Y_2 axis. Both of these effects contribute to the stiffness in the Y_1 , and Y_2 direction decreasing. However, \tilde{C}_{33} increases because the increase in stiffness due to a smaller angle of inclination with the Y_3 axis dominates the decrease in stiffness due to the reinforcements volume fraction decreasing.

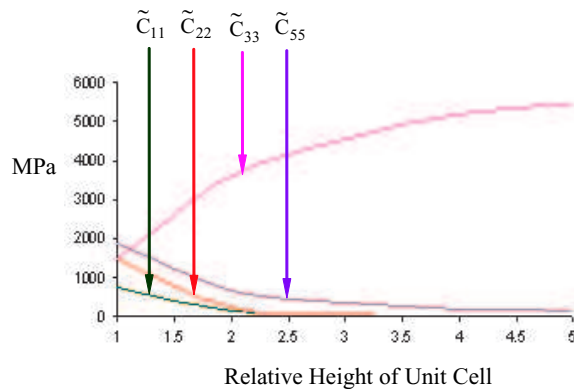


Figure 14. Plot of \tilde{C}_{11} , \tilde{C}_{22} , \tilde{C}_{33} , and \tilde{C}_{55} effective coefficient vs. relative height of the unit cell for S_2 structure shown in Figure 8.

Finally, we are interested to compare a typical effective coefficient of structures S_1 and S_2 by varying the volume fraction. We vary the volume fraction of structure S_1 by varying the reinforcement cross-sectional area and of structure S_2 by varying the relative height of the unit cell. From Figure 15 we see that \tilde{C}_{33} for S_1 increases as the volume fraction increases, as expected for larger diameter reinforcements. However, pertinent to structure S_2 , increasing the volume fraction of the reinforcements is tantamount to decreasing the relative height of the unit cell. This has the effect of increasing the deviation of the reinforcements from the Y_3 axis which dominates the increase in the overall reinforcement volume fraction. Consequently, the net effect is that a decrease in the relative height of the unit cell produces a reduction (in a nonlinear fashion) in the stiffness of the composite structure in the Y_3 direction. Thus, under these circumstances, beyond a certain volume fraction, S_1 is stiffer in the Y_3 direction. Of course these trends can be easily changed. For example, if the volume fraction of the reinforcements of S_2 is changed by keeping all dimensions of unit cell constant (that is, direction cosines pertinent to reinforcements unchanged) and changing their cross-sectional area, then a higher volume fraction would increase \tilde{C}_{33} , and the relative stiffness between the two structures would be different than that depicted in Figure 15. What is important is to realize that the model allows for complete flexibility in designing a structure with desirable mechanical and geometrical characteristics.

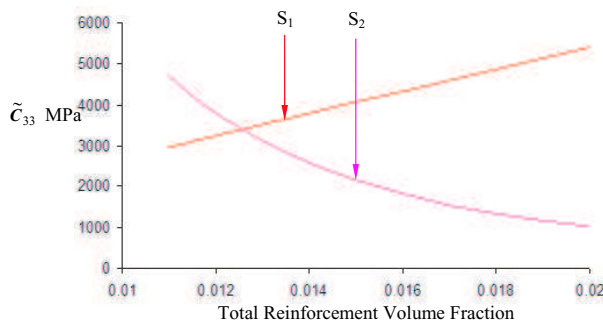


Figure 15. Plot of \tilde{C}_{33} vs. total volume fraction for structures S_1 (Figure 7) and S_2 (Figure 8).

5. Conclusions

A comprehensive three-dimensional micromechanical model pertaining to globally anisotropic periodic composite structures reinforced with a spatial network of isotropic reinforcements is developed. The model, which is developed using the asymptotic homogenization technique, transforms the original boundary value problem into a simpler one that is characterized by some effective elastic coefficients. The effective coefficients are shown to depend only on the pertinent geometric and material characteristics of the periodicity cell and are therefore independent of the global formulation of the problem.

The derived model is illustrated by means of different composite structures with cubic or conical configurations of reinforcements. The usefulness of this work lies in the fact that the model can be used to tailor the effective coefficients of any three-dimensional composite structure to meet the requirements of a particular application by changing such geometric or other parameters as the material, number,

cross-sectional dimensions, and relative angular orientation of the reinforcements. In the particular case in which the reinforcements form only a two-dimensional (planar) network, the results are shown to converge to previous models developed by Kalamkarov [1992] who also used the asymptotic homogenization technique and Pshenichnov [1982] who used stress-strain relationships in the reinforcements.

Appendix A

$$\begin{aligned}
 A_1 &= q_{21}^2 C_{11} + q_{22}^2 C_{66} + q_{23}^2 C_{55}, & A_2 &= q_{21} q_{31} C_{11} + q_{22} q_{32} C_{66} + q_{23} q_{33} C_{55}, \\
 A_3 &= q_{21} q_{22} C_{12} + q_{21} q_{22} C_{66}, & A_4 &= q_{21} q_{32} C_{12} + q_{22} q_{31} C_{66}, \\
 A_5 &= q_{21} q_{23} C_{13} + q_{21} q_{23} C_{55}, & A_6 &= q_{21} q_{33} C_{13} + q_{23} q_{31} C_{55}, \\
 A_7 &= q_{21} C_{11kl} + q_{22} C_{12kl} + q_{23} C_{13kl}, & A_8 &= q_{21} q_{31} C_{11} + q_{22} q_{32} C_{66} + q_{23} q_{33} C_{55}, \\
 A_9 &= q_{31}^2 C_{11} + q_{32}^2 C_{66} + q_{33}^2 C_{55}, & A_{10} &= q_{31} q_{22} C_{12} + q_{21} q_{32} C_{66}, \\
 A_{11} &= q_{31} q_{32} C_{12} + q_{32} q_{31} C_{66}, & A_{12} &= q_{31} q_{23} C_{13} + q_{21} q_{33} C_{55}, \\
 A_{13} &= q_{31} q_{33} C_{13} + q_{33} q_{31} C_{55}, & A_{14} &= q_{31} C_{11kl} + q_{32} C_{12kl} + q_{33} C_{13kl}, \\
 A_{15} &= q_{21} q_{22} C_{66} + q_{21} q_{22} C_{12}, & A_{16} &= q_{21} q_{32} C_{66} + q_{22} q_{31} C_{12}, \\
 A_{17} &= q_{21}^2 C_{66} + q_{22}^2 C_{22} + q_{23}^2 C_{44}, & A_{18} &= q_{21} q_{31} C_{66} + q_{22} q_{32} C_{22} + q_{23} q_{33} C_{44}, \\
 A_{19} &= q_{22} q_{23} C_{23} + q_{22} q_{23} C_{44}, & A_{20} &= q_{22} q_{33} C_{23} + q_{23} q_{32} C_{44}, \\
 A_{21} &= q_{21} C_{12kl} + q_{22} C_{22kl} + q_{23} C_{23kl}, & A_{22} &= q_{31} q_{22} C_{66} + q_{21} q_{32} C_{12}, \\
 A_{23} &= q_{31} q_{32} C_{66} + q_{32} q_{31} C_{12}, & A_{24} &= q_{21} q_{31} C_{66} + q_{22} q_{32} C_{22} + q_{23} q_{33} C_{44}, \\
 A_{25} &= q_{31}^2 C_{66} + q_{32}^2 C_{22} + q_{33}^2 C_{44}, & A_{26} &= q_{32} q_{23} C_{23} + q_{22} q_{33} C_{44}, \\
 A_{27} &= q_{32} q_{33} C_{23} + q_{33} q_{32} C_{44}, & A_{28} &= q_{31} C_{12kl} + q_{32} C_{22kl} + q_{33} C_{23kl}, \\
 A_{29} &= q_{21} q_{23} C_{55} + q_{21} q_{23} C_{13}, & A_{30} &= q_{21} q_{33} C_{55} + q_{23} q_{31} C_{13}, \\
 A_{31} &= q_{22} q_{23} C_{44} + q_{22} q_{23} C_{23}, & A_{32} &= q_{22} q_{33} C_{44} + q_{23} q_{32} C_{23}, \\
 A_{33} &= q_{21}^2 C_{55} + q_{22}^2 C_{44} + q_{23}^2 C_{33}, & A_{34} &= q_{21} q_{31} C_{55} + q_{22} q_{32} C_{44} + q_{23} q_{33} C_{33}, \\
 A_{35} &= q_{21} C_{13kl} + q_{22} C_{23kl} + q_{23} C_{33kl}, & A_{36} &= q_{31} q_{23} C_{55} + q_{21} q_{33} C_{13}, \\
 A_{37} &= q_{31} q_{33} C_{55} + q_{33} q_{31} C_{13}, & A_{38} &= q_{23} q_{32} C_{44} + q_{22} q_{33} C_{23}, \\
 A_{39} &= q_{32} q_{33} C_{44} + q_{33} q_{32} C_{23}, & A_{40} &= q_{21} q_{31} C_{55} + q_{22} q_{32} C_{44} + q_{23} q_{33} C_{33}, \\
 A_{41} &= q_{31}^2 C_{55} + q_{32}^2 C_{44} + q_{33}^2 C_{33}, & A_{42} &= q_{31} C_{13kl} + q_{32} C_{23kl} + q_{33} C_{33kl}.
 \end{aligned}$$

References

- [Bakhvalov and Panasenko 1984] N. Bakhvalov and G. Panasenko, *Homogenisation: averaging processes in periodic media*, Kluwer Academic Publishers, Netherlands, 1984.
- [Bensoussan et al. 1978] A. Bensoussan, J. L. Lions, and G. Papanicolaou, *Asymptotic analysis for periodic structures*, North-Holland Publ. Comp., Amsterdam, 1978.
- [Budiansky 1965] B. Budiansky, "On the elastic moduli of some heterogeneous materials", *J. Mech. Phys. Solids* **13** (1965), 223–227.
- [Caillerie 1984] D. Caillerie, "Thin elastic and periodic plates", *Math. Appl. Sci.* **6** (1984), 159–191.

- [Christensen 1990] R. M. Christensen, “A critical evaluation for a class for a class of micromechanics models”, *J. Mech. Phys. Solids* **38** (1990), 379–404.
- [Cioranescu and Donato 1999] D. Cioranescu and P. Donato, *An introduction to homogenization*, Oxford University Press, Oxford, United Kingdom, 1999.
- [Cioranescu and Paulin 1999] D. Cioranescu and J. S. J. Paulin, *Homogenization of reticulated structures*, Springer-Verlag, New York, 1999.
- [Drugan and Willis 1996] W. J. Drugan and J. R. Willis, “A micromechanics-based nonlocal constitutive equation and estimates of representative volume element size for elastic composites”, *J. Mech. Phys. Solids* **44**:4 (1996), 497–524.
- [Duvaut 1976] G. Duvaut, “Analyse fonctionnelle et mécanique des milieux continus”, pp. 119–132 in *Proceedings of the 14th IUTAM congress*, Delft, 1976.
- [Eshelby 1957] J. D. Eshelby, “The determination of the elastic field of an ellipsoidal inclusion, and related problems”, *Proc. R. Soc. Lond.* **A241** (1957), 376–396.
- [Georgiades and Kalamkarov 2004] A. V. Georgiades and A. L. Kalamkarov, “Asymptotic homogenization models for smart composite plates with rapidly varying thickness: part II-applications”, *Int. J. Multiscale Computational Engineering* **2**:1 (2004), 149–172.
- [Georgiades et al. 2006] A. V. Georgiades, A. L. Kalamkarov, and K. S. Challagulla, “Asymptotic homogenization model for smart network composite reinforced plates”, *Smart Mater. Struct.* **15** (2006), 1197–1210.
- [Guedes and Kikuchi 1990] J. M. Guedes and N. Kikuchi, “Preprocessing and postprocessing for materials based on the homogenization method with adaptive finite element methods”, *Comput. Methods Appl. Mech. Eng.* **83** (1990), 143–198.
- [Hashin 1962] Z. Hashin, “The elastic moduli of heterogeneous materials”, *J. Appl. Mech.* **29** (1962), 143.
- [Hashin and Rosen 1964] Z. Hashin and B. W. Rosen, “The elastic moduli of fiber-reinforced materials”, *J. Appl. Mech.* **31** (1964), 223–232.
- [Hashin and Shtrikman 1963a] Z. Hashin and S. Shtrikman, “A variational approach to the theory of elastic behavior of multiphase materials”, *J. Mech. Phys. Solids* **11** (1963a), 127–140.
- [Hashin and Shtrikman 1963b] Z. Hashin and S. Shtrikman, “Conductivity of polycrystals”, *Phys. Rev.* **130**:1 (1963b), 129–133.
- [Hill 1963] R. Hill, “Elastic properties of reinforced solids”, *J. Mech. Phys. Solids* **11** (1963), 357–372.
- [Hill 1965] R. Hill, “A self-consistent mechanics of composite materials”, *J. Mech. Phys. Solids* **13** (1965), 213–222.
- [Kalamkarov 1992] A. L. Kalamkarov, *Composite and reinforced elements of construction*, Wiley, Chichester, UK, 1992.
- [Kalamkarov and Georgiades 2002] A. L. Kalamkarov and A. V. Georgiades, “Micromechanical modeling of smart composite structures”, *Smart Mater. Struct.* **11** (2002), 423–434.
- [Kalamkarov and Georgiades 2004] A. L. Kalamkarov and A. V. Georgiades, “Asymptotic homogenization models for smart composite plates with rapidly varying thickness: part I-theory”, *Int. J. Multiscale Computational Engineering* **2**:1 (2004), 133–148.
- [Kalamkarov and Kolpakov 2001] A. L. Kalamkarov and A. G. Kolpakov, “A new asymptotic model for a composite piezoelectric plate”, *Int. J. Solids Struct.* **38** (2001), 6027–6044.
- [Kalamkarov and Liu 1998] A. L. Kalamkarov and H. Q. Liu, “A new model for a multiphase fiber-matrix composite materials”, *Compos. B: Eng.* **29B**:5 (1998), 643–653.
- [Kohn and Vogelius 1984] R. V. Kohn and M. Vogelius, “A new model for thin plates with rapidly varying thickness”, *Int. J. Solids Struct.* **20** (1984), 333–350.
- [Kohn and Vogelius 1985] R. V. Kohn and M. Vogelius, “A new model for thin plates with rapidly varying thickness, II: a convergence proof”, *Quart. J. Appl. Math.* **43** (1985), 1–22.
- [Milton 1981] G. W. Milton, “Bounds on the electromagnetic, elastic, and other properties of two-component composites”, *Phys. Rev. Lett.* **46** (1981), 542–545.
- [Milton 1982] G. W. Milton, “Bounds on the elastic and transport properties of two-component composites”, *J. Mech. Phys. Solids* **30** (1982), 177–191.

- [Mori and Tanaka 1973] T. Mori and K. Tanaka, “Average stress in matrix and average energy of materials with misfitting inclusions”, *Acta. Metall. Mater.* **21** (1973), 571–574.
- [Pshenichnov 1982] G. I. Pshenichnov, *Theory of thin elastic network plates and shells*, Nauka, Moscow, 1982. In Russian.
- [Reddy 1997] J. N. Reddy, *Mechanics of laminated composite plates*, CRC Press, New York, 1997.
- [Russel 1973] W. B. Russel, “On the effective moduli of composite materials: effect of fiber length and geometry at dilute concentrations”, *Z. Angew. Math. Phys.* **24** (1973), 581–600.
- [Sanchez-Palencia 1980] E. Sanchez-Palencia, *Non-homogeneous media and vibration theory*, Springer-Verlag, Berlin, 1980.
- [Sendekyj 1974] G. P. Sendekyj, *Elastic behavior of composites*, Composite Materials, Vol. 2. Mechanics of composite materials, Academic Press, New York, 1974.
- [Zeman and Šejnoha 2001] J. Zeman and M. Šejnoha, “Numerical evaluation of effective elastic properties of graphite fiber tow impregnated by polymer matrix”, *J. Mech. Phys. Solids* **49** (2001), 69–90.

Received 21 Jun 2006. Accepted 1 Oct 2006.

KRISHNA S. CHALLAGULLA: kchallag@dal.ca

Department of Mechanical Engineering, Dalhousie University, Halifax, Nova Scotia, B3J 2X4, Canada

ANASTASIS GEORGIADES: tasos.georgiades@dal.ca

Department of Mechanical Engineering, Dalhousie University, Halifax, Nova Scotia, B3J 2X4, Canada

ALEXANDER L. KALAMKAROV: alex.kalamkarov@dal.ca

Department of Mechanical Engineering, Dalhousie University, Halifax, Nova Scotia, B3J 2X4, Canada

THERMAL STRESS ANALYSIS OF FUNCTIONALLY GRADED COMPOSITES WITH TEMPERATURE-DEPENDENT MATERIAL PROPERTIES

H. K. CHING AND J. K. CHEN

Thermomechanical deformation of a functionally graded composite (FGC) in elevated temperature environments is investigated by the meshless local Petrov–Galerkin method. The FGC is modeled as a 2-D linearly elastic solid which consists of ceramic ZrO_2 and alloy Ti-6Al-4V with the volume fraction varying along a predefined direction. Unlike most investigations performed so far, temperature-dependent thermophysical and thermomechanical properties are considered for both constituents in this work. The effective material properties of the FGC are evaluated with the micromechanical models. An FGC hollow cylinder under an internal temperature change is first studied; the numerical results agree very well with those computed by the finite element method. The parametric studies with respect to different profiles of graded FGCs are performed for a clamped-clamped thick beam and a square plate with a central hole, respectively. It is found that inclusion of temperature dependence for the material properties has a great impact on thermomechanical response prediction for FGCs in elevated temperature environments.

1. Introduction

Among functionally graded composites (FGCs), those made from ceramics and metals have received considerable attention in the structural ceramic applications, including gas turbines, hot engine components, packaging encapsulants, thermoelectric generators, and human implants, to name a few. The reasons for receiving such a great attention are two-fold: (1) the ceramic phase provides corrosion, wear and erosion resistance, possesses higher compressive strength, and can protect the structural components from severe thermal or biological environments; (2) a microscopically heterogeneous FGC engineered to a continuous spatial variation by grading the volume fraction of the material constituents can reduce interfacial stresses in a coated structure, minimize stress concentration or intensity factors, and attenuate stress waves, etc.

Numerous theoretical studies have been conducted for investigating linearly elastic thermomechanical response of FGCs. Although analytical approaches provide closed-form solutions [Zimmerman and Lutz 1999; Tarn 2001; Sankar and Tzeng 2002; Vel and Batra 2002; 2003; Ootao and Tanigawa 2004; 2005], they are limited to simple geometries, certain types of gradation of material properties (for example, exponential or power law distribution), special types of boundary conditions and loadings. The above constraints can be relaxed when numerical approaches are applied. In those with finite element methods [Takahashi et al. 1992; Reddy and Chin 1998; Praveen et al. 1999; Wang and Mai 2005], homogeneous elements with different effective material properties are often used to model the macro, nonhomogeneous nature of FGCs. To better treat the nonhomogeneity of the material properties, meshless methods may

Keywords: functionally graded composites, thermomechanics, temperature-dependent material properties, micromechanical model, meshless local Petrov–Galerkin method.

provide a more cost-effective approach for computer-aided design tools for FGM materials. One of the unique features of meshless methods is that only a set of scattered nodes that need not be connected to form closed polygons is required to model the physical domain. They not only can avoid the numerical difficulties of mesh entanglement and distortion during high intensity loading interactions as often encountered in finite element and finite difference analyses, but lend themselves a natural way to treat initiation and growth of voids/cracks as well. It is not our intention to give an exhaustive review for the meshless particle methods; interested readers should refer to the literature for details. One of the well-known meshless methods is the meshless local Petrov–Galerkin (MLPG) method proposed by [Atluri and Zhu \[1998\]](#). It is a truly mesh-free approach in terms of both interpolation of variables and integration of energy because it does not require a background mesh to evaluate various integrals appearing in the local weak formulation of the problem. Recently, the MLPG method has successfully been employed in the thermomechanical analysis of FGCs [[Qian and Ching 2004](#); [Qian and Batra 2004](#); [2005](#); [Sladek et al. 2003](#); [2005](#); [Ching and Yen 2005](#); [Ching and Chen 2006](#)].

Most of the theoretical investigations reported so far have not taken into account the temperature dependence for the material properties. Therefore, those results in general are only adequate for small change of temperature in an FGC or the variation of material properties against temperature being insignificant. To accurately describe thermomechanical behaviors of FGCs, temperature dependence on the material properties should be considered. To our knowledge, only a few studies have included the effects of temperature-dependent material properties [[Praveen et al. 1999](#); [Wang and Mai 2005](#); [Wang and Tian 2005](#)]. The first two works examine deformation and stress in a 1-D axisymmetric hollow cylinder, and the third solves transient heat conduction problems for a 1-D strip. All the effective temperature-dependent properties used are evaluated using the simple rule of mixture, which does not account for the interaction between phases, and thus only give rough approximate values for most of the effective properties. As pointed out by [Ching and Chen \[2006\]](#), the effective material properties evaluated by different homogenization schemes could lead to significantly different thermomechanical response for an FGC material. Accordingly, a higher fidelity, micromechanics based model should be employed in evaluation of the effective material properties.

In this paper, thermomechanical response of a linearly elastic FGC under temperature loading is investigated by using the MLPG method. The FGCs considered consist of spherical particulates ZrO_2 and alloy matrix Ti-6Al-4V with the volume fraction varying over a predefined direction. For simplicity, it is modeled as a macro nonhomogeneous, isotropic, 2-D body. To accurately predict their thermomechanical response, both the temperature-dependent thermophysical and thermomechanical properties of the constituents are employed. The effective material properties of the FGC are evaluated with the micromechanical models. A hollow FGC cylinder is first studied with the effective material properties estimated by the rule of mixtures to validate the present MLPG solution with the finite element result [[Wang and Mai 2005](#)]. Then, parametric studies are performed with respect to different profiles of graded FGCs, for a clamped-clamped thick beam and a square plate with a central hole. The impact of temperature dependence for the material properties on thermo-mechanical response prediction of FGCs in elevated temperature environments is investigated.

2. Governing equations

Consider a 2-D isotropic solid occupying the domain Ω bounded by the boundary Γ and unstressed at a reference temperature. In rectangular Cartesian coordinates $\mathbf{x} = [x_1 \ x_2]^T$, (where the superscript T denotes transposition), the governing equations of elastostatics neglecting body forces and steady-state thermal equilibrium in the absence of internal heat sources are given by

$$\sigma_{ij,j} = 0 \quad \text{in } \Omega, \tag{1}$$

$$q_{j,j} = 0 \quad \text{in } \Omega, \tag{2}$$

where σ_{ij} and q_j are the components of the Cauchy stress tensor and the heat flux vector, respectively. A comma followed by index j denotes the partial differentiation with respect to coordinate x_j of a material point, and a repeated index implies summation over the range of the index. Equations (1) and (2) are supplemented with the boundary conditions

$$u_i = \bar{u}_i \quad \text{on } \Gamma_u, \quad \sigma_{ij}n_j = \bar{t}_i \quad \text{on } \Gamma_t \tag{3}$$

and

$$T = \bar{T} \quad \text{on } \Gamma_T, \quad q_jn_j = \bar{q} \quad \text{on } \Gamma_q, \quad q_jn_j = h(T - T_s) \quad \text{on } \Gamma_h. \tag{4}$$

In these equations the u_i are the displacement components, T is the change of temperature with respect to a reference state, \bar{u}_i are the prescribed displacements on Γ_u and \bar{t}_i are the given tractions on Γ_t where Γ_u and Γ_t are the complementary parts of the boundary Γ , that is, $\Gamma_u \cap \Gamma_t = \emptyset$ and $\Gamma_u \cup \Gamma_t = \Gamma$. The thermal conditions include a prescribed temperature \bar{T} specified on Γ_T , a given heat flux \bar{q} imposed on Γ_q , and a convection heat loss to an ambient temperature T_s occurring on Γ_h . Likewise, Γ_T , Γ_q and Γ_h constitute another set of complementary parts of the boundary. h is the coefficient of the convection, and n_j are the components of the unit outward normal to Γ .

The constitutive equation for thermal stresses is written in the matrix form

$$\boldsymbol{\sigma} = [\sigma_{11} \ \sigma_{22} \ \sigma_{12}]^T = \mathbf{D}\boldsymbol{\epsilon} - \boldsymbol{\beta}T,$$

$\boldsymbol{\epsilon}$ is the infinitesimal strain vector

$$\boldsymbol{\epsilon} = [\epsilon_{11} \ \epsilon_{22} \ \gamma_{12}]^T = \left[\frac{\partial u_1}{\partial x_1} \quad \frac{\partial u_2}{\partial x_2} \quad \frac{\partial u_2}{\partial x_1} + \frac{\partial u_1}{\partial x_2} \right]^T, \tag{5}$$

\mathbf{D} is the stiffness matrix and $\boldsymbol{\beta}$ is the stress-temperature matrix. For a linearly elastic, isotropic 2-D solid

$$\mathbf{D} = \frac{\bar{E}}{1 - \bar{\nu}^2} \begin{bmatrix} 1 & \bar{\nu} & 0 \\ \bar{\nu} & 1 & 0 \\ 0 & 0 & \frac{1}{2}(1 - \bar{\nu}) \end{bmatrix}, \quad \boldsymbol{\beta} = \beta [1 \ 1 \ 0]^T$$

in which $\bar{E} = E/(1 - \nu^2)$, $\bar{\nu} = \nu/(1 - \nu)$, and $\boldsymbol{\beta} = \alpha E/(1 - 2\nu)$ for plane strain with E , ν and α denoting the Young's modulus, Poisson's ratio, and coefficient of thermal expansion, respectively, and $\bar{E} = E$, $\bar{\nu} = \nu$, and $\boldsymbol{\beta} = \alpha E/(1 - \nu)$ for plane stress. The Fourier law for heat flux is $q_j = -\kappa T_{,j}$, where κ is the thermal conductivity. For an FGC material, the material properties E , ν , α , κ are functions of \mathbf{x} in general.

3. The MLPG formulation

3.1. Nodal interpolation. In the MLPG method [Atluri and Zhu 1998] the moving least squares approximation is adopted for forming the basis functions $\phi_i(\mathbf{x})$ for an unknown trial function. Let $f^h(\mathbf{x})$ be an approximation of a scalar function $f(\mathbf{x})$ given by

$$f^h(\mathbf{x}) = \mathbf{p}^T(\mathbf{x})\mathbf{a}(\mathbf{x}) = \sum_{j=1}^m p_j(\mathbf{x})a_j(\mathbf{x}), \quad (6)$$

where $\mathbf{p}(x_1, x_2) = [p_1(\mathbf{x}) \ p_2(\mathbf{x}) \ \dots \ p_m(\mathbf{x})]^T$ is a vector of the complete monomial basis of order m . For a 2-D problem, $\mathbf{p}(x_1, x_2) = [1 \ x_1 \ x_2]^T$ for $m = 3$ and $\mathbf{p}(x_1, x_2) = [1 \ x_1 \ x_2 \ x_1^2 \ x_1x_2 \ x_2^2]^T$ for $m = 6$. The m unknown coefficients $a_j(\mathbf{x})$ are determined by minimizing a weighted discrete L_2 norm given as

$$J = \sum_{i=1}^n W(\mathbf{x} - \mathbf{x}_i) [\mathbf{p}^T(\mathbf{x}_i)\mathbf{a}(\mathbf{x}) - \hat{f}_i]^2, \quad (7)$$

where n is the number of points in the neighborhood of point \mathbf{x} for which the weight function $W(\mathbf{x} - \mathbf{x}_i) > 0$, and \hat{f}_i refers to the nodal parameter of the function f .

Finding the extremum of J in Equation (7) with respect to $\mathbf{a}(\mathbf{x})$ leads to the system of linear equations

$$\mathbf{A}(\mathbf{x})\mathbf{a}(\mathbf{x}) = \mathbf{B}(\mathbf{x})\hat{\mathbf{f}}, \quad (8)$$

where the matrices $\mathbf{A}(\mathbf{x})$ and $\mathbf{B}(\mathbf{x})$ and the vector $\hat{\mathbf{f}}$ are

$$\begin{aligned} \mathbf{A}(\mathbf{x}) &= \sum_{i=1}^n W(\mathbf{x} - \mathbf{x}_i)\mathbf{p}(\mathbf{x}_i)\mathbf{p}^T(\mathbf{x}_i), \\ \mathbf{B}(\mathbf{x}) &= [W(\mathbf{x} - \mathbf{x}_1)\mathbf{p}(\mathbf{x}_1) \ W(\mathbf{x} - \mathbf{x}_2)\mathbf{p}(\mathbf{x}_2) \ \dots \ W(\mathbf{x} - \mathbf{x}_n)\mathbf{p}(\mathbf{x}_n)], \\ \hat{\mathbf{f}} &= [\hat{f}_1 \ \hat{f}_2 \ \dots \ \hat{f}_n]^T. \end{aligned}$$

Solving $\mathbf{a}(\mathbf{x})$ in Equation (8) and substituting it into Equation (6) results in the following relation for the nodal interpolation

$$f^h(\mathbf{x}) = \sum_{i=1}^n \phi_i(\mathbf{x})\hat{f}_i \quad \text{with} \quad \phi_i(\mathbf{x}) = \sum_{j=1}^m p_j(\mathbf{x})[\mathbf{A}^{-1}(\mathbf{x})\mathbf{B}(\mathbf{x})]_{ji},$$

where $\phi_i(\mathbf{x})$ is called the basis function of the moving least squares approximation corresponding to node i . Note that $\phi_i(\mathbf{x}_j)$ need not equal the Kronecker delta δ_{ij} , and thus $\hat{f}_i \neq f^h(\mathbf{x}_i)$ in general. For the matrix \mathbf{A} to be invertible the number of n points must not be smaller than m , that is, $n \geq m$. For $m = 3$ or 6, Chati and Mukherjee [2000] utilized the moving least squares approximation in their boundary node method and suggested that $15 \leq n \leq 30$ gives acceptable results for 2-D elastostatic problems.

In this study, the following Gaussian function is adopted as the weight function:

$$W(\mathbf{x} - \mathbf{x}_i) = \frac{\exp(-(d_i/c_i)^{2k}) - \exp(-(r_i/c_i)^{2k})}{1 - \exp(-(r_i/c_i)^{2k})} \quad \text{for} \quad 0 \leq d_i \leq r_i,$$

where c_i is the distance from node i to its third nearest neighboring node, d_i is the distance $|\mathbf{x} - \mathbf{x}_i|$, and r_i is the radius of the circle outside of which $W(\mathbf{x} - \mathbf{x}_i)$ vanishes, that is, $W = 0$ when $d_i > r_i$. We choose $m = 6$, $k = 1$ and $r_i = 4c_i$.

3.2. Weak formulation and discretization. This section presents weak (or variational) formulations corresponding to the governing equations (1)–(2) and the boundary conditions (3)–(4). The system equations are obtained by discretizing the weak formulation using the moving least squares method.

Thermoelastic analysis. Let $\boldsymbol{\xi}(\mathbf{x}) = [\xi_1 \ \xi_2]^T$ be a set of two linearly independent test functions defined in Ω . We can obtain a useful relation by taking the inner product of Equation (1) with $\boldsymbol{\xi}$ and of Equation (3), left, with $\chi \boldsymbol{\xi}$, integrating the resulting equations over Ω and Γ_u , respectively, and adding them. To simplify it we integrate by parts, use the divergence theorem and impose the natural boundary condition from Equation (3), right, on Γ_t , obtaining

$$\int_{\Omega} \tilde{\boldsymbol{\epsilon}}^T \boldsymbol{\sigma} \, d\Omega - \int_{\Gamma_u} \boldsymbol{\epsilon}^T \mathbf{N} \boldsymbol{\sigma} \, d\Gamma - \int_{\Gamma_t} \boldsymbol{\epsilon}^T \bar{\mathbf{t}} \, d\Gamma + \chi \int_{\Gamma_u} \boldsymbol{\epsilon}^T (\mathbf{u} - \bar{\mathbf{u}}) \, d\Gamma = 0, \tag{9}$$

where the strain vector $\tilde{\boldsymbol{\epsilon}}$ is obtained from Equation (5) by replacing the displacement components u_i with the test functions ξ_i and matrix \mathbf{N} is given by

$$\mathbf{N} = \begin{bmatrix} n_1 & 0 & n_2 \\ 0 & n_2 & n_1 \end{bmatrix}.$$

In Equation (9) χ is a penalty parameter. The penalty method is chosen here for imposing the essential boundary condition in the equations $u_i = \bar{u}_i$ and $T = \bar{T}$ from (3) and (4), due to the lack of the Kronecker delta property of the basis functions. Selection of the value of the penalty parameter still remains a challenge as the parameter cannot be taken “very large” in order to avoid the case of the system matrix being ill-defined. A suitable range for the value of the penalty parameter suggested by Zhu and Atluri [1998] is $\chi = (10^3 \sim 10^7) \cdot E$.

The most distinguished feature of the MLPG method is that the weak formulation is based on a local subdomain rather than a global problem domain. Consider that N nodes are in the domain Ω and S_1, S_2, \dots, S_N are smooth 2-D closed regions, not necessarily disjointed or having the same shape and size. Let $\{\phi_1, \phi_2, \dots, \phi_n\}$ and $\{\psi_1, \psi_2, \dots, \psi_n\}$ be two sets of linearly independent functions defined over a region, say S_α . The unknown trial function \mathbf{u} and the test function $\boldsymbol{\xi}$ can respectively be expressed as

$$\mathbf{u}(\mathbf{x}) = \begin{bmatrix} u_1(\mathbf{x}) \\ u_2(\mathbf{x}) \end{bmatrix} = \sum_{J=1}^n \boldsymbol{\Phi}_J(\mathbf{x}) \hat{\mathbf{u}}_J, \quad \boldsymbol{\xi}(\mathbf{x}) = \begin{bmatrix} \xi_1(\mathbf{x}) \\ \xi_2(\mathbf{x}) \end{bmatrix} = \sum_{I=1}^n \boldsymbol{\Psi}_I(\mathbf{x}) \hat{\xi}_I, \tag{10}$$

where $\boldsymbol{\Phi}_J = \phi_J \mathbf{I}$, $\boldsymbol{\Psi}_I = \psi_I \mathbf{I}$ with \mathbf{I} a 2×2 identity matrix and $\hat{\mathbf{u}}_J, \hat{\xi}_I$ are 2×1 arrays. Various options of the test function that lead to different MLPG formulations have been discussed by Atluri [2005]. Here we equal the test function to the weight function of the moving least squares approximation. Thus, the strain vectors $\boldsymbol{\epsilon}$ and $\tilde{\boldsymbol{\epsilon}}$ become

$$\boldsymbol{\epsilon} = \sum_{J=1}^n \mathbf{B}_J \hat{\mathbf{u}}_J, \quad \tilde{\boldsymbol{\epsilon}} = \sum_{I=1}^n \tilde{\mathbf{B}}_I \hat{\xi}_I, \tag{11}$$

where

$$\mathbf{B}_J = \begin{bmatrix} \frac{\partial \phi_J}{\partial x_1} & 0 \\ 0 & \frac{\partial \phi_J}{\partial x_2} \\ \frac{\partial \phi_J}{\partial x_2} & \frac{\partial \phi_J}{\partial x_1} \end{bmatrix}, \quad \tilde{\mathbf{B}}_I = \begin{bmatrix} \frac{\partial \psi_I}{\partial x_1} & 0 \\ 0 & \frac{\partial \psi_I}{\partial x_2} \\ \frac{\partial \psi_I}{\partial x_2} & \frac{\partial \psi_I}{\partial x_1} \end{bmatrix}.$$

Replacing the domain Ω of integration in Equation (9) by S_α , substituting for \mathbf{u} , $\boldsymbol{\xi}$, $\boldsymbol{\varepsilon}$, and $\tilde{\boldsymbol{\varepsilon}}$ from Equations (10) and (11), and requiring that the resulting equations hold for all choices of $\widehat{\boldsymbol{\xi}}_I$, one arrives at the following linear algebraic equations for $\widehat{\mathbf{u}}_J$:

$$\begin{aligned} \sum_{J=1}^n \int_{S_\alpha} \tilde{\mathbf{B}}_I^T \mathbf{D} \mathbf{B}_J \widehat{\mathbf{u}}_J d\Omega - \sum_{J=1}^n \int_{\Gamma_{\alpha u}} \boldsymbol{\Psi}_I^T \mathbf{S} \mathbf{N} \mathbf{D} \mathbf{B}_J \widehat{\mathbf{u}}_J d\Gamma + \sum_{J=1}^n \chi \int_{\Gamma_{\alpha u}} \boldsymbol{\Psi}_I^T \mathbf{S} \boldsymbol{\Phi}_J \widehat{\mathbf{u}}_J d\Gamma \\ = \int_{S_\alpha} \tilde{\mathbf{B}}_I^T \boldsymbol{\beta} T d\Omega - \int_{\Gamma_{\alpha u}} \boldsymbol{\Psi}_I^T \mathbf{S} \mathbf{N} \boldsymbol{\beta} T d\Omega + \int_{\Gamma_{\alpha t}} \boldsymbol{\Psi}_I^T \bar{\mathbf{t}} d\Gamma + \chi \int_{\Gamma_{\alpha u}} \boldsymbol{\Psi}_I^T \bar{\mathbf{u}} d\Gamma \end{aligned} \quad (12)$$

for $I = 1, 2, \dots, n$, where

$$\mathbf{S} = \begin{bmatrix} S_1 & 0 \\ 0 & S_2 \end{bmatrix}, \quad S_i = \begin{cases} 1 & \text{if } u_i \text{ is prescribed on } \Gamma_{\alpha u}, \\ 0 & \text{if } u_i \text{ is not prescribed on } \Gamma_{\alpha u}. \end{cases}$$

Symbolically, the simultaneous Equation (12) are written in the matrix form

$$\mathbf{K}_\alpha \widehat{\mathbf{u}}_\alpha = \mathbf{F}_\alpha. \quad (13)$$

The final system of equations can be obtained by assembling Equation (13) for all the N nodes over the entire domain.

Nonlinear heat conduction analysis. Let $\eta(\mathbf{x})$ be another test function defined over Ω . Following the procedure in the above thermoelastic analysis yields the weak form associated with the governing Equation (2) and the boundary conditions given in Equation (4), we get

$$\int_{\Omega} (\nabla^T \eta) \mathbf{q} d\Omega - \int_{\Gamma_T} \eta \mathbf{n}^T \mathbf{q} d\Gamma - \int_{\Gamma_q} \eta \bar{\mathbf{q}} d\Gamma - \int_{\Gamma_h} \eta h (T - T_s) d\Gamma + \chi \int_{\Gamma_T} \eta (T - \bar{T}) d\Gamma = 0, \quad (14)$$

where $\mathbf{q} = [q_1 \ q_2]^T$ and $\mathbf{n} = [n_1 \ n_2]^T$. With the unknown trial function T and the test function η expressed in an interpolative form as

$$\mathbf{T}(\mathbf{x}) = \sum_{J=1}^n \phi_J(\mathbf{x}) \widehat{T}_J, \quad \eta(\mathbf{x}) = \sum_{I=1}^n \psi_I(\mathbf{x}) \widehat{\eta}_I \quad (15)$$

one has

$$\nabla T = \sum_{J=1}^n \mathbf{C}_J \widehat{T}_J, \quad \nabla \eta = \sum_{I=1}^n \tilde{\mathbf{C}}_I \widehat{\eta}_I, \quad (16)$$

where

$$\mathbf{C}_J = \begin{bmatrix} \frac{\partial \phi_J}{\partial x_1} \\ \frac{\partial \phi_J}{\partial x_2} \end{bmatrix}, \quad \tilde{\mathbf{C}}_I = \begin{bmatrix} \frac{\partial \psi_I}{\partial x_1} \\ \frac{\partial \psi_I}{\partial x_2} \end{bmatrix}.$$

Substituting for $T, \eta, \nabla T, \nabla \eta$ from Equations (15) and (16) into Equation (14) for a region S_α and requiring that the resulting equations hold for every choices of $\hat{\eta}_I$, we arrive at the following simultaneous equations for $I = 1, 2, \dots, n$

$$\sum_{J=1}^n L_{IJ}(T) \hat{T}_J = \sum_{J=1}^n G_I, \tag{17}$$

where

$$L_{IJ} = \int_{S_\alpha} \tilde{C}_I^T \kappa C_J d\Omega - \int_{\Gamma_{\alpha T}} \psi_I \kappa \mathbf{n}^T C_J d\Gamma + \int_{\Gamma_{\alpha h}} h \psi_I \phi_J d\Gamma - \chi \int_{\Gamma_{\alpha T}} \psi_I \phi_J d\Gamma, \tag{18}$$

$$G_I = - \int_{\Gamma_{\alpha q}} \psi_I \bar{q} d\Gamma - \chi \int_{\Gamma_{\alpha T}} \psi_I \bar{T} d\Gamma + \int_{\Gamma_{\alpha h}} h \psi_I \bar{T}_s d\Gamma. \tag{19}$$

Repeating Equation (17) for all the N nodes in the domain leads to the system of equations for the temperature field. It should be noted that the first two terms on the right-hand side of Equation (18) become nonlinear if the thermal conductivity is temperature-dependent. Hence the system of equations needs to be solved iteratively. The Newton–Raphson method [Cook et al. 1989] is adopted to solve the system of equations here. The solution is assumed to have converged when the criterion

$$\sqrt{\sum_{i=1}^N (\hat{T}_i^{j+1} - \hat{T}_i^j)^2} / \sqrt{\sum_{i=1}^N \hat{T}_i^{j2}} < 10^{-4}, \tag{20}$$

is met, where the superscript j denotes the iteration number.

To utilize the Gauss quadrature rule to evaluate the domain integral on S_α and the line integrals on ∂S_α in Equations (12), (18) and (19), the region S_α and its boundaries $\Gamma_{\alpha u}, \Gamma_{\alpha t}, \Gamma_{\alpha q}, \Gamma_{\alpha T}$ and $\Gamma_{\alpha h}$ are mapped onto a $[-1, 1] \times [-1, 1]$ square domain and a $[-1, 1]$ straight line, respectively. Using this approach no shadow cells are needed for the integration.

4. Temperature-dependent material properties and effective moduli

In this study a ceramic ZrO_2 is taken as the particulate phase and alloy Ti-6Al-4V as the matrix phase. For practice the FGC is treated as a macro-nonhomogeneous isotropic material. The temperature-dependent material properties of the two constituents are given as follows [Tanigawa et al. 1997]:

$$\begin{aligned} ZrO_2 : \quad & E = 132.2 - 50.3 \times 10^{-3}T - 31.4 \times 10^{-6}T^2 \text{ (GPa)}, \\ & \nu = 0.333, \\ & \kappa = 1.71 + 0.21 \times 10^{-3}T + 0.116 \times 10^{-6}T^2 \text{ (W/mK)} \\ & \alpha = 13.31 \times 10^{-6} - 18.9 \times 10^{-9}T + 12.7 \times 10^{-12}T^2 \text{ (1/K)}, \end{aligned} \tag{21}$$

$$\begin{aligned} Ti-6Al-4V: \quad & E = 122.7 - 0.0565T \text{ (GPa)}, \\ & \nu = 0.289 + 32.0 \times 10^{-6}T, \\ & \kappa = 1.1 + 0.017T \text{ (W/mK)}, \\ & \alpha = 7.43 \times 10^{-6} - 5.56 \times 10^{-9}T + 2.69 \times 10^{-12}T^2 \text{ (1/K)}. \end{aligned} \tag{22}$$

The Poisson's ratio ν of ZrO_2 is assumed to be constant here since its dependence on temperature may be weak [Dole and Hunter Jr. 1983]. The first (constant) terms in Equations (21) and (22) are the material properties at temperature $T = 0^\circ\text{K}$, which is assumed as the reference state temperature in this work. At elevated temperatures, for example, $T = 1000^\circ\text{K}$, the changes of the Young's modulus, thermal conductivity, and coefficient of thermal expansion are about -61.8% , 19.1% , and -46.6% , respectively, for ZrO_2 and about -46.1% , 1545.5% and -38.6% respectively for Ti-6Al-4V. Due to the nontrivial change of the material properties, a significant difference of the thermomechanical response prediction can be expected when the constant properties are used. To delineate the influence of temperature dependence for the material properties on thermomechanical response of the FGCs, both the temperature-dependent and constant material properties are incorporated in this paper.

Two homogenization schemes are frequently utilized to evaluate the effective material properties for composites. One is the rule of mixtures, and the other is the micromechanical model. The former is simple to use but does not include the effect of interaction between the different constituents. For a two-phase composite it computes the effective value of a composite material property (P) by

$$P = P_m V_m + P_c V_c, \quad (23)$$

where subscripts m and c are associated with the matrix and particulate phase, respectively; the volume fractions satisfy $V_m + V_c = 1$. On the other hand, the latter evaluates the effective properties of a composite based on elasticity theory by considering the inclusion of particulates or fibers in a matrix phase.

Several micromechanical models have been derived for the effective properties of composite materials [Christensen 1979]. For a two-phase particulate composite the effective bulk and shear moduli K , μ derived by Mori and Tanaka [1973] are given as

$$\frac{K - K_m}{K_c - K_m} = \frac{V_c}{1 + (1 - V_c)(K_c - K_m)/(K_m + 4\mu_m/3)}, \quad (24)$$

$$\frac{\mu - \mu_m}{\mu_c - \mu_m} = \frac{V_c}{1 + (1 - V_c)(\mu_c - \mu_m)/(\mu_m + f_m)}, \quad (25)$$

with $f_m = \mu_m(9K_m + 8\mu_m)/6(K_m + 2\mu_m)$. The effective Young's modulus and Poisson's ratio are related to the bulk and shear moduli by $E = 9K\mu/(3K + \mu)$ and $\nu = (3K - 2\mu)/2(3K + \mu)$, respectively. The effective thermal conductivity κ derived by Hatta and Taya [1985] and the coefficient of thermal expansion α derived by Rosen and Hashin [1970] are

$$\frac{\kappa - \kappa_m}{\kappa_c - \kappa_m} = \frac{V_c}{1 + (1 - V_c)(\kappa_c - \kappa_m)/3\kappa_m}, \quad \frac{\alpha - \alpha_m}{\alpha_c - \alpha_m} = \frac{1/K - 1/K_m}{1/K_c - 1/K_m}. \quad (26)$$

5. Results and discussion

A computer code based on the aforementioned MLPG formulation was developed and used to analyze the steady-state thermoelastic response of 2-D FGCs in elevated temperature environments. Three examples are examined: (1) a hollow cylinder under a temperature change at internal surface, (2) a clamped-clamped thick beam with a temperature change on the top surface, and (3) a square plate with a central hole subjected to a temperature change either at the hole surface or the outer boundary. The effective properties of the FGCs are estimated with the rule of mixtures of Equation (23) for the first example for

comparison with the finite element solution and with the micromechanical models of Equations (24)–(26) for the other two examples.

5.1. A hollow cylinder under temperature change at internal surface. Here we consider a functionally graded hollow cylinder with the inner radius of $r_i = 50$ mm and outer radius of $r_o = 150$ mm. Temperature at the inner surface is suddenly increased to $T_i = 1000^\circ K$ and then kept constant, while the temperature on the outer surface is fixed at the reference temperature, that is, $T_o = 0$. The volume fraction of ceramic phase ZrO_2 is assumed to have the radial dependence by a power-law function as

$$V_c = V_c^o + (V_c^i - V_c^o) \left(\frac{r_o - r}{r_o - r_i} \right)^n, \tag{27}$$

where V_c^i and V_c^o are, respectively, the volume fractions of ZrO_2 on the inner and outer surfaces, and n is the power law index that dictates the volume fraction profile across the thickness of the cylinder. With the symmetry boundary conditions, a quadrant of the circular cross-section of the cylinder is analyzed as though it were essentially a 1-D axisymmetric problem. A total of 21×40 nodes are equally spaced along the radial and circumferential directions, respectively. Plane strain condition is assumed. All the results presented below are normalized by

$$[\bar{r}, \bar{T}, \bar{u}_r, \bar{\sigma}_\theta] = \left[\frac{r}{r_i}, \frac{T}{T_i}, \frac{10u_r}{(r_o - r_i)\alpha_{Ti}^0 T_i}, \frac{10\sigma_\theta}{E_{Ti}^0 \alpha_{Ti}^0 T_i} \right],$$

where σ_θ , E_{Ti}^0 and α_{Ti}^0 are the hoop stress, the (constant) Young’s modulus and thermal expansion coefficient of Ti-6Al-4V at $T = 0$.

Figure 1 shows the through-the-thickness variation of the temperature and hoop stress respectively, for the case of $V_c^i = 1$, $V_c^o = 0$ and $n = 1$. Apparently, the present MLPG solution agrees very well with

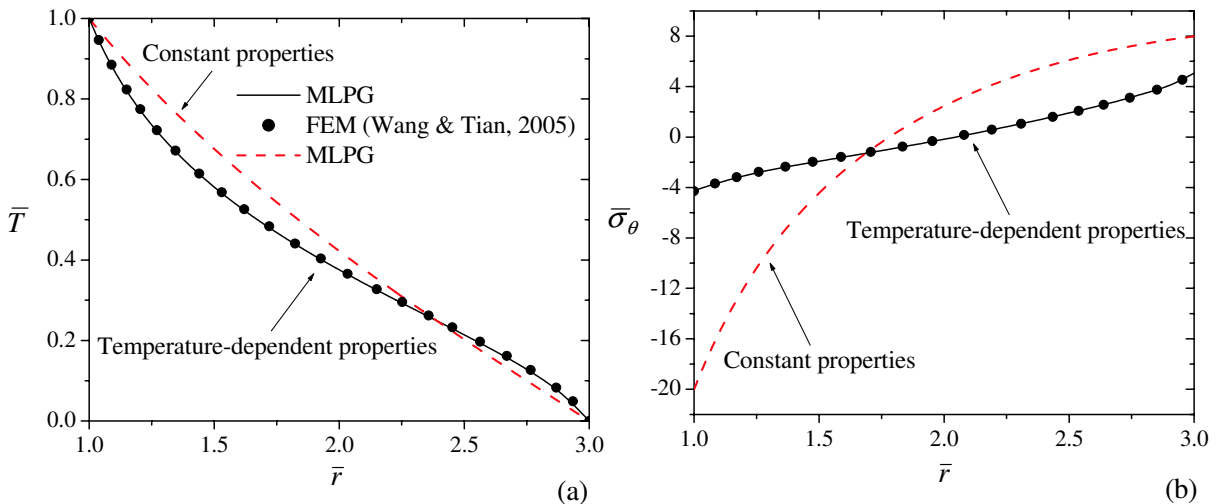


Figure 1. Through-the-thickness variations of the normalized (a) temperature change and (b) hoop stress obtained by the finite element method and MLPG method; effective material properties are computed by the rule of mixtures with $V_c^o = 0$, $V_c^i = 1$ and $n = 1$.

the 1-D axisymmetric finite element result [Wang and Mai 2005], which is obtained with 100 elements. The FGC in each element is assumed to be homogeneous but different from one another. In the present analysis 21 nodes are used through the thickness direction. The results computed with the constant material properties are also included in Figure 1. It can be seen from Figure 1(b) that the resulting hoop stress is quite different when the temperature dependence on the material properties is excluded. For example, the dimensionless hoop stress on the inner surface computed with the temperature-dependent material properties is about -4 , and changes to -20 when the properties are assumed to be constant. The discrepancy found here suggests that the temperature dependence of material properties should not be ignored in thermomechanical analysis when an FGC is under severe thermal loading.

Figure 2 displays the through-the-thickness variation of the effective Young's modulus, Poisson's ratio, thermal conductivity, and coefficient of thermal expansion for the case of $V_c^i = 1$, $V_c^o = 0$ and $n = 1$,

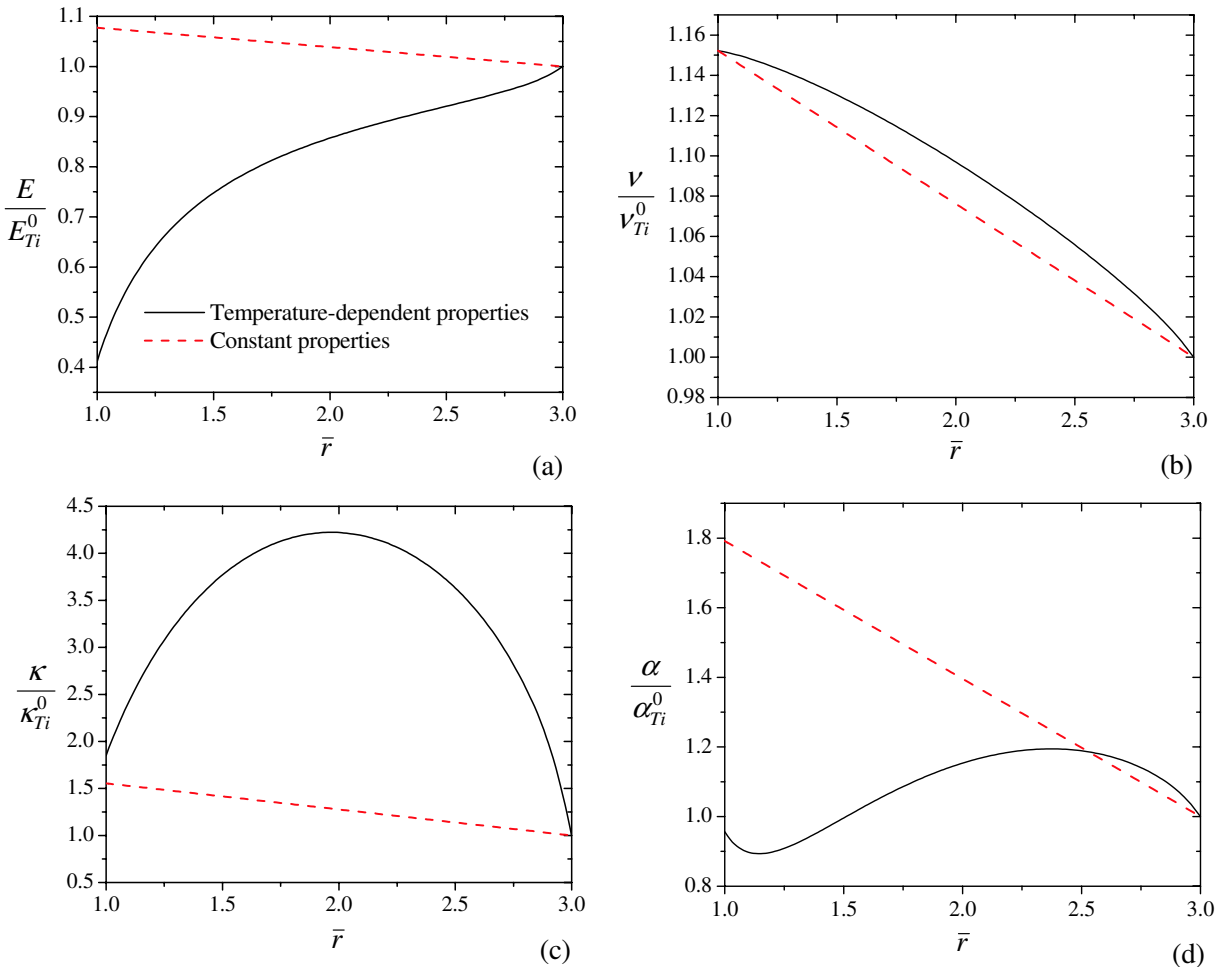


Figure 2. Through-the-thickness variations of effective material properties computed by the rule of mixtures for the case of $V_c^o = 0$, $V_c^i = 1$ and $n = 1$: (a) Young's modulus, (b) Poisson's ratio, (c) thermal conductivity; (d) coefficient of thermal expansion.

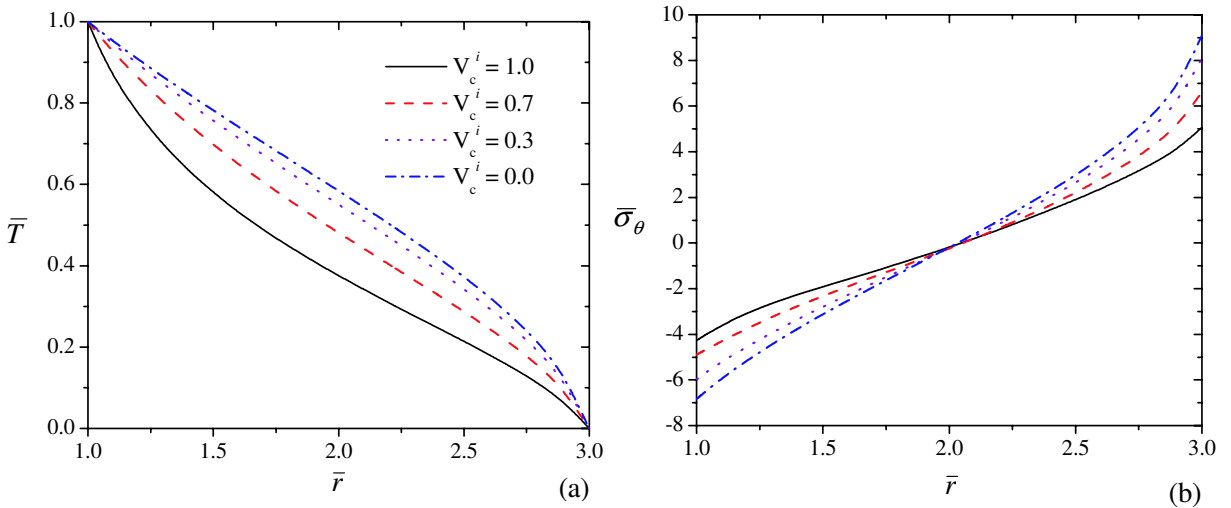


Figure 3. Distribution of the normalized (a) temperature change and (b) hoop stress over the thickness of the cylinder for different values of V_c^i with $V_c^o = 0$ and $n = 1$, calculated with the temperature-dependent material properties.

normalized by the corresponding constant properties of Ti-6Al-4V. For the case of constant material properties, all the properties are linear functions of r as dictated by Equation (27). However, the linear relations no longer exist when the temperature dependence of material properties is taken into account. Figure 2(a) shows that the effective Young's modulus monotonically increases from the inner surface to the outer surface, whereas the trend is opposite when the temperature dependence is neglected. The normalized values at the inner surface are 0.411 versus 1.08. Neither the thermal conductivity nor the coefficient of thermal expansion vary monotonically; see Figures 2(c) and 2(d).

Variations of the temperature change and hoop stress are further evidenced in Figure 3 for different values of V_c^i with $V_c^o = 0$ and $n = 1$, calculated with the temperature-dependent material properties. The case of $V_c^i = 0$ corresponds to a pure Ti-6Al-4V cylinder. Figure 3(a) shows the temperature decreases with increase of the ceramic content except for those at the inner and outer surface, where the temperatures remain constant specified by the boundary conditions. It is also found from Figure 3(b) that the magnitude of the hoop stress reduces as the ceramic ZrO_2 increases in the FGC.

Figure 4 shows the normalized radial displacement at the inner and outer surfaces as a function of n with $V_c^i = 1$ and $V_c^o = 0$. An increase of the value in n means that the FGC cylinder has more composition of Ti-6Al-4V. The pure ZrO_2 cylinder is the limit case of $n = 0$. By comparing the results in the two parts of the figure we can ascertain that the trend of net expansion of the wall thickness with n is opposite when the temperature dependence of the material properties is neglected. In addition, use of the constant material properties overestimates the net wall thickness expansion for small n , but underestimates the expansion for large n .

5.2. A clamped-clamped thick beam with temperature change on top surface. A clamped-clamped FGC beam of length $L = 50$ mm and thickness $H = 10$ mm is subjected to a sinusoidal temperature

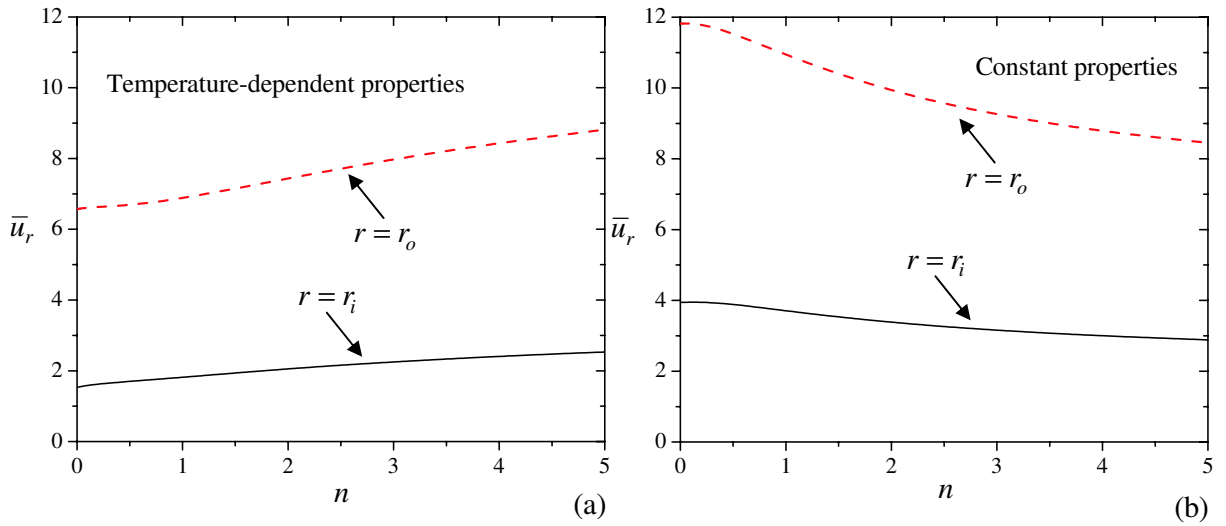


Figure 4. Variations of the normalized radial displacement on the inner and outer surfaces with the power law index n for $V_c^i = 1$ and $V_c^o = 0$: (a) temperature-dependent material properties and (b) constant material properties.

change $T = T_0 \sin(\pi x_1/L)$ with $T_0 = 1000^\circ K$, on the top surface; see Figure 5. The bottom surface and the two edges of the beam are at the reference temperature. The origin of the rectangular Cartesian coordinates (x_1, x_2) is located at the left bottom corner of the beam, and the x_1 -axis is parallel to the long edges. Plane strain condition is assumed. The volume fraction of the ceramics phase varies over the beam thickness by a power law function as

$$V_c = V_c^- + (V_c^+ - V_c^-) \left(\frac{x_2}{H}\right)^n, \tag{28}$$

where V_c^+ and V_c^- are the volume fractions of ZrO_2 on the top and the bottom surfaces, respectively, and n is the power law index. Instead of using the rule of mixtures, the effective material properties are computed with the micromechanical models described in Section 4.

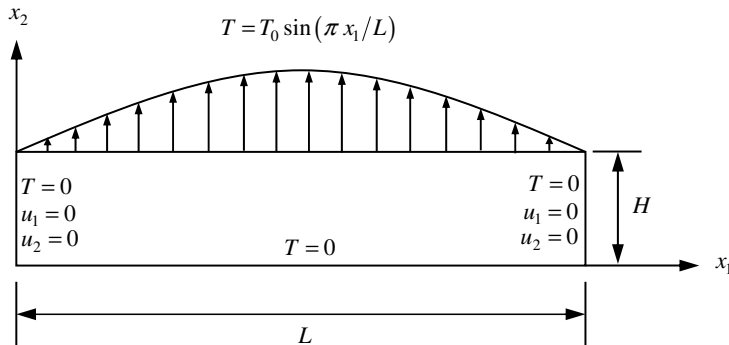


Figure 5. An FGC thick beam subjected to a sinusoidal temperature load on the top surface.

Due to the symmetry to the vertical centroidal plane, the left half of the domain is analyzed with a uniform mesh of 55 nodes along x_1 -direction and 25 nodes along the x_2 -direction, for which the solution has been tested to be convergent. The physical quantities presented below are normalized by

$$[\bar{x}_1, \bar{x}_2, \bar{T}, \bar{u}_2, \bar{\sigma}_{11}, \bar{\sigma}_{12}] = \left[\frac{x_1}{L}, \frac{x_2}{H}, \frac{T}{T_0}, \frac{10Hu_2}{\alpha_{Ti}^0 T_0 L^2}, \frac{10\sigma_{11}}{E_{Ti}^0 \alpha_{Ti}^0 T_0}, \frac{10L\sigma_{12}}{E_{Ti}^0 \alpha_{Ti}^0 T_0 H} \right]. \quad (29)$$

Figure 6 plots the distributions of the effective Young’s modulus, thermal conductivity, and coefficient

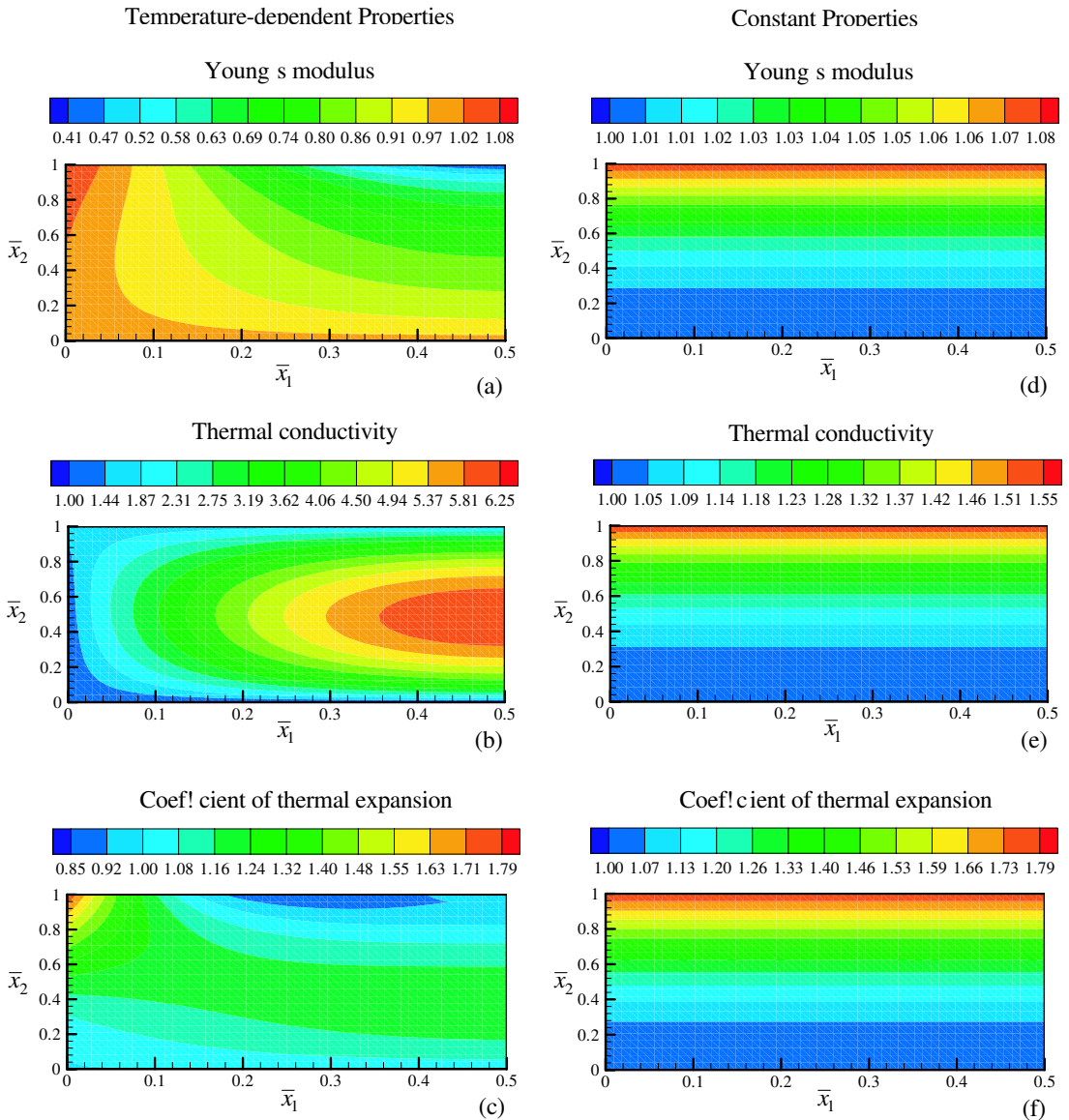


Figure 6. Distributions of normalized effective properties computed with $V_c^+ = 1$, $V_c^- = 0$ and $n = 2$.

of thermal expansion normalized by the corresponding constants of Ti-6Al-4V. The values of $V_c^+ = 1$, $V_c^- = 0$ and $n = 2$ were chosen. The left-hand panes of the figure clearly show that, for constant material properties, the dependence is on x_1 only and the maximum value always occurs on the top surface (pure ZrO_2), basically following the volume fraction distribution of ZrO_2 described by Equation (28). When the temperature dependence is included, the overall material properties no longer follow the graded material pattern; see left side of Figure 6.

Figure 7 shows the influence of temperature dependence of material properties on the deformation, temperature, and longitudinal stress (σ_{11}) in the beam for $V_c^+ = 1$, $V_c^- = 0$ and $n = 2$. The top row

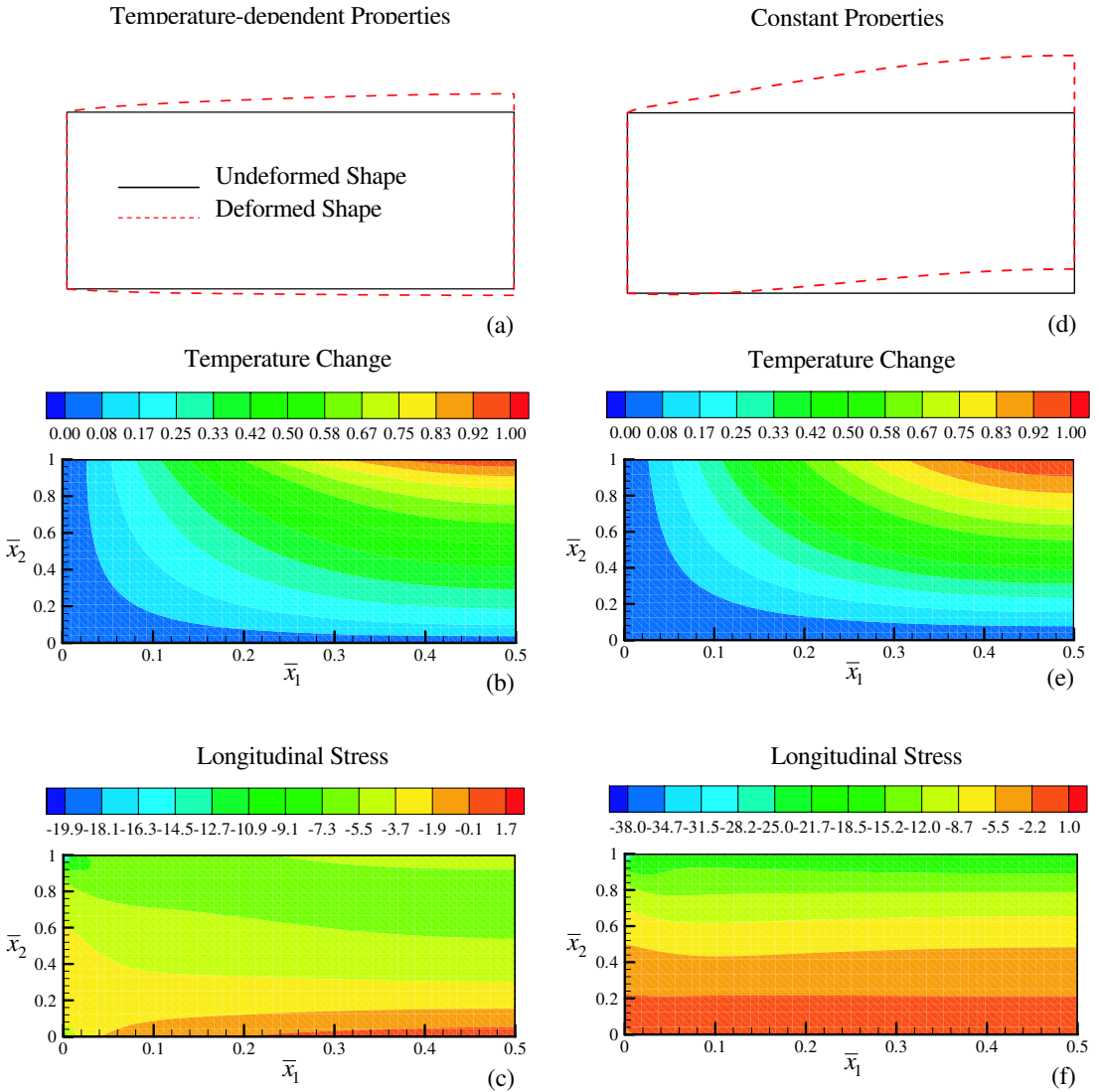


Figure 7. Comparison of the thermomechanical response of the FGC beam with $V_c^+ = 1$, $V_c^- = 0$ and $n = 2$ computed with temperature-dependent material properties and constant material properties; deformations in (a) and (d) are enlarged by 20 times.

shows that, when subjected to temperature rise on the top surface, the beam expands, but the amount of expansion is different between the two cases. Apparently, use of the constant material properties not only predicts a larger increase for the beam thickness, but a larger deflection as well. This can be seen by examining the values of $\alpha\Delta T$ and $\alpha E\Delta T$ over the thickness. The impact of the temperature dependence of material properties on the steady-state temperature response is less pronounced; see middle row of Figure 7. With the temperature dependence, the resulting maximum normalized longitudinal stress, however, can be decreased by nearly 100%, from -38.0 to -19.9 ; see bottom row of the figure.

Figure 8 displays the distribution of normalized temperature, transverse displacement, longitudinal stress, and transverse shear stress over the thickness of the FGC beam for four different values of V_c^+

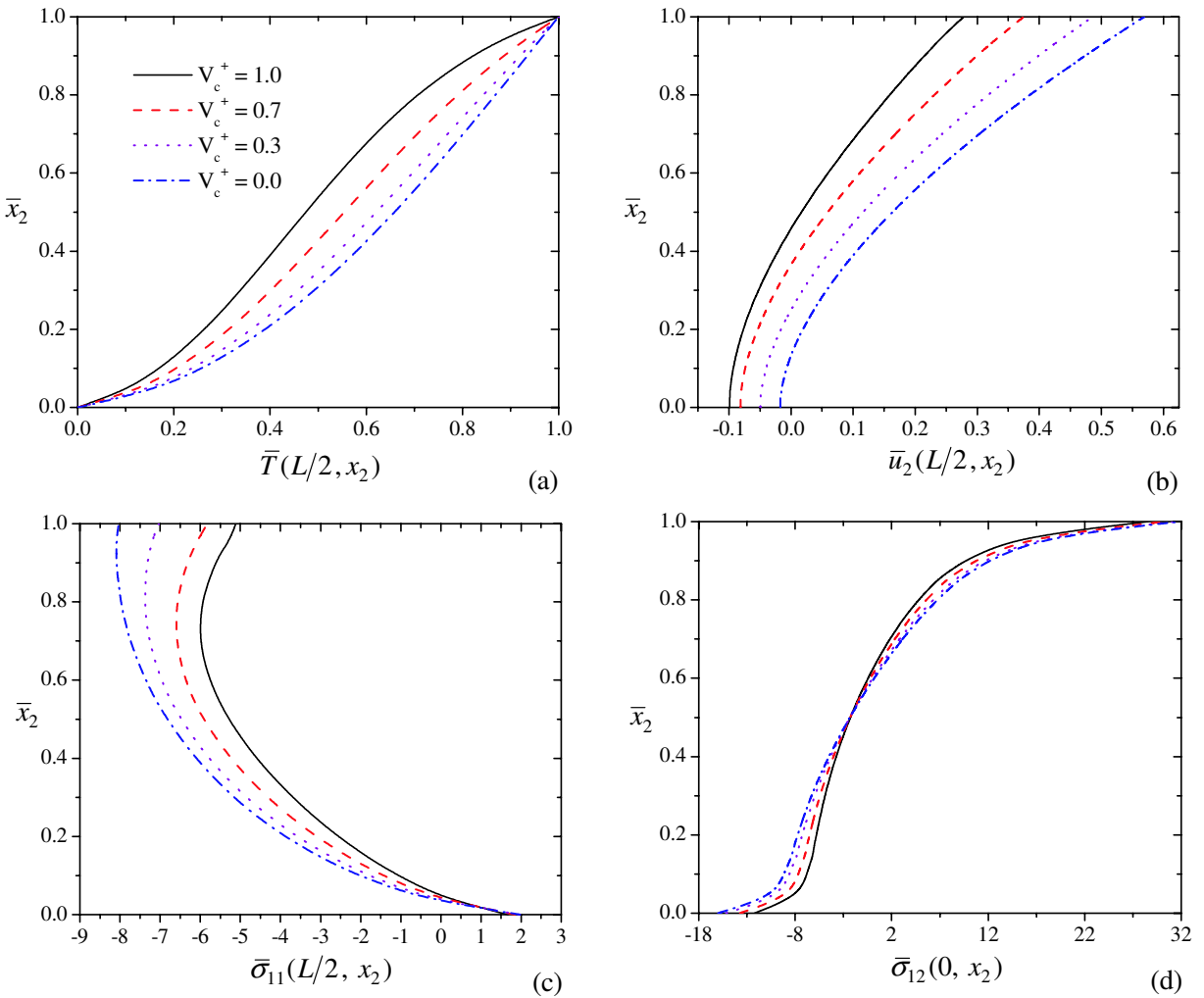


Figure 8. Distribution of the normalized (a) temperature change, (b) transverse displacement, (c) longitudinal stress, and (d) transverse shear stress over the thickness of the beam for different values of V_c^+ with $V_c^- = 0$ and $n = 2$, computed with the temperature-dependent material properties.

with $V_c^- = 0$ and $n = 2$. These results are calculated with the temperature-dependent material properties. Like the results in the previous cylinder case, the temperature change, transverse displacement and the magnitude of stresses all decrease as V_c^+ increases.

Figure 9 illustrates the temperature change, transverse displacement, longitudinal stress, and transverse shear stress as functions of the power index n at some points of interest. Again, the significant differences between the two cases found here reveal the importance of the temperature dependence of material properties in simulation of thermomechanical response of the FGCs in elevated temperature environments.

5.3. A square plate with a central hole under temperature change along boundaries. The analysis for a centrally-holed FGC square plate under the temperature change along boundaries is conducted. The

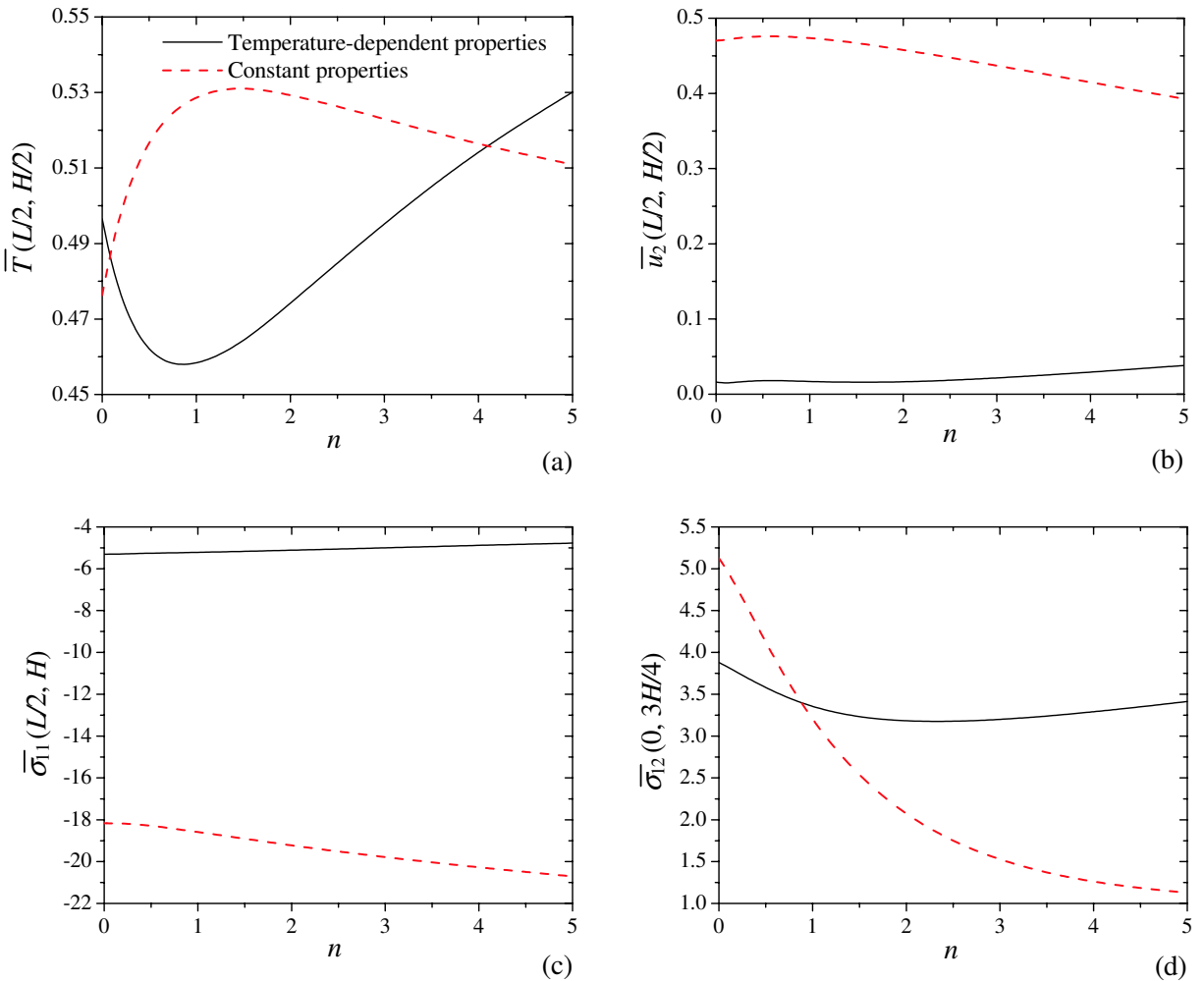


Figure 9. The normalized (a) temperature change, (b) transverse displacement, (c) longitudinal stress, and (d) transverse shear stress at some points of interest in the FGC beam as functions of the power law index n with $V_c^+ = 1$, $V_c^- = 0$.

edge length of the plate is $L = 4$ mm and the radius of the hole is $r_a = 1.5$ mm. The origin of the rectangular Cartesian coordinates (x_1, x_2) coincides with the center of the hole, and the x_1 -axis points to the middle point of the right vertical edge. For convenience, a polar coordinate system (r, θ) is also set at the center of the hole with θ measured counterclockwise from the positive x_1 -axis. The volume fraction of the ceramic is assumed to vary along the radial direction r with

$$V_c = V_c^- + (V_c^+ - V_c^-) \left(\frac{r - r_a}{r_d - r_a} \right)^n,$$

where r_d is the radial distance measured from a point on the surface of the hole to the corresponding point at the outer boundary of the plate and V_c^+ and V_c^- are the volume fractions of ZrO_2 at the outer boundary and the hole surface, respectively. Two temperature loadings are considered: (a) a temperature rise of $T_0 = 1000^\circ\text{K}$ is applied on the outer boundary while the surface of the hole is kept at $T = 0$, and (b) a temperature rise of $T_0 = 1000^\circ\text{K}$ is applied on the surface of the hole while the outer boundary is kept at $T = 0$. Since a ceramic-rich layer usually is in the hotter region, $V_c^+ = 1.0$ and $V_c^- = 0$ are assumed for the loading condition (a) and $V_c^+ = 0$ and $V_c^- = 1.0$ for the condition (b). Plane stress condition is assumed.

Only the first quadrant of the plate is analyzed with the symmetric boundary conditions imposed on the x_1 - and x_2 -axis. A total of 1025 nodes, the effect of which passed the convergence test for the nodal density, is meshed. The results presented below are normalized as follows

$$[\bar{x}_1, \bar{x}_2, \bar{\sigma}_{22}, \bar{\sigma}_\theta, \bar{\sigma}_e] = \left[\frac{x_1}{a}, \frac{x_2}{a}, \frac{10\sigma_{22}}{E_{T_i}^0 \alpha_{T_i}^0 T_0}, \frac{10\sigma_\theta}{E_{T_i}^0 \alpha_{T_i}^0 T_0}, \frac{10\sigma_e}{E_{T_i}^0 \alpha_{T_i}^0 T_0} \right].$$

The normal stress $\bar{\sigma}_{22}$ along the x_1 -axis and the hoop stress $\bar{\sigma}_\theta$ around the surface of the hole for different values of n are presented in [Figure 10](#) for condition (a). As expected, the stress σ_{22} is in tension near the hole and in compression near the edge regardless of the value of n . It is clear from the top row of [Figure 10](#) that for the case of temperature-dependent material properties the magnitude of σ_{22} increases as n increases; however, the trend is opposite when temperature dependence is excluded. The tensile stress σ_{22} in the region near the hole computed with the temperature-dependent material properties increases as n decreases. A similar conclusion also applies to the hoop stress σ_θ around the surface of the hole; see bottom row of the figure. Maximum σ_θ occurs at $\theta = 0, \pm\pi/2$ and π , while the minimum occurs at $\theta = \pm\pi/4$ and $\pm3\pi/4$.

[Figure 11](#) compares the normalized effective stress $\bar{\sigma}_e$ in the plate for $n = 2$, calculated with and without the temperature dependence on the material properties. It appears that the peak effective stress occurs at the intersections between the surface of the hole and the x_1 - and x_2 -axis. A comparison of the values of $\bar{\sigma}_e$ in the two halves of [Figure 11](#) indicates that use of the constant material properties would underpredict the effective stress for the graded FGC with $V_c^+ = 1.0$, $V_c^- = 0$ and $n = 2$.

For the condition (b) the resulting thermal stresses σ_{22} and σ_θ are in an opposite sense from those for condition (a). [Figure 12](#) exhibits the contour of the normalized effective stress $\bar{\sigma}_e$ in the plate for $n = 2$ calculated with and without the temperature dependence on the material properties. The maximum effective stress is present at the middle points of the outer edges for the case of temperature-dependent material properties, but at the intersections between the surface of the hole and the x_1 - and x_2 -axis for

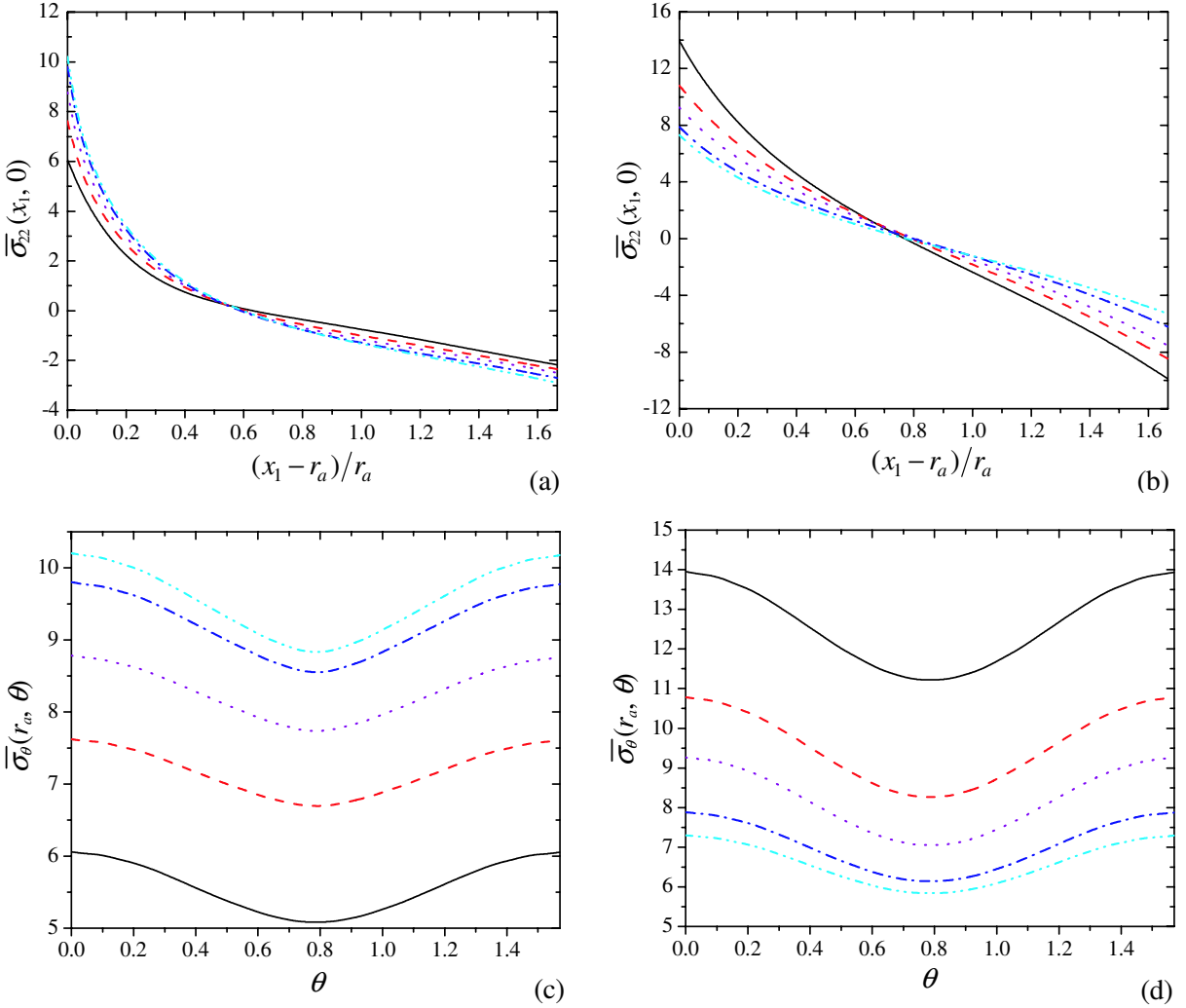


Figure 10. Variations of σ_{22} along the x_1 -axis and hoop stress along the surface of the hole for different values of n with $V_c^+ = 1$ and $V_c^- = 0$. Left: temperature-dependent material properties; right: constant material properties. The temperature load is applied on the outer boundary.

the case of the constant material properties. The difference of the maximum $\bar{\sigma}_e$ calculated with the two sets of the material properties is much larger for condition (b) than for condition (a).

6. Conclusions

Due to the complex features of material nonhomogeneity in FGC materials and the temperature dependence on material properties it is almost impossible to obtain an exact solution for the thermomechanical response. In this work we have analyzed the thermomechanical deformation in the 2-D ZrO_2 and Ti-6Al-4V FGCs under elevated temperature loading using the mesh-free MLPG particle method. Both the rule

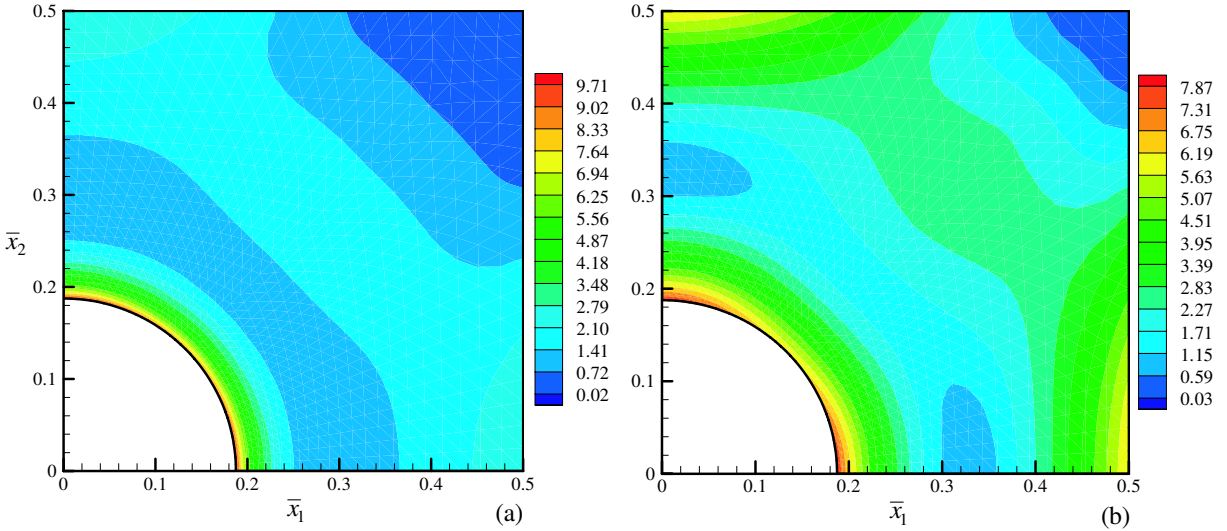


Figure 11. Normalized effective stress contours in the plate with $V_c^+ = 1$, $V_c^- = 0$, and $n = 2$ computed with (a) temperature-dependent material properties and (b) constant material properties; the temperature load is applied on the outer boundary.

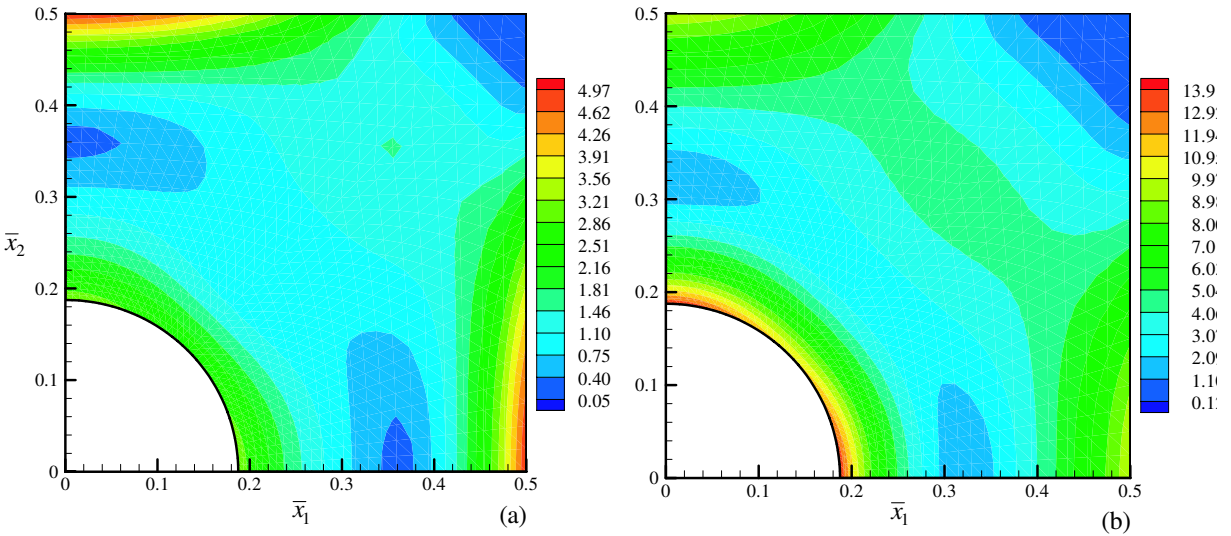


Figure 12. Normalized effective stress contours in the plate with $V_c^+ = 0$, $V_c^- = 1$, and $n = 2$ computed with (a) temperature-dependent material properties and (b) constant material properties; the temperature load is applied on the inner surface of the hole.

of mixtures and the micromechanical models are adopted to evaluate the effective material properties. Three illustrated examples, including a hollow cylinder, a clamped-clamped thick beam, and a square plate with a central hole, are presented. The numerical results show that the deformation and thermal stresses in an FGC computed temperature-dependent material properties are quite different than those

predicted with the constant material properties. Therefore, analyses that fail to consider the temperature dependence of material properties could result in a considerable error in thermomechanical response for an FGC in elevated temperature environments. More importantly, the FGC may not perform as initially expected if it is graded based on the constant material properties.

To accurately predict the thermomechanical responses for nonhomogeneous FGCs a high fidelity numerical tool is essential. Unlike the finite element method, the MLPG method requires only a set of nodes for both the interpolation of the trial functions and the integration of the weak forms. Besides, this method dictates the continuous material properties of FGMs directly to a quadrature point. These prominent features make the MLPG method well suited in the analysis of functionally graded composite structures.

References

- [Atluri 2005] S. N. Atluri, *The meshless method (MLPG) for domain and BIE discretizations*, Tech Science Press, Los Angeles, 2005.
- [Atluri and Zhu 1998] S. N. Atluri and T. Zhu, “A new meshless local Petrov–Galerkin (MLPG) approach in computational mechanics”, *Comput. Mech.* **22**:2 (1998), 117–127.
- [Chati and Mukherjee 2000] M. K. Chati and S. Mukherjee, “The boundary node method for three-dimensional problems in potential theory”, *Int. J. Numer. Methods Eng.* **47**:9 (2000), 1523–1547.
- [Ching and Chen 2006] H. K. Ching and J. K. Chen, “Thermomechanical analysis of functionally graded composites under laser heating by the MLPG method”, *Comput. Model. Eng. Sci.* **13**:3 (2006), 199–218.
- [Ching and Yen 2005] H. K. Ching and S. C. Yen, “Meshless local Petrov–Galerkin analysis for 2-D functionally graded elastic solids under mechanical and thermal loads”, *Compos. B Eng.* **36**:3 (2005), 223–240.
- [Christensen 1979] R. M. Christensen, *Mechanics of composite materials*, Wiley, New York, 1979.
- [Cook et al. 1989] R. D. Cook, D. S. Malkus, and M. E. Plesha, *Concepts and applications of finite element analysis*, 3rd ed., Wiley, 1989.
- [Dole and Hunter Jr. 1983] S. L. Dole and O. Hunter Jr., “Elastic properties of hafnium and zirconium oxides stabilized with praseodymium or terbium oxide”, *J. Am. Ceram. Soc.* **66**:3 (1983), C–47–C–49.
- [Hatta and Taya 1985] H. Hatta and M. Taya, “Effective thermal conductivity of a misoriented short fiber composite”, *J. Appl. Phys.* **58**:7 (1985), 2478–2486.
- [Mori and Tanaka 1973] T. Mori and K. Tanaka, “Average stress in matrix and average elastic energy of materials with misfitting inclusions”, *Acta Metall.* **21**:5 (1973), 571–574.
- [Ootao and Tanigawa 2004] Y. Ootao and Y. Tanigawa, “Transient thermoelastic problem of functionally graded thick strip due to nonuniform heat supply”, *Compos. Struct.* **63**:2 (2004), 139–146.
- [Ootao and Tanigawa 2005] Y. Ootao and Y. Tanigawa, “Three-dimensional solution for transient thermal stresses of functionally graded rectangular plate due to nonuniform heat supply”, *Int. J. Mech. Sci.* **47**:11 (2005), 1769–1788.
- [Praveen et al. 1999] G. N. Praveen, C. D. Chin, and J. N. Reddy, “Thermoelastic analysis of functionally graded ceramic-metal cylinder”, *J. Eng. Mech.* **125**:11 (1999), 1259–1267.
- [Qian and Batra 2004] L. F. Qian and R. C. Batra, “Transient thermoelastic deformations of a thick functionally graded plate”, *J. Therm. Stresses* **27**:8 (2004), 705–740.
- [Qian and Batra 2005] L. F. Qian and R. C. Batra, “Three-dimensional transient heat conduction in a functionally graded thick plate with a higher-order plate theory and a meshless local Petrov–Galerkin method”, *Comput. Mech.* **35**:3 (2005), 214–226.
- [Qian and Ching 2004] L. F. Qian and H. K. Ching, “Static and dynamic analysis of 2-D functionally graded elasticity by using meshless local Petrov–Galerkin method”, *J. Chin. Inst. Eng.* **27** (2004), 491–503.
- [Reddy and Chin 1998] J. N. Reddy and C. D. Chin, “Thermomechanical analysis of functionally graded cylinders and plates”, *J. Therm. Stresses* **21** (1998), 593–626.

- [Rosen and Hashin 1970] B. W. Rosen and Z. Hashin, “Effective thermal expansion coefficients and specific heats of composite materials”, *Int. J. Eng. Sci.* **8**:2 (1970), 157–173.
- [Sankar and Tzeng 2002] B. V. Sankar and J. T. Tzeng, “Thermal stresses in functionally graded beams”, *AIAA J.* **40**:6 (2002), 1228–1232.
- [Sladek et al. 2003] J. Sladek, V. Sladek, and C. Zhang, “Application of meshless local Petrov–Galerkin (MLPG) method to elastodynamic problems in continuously nonhomogeneous solids”, *Comput. Model. Eng. Sci.* **4**:6 (2003), 637–647.
- [Sladek et al. 2005] J. Sladek, V. Sladek, J. Krivacek, and C. Zhang, “Meshless local Petrov–Galerkin method for stress and crack analysis in 3-D axisymmetric FGM bodies”, *Comput. Model. Eng. Sci.* **8**:3 (2005), 259–270.
- [Takahashi et al. 1992] H. Takahashi, T. Ishikawa, D. Okugawa, and T. Hashida, “Laser and plasma-arc thermal shock fatigue evaluation procedure for functionally graded materials”, pp. 543–554 NATO ASI Series E: Appl. Sci. **241**, 1992.
- [Tanigawa et al. 1997] Y. Tanigawa, M. Matsumoto, and T. Ahai, “Optimization of material composition to minimize thermal stresses in nonhomogeneous plate subjected to unsteady heat supply”, *JSME Int. J. Ser. A Solid Mech. Mater. Eng.* **40** (1997), 84–93.
- [Tarn 2001] J. Q. Tarn, “Exact solutions for functionally graded anisotropic cylinders subjected to thermal and mechanical loads”, *Int. J. Solids Struct.* **38**:46-47 (2001), 8189–8206.
- [Vel and Batra 2002] S. S. Vel and R. C. Batra, “Exact solution for thermoelastic deformations of functionally graded thick rectangular plates”, *AIAA J.* **40**:7 (2002), 1421–1433.
- [Vel and Batra 2003] S. S. Vel and R. C. Batra, “Three-dimensional analysis of transient thermal stresses in functionally graded plates”, *Int. J. Solids Struct.* **40**:25 (2003), 7181–7196.
- [Wang and Mai 2005] B. L. Wang and Y. W. Mai, “Transient one-dimensional heat conduction problems solved by finite element”, *Int. J. Mech. Sci.* **47**:2 (2005), 303–317.
- [Wang and Tian 2005] B. L. Wang and Z. H. Tian, “Application of finite element–finite difference method to the determination of transient temperature field in functionally graded materials”, *Finite Elem. Anal. Des.* **41**:4 (2005), 335–349.
- [Zhu and Atluri 1998] T. Zhu and S. N. Atluri, “A modified collocation method and a penalty formulation for enforcing the essential boundary conditions in the element free Galerkin method”, *Comput. Mech.* **21**:3 (1998), 211–222.
- [Zimmerman and Lutz 1999] R. W. Zimmerman and M. P. Lutz, “Thermal stresses and thermal expansion in a uniformly heated functionally graded cylinder”, *J. Therm. Stresses* **22**:2 (1999), 177–188.

Received 9 Sep 2006. Accepted 29 Nov 2006.

H. K. CHING: *Department of Mechanical and Aerospace Engineering, University of Missouri, Columbia, MO 65201, United States*

J. K. CHEN: ChenJnK@missouri.edu

Department of Mechanical and Aerospace Engineering, University of Missouri, Columbia, MO 65201, United States

FINITE ELEMENT MODELING OF A LAYERED, MULTIPHASE MAGNETOELECTROELASTIC CYLINDER SUBJECTED TO AN AXISYMMETRIC TEMPERATURE DISTRIBUTION

N. GANESAN, A. KUMARAVEL AND RAJU SETHURAMAN

This paper presents finite element formulation for dynamic behavior of magnetoelastoelectric axisymmetric cylinder coupled with a thermal field. The finite element formulation derived based on the interaction between mechanical, electrical, magnetic and thermal fields. The formulation is reduced to static case to analyze the static behavior of layered and multiphase magnetoelastoelectric axisymmetric cylinder under the circumstances of axisymmetric temperature distribution. The finite element model is developed using a four-noded axisymmetric element with four nodal degrees of freedom that is, two elastic displacements (u_r, u_z) with two potentials, electric (ϕ) and magnetic (ψ). The static behavior of axial and radial displacements, electric potential, magnetic potential and stresses on radially symmetric magnetoelastoelectric cylinder is investigated. The numerical results are compared between layered and multiphase magnetoelastoelectric cylinder with different boundary conditions.

1. Introduction

The combination of piezoelectric phase and piezomagnetic phase forms the layered and multiphase magnetoelastoelectric composites, which exhibit coupling effects between the mechanical/thermal, electrical and magnetic fields. It is also observed that the piezoelectric and piezomagnetic composites used for engineering structures, particularly in smart and intelligent structure systems in the recent years. Due to their ability of converting energy from one form to the other (among magnetic, electric and mechanical energies) these materials have been widely used in ultrasonic imaging devices, sensors, actuators, transducers and many other emerging components [Nan 1994; Harshe et al. 1993; Benveniste 1995; Ding et al. 2005]. There is a strong need for theories or techniques that can predict the coupled response of these smart materials, as well as structure composed of them. Various numerical studies have been carried out to study the behavior of composite laminates that consist of elastic and piezoelectric materials [Lee and Jian 1996; Heyliger 1997; Lee and Saravanas 1997, 2000; Vel and Batra 2000]. The generalized thermoelastic-piezoelectric coupled finite element equations are derived by Tianhu et al. [2002], based on the theory of Green–Lindsay with two relaxation times to solve the thermal shock problem. Buchanan [2003] has studied the behavior of infinitely long magnetoelastoelectric cylindrical shells using semianalytical finite element methods. Micro-mechanical analysis of fully coupled electromagnetothermoelastic composites has been carried out by Aboudi [2001] for prediction of the effective moduli of magnetoelastoelectric composites. Sunar et al. [2002] derived the finite element equations for thermopiezomagnetic medium based on linear constitutive equations using Hamilton’s principle. Wang and Zhong [2003] analytically

Keywords: layered and multiphase, axisymmetric temperature distribution, magnetoelastoelectric composites, dynamic behavior.

investigated a long cylindrical shell of piezoelectric/piezomagnetic composite under pressure loading and temperature change through the power series expansion method and the Fourier series expansion method. Surveying the literature, we found that there have been no studies are on magneto-electroelastic cylinder using finite element method under thermal environment. In this paper layered and multiphase magneto-electroelastic cylinder subjected to axisymmetric temperature distribution under different boundary conditions is investigated. Even though this paper presents the fully coupled finite element formulation, the numerical study is carried out for the thermal field decoupled with other fields.

2. Finite element formulation

The generalized governing differential equations for magneto-electrothermoelastic problem without body force, free charge, free current density or inner heat source can be written as

$$\sigma_{i,j} = \rho \ddot{u}_i, \quad D_{i,i} = 0, \quad B_{i,i} = 0, \quad q_{i,i} = -T_0 \rho \dot{\eta},$$

where ρ represents the mass density and T_0 represents the reference temperature. In a cylindrical coordinate system (r, θ, z) , the coupled constitutive equation for linearly magneto-electroelastic three-dimensional solid with thermal effect can be written as

$$\begin{aligned} \sigma_i &= c_{ij} S_j - e_{ik} E_k - d_{ik} H_k - \beta_{ij} \Theta, & D_l &= e_{lj} S_j + \varepsilon_{lk} E_k + m_{lk} H_k + p_l \Theta, \\ B_l &= d_{lj} S_j + m_{lk} E_k + \mu_{lk} H_k + \tau_l \Theta, & \rho \eta &= \beta_{ij} S_j + p_k E_k + \tau_k H_k + a \Theta, \end{aligned} \quad (1)$$

where $i, j = 1, \dots, 6$ and $l, k = 1, \dots, 3$. The reduced notation has been used for each tensor representations, ($\sigma_1 = \sigma_{rr}, \sigma_2 = \sigma_{\theta\theta}, \sigma_3 = \sigma_{zz}, \sigma_4 = \sigma_{\theta z}, \sigma_5 = \sigma_{rz}$ and $\sigma_6 = \sigma_{r\theta}$). σ_i, D_l, B_l, η are the components of stress, electric displacement, magnetic induction and entropy per unit volume; $c_{ij}, \varepsilon_{lk}, \mu_{lk}$ are the elastic, dielectric and magnetic permeability coefficients; e_{ki}, d_{ki}, m_{ik} are the piezoelectric, piezomagnetic and magneto-electric material coefficients; $\beta_{ij}, p_l, \tau_l, \Theta$ are stress temperature coefficient, pyroelectric constant, pyromagnetic constant and temperature difference; S_j, E_k, H_k are linear strain tensor, electric field and magnetic field vectors. $a = \rho C_E / T_0$, where C_E is the specific heat of the material. and $\Theta = T - T_0$ where T is absolute temperature and T_0 is reference temperature. The discretization of the finite element model is shown in [Figure 1](#).

The strain-displacement, electric field-electric potential and magnetic field-magnetic potential are used in the finite element analysis along with the constitutive [Equation \(1\)](#). The strain-displacement relation for axisymmetric case can be written as

$$S_{rr} = S_1 = \frac{\partial u_r}{\partial r}, \quad S_{\theta\theta} = S_2 = \frac{u_r}{r}, \quad S_{zz} = S_3 = \frac{\partial u_z}{\partial z}, \quad S_{zr} = S_5 = \frac{\partial u_z}{\partial r} + \frac{\partial u_r}{\partial z}.$$

The electric fields E_i , magnetic fields H_i and heat flux q_i are related to electric potential ϕ , magnetic potential ψ and temperature distribution Θ for axisymmetric case as

$$\begin{aligned} E_r &= E_1 = -\frac{\partial \phi}{\partial r}, & E_z &= E_3 = -\frac{\partial \phi}{\partial z}, & H_r &= H_1 = -\frac{\partial \psi}{\partial r}, & H_z &= H_3 = -\frac{\partial \psi}{\partial z}, \\ q_r &= q_1 = -k_{rr} \frac{\partial \Theta}{\partial r}, & q_z &= q_3 = -k_{zz} \frac{\partial \Theta}{\partial z}, \end{aligned}$$

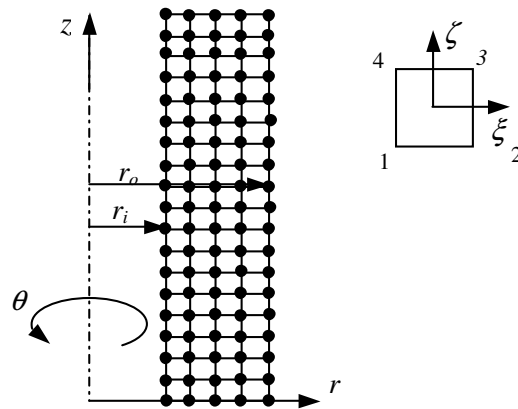


Figure 1. Schematic diagram of discretization of magnetoelectroelastic cylinder with four noded axisymmetric element.

where k is thermal conductivity of the material. For an axisymmetric cylinder geometry, load and material property does not vary in the circumferential direction. Semianalytical finite element approach for the axisymmetric problem, the displacements, electric potential and magnetic potential are expressed using Fourier series in the circumferential θ direction as

$$u_r = \sum u_r^n \cos n\theta, \quad u_\theta = \sum u_\theta^n \sin n\theta, \quad u_z = \sum u_z^n \cos n\theta, \quad \phi = \sum \phi^n \cos n\theta, \quad \psi = \sum \psi^n \cos n\theta,$$

where $n = 0$ for the axisymmetric problem. The analysis has been reduced for finite element in radial and axial direction. The finite element formulation of the coupled magnetoelectrothermoelastic problem is derived by approximating the displacement, electric potential, magnetic potential and temperature fields on the element level using two sets of shape functions:

$$\{u\} = [N_1^e]\{u^e\}, \quad \phi = [N_2^e]\{\phi^e\}, \quad \psi = [N_2^e]\{\psi^e\}, \quad \Theta = [N_2^e]\{\Theta^e\},$$

where $\{u^e\} = \{u_r \ u_\theta \ u_z\}^T$ is the displacement vector. For obtaining the element level governing equations, $\{S\}$, $\{E\}$ and $\{H\}$ are expressed in terms of derivatives of shape functions and elemental level degrees of freedom as,

$$\{S\} = [B_1]\{u^e\}, \quad \{E\} = -[B_2]\{\phi^e\}, \quad \{H\} = -[B_2]\{\psi^e\}, \quad \{\Theta'\} = [B_2]\{\Theta^e\},$$

where $[B]$ is the derivative of shape function matrix. It can be written as

$$[B_1] = \begin{bmatrix} \frac{\partial}{\partial r} & 0 \\ \frac{1}{r} & 0 \\ 0 & \frac{\partial}{\partial z} \\ \frac{\partial}{\partial z} & \frac{\partial}{\partial r} \end{bmatrix} \begin{bmatrix} N_1 & 0 & N_2 & 0 & N_3 & 0 & N_4 & 0 \\ 0 & N_1 & 0 & N_2 & 0 & N_3 & 0 & N_4 \end{bmatrix}, \quad [B_2] = \begin{bmatrix} -\frac{\partial}{\partial r} \\ -\frac{\partial}{\partial z} \end{bmatrix} [N_1 \ N_2 \ N_3 \ N_4].$$

Considering the body force $\{f\}$, the virtual displacement principle can be written as

$$\int_V (\delta\{S\}^T\{\sigma\} - \delta\{E\}^T\{D\} - \delta\{H\}^T\{B\} - \delta\Theta T_0\{\dot{\eta}\})dV = \int_V \delta\{u\}^T(\{f\} - \rho\{\ddot{u}\})dV + \int_{A_\sigma} \delta\{u\}^T\{\bar{t}\}dA + \int_{A_q} \delta\Theta\bar{q}dA, \quad (2)$$

where $\{\bar{t}\}$ represents the components of the traction vector and \bar{q} represents the heat flux. Substituting the constitutive relations from Equation (1) into Equation (2) and simplifying leads to

$$\int_V \delta\{S\}^T\{\sigma\}dV = \delta\{u^e\}^T \int_V [B_1]^T \left([c][B_1]\{u^e\} - [e](-[B_2]\{\phi^e\}) - [d](-[B_2]\{\psi^e\}) - \{\beta\}[N_2^e]^T\{\Theta^e\} \right) dV = \delta\{u^e\}^T \left([K_{uu}^e]\{u^e\} + [K_{u\phi}^e]\{\phi^e\} + [K_{u\psi}^e]\{\psi^e\} - [K_{u\Theta}^e]\{\Theta^e\} \right), \quad (3)$$

$$\int_V (-\delta\{E\}^T\{D\})dV = \delta\{\phi^e\}^T \int_V [B_2]^T \left([e]^T[B_1]\{u^e\} + [\varepsilon](-[B_2]\{\phi^e\}) + [m](-[B_2]\{\psi^e\}) + \{p\}[N_2^e]^T\{\Theta^e\} \right) dV = \delta\{\phi^e\}^T \left([K_{\phi u}^e]\{u^e\} - [K_{\phi\phi}^e]\{\phi^e\} - [K_{\phi\psi}^e]\{\psi^e\} + [K_{\phi\Theta}^e]\{\Theta^e\} \right), \quad (4)$$

$$\int_V (-\delta\{H\}^T\{B\})dV = \delta\{\psi^e\}^T \int_V [B_2]^T \left([d]^T[B_1]\{u^e\} + [m](-[B_2]\{\phi^e\}) + [\mu](-[B_2]\{\psi^e\}) + \{\tau\}[N_2^e]^T\{\Theta^e\} \right) dV = \delta\{\psi^e\}^T \left([K_{\psi u}^e]\{u^e\} - [K_{\psi\phi}^e]\{\phi^e\} - [K_{\psi\psi}^e]\{\psi^e\} + [K_{\psi\Theta}^e]\{\Theta^e\} \right), \quad (5)$$

$$\int_V (-\delta\Theta T_0\{\dot{\eta}\})dV = -\delta\{\Theta^e\}^T \int_V \left(T_0[N_2^e]\{\beta\}^T[B_1]\{\dot{u}^e\} + \{p\}^T(-[B_2]\{\dot{\phi}^e\}) + \{\tau\}^T(-[B_2]\{\dot{\psi}^e\}) + a[N_2^e]^T\{\dot{\Theta}^e\} \right) dV = \delta\{\Theta^e\}^T \left(-[C_{\Theta u}^e]\{\dot{u}^e\} + [C_{\Theta\phi}^e]\{\dot{\phi}^e\} + [C_{\Theta\psi}^e]\{\dot{\psi}^e\} - [C_{\Theta\Theta}^e]\{\dot{\Theta}^e\} \right), \quad (6)$$

$$\int_V \delta\{\Theta^e\}^T\{q\}dV = \delta\{\Theta^e\}^T \int_V [B_2]^T(-[k][B_2]\{\Theta^e\})dV = \delta\{\Theta^e\}^T(-[K_{\Theta\Theta}^e]\{\Theta^e\}), \quad (7)$$

$$\int_V \delta\{u\}^T(\{f\} - \rho\{\ddot{u}\})dV = \delta\{u^e\}^T \int_V [N_1^e]^T(\{f\} - \rho[N_1^e]\{\ddot{u}^e\})dV = \delta\{u^e\}^T(\{f_m^e\} - [M_{uu}^e]\{\ddot{u}^e\}), \quad (8)$$

$$\int_{A_\sigma} \delta\{u\}^T\{\bar{t}\}dA = \delta\{u^e\}^T \int_{A_\sigma} [N_1^e]\{\bar{t}\}dA = \delta\{u^e\}^T\{T_u^e\}, \quad (9)$$

$$\int_{A_q} \delta\Theta\{\bar{q}\}dA = \delta\{\Theta^e\}^T \int_{A_q} [N_2^e]\{\bar{q}\}dA = \delta\{\Theta^e\}^T\{T_\Theta^e\}. \quad (10)$$

From Equations (3)–(10) we can obtain

$$\begin{aligned}
 [M_{uu}^e]\{\ddot{u}^e\} - [C_{u\Theta}^e]\{\dot{\Theta}^e\} + [K_{uu}^e]\{u^e\} + [K_{u\phi}^e]\{\phi^e\} + [K_{u\psi}^e]\{\psi^e\} - [K_{u\Theta}^e]\{\Theta^e\} &= \{f_u^e\} + \{T_u^e\} \\
 [K_{u\phi}^e]^T\{u^e\} - [K_{\phi\phi}^e]\{\phi^e\} - [K_{\phi\psi}^e]\{\psi^e\} + [K_{\phi\Theta}^e]\{\Theta^e\} &= 0 \\
 [K_{u\psi}^e]^T\{u^e\} - [K_{\phi\psi}^e]^T\{\phi^e\} - [K_{\psi\psi}^e]\{\psi^e\} + [K_{\psi\Theta}^e]\{\Theta^e\} &= 0 \\
 [C_{\Theta u}^e]\{\dot{u}^e\} - [C_{\Theta\phi}^e]\{\dot{\phi}^e\} - [C_{\Theta\psi}^e]\{\dot{\psi}^e\} + [C_{\Theta\Theta}^e]\{\dot{\Theta}^e\} + [K_{\Theta\Theta}^e]\{\Theta^e\} &= -\{T_{\Theta}^e\}.
 \end{aligned}$$

Above equation can be expressed in the matrix form

$$\begin{aligned}
 \begin{bmatrix} M_{uu}^e & 0 & 0 & 0 \\ 0 & 0 & 0 & 0 \\ 0 & 0 & 0 & 0 \\ 0 & 0 & 0 & 0 \end{bmatrix} \begin{bmatrix} \ddot{u}^e \\ \ddot{\phi}^e \\ \ddot{\psi}^e \\ \ddot{\Theta}^e \end{bmatrix} + \begin{bmatrix} 0 & 0 & 0 & -C_{u\Theta}^e \\ 0 & 0 & 0 & 0 \\ 0 & 0 & 0 & 0 \\ C_{\Theta u}^e & -C_{\Theta\phi}^e & -C_{\Theta\psi}^e & C_{\Theta\Theta}^e \end{bmatrix} \begin{bmatrix} \dot{u}^e \\ \dot{\phi}^e \\ \dot{\psi}^e \\ \dot{\Theta}^e \end{bmatrix} + \\
 \begin{bmatrix} K_{uu}^e & K_{u\phi}^e & K_{u\psi}^e & -K_{u\Theta}^e \\ K_{\phi u}^e & -K_{\phi\phi}^e & -K_{\phi\psi}^e & K_{\phi\Theta}^e \\ K_{\psi u}^e & -K_{\psi\phi}^e & -K_{\psi\psi}^e & K_{\psi\Theta}^e \\ 0 & 0 & 0 & K_{\Theta\Theta}^e \end{bmatrix} \begin{bmatrix} u^e \\ \phi^e \\ \psi^e \\ \Theta^e \end{bmatrix} = \begin{bmatrix} f_u^e + T_u^e \\ 0 \\ 0 \\ -T_{\Theta}^e \end{bmatrix}, \quad (11)
 \end{aligned}$$

where different elemental matrices in Equation (11) are defined as

$$\begin{aligned}
 [K_{uu}^e] &= \int_V [B_1]^T [c] [B_1] dV, & [K_{u\phi}^e] &= \int_V [B_1]^T [e] [B_2] dV, \\
 [K_{u\psi}^e] &= \int_V [B_1]^T [d] [B_2] dV, & [K_{\phi\phi}^e] &= \int_V [B_2]^T [\varepsilon] [B_2] dV, \\
 [K_{\psi\psi}^e] &= \int_V [B_2]^T [\mu] [B_2] dV, & [C_{\Theta u}^e] &= \int_V T_0 [N_2]^T \{\beta\}^T [B_1] dV, \\
 [C_{\Theta\phi}^e] &= \int_V T_0 [N_2]^T \{p\}^T [B_2] dV, & [C_{\Theta\psi}^e] &= \int_V T_0 [N_2]^T \{\tau\}^T [B_2] dV, \\
 [K_{u\Theta}^e] &= \int_V [B_1]^T \{\beta\} [N_2]^T dV, & [K_{\phi\psi}^e] &= \int_V [B_2]^T [m] [B_2] dV, \\
 [K_{\phi\Theta}^e] &= \int_V [B_2]^T \{p\} [N_2]^T dV, & [K_{\psi\Theta}^e] &= \int_V [B_2]^T \{\tau\} [N_2]^T dV, \\
 [C_{\Theta\Theta}^e] &= \int_V T_0 [N_2]^T a [N_2] dV, & [K_{\Theta\Theta}^e] &= \int_V [B_2]^T [k] [B_2] dV, \\
 [M_{uu}^e] &= \int_V [N_1]^T \rho [N_1] dV, & \{f_u^e\} &= \int_V [N_1^e] \{f\} dV, \\
 \{T_u^e\} &= \int_{A_\sigma} [N_1^e]^T \{\bar{t}\} dA, & \{T_{\Theta}^e\} &= \int_{A_q} [N_2^e] \bar{q} dA.
 \end{aligned}$$

The volume integration is replaced with $dV = 2\pi r dr dz$ for axisymmetric problems. From Equation (11), assembling the all element contributions, the equation of motion can be written as,

$$[M]\{\ddot{v}\} + [D]\{\dot{v}\} + [K]\{v\} = \{F\}, \quad (12)$$

where

$$[M] = \begin{bmatrix} M_{uu} & 0 & 0 & 0 \\ 0 & 0 & 0 & 0 \\ 0 & 0 & 0 & 0 \\ 0 & 0 & 0 & 0 \end{bmatrix}, \quad [D] = \begin{bmatrix} 0 & 0 & 0 & -C_{u\Theta} \\ 0 & 0 & 0 & 0 \\ 0 & 0 & 0 & 0 \\ C_{\Theta u} & -C_{\Theta\phi} & -C_{\Theta\psi} & C_{\Theta\Theta} \end{bmatrix},$$

$$[K] = \begin{bmatrix} K_{uu} & K_{u\phi} & K_{u\psi} & -K_{u\Theta} \\ K_{\phi u} & -K_{\phi\phi} & -K_{\phi\psi} & K_{\phi\Theta} \\ K_{\psi u} & -K_{\psi\phi} & -K_{\psi\psi} & K_{\psi\Theta} \\ 0 & 0 & 0 & K_{\Theta\Theta} \end{bmatrix}, \quad \{F\} = \begin{bmatrix} f_u + T_u \\ 0 \\ 0 \\ -T_\Theta \end{bmatrix}, \quad \{v\} = \begin{bmatrix} u \\ \phi \\ \psi \\ \Theta \end{bmatrix},$$

with $\{u\} = [u_r \ u_z]^T$. The equation of motion (12) can be used to investigate the dynamic behavior of the magnetoelctrothermoelastic material where mechanical, electrical, magnetic and thermal fields are fully coupled. To investigate the static behavior of magnetoelctroelastic cylinder the above equation is reduced along with the following assumptions,

1. Absence of body force, free charge density and free current density.
2. The temperature distribution is evaluated explicitly assuming the coupling between mechanical, electrical and magnetic fields.

The finite element equation can be written as,

$$\begin{aligned} [K_{uu}]\{u\} + [K_{u\phi}]\{\phi\} + [K_{u\psi}]\{\psi\} &= \{F_{th}\}, \\ [K_{u\phi}]^T\{u\} - [K_{\phi\phi}]\{\phi\} - [K_{\phi\psi}]\{\psi\} &= 0, \\ [K_{u\psi}]^T\{u\} - [K_{\phi\psi}]^T\{\phi\} - [K_{\psi\psi}]\{\psi\} &= 0. \end{aligned} \quad (13)$$

The thermal load vector can be written as $\{F_{th}^e\} = \int_V [B_1]^T \{\beta\} \Theta dv$. By using standard condensation techniques, the equivalent stiffness matrix is derived by eliminating the electric potential ϕ and magnetic potential ψ in Equation (13). The derived stiffness matrix $[K_{eq}]$ and load vector $\{F_{th}\}$ is used to solve for nodal thermal displacements.

$$[K_{eq}]\{u\} = \{F_{th}\}, \quad (14)$$

where $[K_{eq}] = [K_{uu}] + [K_{u\phi}][K_{II}]^{-1}[K_I] + [K_{u\psi}][K_{IV}]^{-1}[K_{III}]$, and

$$\begin{aligned} [K_I] &= [K_{u\phi}]^T - [K_{\phi\psi}][K_{\psi\psi}]^{-1}[K_{u\psi}]^T, & [K_{II}] &= [K_{\phi\phi}] - [K_{\phi\psi}][K_{\psi\psi}]^{-1}[K_{\phi\psi}]^T, \\ [K_{III}] &= [K_{u\psi}]^T - [K_{\phi\psi}]^T[K_{\phi\phi}]^{-1}[K_{u\phi}]^T, & [K_{IV}] &= [K_{\psi\psi}] - [K_{\phi\psi}]^T[K_{\phi\phi}]^{-1}[K_{\phi\psi}]. \end{aligned}$$

The coupled magnetoelctroelastic finite element Equation (14) is solved subject to thermal loading. The four-point gaussian integration scheme has been adopted to evaluate the integrals involved in different elemental stiffness matrices and thermal load vectors. The elemental stiffness matrices and thermal load vectors are assembled to get the global stiffness matrices and global thermal load vector. The coupled equivalent stiffness matrix $[K_{eq}]$ of magnetoelctroelastic system has been inverted to evaluate the thermal displacements. After evaluating the thermal displacements, the electric potential ϕ and magnetic potential ψ can be derived at each nodal points using the following equations,

$$\phi = [K_{II}]^{-1}[K_I]\{u\}, \quad \psi = [K_{IV}]^{-1}[K_{III}]\{u\}.$$

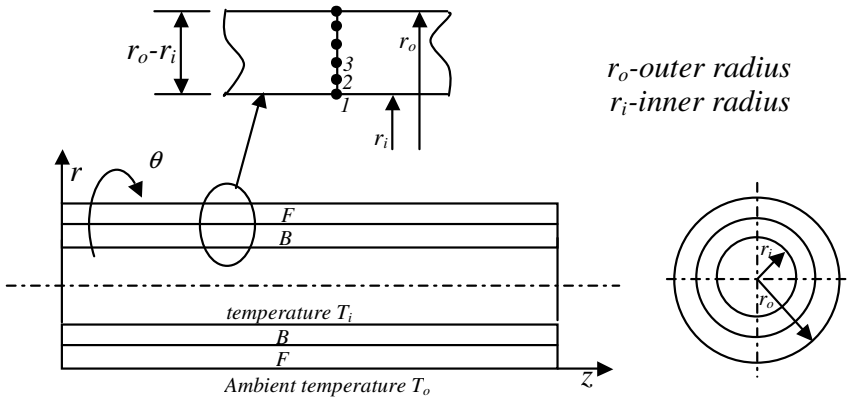


Figure 2. Schematic diagram of layered magneto-electro-elastic hollow cylinder along with thermal boundary conditions.

3. Evaluation of temperature distribution across the thickness of the axisymmetric cylinder under steady state heat conduction

We consider steady state one-dimensional heat conduction analysis to evaluate the temperature distribution across the thickness of the magneto-electro-elastic cylinder under temperature boundary conditions. The temperature along the length of the cylinder is constant subject to axisymmetric temperature distribution. Figure 2 shows the schematic diagram of problem considered for steady state heat conduction analysis and finite element discretization across thickness direction. The finite element formulation used in the present work is based on the procedure reported in [Reddy 1984]. By neglecting the convective and radiation heat transfers, the governing differential equation for steady state heat conduction equation in radial direction is given by

$$-\frac{d}{dr} \left(k(r) \frac{dT}{dr} \right) = 0.$$

In the present study, thermal boundary conditions considered in such a way that T_i is the temperature on the inner surface of the cylinder and T_0 is the temperature on the outer surface of the cylinder, which is normally ambient temperature. Applying variational principle on the governing equation, the finite element equation $[K_{cond}]\{T\} = 0$, to evaluate temperature distribution due to heat conduction is obtained [Ross 1990]. Here $[K_{cond}]$ is the heat conduction matrix and $\{T\}$ is the vector of nodal temperature.

The above equation is solved for the specified temperature boundary condition at the inner and outer surface to obtain the temperature distribution across the radial direction.

4. Validation of the present formulation

The present formulation developed for the analysis of layered and multiphase magneto-electro-elastic cylinder has been validated with the stresses reported in [Wang and Zhong 2003] under internal pressure loading.

The dimensions of cylinder are as follows: length of the cylinder (l) = 4.0 m, inner radius (r_i) = 0.7 m and thickness of the cylinder (t) = 0.6 m. Figure 3 illustrates the comparison of results of axial

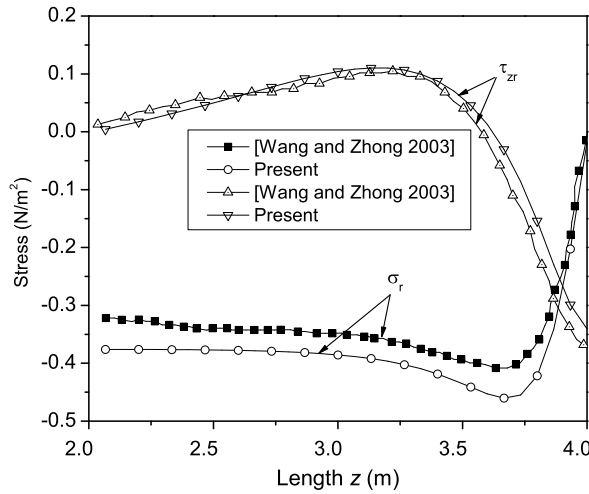


Figure 3. Variation of normal radial stress σ_r and shear stress τ_{zr} on the outer surface at $r = r_o$ along the axial direction subjected to internal pressure loading under simply supported boundary condition.

stresses for B/F layered magneto-electroelastic cylinder under internal pressuring loading with simply supported boundary condition. The thermal load vector have been validated using commercial finite element software [ANSYS 1999], by evaluating the thermal displacement along the axial length of simply supported piezoelectric cylinder under uniform temperature rise of 75°C .

Figure 4 illustrates the comparison of results on thermal displacement for simply supported piezoelectric cylinder. This was performed primarily because of the lack of literature on the evaluation of thermal

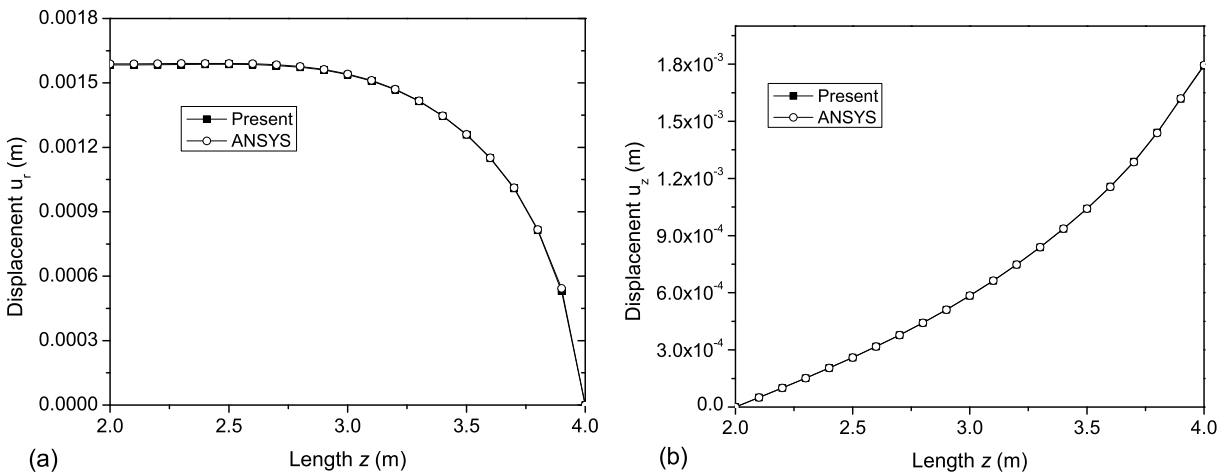


Figure 4. Variation (a) radial displacement u_r and (b) axial displacement u_z on the outer surface at $r = r_o$ subjected to uniform temperature rise.

stresses of magneto-electroelastic cylinder using finite element method. Observe that the results obtained by present formulation are in close agreement with the available literature and commercial finite element software ANSYS.

5. Results and discussions

We consider a two layered and multiphase magneto-electroelastic composite cylinder composed of piezo-electric BaTiO₃ and piezomagnetic CoFe₂O₄ materials. Two-layered cylinder is made of the inner surface with piezoelectric BaTiO₃ material and outer surface made of piezomagnetic CoFe₂O₄ material (B/F). The multiphase magneto-electroelastic cylinder made of piezomagnetic (CoFe₂O₄) matrix reinforced by piezoelectric (BaTiO₃) material for different volume fraction. The $V_f = 1.0$ corresponds to piezoelectric (BaTiO₃) material and $V_f = 0.0$ corresponds to piezomagnetic (CoFe₂O₄) material. The dimensions of cylinder are as follows: length of the cylinder (l) = 4.0 m, inner radius (r_i) = 0.995 m, thickness of the cylinder (t) = 0.01 m, r/t ratio = 100, l/r ratio = 4.0. The present finite element model is discretized using 600 four-noded axisymmetric elements with 3355 degrees of freedom (dof): 2013 displacement dof, 671 electric dof and 671 magnetic dof. The simply supported and clamped-clamped ($u_r = \phi = \psi = 0$ at simply supported edge and $u_r = u_z = \phi = \psi = 0$ at clamped edge) boundary conditions are adopted. The material constants listed in Table 1 reported by Aboudi [2001] are used for the present study. The thermal conductivity k and the coefficient of thermal expansion α are obtained from the literature as reported by Ootao and Tanigawa [2005]. In the above literature the coefficient of thermal expansion α is taken for CoFe₂O₄. The diffusivities for BaTiO₃ and CoFe₂O₄ given in [Ootao and Tanigawa 2005] are not needed, since the present analysis assumed as steady state problem. Thermal properties are not reported in the literature for different volume fraction. The coefficient of thermal expansion are evaluated from the values of BaTiO₃ and CoFe₂O₄ for different volume fractions of 0.2, 0.4, 0.6 and 0.8 using the following expression [Tan and Tong 2002]:

$$\alpha_{11} = c_{11} \left(\frac{V_f \alpha_{11}^p}{c_{11}^p} + \frac{(1 - V_f) \alpha_{11}^m}{c_{11}^m} \right), \quad \alpha_{33} = V_f \alpha_{33}^p + (1 - V_f) \alpha_{33}^m + \frac{c_{13} \alpha_{11}}{c_{11}} - \frac{V_f c_{13}^p \alpha_{11}^p}{c_{11}^p} - \frac{(1 - V_f) c_{13}^m \alpha_{11}^m}{c_{11}^m}.$$

The densities reported by Ramirez et al. [2006] for BaTiO₃ and CoFe₂O₄ are used for the present analysis. The density and thermal conductivities are evaluated from the values of BaTiO₃ and CoFe₂O₄ using the rule of mixture,

$$\rho = V_f \rho^p + (1 - V_f) \rho^m, \quad k_{11} = k_{33} = V_f k_{11}^p + (1 - V_f) k_{11}^m,$$

where the superscript p stands for piezoelectric and m stands for piezomagnetic.

Evaluation of temperature distribution. The magneto-electroelastic cylinder is discretized using two-noded element with temperature degree of freedom as shown in Figure 2. These nodal temperatures are used to evaluate the element temperature of four-noded axisymmetric element and utilized to evaluate thermal load vector. Figure 5 shows the temperature distribution across thickness direction for layered and multiphase magneto-electroelastic cylinder.

Distribution of displacement, electric potential, magnetic potential and thermal stresses subjected to simply supported boundary condition. Figure 6(a) shows the distribution of radial displacement u_r on

	$V_f = 0.0$	$V_f = 0.2$	$V_f = 0.4$	$V_f = 0.6$	$V_f = 0.8$	$V_f = 1.0$
<i>Elastic constants</i>						
c_{11}	269.5	240	220	190	170	162
$c_{12} = c_{13}$	170	145	125	110	100	78
c_{23}	173	146	125	110	100	77
$c_{22} = c_{33}$	286	250	225	200	175	166
c_{55}	45.3	45	45	45	50	43
<i>Piezoelectric constants</i>						
e_{11}	0	4	7	11	14	18.6
$e_{12} = e_{13}$	0	-2	-3	-3.5	-4	-4.4
e_{35}	0	0	0	0	0	11.6
<i>Dielectric constants</i>						
ϵ_{11}	0.093	2.5	5.0	7.5	10	12.6
ϵ_{33}	0.08	0.33	0.8	0.9	1.0	11.2
<i>Magnetic permeability constants</i>						
μ_{11}	1.57	1.33	1.0	0.75	0.5	0.1
μ_{33}	-5.9	-3.9	-2.5	-1.5	-0.8	0.05
<i>Piezomagnetic constants</i>						
q_{11}	700	550	380	260	120	0
$q_{12} = q_{13}$	580	410	300	200	100	0
q_{35}	560	340	220	180	80	0
<i>Magnetolectric constants</i>						
m_{11}	0	2000	2750	2500	1500	0
m_{33}	0	2.8	4.8	6.0	6.8	0
<i>Coefficient of thermal expansion</i>						
α_{11}	10.0	9.72	9.15	8.37	7.44	6.4
α_{33}	10.0	11.7	13.0	14.11	14.98	15.7
<i>Density</i>						
ρ	5300	5400	5500	5600	5700	5800
<i>Thermal conductivity</i>						
$k_{11} = k_{33}$	3.2	3.06	2.92	2.78	2.64	2.5

Table 1. Material properties as a percentage (volume fraction V_f) of $\text{CoFe}_2\text{O}_4 - \text{BaTiO}_3$, where c_{ij} is measured in 10^9 N/m^2 , e_{ij} in C/m^2 , ϵ_{ij} in 10^{-9} C/Vm , q_{ij} in N/Am , μ_{ij} in $10^{-4} \text{ N s}^2/\text{C}^2$, m_{ij} in 10^{-12} N s/VC , α_{ij} in $1/\text{K}$, ρ in kg/m^3 , and k_{ij} in W/mK .

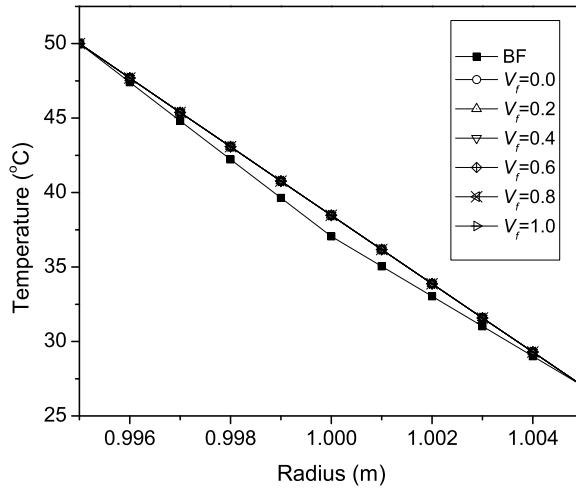


Figure 5. Distribution of temperature across thickness direction for layered and multi-phase magnetoelastoelectroelastic cylinder.

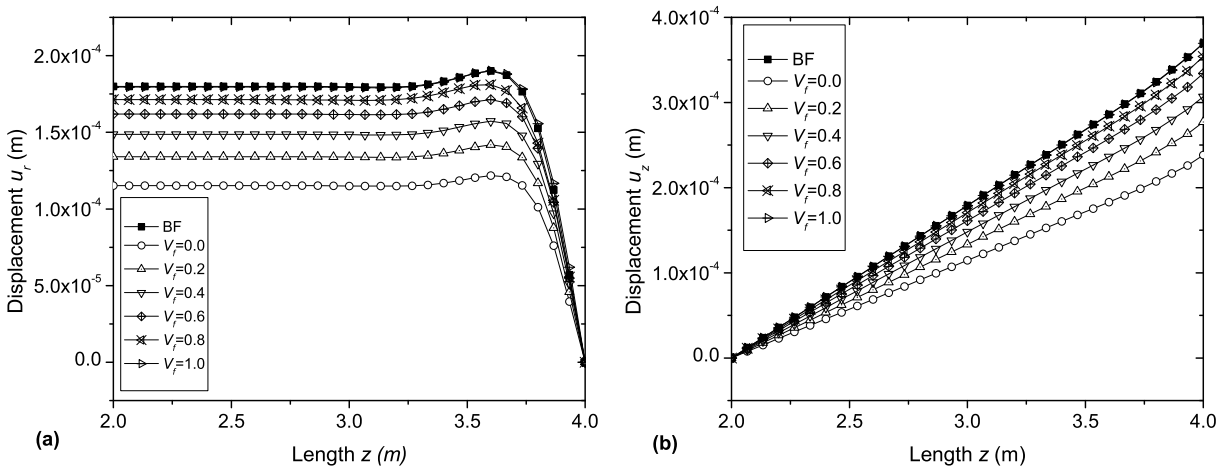


Figure 6. Distribution of (a) radial displacement u_r and (b) axial displacement u_z on the outer surface at $r = r_o$ along the axial direction under simply-supported boundary condition.

the outer surface along the axial direction for B/F layered and multiphase with different volume fraction of magnetoelastoelectroelastic cylinder. It is observed that the radial displacement u_r of B/F layered cylinder is slightly higher as compared to multiphase magnetoelastoelectroelastic cylinder with $V_f = 1.0$. The radial displacement is increasing with volume fraction of multiphase magnetoelastoelectroelastic cylinder and the magnitude is higher near the simply supported edge. Figure 6(b) shows the axial displacement u_z on the outer surface along the axial direction. Observe that the magnitude of axial displacement u_z is higher at

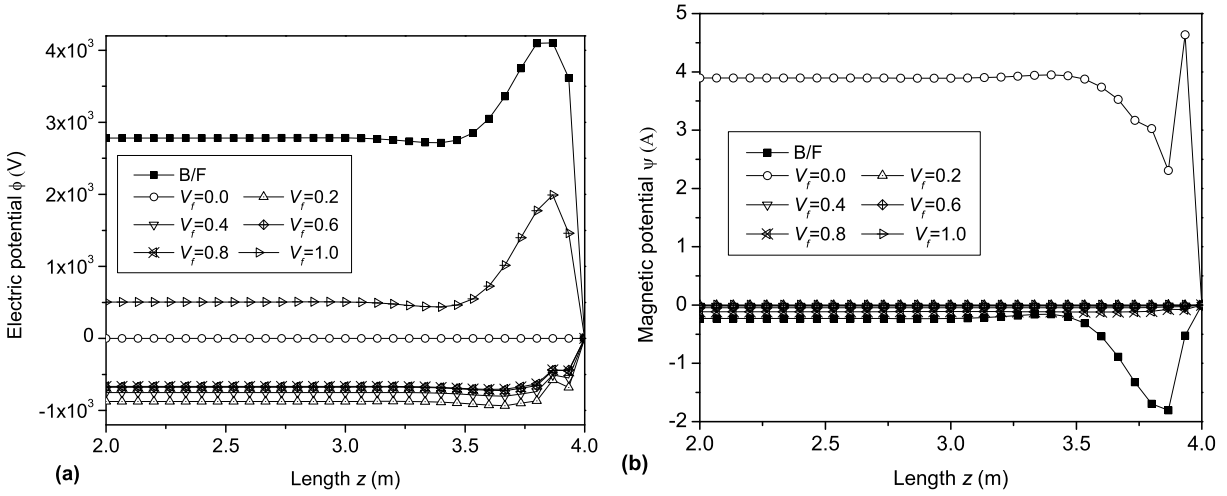


Figure 7. Distribution of (a) electric potential ϕ and (b) magnetic potential ψ on the outer surface at $r = r_o$ along the axial direction under simply-supported boundary condition.

the simply supported edge. The axial displacement u_z is increasing with volume fraction of multiphase magneto-electroelastic cylinder.

Figure 7(a) shows the distribution of electric potential ϕ on the outer surface along the axial direction for B/F layered and multiphase with different volume fraction of magneto-electroelastic cylinder. It is observed that the electric potential is higher for B/F layered case as compared to multiphase magneto-electroelastic cylinder and magnitude is higher near the simply supported edge. Figure 7(b) shows the distribution of magnetic potential ψ on the outer face along the axial direction.

The magnetic potential is higher for $V_f = 0.0$ as compared to other volume fraction and B/F layered cylinder. Figure 8(a) shows the distribution of radial displacement u_r at $z = l/2$ along the radial direction for B/F layered and multiphase with different volume fraction of magneto-electroelastic cylinder. Observe that the B/F layered radial displacement u_r is higher as compared to multiphase magneto-electroelastic cylinder. It is increases with volume fraction for multiphase case. Figure 8(b) shows the distribution of axial displacement u_z at $z = l$ along the radial direction for B/F layered and multiphase magneto-electroelastic cylinder. Note that the similar trend is observed for axial displacement u_z .

Figure 9 illustrates the distribution of electric potential ϕ and magnetic potential ψ at $z = l/2$ along the radial direction for B/F layered and multiphase multiphase magneto-electroelastic cylinder. Observe that the electric potential ϕ is higher for layered magneto-electroelastic case and magnetic potential ψ is higher for $V_f = 0.0$. Note that variation of electric potential ϕ in the piezoelectric phase and constant in the piezomagnetic phase. The electric potential ϕ is zero for $V_f = 0.0$ due to the fact that the piezoelectric constants are zero. Figure 9(b) illustrates the variation of magnetic potential ψ at $z = l/2$ along the radial direction for B/F layered and multiphase magneto-electroelastic cylinder.

Figure 10 illustrates the distribution of normal stress σ_r and shear stress τ_{zr} at $r = 0.005$ m along the axial direction for B/F layered and multiphase magneto-electroelastic cylinder. Observe that the normal

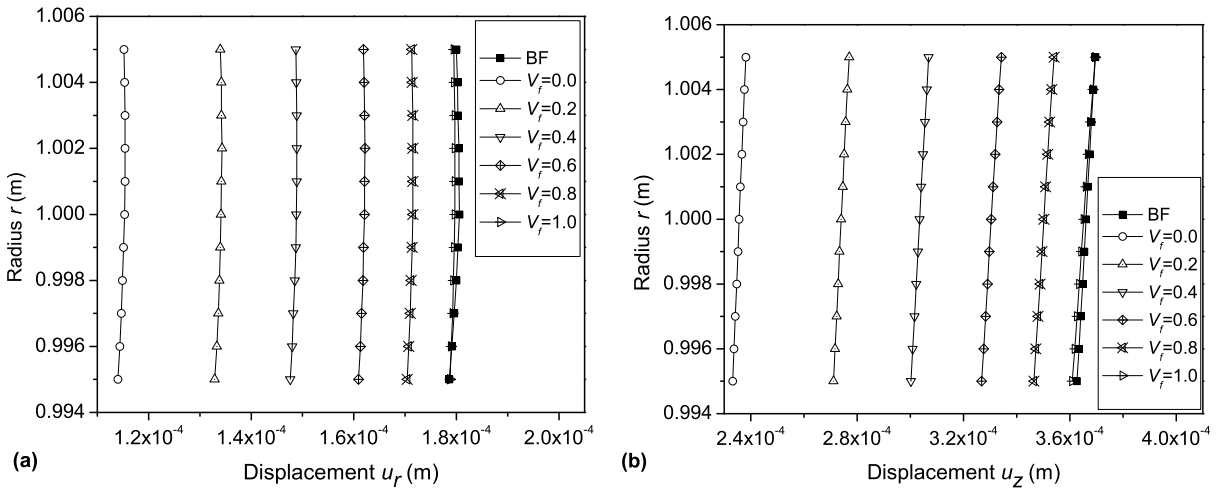


Figure 8. Distribution of (a) radial displacement u_r at $z = l/2$ and (b) axial displacement u_z at $z = l$ along the radial direction under simply-supported boundary condition.

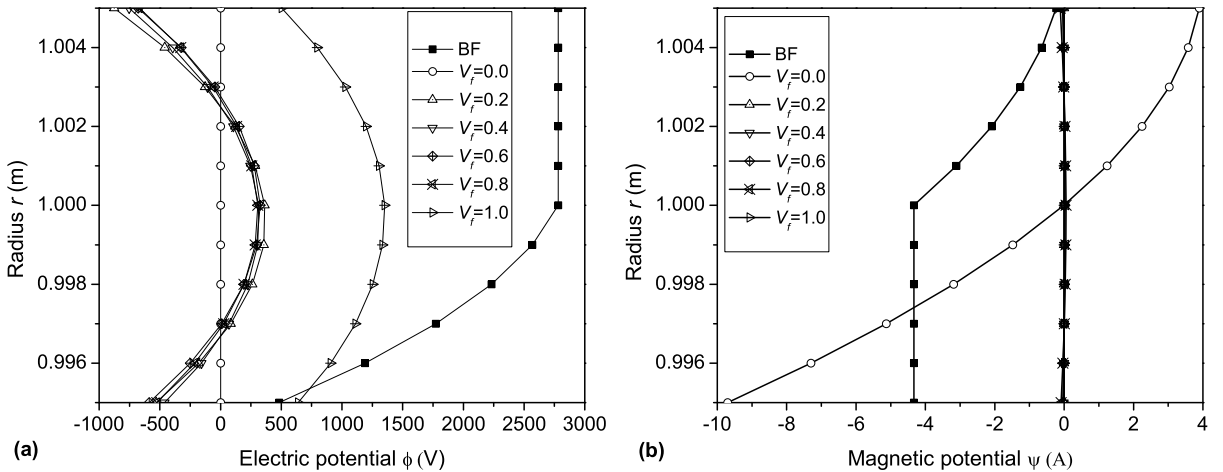


Figure 9. Distribution of (a) electric potential ϕ and (b) magnetic potential ψ at $z = l/2$ along the radial direction under simply-supported boundary condition.

stress σ_r for layered cylinder is higher as compared to multiphase cylinder and there is no significant effect on shear stress τ_{zr} . [Figure 11](#) illustrates the distribution of normal stress σ_r and σ_θ for B/F layered magnetoelastoelectroelastic cylinder at $z = l/2$ along the radial direction.

Note the discontinuity of radial stress σ_r at the material interface. Observe that the normal stress σ_θ compressive in nature at the inner surface and tensile on the outer surface. [Figure 12](#) shows the distribution of normal stress σ_r and σ_θ at $z = l/2$ along the radial direction. It is noticed that the normal stress σ_r increases with volume fraction decreases for multiphase magnetoelastoelectroelastic cylinder. It can

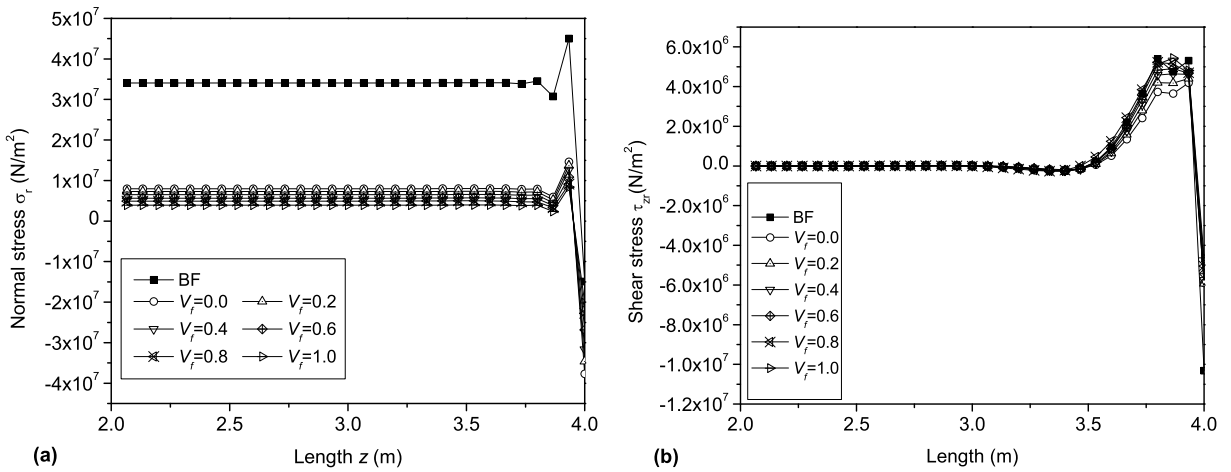


Figure 10. Distribution of (a) normal stress σ_r and (b) shear stress τ_{zr} at $r = 0.005$ m along the axial direction under simply-supported boundary condition.

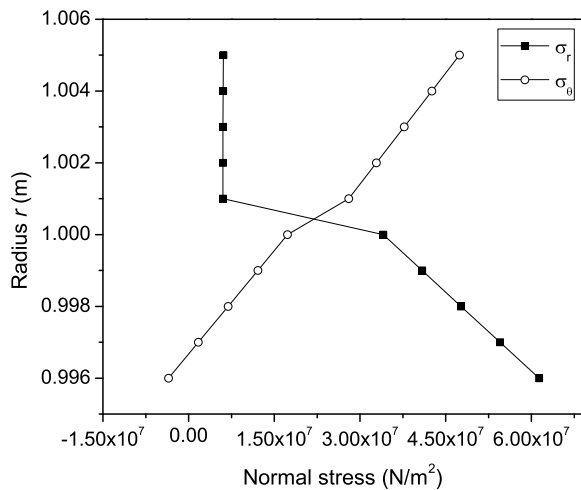


Figure 11. Distribution of normal stress σ_r and σ_θ for B/F layered magneto-electro-elastic cylinder at $z = l/2$ along the radial direction under simply-supported boundary condition.

be seen that the normal stress σ_θ compressive in nature at the inner surface and tensile on the outer surface. Its magnitude is minimum for $V_f = 0.0$ and maximum for $V_f = 1.0$.

Distribution of displacement, electric potential, magnetic potential and thermal stresses subjected to clamped-clamped boundary condition. Figure 13(a) shows the distribution of radial displacement u_r on the outer surface along the axial direction for B/F layered and multiphase with different volume fraction of magneto-electro-elastic cylinder under clamped-clamped boundary condition.

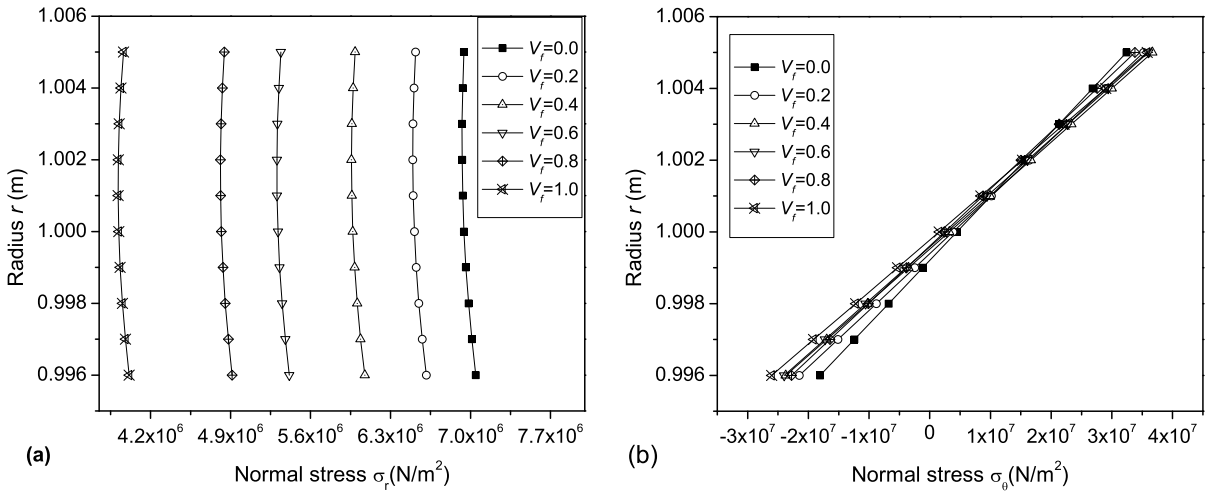


Figure 12. Distribution of (a) normal stress σ_r and (b) normal stress σ_θ at $z = l/2$ along the radial direction under simply-supported boundary condition.

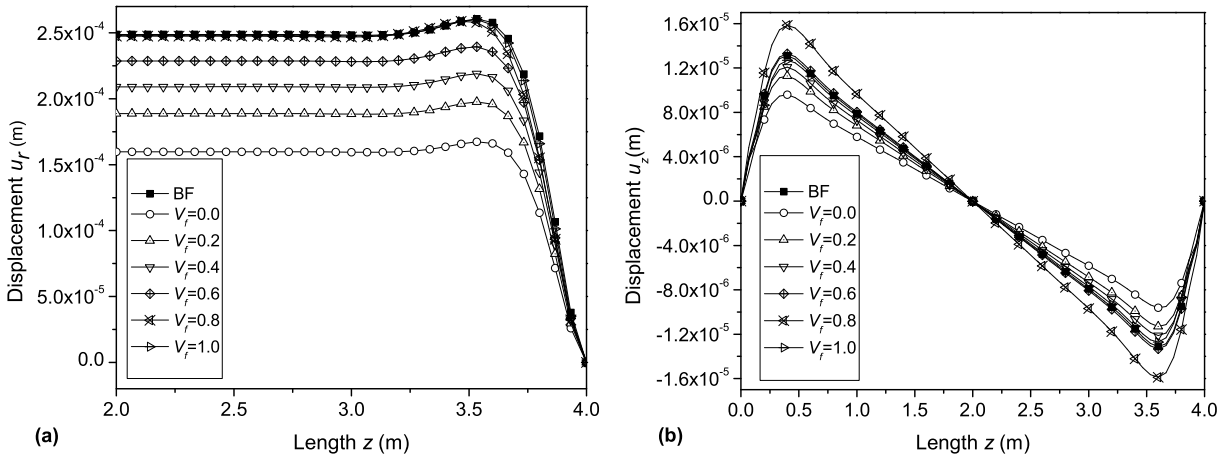


Figure 13. Distribution of (a) radial displacement u_r ($l = 2.0$ to 4.0 m) and (b) axial displacement u_z ($l = 0.0$ to 4.0 m) on the outer surface at $r = r_o$ along the axial direction under clamped-clamped boundary condition.

A similar trend is observed compared to simply supported boundary condition with higher radial displacement. From [Figure 13\(b\)](#), it is observed that the maximum axial displacement occurs near the clamped edge and the distribution is quite different as compared to simply supported boundary condition. [Figure 14\(a\)](#) shows the distribution of electric potential ϕ on the outer surface along the axial direction for clamped-clamped boundary condition. The maximum electric potential occurs close to the clamped edge, further the electric potential decreases and remains constant in magnitude over the length of the cylinder. The zero electric potential for $V_f = 0.0$ due to fact that the piezoelectric constants are zero.

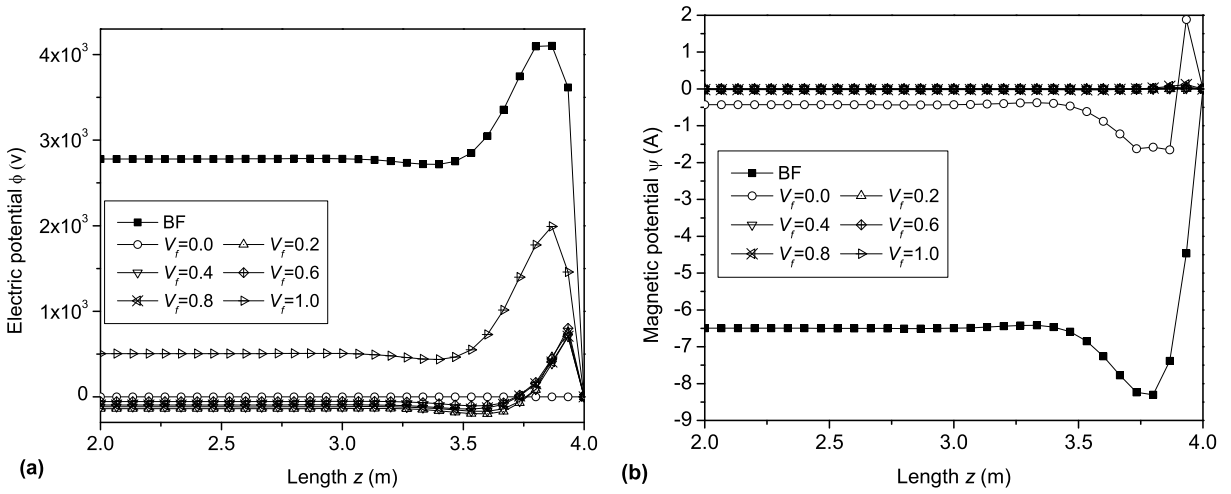


Figure 14. Variation of (a) electric potential ϕ and (b) magnetic potential ψ on the outer surface at $r = r_o$ along the axial direction under clamped-clamped boundary condition.

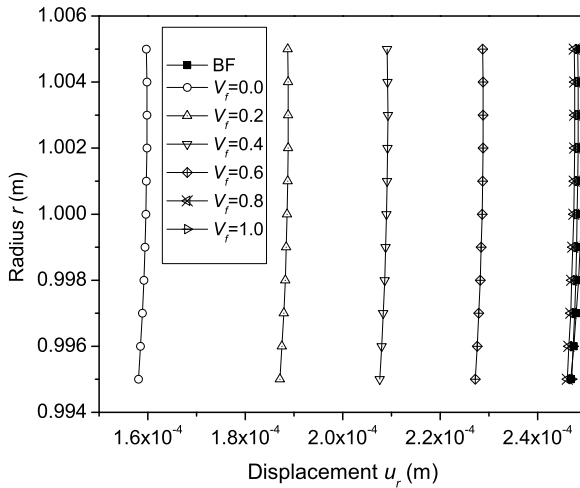


Figure 15. Distribution of radial displacement u_r at $z = l/2$ along the radial direction subjected to thermal loading under clamped-clamped boundary condition.

Figure 14(b) shows the distribution of magnetic potential ψ on the outer surface along the axial direction for clamped-clamped boundary condition.

Figure 15 shows the distribution of radial displacement u_r at $z = l/2$ along the radial direction subjected to thermal loading under clamped-clamped boundary condition. Observe that the radial displacement u_r is higher as compared to simply supported boundary condition and increasing with volume fraction. This is because the stiffness is greater for $V_f = 0.0$ and less for $V_f = 1.0$ due to elastic properties of materials.

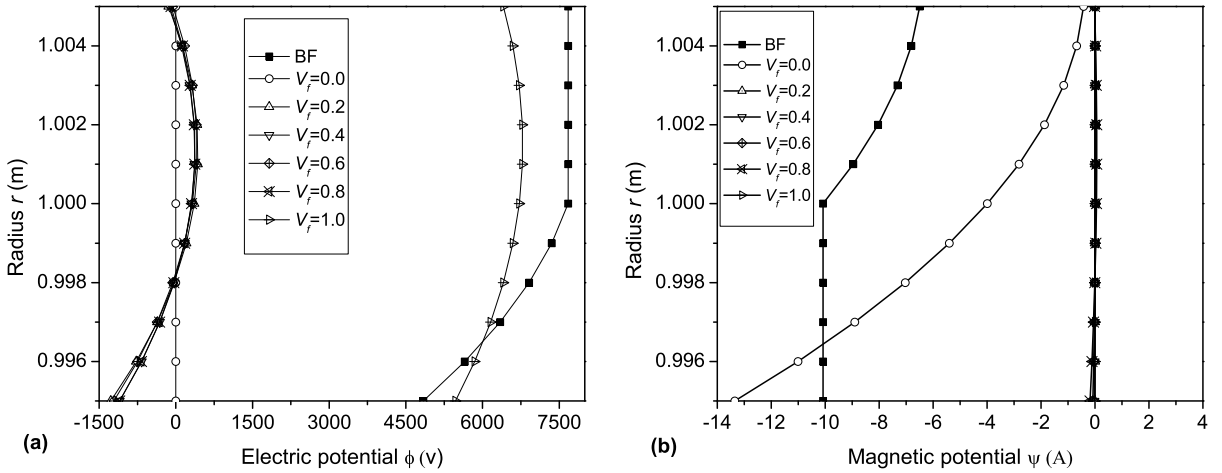


Figure 16. Distribution of (a) electric potential ϕ and (b) magnetic potential ψ at $z = l/2$ along the radial direction subjected to thermal loading under clamped-clamped boundary condition.

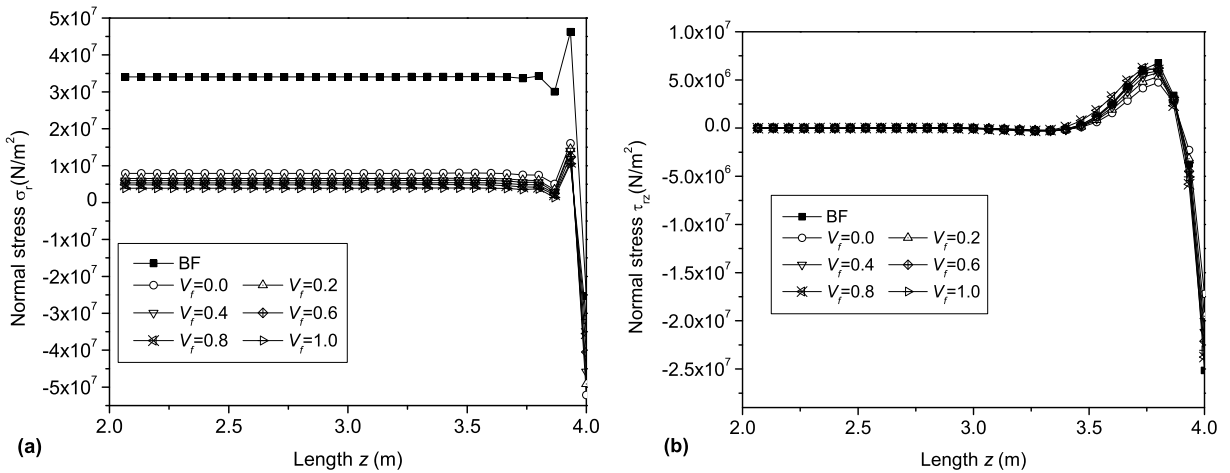


Figure 17. Distribution of (a) normal stress σ_r and (b) shear stress τ_{zr} at $r = 0.005$ m along the axial direction under clamped-clamped boundary condition.

Figure 16 illustrates the distribution of electric potential ϕ and magnetic potential ψ at $z = l/2$ along the radial direction for clamped-clamped magneto-electroelastic cylinder. A similar trend is observed with higher magnitude compared to simply supported boundary condition. Figure 17 illustrates the distribution of normal stress σ_r and shear stress τ_{zr} at $r = 0.005$ m along the axial direction for clamped-clamped magneto-electroelastic cylinder. Observe that the normal stress σ_r is higher for B/F layered cylinder.

There is no significant difference along the length and higher in the clamped end as compared to Simply-Supported boundary condition. Figures 18 and 19 illustrate the distribution of normal stress σ_r ,

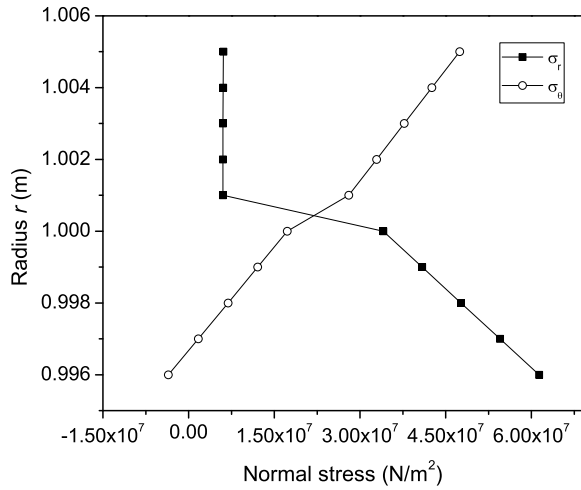


Figure 18. Distribution of normal stress σ_r and σ_θ for B/F layered magneto-electroelastic shell at $z = l/2$ along the radial direction under clamped-clamped boundary condition.

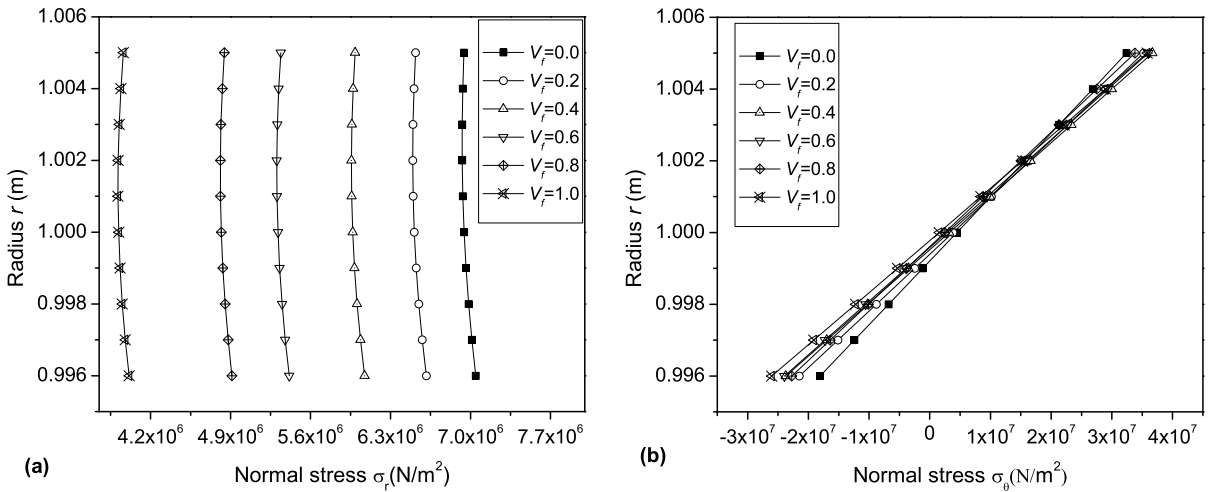


Figure 19. Distribution of (a) normal stress σ_r and (b) normal stress σ_θ at $z = l/2$ along the radial direction subjected to thermal loading under clamped-clamped boundary condition.

and σ_θ for B/F layered magneto-electroelastic cylinder at $z = l/2$ along the radial direction and normal stress σ_r and σ_θ for multiphase magneto-electroelastic cylinder at $z = l/2$ along the radial direction. A similar behavior is observed compared to afore mentioned boundary condition.

6. Conclusions

A semi-analytical finite element model is used for the analysis of layered and multiphase magneto-electro-elastic cylinder under axisymmetric temperature distribution. The finite element formulation for transient analysis of magneto-electrothermoelastic cylinder has been derived from coupled constitutive equations. The numerical results are presented based on the coupling between mechanical, electrical and magnetic fields. The thermal field is coupled with mechanical fields alone. It is found that the layered magneto-electroelastic cylinder have substantial effect on induced magnetic, electric and elastic fields as compared to multiphase magneto-electroelastic cylinder with different volume fraction under different boundary conditions. We feel that the present numerical study is highly useful for design of magneto-electroelastic sensors and actuators.

References

- [Aboudi 2001] J. Aboudi, "Micromechanical analysis of fully coupled electro-magneto-thermo-elastic multiphase composites", *Smart Mater. Struct.* **10** (2001), 867–877.
- [ANSYS 1999] ANSYS Inc., *ANSYS theory manual, Structural analysis guide*, ANSYS Inc., 1999.
- [Benveniste 1995] Y. Benveniste, "Magneto-electric effect in fibrous composites with piezoelectric and piezomagnetic phases", *Phys. Rev. B* **51** (1995), 16424–16427.
- [Buchanan 2003] B. R. Buchanan, "Free vibration of an infinite magneto-electro-elastic cylinder", *J. Sound Vib.* **268** (2003), 413–426.
- [Ding et al. 2005] H. Ding, A. Jiang, P. Hou, and W. Chen, "Green's functions for two-phase transversely isotropic magneto-electro-elastic media", *Eng. Anal. Bound. Elem.* **29** (2005), 551–561.
- [Harshe et al. 1993] G. Harshe, J. P. Dougherty, and R. E. Mewham, "Theoretical modeling of multilayer magneto-electric composites", *Int. J. Appl. Electromagn. Mater.* **4** (1993), 145–159.
- [Heyliger 1997] P. Heyliger, "Exact solutions for simply supported laminated piezoelectric plates", *J. Appl. Mech.* **64** (1997), 299–306.
- [Lee and Jian 1996] J. S. Lee and L. Z. Jian, "Exact electroelastic analysis of piezoelectric laminae via state space approach", *Int. J. Solids Struct.* **33** (1996), 977–990.
- [Lee and Saravanos 1997] H. J. Lee and D. A. Saravanos, "Generalized finite element formulation for smart multilayered thermal piezoelectric composite plates", *Int. J. Solids Struct.* **34** (1997), 3355–3371.
- [Lee and Saravanos 2000] H. J. Lee and D. A. Saravanos, "A mixed multi-field finite element formulation for thermopiezoelectric composite shells", *Int. J. Solids Struct.* **37** (2000), 4949–4967.
- [Nan 1994] C. W. Nan, "Magneto-electric effect in composites of piezoelectric and piezomagnetic phases", *Phys. Rev. B* **50** (1994), 6082–6088.
- [Ootao and Tanigawa 2005] Y. Ootao and Y. Tanigawa, "Transient analysis of multilayered and magneto-electro-thermo elastic strip due to nonuniform heat supply", *Compos. Struct.* **68**:4 (2005), 471–479.
- [Ramirez et al. 2006] F. Ramirez, P. R. Heyliger, and E. Pan, "Free vibration response of two-dimensional magneto-electro-elastic laminated plates", *J. Sound Vib.* **292** (2006), 626–644.
- [Reddy 1984] J. N. Reddy, *An introduction to the finite element method*, McGraw-Hill, Singapore, 1984. International Editions.
- [Ross 1990] C. T. F. Ross, *Pressure Vessels under External Pressure: Static and Dynamics*, Elsevier Applied Science, London, 1990.
- [Sunar et al. 2002] M. Sunar, Z. Ahmed, M. H. A. Al-Garni, and R. Kahraman, "Finite Element modeling of thermopiezomagnetic smart structures", *AIAA J.* **40** (2002), 1846–1851.
- [Tan and Tong 2002] P. Tan and L. Tong, "Modeling for the electro-magneto-thermo-elastic properties of piezoelectric-magnetic fiber reinforced composites", *Compos. Part A* **33** (2002), 631–645.

- [Tianhu et al. 2002] H. Tianhu, T. Xiaogeng, and S. Yapeng, “Two-dimensional generalized thermal shock problem of a thick piezoelectric plate of infinite extent”, *Int. J. Eng. Sci.* **40** (2002), 2249–2264.
- [Vel and Batra 2000] S. S. Vel and R. C. Batra, “Three-dimensional analytical solution for hybrid multilayered piezoelectric plates”, *J. Appl. Mech.* **67** (2000), 558–567.
- [Wang and Zhong 2003] X. Wang and Z. Zhong, “A finitely long circular cylindrical shell of piezoelectric/piezomagnetic composite under pressuring and temperature change”, *Int. J. Eng. Sci.* **41** (2003), 2429–2445.

Received 16 Sep 2006. Accepted 27 Jan 2007.

N. GANESAN: nganesan@iitm.ac.in

Department of Mechanical Engineering, Indian Institute of Technology, Madras, Chennai 600 036, India

A. KUMARAVEL: ME05D004@iitm.ac.in

Department of Mechanical Engineering, Indian Institute of Technology, Madras, Chennai 600 036, India

RAJU SETHURAMAN: sethu@iitm.ac.in

Department of Mechanical Engineering, Indian Institute of Technology, Madras, Chennai 600 036, India

A LINEAR CURVED-BEAM MODEL FOR THE ANALYSIS OF GALLOPING IN SUSPENDED CABLES

ANGELO LUONGO, DANIELE ZULLI AND GIUSEPPE PICCARDO

A linear model of curved, prestressed, no-shear, elastic beam, loaded by wind forces, is formulated. The beam is assumed to be planar in its reference configuration, under its own weight and static wind forces. The incremental equilibrium equations around the prestressed state are derived, in which shear forces are condensed. By using a linear elastic constitutive law and accounting for damping and inertial effects, the complete equations of motion are obtained. They are then greatly simplified by estimating the order of magnitude of all their terms, under the hypotheses of small sag-to-span ratio, order-1 aspect ratio of the (compact) section, characteristic section radius much smaller than length (slender cable), small transversal-to-longitudinal and transversal-to-torsional wave velocity ratios. A system of two integrodifferential equations is drawn in the two transversal displacements only. A simplified model of aerodynamic forces is then developed according to a quasisteady formulation. The nonlinear, nontrivial equilibrium path of the cable subjected to increasing static wind forces is successively evaluated, and the influence of the angle of twist on the equilibrium is discussed. Then stability is studied by discretizing the equations of motion via a Galerkin approach and analyzing the small oscillations around the nontrivial equilibrium. Finally, the role of the angle of twist on the dynamic stability of the cable is discussed for some sample cables.

1. Introduction

The analysis of galloping oscillations of iced cables requires a careful formulation both of the mechanical model and of the aeroelastic forces, especially concerning nonlinear regimes [Luongo and Piccardo 1998]. The forces are usually modeled referring to the quasisteady theory, and they depend on the mean wind speed and on the angle of attack, which in turn depends on the velocity of the structure and on its surrounding flow. The structure is generally modeled as a perfectly flexible cable, that is as a one-dimensional continuum capable of translational displacements only [Luongo et al. 1984; Lee and Perkins 1992]. This assumption is reliable, since the torsion stiffness of the single cable is usually high and the bending stiffness is negligible, compared to the geometric one, because of the slenderness of the structure. However, simplified models of cables have highlighted the importance of the twist angle on the determination of aerodynamic forces and, therefore, on the dynamical behavior of the system. In particular, although Yu et al. [1993a], McConnel and Chang [1986], and White et al. [1991] have considered a sophisticated constitutive law, based on experimental results, in which the axial stress and torque depend both on elongation and torsion, they have neglected the initial curvature of the cable; as a result, the moment equilibrium around the tangent to the cable is violated, since the bending moment

Keywords: cables, twist, galloping, aeroelasticity, instability, bifurcation.

This work has been partially supported by a PRIN-2005 grant.

is not taken into account. In an earlier paper [Luongo and Piccardo 1996] we have tried to correct the classic model, adding an energy of pure torsion to the elastic potential energy of the flexible cable, still ignoring every term of mechanical coupling. Therefore, the formulation of a consistent cable-beam model is a matter of great interest, able to take into account all the stiffnesses involved in the problem. To the best of our knowledge, similar models are usually employed in fully numerical approaches — see for instance [Diana et al. 1998] in the linear field, or [Lu and Perkins 1994] in somewhat different nonlinear problems — but they are not yet employed in semi-analytical analysis, like the one proposed here. A first approach to the subject was presented in [Luongo et al. 2005].

In this paper a linear model of curved elastic prestressed beam, subjected to aerodynamic forces induced by wind, is formulated. By taking into account the high slenderness of the body, the model is remarkably simplified via an analysis of the magnitude orders of all terms in the equations of motion. As a major result, it is shown that, at the leading order, the dynamic behavior of the cable is governed by the same equations as the perfectly flexible model in which, however, the positional and velocity-dependent forces also depend on the angle of twist, which is an integral function of the transversal displacements. In other words, the twist is a *passive variable*, slave to the normal and binormal translations. The reduced model thus obtained permits one to investigate the critical aeroelastic behavior of the cable, by highlighting the role of torsion on the stability of the structure.

The paper is organized as follows. The complete equations of motion are derived in Section 2 under the hypothesis of no-shear deformation of the beam. In Section 3 a reduced model is drawn from the complete one by neglecting small terms and statically condensing the tangent displacement and the angle of twist; therefore, two integrodifferential equations are obtained, in the transversal displacements only. In Section 4 an approximate model for the aerodynamic forces acting on the cable is developed, consistent with the approximations introduced. In Section 5 the nontrivial equilibrium path of the cable subjected to static wind forces is evaluated, and bifurcations causing galloping (Hopf bifurcations) are detected. Numerical results are discussed in Section 6, and some conclusions are drawn in Section 7.

2. Mechanical model

The cable is modeled as a beam constituted by a flexible centerline and rigid cross-sections. It is assumed that the cable, under its self-weight and the static component of the wind forces, takes a planar equilibrium configuration $\bar{\mathcal{C}}$ at time $t = 0$, which is selected as the reference configuration. The linear equations of motion governing the small oscillations around such equilibrium position are sought.

Let $\bar{\mathbf{x}} = \bar{\mathbf{x}}(s)$ be the parametric equation of the centerline in $\bar{\mathcal{C}}$, where $\bar{\mathbf{x}}$ is the position vector and $s \in [0, \ell]$ is a curvilinear abscissa. It is supposed that the inertia principal axes of the section coincide in $\bar{\mathcal{C}}$ with the Frenet triad $\bar{\boldsymbol{\beta}}(s) := \{\bar{\mathbf{a}}_1(s), \bar{\mathbf{a}}_2(s), \bar{\mathbf{a}}_3(s)\}$, where $\bar{\mathbf{a}}_1 \equiv \bar{\mathbf{x}}'$ (with $' = d/ds$) is the unit vector tangent to the curve, $\bar{\mathbf{a}}_2$ is the normal and $\bar{\mathbf{a}}_3$ the binormal (Figure 1, left). According to the Frenet formulas, it follows that $\bar{\mathbf{a}}_1' = \bar{\kappa}\bar{\mathbf{a}}_2$, $\bar{\mathbf{a}}_2' = -\bar{\kappa}\bar{\mathbf{a}}_1$, $\bar{\mathbf{a}}_3' = \mathbf{0}$, where $\bar{\kappa} = \bar{\kappa}(s)$ is the modulus of the curvature vector $\bar{\boldsymbol{\kappa}} = \bar{\kappa}\bar{\mathbf{a}}_3$ in $\bar{\mathcal{C}}$.

Now consider an adjacent configuration \mathcal{C} , assumed by the cable at the time $t > 0$. Denoting by $\mathbf{u}(s, t)$ and $\boldsymbol{\vartheta}(s, t)$ the translation of the centerline and the (infinitesimal) rotation of the cross-section at abscissa s , respectively, the position vector $\mathbf{x}(s, t)$ and the attitude of the inertia principal triad $\boldsymbol{\beta} :=$

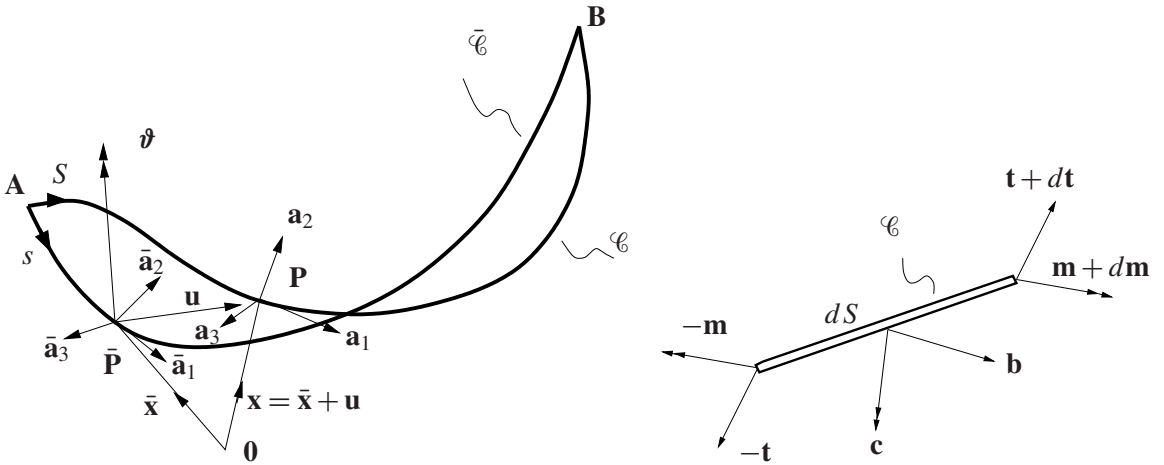


Figure 1. Left: configurations of the cable. Right: forces and couples on an infinitesimal element.

$\{\mathbf{a}_1(s, t), \mathbf{a}_2(s, t), \mathbf{a}_3(s, t)\}$ in \mathcal{C} are given by (see Figure 1, left):

$$\mathbf{x} = \bar{\mathbf{x}} + \mathbf{u}, \quad \mathbf{a}_i = \bar{\mathbf{a}}_i + \vartheta \times \bar{\mathbf{a}}_i \quad \text{for } i = 1, 2, 3. \tag{1}$$

The slenderness of the beam suggests one may neglect the shear deformation; therefore the cross-sections are assumed to remain orthogonal to the centerline in any configuration. This internal constraint is expressed by the condition $\mathbf{x}' = (1 + \varepsilon)\mathbf{a}_1$, \mathbf{a}_1 being normal to the section and $d\mathbf{x}/dS = \mathbf{x}'/(1 + \varepsilon)$ the unit vector tangent to the strained centerline at the actual abscissa $S = S(s)$, with $\varepsilon := dS/ds - 1$ the *unit extension*. By letting $\mathbf{u} = u\mathbf{a}_1 + v\mathbf{a}_2 + w\mathbf{a}_3$ and $\vartheta = \vartheta_1\mathbf{a}_1 + \vartheta_2\mathbf{a}_2 + \vartheta_3\mathbf{a}_3$, and taking into account that $\varepsilon \ll 1$, it follows that

$$\vartheta_2 = -w', \quad \vartheta_3 = v' + \bar{\kappa}u \tag{2}$$

and

$$\varepsilon = u' - \bar{\kappa}v.$$

Due to the constraints (2), the configuration variables $u, v, w, \vartheta_1, \vartheta_2, \vartheta_3$ are reduced to the three translation components and the unique rotation component $\vartheta := \vartheta_1$, called the *twist angle*.

Finally, by defining the incremental curvature vector $\boldsymbol{\kappa} := \partial\vartheta/\partial s$, using (2) and projecting on $\bar{\boldsymbol{\beta}}$, the torsion κ_1 and the bendings κ_2 and κ_3 are found to be

$$\kappa_1 = \vartheta' + \bar{\kappa}w', \quad \kappa_2 = -w'' + \bar{\kappa}\vartheta, \quad \kappa_3 = v'' + (\bar{\kappa}u)'. \tag{3}$$

We next derive the equilibrium equations. By considering an infinitesimal cable element in the actual configuration (Figure 1, right), and denoting by $\mathbf{t}(s, t)$ and $\mathbf{m}(s, t)$ the internal contact force and couple, respectively, acting at abscissa s at time t , the balance equations become, in Lagrangian form,

$$\mathbf{t}' + \mathbf{b} = \mathbf{0}, \quad \mathbf{m}' + \mathbf{x}' \times \mathbf{t} + \mathbf{c} = \mathbf{0}, \tag{4}$$

where $\mathbf{b} := \mathbf{b}(s, t)$ and $\mathbf{c} := \mathbf{c}(s, t)$ are the body force and couple densities per undeformed arc-length, including inertial and damping effects. It is assumed that in the planar reference configuration $\bar{\mathcal{C}}$ the

cable is loaded by body forces $\hat{\mathbf{b}}(s)$ and no couples: $\hat{\mathbf{c}}(s) \equiv \mathbf{0}$. By neglecting flexural effects in its own plane, the cable is stressed in $\hat{\mathcal{C}}$ exclusively by axial forces, namely $\hat{\mathbf{t}} = \bar{T}\hat{\mathbf{a}}_1$ and $\hat{\mathbf{m}} = \mathbf{0}$, with $\hat{\mathbf{t}}' + \hat{\mathbf{b}} = \mathbf{0}$. By subtracting this latter from (4)₁, we obtain *incremental equilibrium equations*

$$(\mathbf{t}' - \bar{\mathbf{t}}') + \hat{\mathbf{b}} = \mathbf{0}, \quad \mathbf{m}' + \mathbf{x}' \times \mathbf{t} + \hat{\mathbf{c}} = \mathbf{0},$$

with $\hat{\mathbf{b}} := \mathbf{b} - \bar{\mathbf{b}}$ and $\hat{\mathbf{c}} := \mathbf{c} - \bar{\mathbf{c}}$. By letting $\mathbf{t} = (\bar{T} + \hat{T}_1)\mathbf{a}_1 + \hat{T}_2\mathbf{a}_2 + \hat{T}_3\mathbf{a}_3$, $\mathbf{m} = \hat{M}_1\mathbf{a}_1 + \hat{M}_2\mathbf{a}_2 + \hat{M}_3\mathbf{a}_3$, using (1) and projecting onto $\hat{\boldsymbol{\beta}}$, six scalar equations follow. After linearization in the incremental quantities and condensation of the reactive stresses \hat{T}_2 and \hat{T}_3 , the following four equilibrium equations are obtained in the active stresses $\hat{T}_1, \hat{M}_1, \hat{M}_2, \hat{M}_3$ (hats omitted):

$$\begin{aligned} T_1' - \bar{T}\bar{\kappa}(v' + \bar{\kappa}u) + M_3'\bar{\kappa} + \tilde{b}_1 &= 0, \\ -M_3'' + (\bar{T}(v' + \bar{\kappa}u))' + T_1\bar{\kappa} + \tilde{b}_2 &= 0, \\ M_2'' + (M_1\bar{\kappa})' + (\bar{T}w')' + \tilde{b}_3 &= 0, \\ M_1' - M_2\bar{\kappa} + c_1 &= 0, \end{aligned} \quad (5)$$

where

$$\tilde{b}_1 := b_1 + \bar{\kappa}c_3, \quad \tilde{b}_2 := b_2 - c_3', \quad \tilde{b}_3 := b_3 + c_2'.$$

Finally, a linear, uncoupled, elastic law is assumed between the incremental active stress and strain components:

$$T_1 = EA\varepsilon, \quad M_1 = GJ\kappa_1, \quad M_2 = EI_2\kappa_2, \quad M_3 = EI_3\kappa_3, \quad (6)$$

in which EA, GJ, EI_2 and EI_3 are the axial, torsional and flexural stiffnesses of the cable and hats have been dropped. In view of (6), the equations of motion (5) become

$$\begin{aligned} EA(u' - \bar{\kappa}v)' + EI_3\bar{\kappa}(v'' + (\bar{\kappa}u)')' - \bar{T}\bar{\kappa}(v' + \bar{\kappa}u) + \tilde{b}_{a_1} - c_u\dot{u} - m\ddot{u} &= 0, \\ EA\bar{\kappa}(u' - \bar{\kappa}v) - EI_3(v'' + (\bar{\kappa}u)')' + (\bar{T}(v' + \bar{\kappa}u))' + \tilde{b}_{a_2} - c_v\dot{v} - m\ddot{v} &= 0, \\ EI_2(-w'' + \bar{\kappa}\vartheta)'' + GJ(\bar{\kappa}(\bar{\kappa}w' + \vartheta'))' + (\bar{T}w')' + \tilde{b}_{a_3} - c_w\dot{w} - m\ddot{w} &= 0, \\ GJ(\bar{\kappa}w' + \vartheta')' - EI_2\bar{\kappa}(-w'' + \bar{\kappa}\vartheta) + c_{a_1} - c_\vartheta\dot{\vartheta} - \mathcal{J}_1\ddot{\vartheta} &= 0, \end{aligned} \quad (7)$$

where the body forces \tilde{b}_i and couple c_1 have been expressed as the sum of aerodynamic (index a), damping and inertia effects, $c_u, c_v, c_w, c_\vartheta$ being structural damping coefficients, m the mass linear density and \mathcal{J}_1 the inertia polar moment of the section. It is worth noting that Equations (7) are block-uncoupled; that is, the in-plane oscillations of the cable are independent of out-of-plane oscillations, the latter involving torsion. However, if the forces \tilde{b}_i depend on the configuration variables, as occurs for the aerodynamic forces, the equations are coupled.

Equations (7) must be accompanied by suitable boundary conditions. If the cable is restrained at both ends by spherical hinges, the displacements and moments must vanish there:

$$\left. \begin{aligned} u &= 0, & GJ(\vartheta' + \bar{\kappa}w') &= 0, \\ v &= 0, & EI_2(-w'' + \bar{\kappa}\vartheta) &= 0, \\ w &= 0, & EI_3(v'' + (\bar{\kappa}u)') &= 0, \end{aligned} \right\} \quad \text{at } s = 0, \ell. \quad (8)$$

The problem is completed by the initial conditions; here it is assumed that the body is at rest at $t = 0$.

3. Reduced equations of motion

The equations of motion previously obtained are too complicated to be treated analytically; therefore, a simplified model is developed in this Section. First, the classical hypothesis of small sag-to-span ratio d/ℓ is introduced [Luongo et al. 1984; Lee and Perkins 1992; Irvine and Caughey 1984], commonly accepted for cables falling into the technical range. Then, advantage is drawn from the fact that the cable is a very slender body; hence, the flexural-torsional effects are expected to be smaller than the funicular effects, except close to the boundaries. On the other hand, bending effects cannot be completely neglected, since, due to the (small but finite) initial curvature, the bending moment contributes to the moment equilibrium around the tangent to the cable.

3.1. Order-of-magnitude analysis. According to the previous ideas, we perform an order-of-magnitude analysis of all the terms in the equations of motion (7) and boundary conditions (8). First, equations (7) and (8) are written in a nondimensional form. We set

$$s^* = \frac{s}{\ell}, \quad \omega = \frac{\pi}{\ell} \sqrt{\frac{\bar{T}}{m}}, \quad t^* = \omega t, \quad u^* = \frac{u}{\ell}, \quad v^* = \frac{v}{\ell}, \quad w^* = \frac{w}{\ell}, \quad \vartheta^* = \vartheta, \quad (9)$$

$$c_\alpha^* = \frac{\omega \ell^2}{EA} c_\alpha, \quad c_\vartheta^* = \frac{\omega}{EA} c_\vartheta, \quad m^* = \frac{\omega^2 \ell^2}{EA} m, \quad \mathcal{F}_1^* = \frac{\omega^2}{EA} \mathcal{F}_1, \quad b_{a_i}^* = \frac{\ell}{EA} \tilde{b}_{a_i}, \quad c_{a_1}^* = \frac{\tilde{c}_{a_1}}{EA}, \quad \kappa^* = \bar{\kappa} \ell,$$

where α assumes the values u, v, w , and we introduce the nondimensional quantities

$$\delta = \frac{8d}{\ell}, \quad \tau = \frac{\bar{T}}{EA}, \quad \varrho = \frac{r}{\ell}, \quad \beta = \frac{GJ}{EI}. \quad (10)$$

The equations then become

$$\begin{aligned} (u' - \kappa v)' + \varrho^2 \kappa (v'' + (\kappa u)')' - \tau \kappa (v' + \kappa u) + b_{a_1} - c_u \dot{u} - m \ddot{u} &= 0, \\ \kappa (u' - \kappa v) - \varrho^2 (v'' + (\kappa u)')'' + (\tau (v' + \kappa u))' + b_{a_2} - c_v \dot{v} - m \ddot{v} &= 0, \\ \varrho^2 (-w'' + \kappa \vartheta)'' + \varrho^2 \beta (\kappa (\kappa w' + \vartheta'))' + (\tau w')' + b_{a_3} - c_w \dot{w} - m \ddot{w} &= 0, \\ \beta \varrho^2 (\kappa w' + \vartheta')' - \varrho^2 \kappa (-w'' + \kappa \vartheta) + c_{a_1} - c_\vartheta \dot{\vartheta} - \mathcal{F}_1 \ddot{\vartheta} &= 0, \end{aligned} \quad (11)$$

together with

$$\left. \begin{aligned} u &= 0, & \beta \varrho^2 (\vartheta' + \kappa w') &= 0, \\ v &= 0, & \varrho^2 (-w'' + \kappa \vartheta) &= 0, \\ w &= 0, & \varrho^2 (v'' + (\kappa u)') &= 0 \end{aligned} \right\} \text{ at } s = 0, 1. \quad (12)$$

where the star has been omitted for the sake of simplicity, the dot stands for differentiation with respect to t^* and the prime stands for differentiation with respect to s^* . In (10), δ is the nondimensional sag, τ the nondimensional prestress, ϱ the nondimensional inertia radius $r = \sqrt{I/A}$ of the section, assumed to be circular ($I_2 = I_3 \equiv I$), and β the nondimensional torsional stiffness. For a commonly employed overhead transmission line, $\delta = \mathcal{O}(10^{-1})$, $\tau \leq \mathcal{O}(\delta^3)$ and $\varrho \leq \mathcal{O}(\delta^3)$, while $\beta = \mathcal{O}(1)$. Moreover, from the catenary theory, it is well known that $\tau(s) = \tau(1/2) + \delta^2 f(s)$ and $\kappa(s) = \delta + \delta^2 g(s)$, with $\mathcal{O}(f(s)) = 1$, $\mathcal{O}(g(s)) = 1$. Therefore, according to parabolic cable theory (see [Irvine and Caughey 1984]), we can

consider, with an error of second order in δ ,

$$\tau(s) = \text{const}, \quad \kappa(s) = \text{const}.$$

Next we must estimate the order of magnitude of the displacement component ratios. We assume that

$$\mathbb{O}\left(\frac{u}{v}\right) = \delta, \quad \mathbb{O}\left(\frac{\vartheta}{w}\right) = \frac{1}{\delta}, \quad \mathbb{O}\left(\frac{v}{w}\right) = 1, \tag{13}$$

together with

$$\frac{\partial^n u}{\partial s^n} = \mathbb{O}(u), \quad \frac{\partial^n v}{\partial s^n} = \mathbb{O}(v), \quad \frac{\partial^n w}{\partial s^n} = \mathbb{O}(w), \quad n = 1, 2, \dots \tag{14}$$

and

$$\frac{\partial \vartheta}{\partial s} = \mathbb{O}(w\delta), \quad \frac{\partial^2 \vartheta}{\partial s^2} = \mathbb{O}(w\delta). \tag{15}$$

Equation (13)₁ is suggested by the linear theory [Irvine and Caughey 1984], and by the fact that $u \rightarrow 0$ in the (prevalently) transversal motions ($v \gg u$) when $\delta \rightarrow 0$. Equations (14) also follow from the linear theory, when the trigonometric nature of the eigenfunctions is recognized. Estimates (13)₂ and (15) are instead drawn by inspection of the solution of the linearized Equation (11)₄ and the relevant boundary conditions (see Appendix A). Equation (13)₃ is self-explanatory. It is worth noting that, due to the different boundary conditions, the translations u , v and w must vanish at the ends, and therefore they are *fast-varying functions in space* (that is, their dimensional counterparts vary on a scale of typical length ℓ), whereas the twist angle ϑ , being different from zero at the ends, can vary in a much slower manner (that is, on a scale of much larger typical length). As illustrated in detail in Appendix A, ϑ is indeed a *slow-varying function* (in space) in symmetrical modes (in which $\vartheta = \mathbb{O}(w/\delta)$), and again a fast-varying function in antisymmetrical modes (in which $\vartheta = \mathbb{O}(w\delta)$). The upper estimate of ϑ has been adopted for all motions, in order to account also for nonsymmetrical modes of cables supported at different levels.

By using previous the estimates in (11) and (12) and retaining only the dominant terms, we obtain a set of *reduced equations*. Returning to dimensional form, they read

$$\begin{aligned} EA(u' - \bar{\kappa}v)' + b_{a_1} - c_u \dot{u} - m\ddot{u} &= 0, \\ EA\bar{\kappa}(u' - \bar{\kappa}v) + \bar{T}v'' + b_{a_2} - c_v \dot{v} - m\ddot{v} &= 0, \\ \bar{T}w'' + b_{a_3} - c_w \dot{w} - m\ddot{w} &= 0, \\ GJ\vartheta'' - EI\bar{\kappa}^2\vartheta + (EI + GJ)\bar{\kappa}w'' + c_{a_1} - c_\vartheta \dot{\vartheta} - \mathcal{J}_1 \ddot{\vartheta} &= 0, \end{aligned} \tag{16}$$

with boundary conditions

$$u = 0, \quad v = 0, \quad w = 0, \quad GJ(\vartheta' + \bar{\kappa}w') = 0 \quad \text{at } s = 0, \ell. \tag{17}$$

The first three equations in (16) are identical to those of the flexible cable [Lee and Perkins 1992]. The fourth (16) is also known in the literature, since it represents the moment equilibrium around the tangent of a planar circular arch [Lee and Chao 2000]. It follows directly from Equations (3), (5)₄ and (6), since all its terms, being of the same order, were retained in the analysis. In spite of this apparently simplistic result, and as a major finding of this paper, Equations (16) prove that the perfectly flexible

cable and the twisting of a circular arch are *consistent models*. In other words, neglecting bending effects in translational equilibrium, while retaining them in rotational equilibrium, does not entail ordering violation from an asymptotic point of view.

From (16) it follows that, if the body forces are independent of ϑ or even zero (as happens in free vibrations), the translational motion is independent of ϑ , which is therefore a *passive variable*, slave to translations; whereas, if the body forces depend on ϑ , as in the aerodynamic case, the twist angle does affect the dynamics of the body.

The reduced equations (16) inconsistently appear to be non-self-adjoint in the elastic part. Indeed, the symmetry of the differential operator has been destroyed by the neglecting of the term $(EI + GJ)\bar{\kappa}(\vartheta w)'$ in the out-of-plane equation of motion (16)₃, compared to the dominant term $\bar{T}w''$. However, this inconsistency turns out to be only of formal type, as has been checked numerically (see Section 6.1); it can easily be removed by reintroducing the small term.

Equations (16) are accompanied by the boundary conditions (17); equations expressing the vanishing of the bending moments have been ignored, consistently with the approximation adopted, which does not permit description of the boundary layers.

3.2. Static condensation. It is well known that, in the framework of parabolic cable theory, the tangential inertia force $-m\ddot{u}$ (and the damping force $c_u\dot{u}$) can be neglected in the prevalently transversal motions, since the longitudinal natural frequencies are much higher than the transversal ones (quasisteady stretching). This allows one to statically condense the tangent displacement u by expressing it as an integral of the transverse displacement v :

$$u(s, t) = \bar{\kappa} \left(\int_0^s v(\xi, t) d\xi - \frac{s}{\ell} \int_0^\ell v(\xi, t) d\xi \right), \tag{18}$$

where $b_{a_1} = 0$ has been considered for simplicity.

Here we apply an analogous procedure to the equation (16)₄ governing the twist. First, observe that the squared torsional frequencies of a single cable are much higher than the transversal ones. For example, for the commonly used strand cables, which are relatively soft in torsion, this ratio is of the order of 10^{-2} (a case study is discussed in Section 6). The inertia couple $-\mathcal{J}_1\ddot{\vartheta}$ and the damping couple $c_\vartheta\dot{\vartheta}$ are neglected in (16)₄, and ϑ is obtained in integral form (quasisteady twisting). Taking $c_{a_1} = 0$ for simplicity, we obtain

$$\vartheta(s, t) = -\frac{GJ + EI}{\sqrt{GJ EI}} \int_0^s w''(\xi, t) \sinh[k(s - \xi)] d\xi + A \cosh ks + B \sinh ks, \tag{19}$$

where we have set $k := \bar{\kappa}\sqrt{EI/GJ}$ and the arbitrary constants A and B are determined by the boundary conditions in the second line of (8).

4. Aerodynamic forces

Modeling aerodynamic loads is a very difficult task, often handled in the literature under simplifying hypotheses. The most popular model adopted for the structure is the unbounded rigid cylinder; however, the iced cable problem adds further difficulties, due to the curvature of its centerline and the random

variation of the section. To tentatively tackle the problem, a simple model is adopted here, by introducing the following assumptions: (a) *quasisteady theory* [Blevins 1990] is believed applicable, according to which the loads acting on the moving body at a certain instant are identical to those exerted on the body at rest in the same position; (b) the curvature of the cable is negligibly small; (c) loads are evaluated in the current configuration \mathcal{C} , by accounting for the twist angle ϑ , but neglecting the smaller flexural rotations $\vartheta_{2,3} = \mathcal{O}(\vartheta\delta)$ (remember Equations (2) and (13)₂), which, according to the so-called *cosine rule* [Strømmen and Hjorth-Hansen 1995], have small influence; (d) the ice is assumed to be uniformly distributed along the cable, consistently with the hypothesis of planar reference configuration; (e) aerodynamic couples are neglected.

Now consider a wind flow of mean velocity $\mathbf{U} = U\mathbf{a}_z$, blowing horizontally and normally to the initial (no wind) planar configuration of the cable (Figure 2, left). Three different attitudes of the cross-section in its own plane are considered (Figure 2, right): (a) the initial configuration \mathcal{C}_0 (axes $\mathbf{a}_{20}, \mathbf{a}_{30} \equiv \mathbf{a}_z$), in which the cable is only subjected to gravity; (b) the reference configuration $\bar{\mathcal{C}}$ (axes $\bar{\mathbf{a}}_2, \bar{\mathbf{a}}_3$), in which the cable is also loaded by (uniform) static wind forces; (c) the actual configuration \mathcal{C} (axes $\mathbf{a}_2, \mathbf{a}_3$), in which the cable is also loaded by (non uniform) dynamic wind forces. The twist angle caused by the static forces coincides, within small quantities of order $\mathcal{O}(\delta^2)$, with the angle of rotation φ experienced by the cable passing from \mathcal{C}_0 to $\bar{\mathcal{C}}$ (see Figure 2), which depends only on the mean wind velocity U . The twist angle ϑ caused by the dynamic forces depends, in addition to U , on the abscissa s and on time t . The angle φ is assumed to be large; the angle ϑ is assumed to be small.

According to quasisteady theory, the flow exerts the following aerodynamic force on the section:

$$\mathbf{b}_a = \frac{1}{2}\rho_a V r (c_d(\gamma)\mathbf{V} + c_l(\gamma)\mathbf{a}_1 \times \mathbf{V}), \tag{20}$$

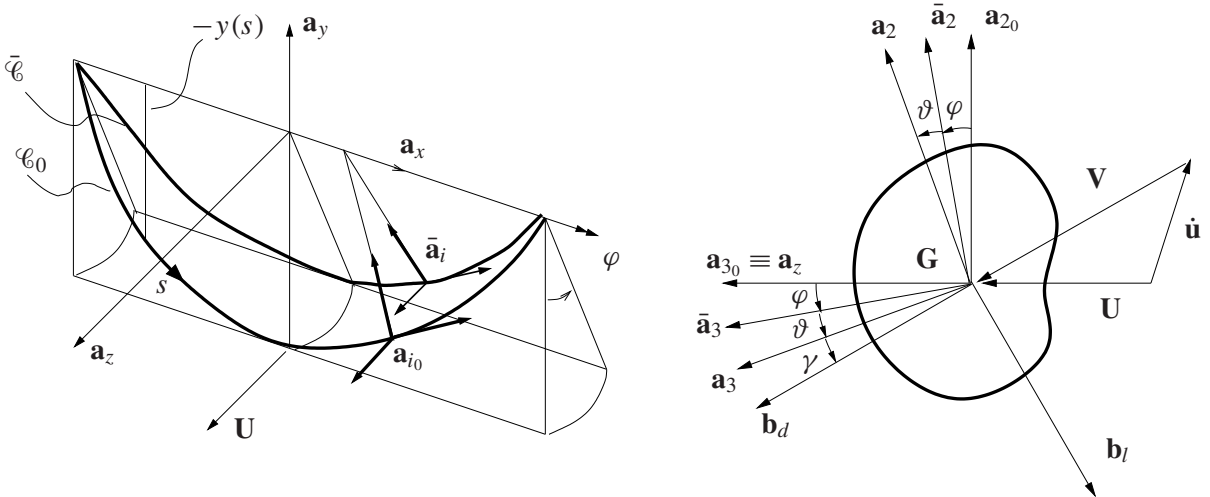


Figure 2. Aerodynamic forces. Left: cable configuration. Right: transversal section, mean wind velocity \mathbf{U} , relative wind velocity \mathbf{V} , angle of attack γ , drag force \mathbf{b}_d and lift force \mathbf{b}_l .

where ρ_a is the air density, \mathbf{V} is the relative velocity of the wind with respect to the section, $V = \|\mathbf{V}\|$ its modulus, and c_d and c_l two aerodynamic coefficients, called of *drag* and *lift*, respectively. These coefficients depend on the shape of the section and on the *angle of attack*,

$$\gamma := -\arcsin\left(\frac{\mathbf{V}}{V} \cdot \mathbf{a}_2\right), \tag{21}$$

that is, the angle between \mathbf{V} and a reference material axis, taken as \mathbf{a}_3 here. The two components of \mathbf{b}_a , along-wind \mathbf{b}_d and cross-wind \mathbf{b}_l , are usually known as drag and lift forces, respectively; see [Figure 2](#), right.

Equations (20) and (21) allow one to evaluate the force \mathbf{b}_a once the relative velocity \mathbf{V} is known. If the section underwent only a translation, the relative velocity would be easily obtained as $\mathbf{V} = \mathbf{U} - \dot{v}\bar{\mathbf{a}}_2 - \dot{w}\bar{\mathbf{a}}_3$. In contrast, a nonvanishing twist velocity $\dot{\vartheta}$ entails some difficulties, since \mathbf{V} becomes a function of the point \mathbf{P} on the boundary. To overcome the problem, the notion of *characteristic radius* [[Blevins 1990](#)] has been introduced in the literature, which consists of selecting a special point \mathbf{P}_c on the boundary of the section, in which to evaluate a “characteristic relative velocity” \mathbf{V}_c , to be attributed to all the points of the section. The problem at hand, however, is simpler. Indeed, the ratio between the velocity of *any* point of the boundary due to the twist and the velocity of the centerline is of the order $\mathcal{O}(\dot{\vartheta}r/\dot{w}) = \mathcal{O}(\dot{\vartheta}^*\varrho/\dot{w}^*)$. Since, by [Equation \(13\)₂](#), $\mathcal{O}(\dot{\vartheta}^*/\dot{w}^*) \leq 1/\delta$, the previous contribution is at most of the order $\mathcal{O}(\varrho/\delta) = \mathcal{O}(\delta^2)$, and therefore it is negligible. Hence, *the twist velocity $\dot{\vartheta}$ has practically no effects on the aerodynamic forces of cables not having evanescent sag*. In contrast, the twist angle ϑ *does affect* the forces via the angle of attack γ ; consequently $\mathbf{b}_a = \mathbf{b}_a(\vartheta, \dot{v}, \dot{w}; \varphi(U), U)$.

By letting $\mathbf{V} = \mathbf{U} - \dot{v}\bar{\mathbf{a}}_2 - \dot{w}\bar{\mathbf{a}}_3$ in (20) and (21) and linearizing these equations in \dot{v} , \dot{w} and ϑ , we get

$$V = U\left(1 - \frac{\dot{v}}{U} \sin \varphi - \frac{\dot{w}}{U} \cos \varphi\right), \tag{22}$$

$$\gamma = -\varphi - \vartheta + \frac{\dot{v}}{U} \cos \varphi - \frac{\dot{w}}{U} \sin \varphi. \tag{23}$$

[Equation \(23\)](#) shows that when \mathcal{C} approaches $\bar{\mathcal{C}}$, that is, when $\vartheta, \dot{v}, \dot{w}$ approach zero, the angle γ approaches $-\varphi$. Hence, by expanding the aerodynamic coefficients $c_\alpha(\gamma)$ ($\alpha = d, l$) around $\gamma = -\varphi$, one has

$$c_\alpha(\gamma) = \bar{c}_\alpha + (\gamma + \varphi)\bar{c}'_\alpha + \frac{1}{2}(\gamma + \varphi)^2\bar{c}''_\alpha + \dots, \quad \alpha = d, l, \tag{24}$$

where $\bar{c}_\alpha, \bar{c}'_\alpha, \dots$, are the values assumed by c_α and its derivatives at $\bar{\mathcal{C}}$. Finally, by substituting (22)–(24) into (20) and projecting this last equation onto the $\bar{\mathbf{a}}_2$ and $\bar{\mathbf{a}}_3$ axes, the following force components are derived:

$$\begin{aligned} b_{a_2} &= \bar{b}_{a_2}(\varphi) + c_{2\vartheta}(\varphi)\vartheta + c_{2v}(\varphi)\dot{v} + c_{2w}(\varphi)\dot{w}, \\ b_{a_3} &= \bar{b}_{a_3}(\varphi) + c_{3\vartheta}(\varphi)\vartheta + c_{3v}(\varphi)\dot{v} + c_{3w}(\varphi)\dot{w}. \end{aligned} \tag{25}$$

In these equations, the \bar{b}_{a_i} are the static forces, and c_{ij} are coefficients depending on c_d, c_l and their derivatives with respect to γ , all evaluated at $\bar{\mathcal{C}}$; they are reported in [Appendix B](#).

5. Equilibrium path and stability

Consider the cable in the equilibrium reference configuration $\bar{\mathcal{C}}$, in which it is loaded by its own weight $-mg\mathbf{a}_y$, g being the gravity acceleration, and by the steady-state part $\bar{\mathbf{b}}_a(\varphi, U)$ of the aerodynamic force.

Since, by hypothesis, $\bar{\mathcal{C}}$ is planar, equilibrium requires that the resultant force $\bar{\mathbf{b}}(\varphi, U) := \bar{\mathbf{b}}_a(\varphi, U) - mg\mathbf{a}_y$ lies in the plane of the cable. By enforcing the condition $\bar{\mathbf{b}}(\varphi, U) \cdot \bar{\mathbf{a}}_3 = 0$ (vanishing of the force component along the binormal direction), we obtain, since $\mathbf{a}_y \cdot \bar{\mathbf{a}}_3 = -\sin \varphi$,

$$\sin \varphi = -\frac{\bar{b}_{a_3}(\varphi, U)}{mg}.$$

This equation implicitly defines the nonlinear, nontrivial equilibrium path $\varphi = \varphi(U)$.

The stability of the equilibrium of a generic point of this path is governed by the incremental equations of motion linearized around the reference configuration, namely (16), together with the relevant boundary conditions. Taking into account (18) and (19) for the tangential displacement and twist angle, and (25) for the aerodynamic forces, the problem becomes

$$\begin{aligned} \bar{T}v'' - EA \frac{\bar{\kappa}^2}{\ell} \int_0^\ell v ds + c_{2\vartheta} \vartheta + \hat{c}_{2v} \dot{v} + c_{2w} \dot{w} &= m\ddot{v}, \\ \bar{T}w'' + c_{3\vartheta} \vartheta + c_{3v} \dot{v} + \hat{c}_{3w} \dot{w} &= m\ddot{w}, \\ \vartheta(s, t) &= -\frac{GJ + EI}{\sqrt{GJ EI}} \int_0^s w''(\xi, t) \sinh(k(s - \xi)) d\xi + A \cosh ks + B \sinh ks, \\ v = 0, \quad w = 0, \quad \vartheta' + \bar{\kappa}w' &= 0 \quad \text{at } s = 0, \ell, \end{aligned} \tag{26}$$

where the coefficients \hat{c}_{2v} and \hat{c}_{3w} include structural damping (see Appendix B). All the coefficients c_{ij} depend on the wind velocity. Equations (26) represent a linear eigenvalue problem, of non-self-adjoint type, due to the presence of dissipative (velocity-dependent) and circulatory (position-dependent) forces. It admits infinite solutions of type $v(s, t) = \hat{v}(s)e^{i\lambda t}$, $w(s, t) = \hat{w}(s)e^{i\lambda t}$, where the eigenvalues λ depend on the velocity U . For small U we have $\text{Re } \lambda < 0$ for any λ , so $\bar{\mathcal{C}}$ is a stable equilibrium configuration. At a critical wind velocity U_c , however, the couple of complex conjugate eigenvalues having maximum real part crosses the imaginary axes: $\max \text{Re } \lambda = 0$. This circumstance causes loss of stability of the equilibrium through a Hopf bifurcation, from which a limit cycle arises, of stable (supercritical, $U \geq U_c$) or unstable (undercritical, $U \leq U_c$) kind.

To solve the boundary value problem (26) we follow a Galerkin approach, in which the in-plane (ϕ_{v_j}) and out-of-plane ($\phi_{w_k}, \phi_{\vartheta_k}$) eigenfunctions of the associated Hamiltonian problem ($c_{ij} = 0$) are taken as trial functions:

$$\begin{pmatrix} \vartheta(s, t) \\ v(s, t) \\ w(s, t) \end{pmatrix} = \sum_{j=1}^m \begin{pmatrix} 0 \\ \phi_{v_j} \\ 0 \end{pmatrix} q_j^i + \sum_{k=1}^n \begin{pmatrix} \phi_{\vartheta_k} \\ 0 \\ \phi_{w_k} \end{pmatrix} q_k^o, \tag{27}$$

where $q_j^i, j = 1, \dots, m$, are the unknown amplitudes for the in-plane trial functions and $q_k^o, k = 1, \dots, n$, are the unknown amplitudes for the out-plane trial functions. By using standard methods, we obtain the algebraic eigenvalue problem

$$\mathbf{M}\ddot{\mathbf{q}} + \mathbf{C}\dot{\mathbf{q}} + (\mathbf{K} + \mathbf{H})\mathbf{q} = \mathbf{0}, \tag{28}$$

where $\mathbf{q} = (q_j^i, q_k^o)$ is the $m + n$ -vector of the Lagrangian parameters, and $\mathbf{M}, \mathbf{C}, \mathbf{K}$ and \mathbf{H} are the mass, damping (structural plus aerodynamic), stiffness and circulatory matrices, respectively. These are found

to be block-diagonal, due to symmetric-antisymmetric character of the eigenfunctions. Their coefficients are reported in [Appendix C](#) for $m = n = 1$.

6. Numerical results

A numerical analysis has been performed on a sample cable, already analyzed in the literature [[Luongo and Piccardo 1998](#); [Yu et al. 1993a](#); [1993b](#)], having an axial stiffness $EA = 29.7 \times 10^6$ N, a torsional stiffness $GJ = 159$ Nm², a diameter $D = 0.0281$ m, a length $\ell = 267$ m, a sag $d = 6.18$ m and damping ratio coefficients equal to 0.44%; moreover, a bending stiffness $EI = 2100$ Nm² has been assumed, consistently with experimental observations on several types of cables with sufficiently high axial tension and small curvature values [[Hong et al. 2005](#)]. According to these values, the cable is initially close to the first cross-over point [[Irvine and Caughey 1984](#)]. The squared ratio between the transversal frequency ω_v and the torsional frequency ω_ϑ (evaluated for the string and the shaft, respectively), is

$$\left(\frac{\omega_v}{\omega_\vartheta}\right)^2 = \frac{\bar{T}}{GJ} \frac{\mathcal{F}_1}{m} \simeq 1.5 \cdot 10^{-2},$$

thus justifying the assumption of quasisteady twisting.

6.1. Model validation. A preliminary investigation has been conducted to validate the model. First, the results furnished by the reduced equations of motion (16) and by the complete equations (7) have been compared, in order to numerically check the accuracy of the approximation introduced. A finite-difference analysis has been performed by the algorithm `bvp4c` in MATLAB to evaluate: (a) the static response of the cable to uniformly distributed forces acting orthogonally to the planar configuration \mathcal{C}_0 ([Figure 2](#), left) and, (b) the modal shape assumed by the cable in its first and second out-of-plane normal modes. The results in terms of displacements w , twist ϑ and out-of-plane bending κ_2 are displayed in [Figure 3](#) for static analysis and [Figure 4](#) for dynamic analysis.

Very small differences are furnished by the two models almost everywhere, except for the bending close to the constraints, where, as already noted, the boundary layer is lost using the simplified model. The frequencies computed by both complete and reduced model are $\omega_1 = 1.40$ rad/s, $\omega_2 = 2.80$ rad/s, with differences lower than 0.2%.

The question raised about the non-self-adjointness of the reduced elastic operator was then addressed. It entails that, while out-of-plane displacements w trigger twist rotations ϑ , on the contrary the latter do not force the former. The missing term, believed small, was then reintroduced into the reduced equation, and a static torque applied at one end of the cable, in order to observe out-of-plane displacements. These, however, turned out to be very small, namely $w_{\max}/(\vartheta_{\max}d) = 8 \cdot 10^{-9}$, confirming the accuracy of the reduced model. It is interesting to observe that, in this problem, the bending moment M_2 equilibrating the derivative of the torque M_1' ([Equation \(5\)₄](#)) is almost completely induced by the twist angle ϑ , namely $M_2 \simeq EI\bar{\kappa}\vartheta$ ([Equations \(6\)₃](#) and [\(3\)₂](#)), that is, the cable remains planar.

Finally, the Galerkin approach ([Equations \(27\)–\(28\)](#)) has been tested in the evaluation of the critical wind velocity and corresponding critical mode. The exact solution, carried out by the finite-difference analysis, and the approximate solution, obtained by using just one test function for in-plane and out-of-plane motions ($m = n = 1$), have been compared for the sample cable CS2 described further on (with $d = 3$ m and structural damping equal to 0.44%). The first critical velocity is practically coincident in the

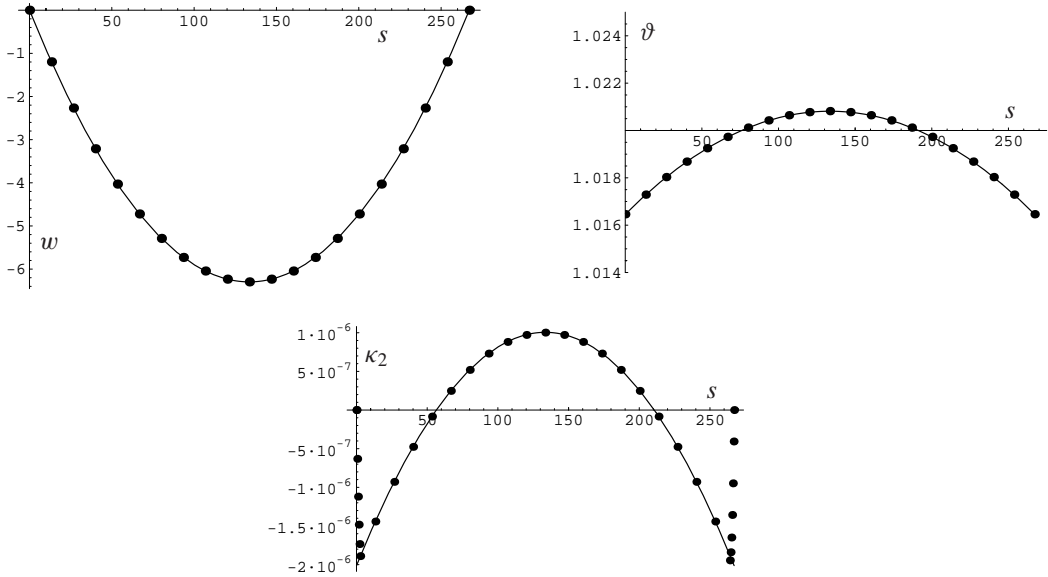


Figure 3. Static response to uniformly distributed forces (dots: complete model; continuous line: reduced model).

two different approaches (about 6.2 m/s). [Figure 5](#) highlights the excellent agreement between critical modes obtained from complete and reduced models: the small differences in the twist angle may be put down to static condensation.

6.2. Parametric analysis. A parametric analysis has been conducted to detect the condition of the incipient galloping of cables. Two different U-shaped conductors have been taken into account, already considered in the literature: a cross-section with the symmetry axis placed on \mathbf{a}_z -direction (CS1 in the sequel), having its maximum ice eccentricity opposite to the mean wind ($m = 1.80$ kg/m, ice included; see [\[Yu et al. 1993b\]](#)), and a cross-section with the symmetry axis rotated through -44.4° with respect to \mathbf{a}_z -direction (CS2 in the sequel), having greater ice thickness ($m = 2.00$ kg/m, ice included; see [\[Tunstall 1989\]](#)). In both cases the specified configuration is the most prone to galloping. It should be noted that, in the proposed theory, this position corresponds to no-wind conditions since the angle of attack γ is also statically varying through the angle of rotation φ ; see [Equation \(23\)](#). Therefore, when galloping actually occurs, the cable cross-section is rotated from the more dangerous initial position.

At the lower level, the displacement field $v(s, t)$, $w(s, t)$ and $\vartheta(s, t)$ are approximated by the first symmetric in-plane $\phi_v(s)$ and out-of-plane ($\phi_w(s)$, $\phi_\vartheta(s)$) eigenfunctions of the corresponding Hamiltonian system. [Figure 6](#) shows the nonlinear equilibrium path $\varphi = \varphi(U)$ for the two different cross-sections in the basic case, and the changes in the prestress \bar{T} due to the static loads. Differences are due to aerodynamic coefficients and to cable mass. When the mean wind velocity increases, the rotation soon achieves relevant values and the prestress is subjected to nonnegligible alterations. The conditions of incipient instability are examined by evaluating the real part of the two couples of complex conjugate eigenvalues for the discretized system. The objective is to point out the possible role of the dynamic twist angle ϑ (that is, the circulatory matrix \mathbf{H}) on the critical wind velocity U_c . For both cross-sections,

Figure 7 shows the real part of the critical eigenvalue considering (continuous lines) or neglecting (dashed lines) the circulatory matrix \mathbf{H} . For CS1 (Figure 7, left), the equilibrium configuration \mathcal{C} loses stability at the first bifurcation point B_1 , then it regains stability at the second bifurcation point B_2 . Differences in the two models are small and slight influence occurs on point B_2 . Concerning CS2 (Figure 7, right), the circulatory matrix has again quantitatively small influence, but it is decisive to the occurrence or not of both bifurcations.

It was previously found that the dynamic twist ϑ is much higher in symmetric modes than in anti-symmetric ones. In order to quantify these results, the nonzero coefficients h_{12} and h_{22} of the matrix \mathbf{H} obtained by the Galerkin procedure for $m = n = 1$ (Appendix C), and evaluated for symmetric and antisymmetric modes, were compared; see Figure 8. Three values of $d = d_i$ were considered to explore the situation of almost slack ($d_3 = 15$ m) and almost taut ($d_1 = 3$ m) cable, beside the basic case ($d_2 = 6.18$ m), maintaining the original length $\ell = 267$ m. In the range of the examined velocities, concerning the

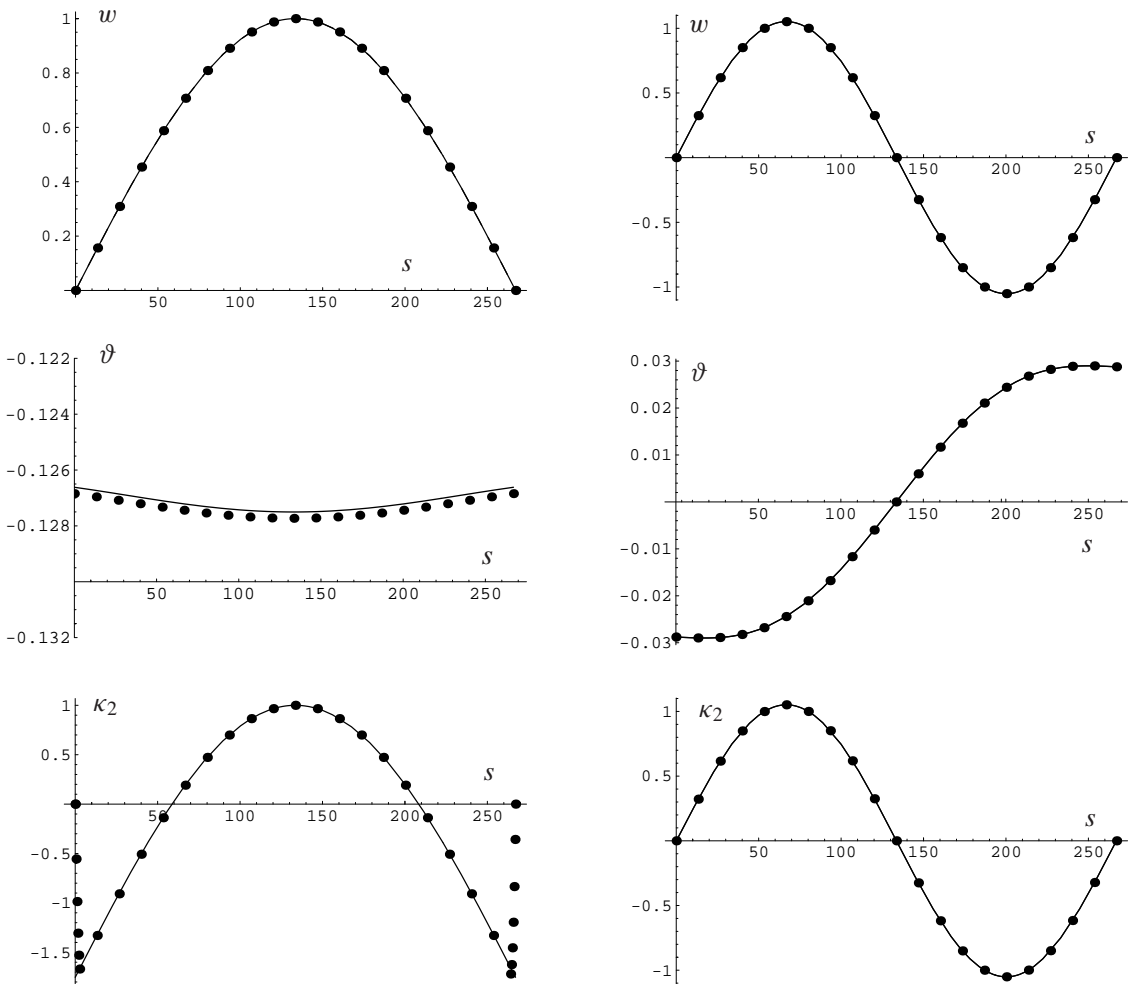


Figure 4. First (left) and second (right) out-of-plane normal mode (dots: complete model; continuous line: reduced model).

antisymmetric modes, the effective influence of the dynamic twist seems to be nonnegligible only for high values of the sag, close to the limits of the proposed theory. By contrast, as regards symmetric modes, the dynamic twist appears remarkable when the curvature (sag) is sufficiently small.

To investigate this aspect with its implications for the system stability, the previous examples related to symmetric modes are reconsidered with suitable changes in mechanical and aerodynamic parameters. Concerning CS1, a reduction of sag and an increase of damping mean that a cable, that is unstable when ignoring the dynamic torsion, is actually stable (Figure 9, left). Moreover, starting the analysis with a cross-section slightly rotated (for example, -1°) as regards the position more prone to galloping, the cable cross-section reaches the most dangerous attitude for instability in proximity of the bifurcation points. In this way, bifurcations in both the solutions exist and appreciable differences appear (Figure 9, right).

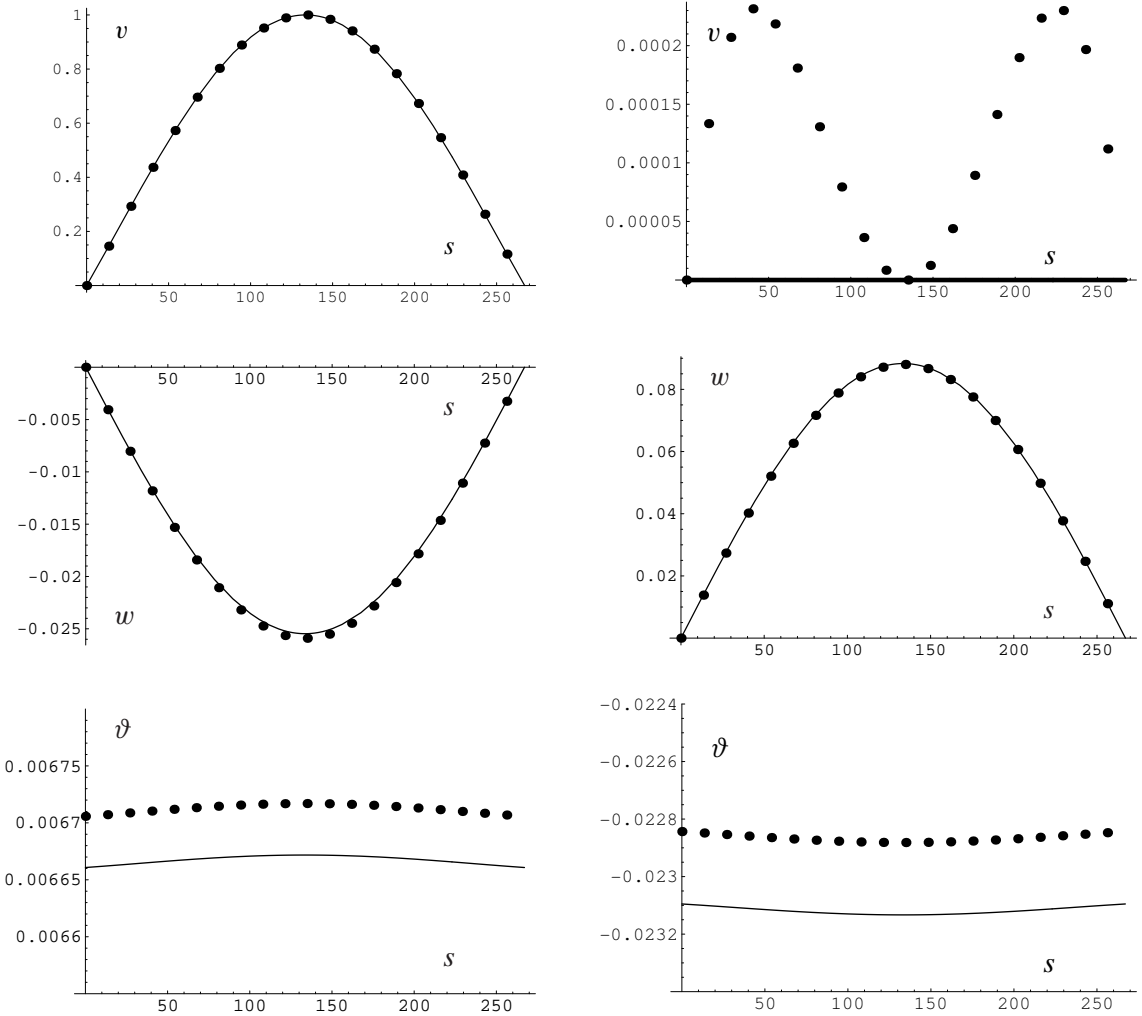


Figure 5. Real (left) and imaginary (right) part of the critical mode (dots: complete model; continuous line: reduced model).

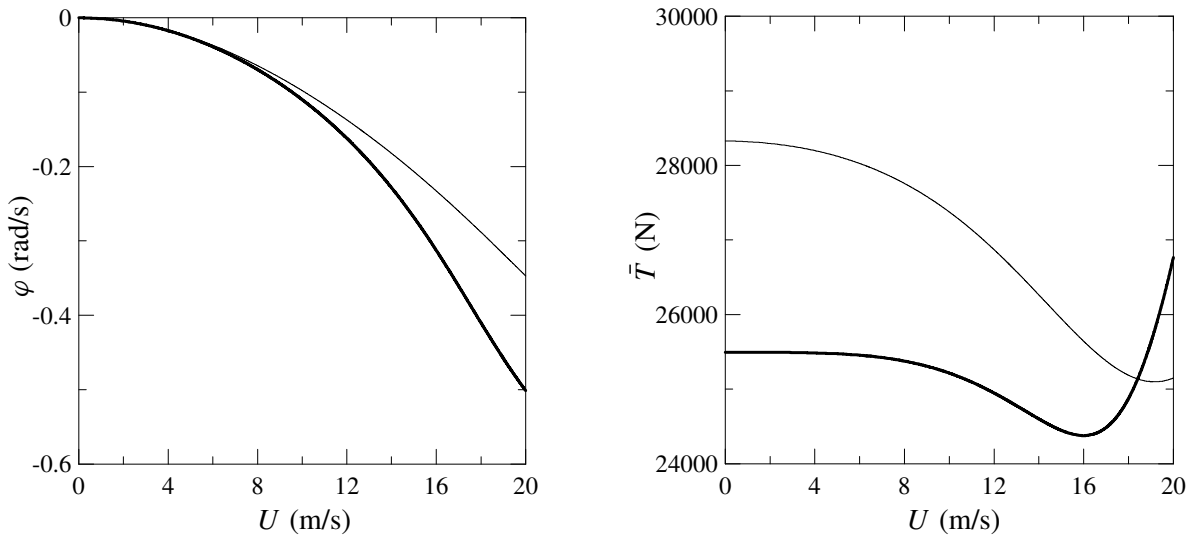


Figure 6. Left: nonlinear equilibrium path $\varphi = \varphi(U)$ for the two different cross-sections in the basic case (thick lines: CS1; thin lines: CS2). Right: changes in the prestress \bar{T} due to the static loads.

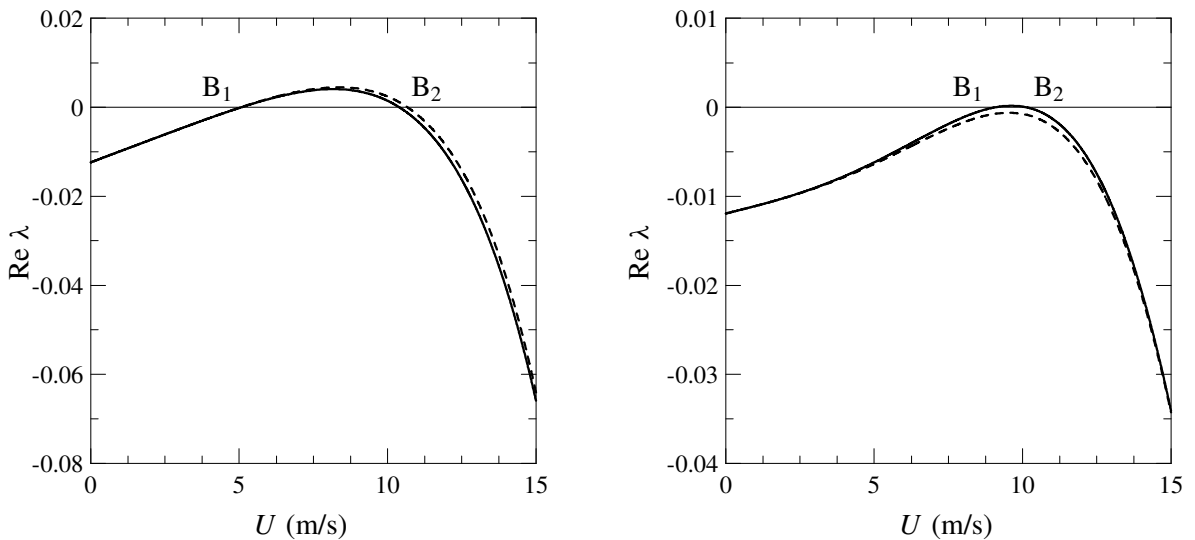


Figure 7. Real part of the critical eigenvalue for CS1 (left) and CS2 (right). Thick lines are used for results obtained with the complete model; dashed lines, for those obtained neglecting the circulatory matrix \mathbf{H} .

Even larger alteration can be obtained with further increases in the damping ratio. In these latest examples, the contribution of dynamic torsion improves the system stability, but this condition does not appear as a general rule. The influence of dynamic torsion is still more pronounced on the CS2. Maintaining the basic sag and considering an initial rotation of the cross-section equal to -47° (instead of the basic value

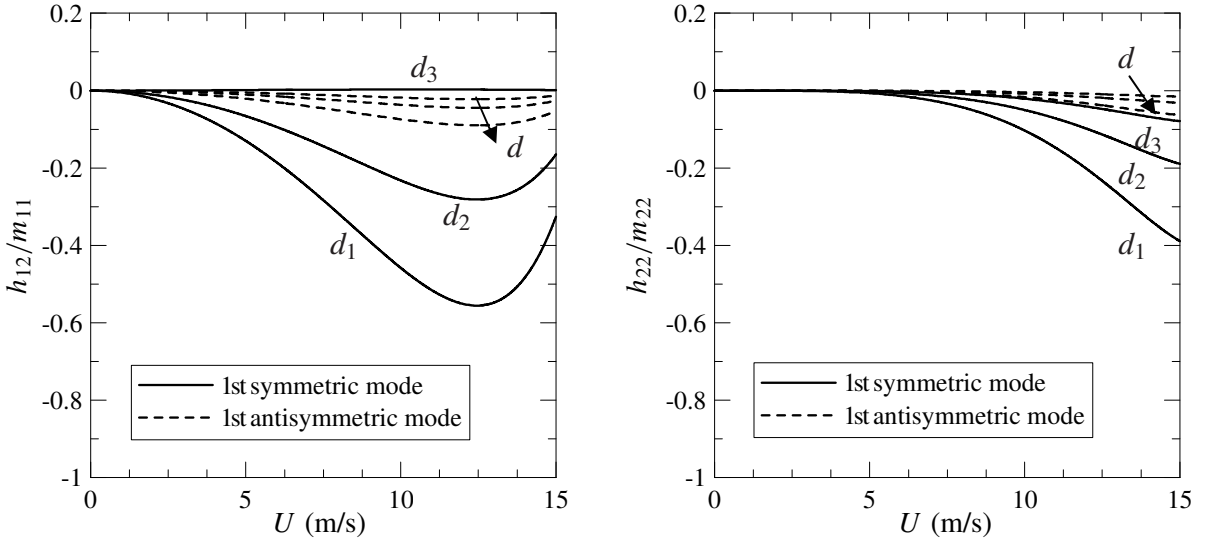


Figure 8. Coefficients of the circulatory matrix \mathbf{H} : left, coupling terms; right, terms modifying the structural stiffness ($d_1 = 3$ m; $d_2 = 6.18$ m; $d_3 = 15$ m; $\ell = 267$ m; CS1).

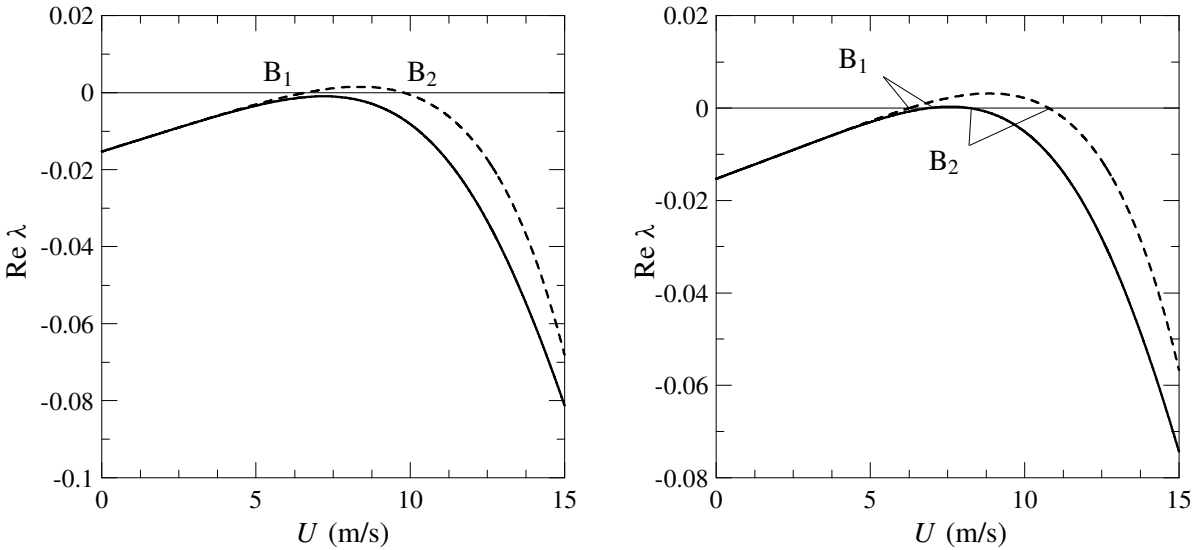


Figure 9. Real part of the critical eigenvalue of the CS1: left, $d = 3$ m; right, $d = 3$ m and sectional symmetry axis rotated through -1° in no-wind conditions (damping coefficients equal to 0.65%). Continuous lines, complete model; dashed lines, matrix \mathbf{H} neglected.

of -44.4°) differences between the two bifurcation points are found immediately (Figure 10, left). If the role of the torsion is exalted by decreasing the sag (Figure 10, right), large alterations of the critical wind velocities appear.

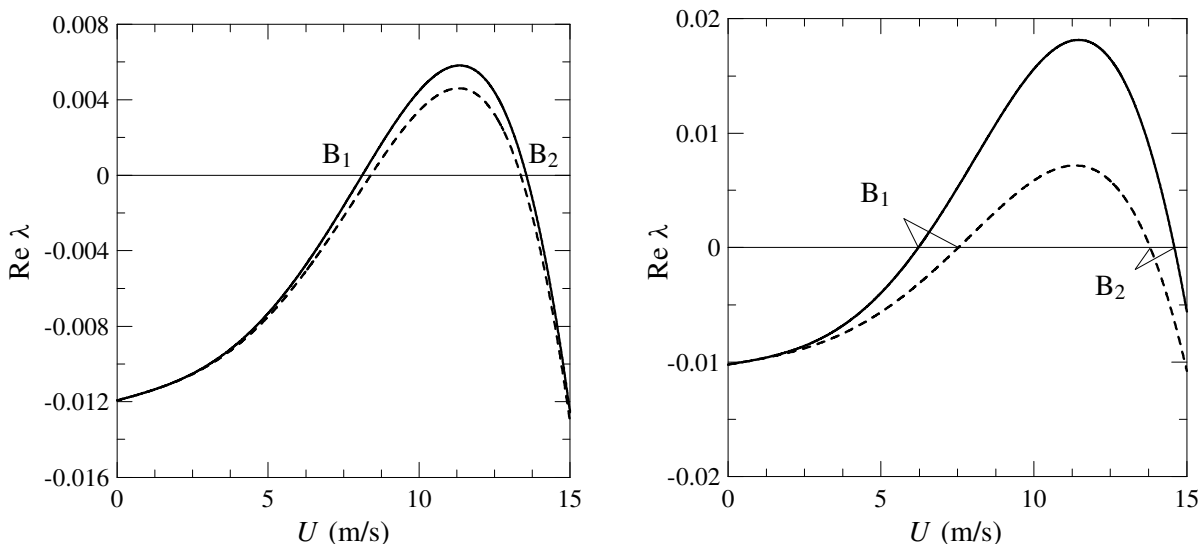


Figure 10. Real part of the critical eigenvalue of the CS2: left, $d = 6.18$ m; right, $d = 3$ m (sectional symmetry axis rotated through -47° in no-wind conditions). Continuous lines, complete model; dashed lines, matrix \mathbf{H} neglected.

Repeating previous investigations of stability of the antisymmetric modes, qualitatively similar behavior has been obtained, with critical wind velocities equal to, smaller or greater than the critical velocities of symmetric modes. Sometimes, antisymmetric modes always turned out to be stable, since the relevant eigenvalues approach the imaginary axis and then veer away without crossing it. Most importantly, in all the examples considered (not reported here for brevity), the influence of dynamic twist ϑ on the system stability resulted negligible, according to previous theoretical findings.

7. Conclusions

The aim of this paper concerns the formulation of a consistent cable-beam model able to take into account twist angle effects, which can be very important in determining the aeroelastic behavior of these kinds of structure. Several points are worth highlighting.

A consistent model of a linear, curved, prestressed, no-shear, elastic cable-beam has been formulated. Reduced equations of motion have been deduced through a suitable magnitude order analysis; this has made it possible to clarify the different role of the dynamic twist angle on symmetrical and antisymmetrical modes. As a major result, the reduced equations of motion are identical to those of a flexible cable, with an additional equation in the twist angle, which therefore represents a passive variable. The aerodynamic forces have been evaluated taking into account both the angle of static rotation induced by the mean wind and the dynamic twist angle.

Numerical results have been obtained using a Galerkin procedure with translational and twist eigenfunctions, in order to study conditions of incipient instability. It has been proved that the dynamic twist angle is able to influence the critical conditions of the system considerably, through the circulatory matrix, when symmetrical modes are taken into account, especially for small values of sag. The presence of twist

angle may imply the appearance or disappearance of criticality, and may lead to remarkable differences in aeroelastic critical velocities. These alterations are more pronounced when a cross-section is considered in an initially nonsymmetric position.

Appendix A. Magnitude order of the twist angle

The linearized nondimensional equation (11)₄ is considered, in which $c_{a1} = 0$, $\kappa = \text{const}$ and $\beta = 1$ are assumed. Moreover,

$$w = \begin{cases} \cos(n\pi s) & n = 1, 3, \dots \\ \sin(n\pi s) & n = 2, 4, \dots \end{cases} \quad s \in \left[-\frac{1}{2}, \frac{1}{2}\right] \tag{29}$$

is taken, for symmetric and antisymmetric modes, respectively. The equation admits the following approximate solution:

$$\vartheta \simeq \begin{cases} A - 2\kappa \cos(n\pi s) & n = 1, 3, \dots, \\ B\kappa s - 2\kappa \sin(n\pi s) & n = 2, 4, \dots, \end{cases}$$

since $\kappa \ll 1$ and therefore $\cosh \kappa s \simeq 1$ and $\sinh \kappa s \simeq \kappa s$ in the interval of interest. By requiring $\vartheta' + \kappa w' = 0$ at $s = \pm 1/2$, the arbitrary constants are found to be $A = \pm 2n\pi/\kappa$, $B = \pm n\pi$, from which, since $\kappa \simeq \delta$ and for n small:

$$\frac{\vartheta}{w} = \begin{cases} \mathcal{O}\left(\frac{1}{\delta}\right) & n = 1, 3, \dots \\ \mathcal{O}(\delta) & n = 2, 4, \dots \end{cases} \tag{30}$$

Using (30), the first and second derivatives of ϑ are found as in (15), both for symmetric and antisymmetric modes. By summarizing, since the symmetric mode is slow-varying in space, in order to satisfy boundary conditions amplitude A must be large; on the other hand, since the antisymmetric mode is fast-varying in space, amplitude B must, on the contrary, be small.

Appendix B. Static wind forces and aerodynamic coefficients

The static wind force components \bar{b}_{a_i} and the coefficients c_{ij} expressing the dynamic wind force components $b_{a_i} - \bar{b}_{a_i}$, all appearing in Equations (25), are

$$\begin{aligned} \bar{b}_{a_2} &= \frac{1}{2}\rho_a U^2 r (-c_l \cos \varphi + c_d \sin \varphi), \\ c_{2\vartheta} &= \frac{1}{2}\rho_a U^2 r (c'_l \cos \varphi - c'_d \sin \varphi), \\ c_{2v} &= \frac{1}{4}\rho_a U r (-3c_d - c'_l + (c_d - c'_l) \cos 2\varphi + (c'_d + c_l) \sin 2\varphi), \\ c_{2w} &= \frac{1}{4}\rho_a U r (-c'_d + 3c_l + (c'_d + c_l) \cos 2\varphi - (c_d - c'_l) \sin 2\varphi), \\ \bar{b}_{a_3} &= \frac{1}{2}\rho_a U^2 r (c_d \cos \varphi + c_l \sin \varphi), \\ c_{3\vartheta} &= -\frac{1}{2}\rho_a U^2 r (c'_d \cos \varphi + c'_l \sin \varphi), \\ c_{3v} &= -\frac{1}{4}\rho_a U r (-c'_d + 3c_l - (c'_d + c_l) \cos 2\varphi + (c_d - c'_l) \sin 2\varphi), \\ c_{3w} &= -\frac{1}{4}\rho_a U r (3c_d + c'_l + (c_d - c'_l) \cos 2\varphi + (c'_d + c_l) \sin 2\varphi). \end{aligned}$$

To include structural damping, the coefficients c_{2v} and c_{3w} are then modified:

$$\hat{c}_{2v} = c_{2v} + c_v, \quad \hat{c}_{3w} = c_{3w} + c_w.$$

Appendix C. Coefficients of the algebraic eigenvalue problem

When $m = n = 1$ in the algebraic problem (28), the Lagrangian parameters vector is $\mathbf{q} = (q_1^i, q_1^o)$. The mass matrix is

$$\mathbf{M} = \begin{bmatrix} m_{11} & 0 \\ 0 & m_{22} \end{bmatrix},$$

where

$$m_{11} = -m \int_0^\ell \phi_{v_1}^2 ds, \quad m_{22} = -m \int_0^\ell \phi_{w_1}^2 ds.$$

The structural stiffness matrix is

$$\mathbf{K} = \begin{bmatrix} k_{11} & 0 \\ 0 & k_{22} \end{bmatrix},$$

where

$$k_{11} = \bar{T} \int_0^\ell \phi_{v_1} \phi_{v_1}'' ds - \frac{EA\bar{\kappa}^2}{\ell} \int_0^\ell \left[\int_0^\ell \phi_{v_1} ds \right] \phi_{v_1} ds, \quad k_{22} = \bar{T} \int_0^\ell \phi_{w_1} \phi_{w_1}'' ds.$$

The circulatory matrix is

$$\mathbf{H} = \begin{bmatrix} 0 & h_{12} \\ 0 & h_{22} \end{bmatrix},$$

where

$$h_{12} = c_{2\vartheta} \int_0^\ell \phi_{v_1} \phi_{\theta_1} ds, \quad h_{22} = c_{3\vartheta} \int_0^\ell \phi_{w_1} \phi_{\theta_1} ds$$

The damping matrix \mathbf{C} , containing both structural and aerodynamic damping, is

$$\mathbf{C} = \begin{bmatrix} c_{11} & c_{12} \\ c_{21} & c_{22} \end{bmatrix}, \tag{31}$$

where

$$c_{11} = \hat{c}_{2v} \int_0^\ell \phi_{v_1}^2 ds, \quad c_{21} = c_{3v} \int_0^\ell \phi_{v_1} \phi_{w_1} ds, \quad c_{12} = c_{2w} \int_0^\ell \phi_{v_1} \phi_{w_1} ds, \quad c_{22} = \hat{c}_{3w} \int_0^\ell \phi_{w_1}^2 ds.$$

In particular, structural damping is introduced directly as modal damping:

$$c_{11} = c_{2v} \int_0^\ell \phi_{v_1}^2 ds + 2\xi_1 \sqrt{m_{11}k_{11}}, \quad c_{22} = c_{3w} \int_0^\ell \phi_{w_1}^2 ds + 2\xi_2 \sqrt{m_{22}k_{22}},$$

where ξ_1, ξ_2 are the modal damping factors.

References

- [Blevins 1990] R. D. Blevins, *Flow-induced vibration*, 2nd ed., Van Nostrand Reinhold, New York, 1990. Reprinted Krieger, Melbourne (FL), 2001.
- [Diana et al. 1998] G. Diana, S. Bruni, F. Cheli, F. Fossati, and A. Manenti, "Dynamic analysis of the transmission line crossing 'Lago de Maracaibo' ", *J. Wind Eng. Ind. Aerod.* **74-76** (1998), 977–986.
- [Hong et al. 2005] K. J. Hong, A. D. Kiureghian, and J. L. Sackman, "Bending behavior of helically wrapped cables", *J. Eng. Mech. (ASCE)* **131**:5 (2005), 500–511.

- [Irvine and Caughey 1984] H. M. Irvine and T. K. Caughey, “The linear theory of free vibrations of a suspended cable”, *Proc. R. Soc. London Ser. A* **341** (1984), 299–315.
- [Lee and Chao 2000] S. Y. Lee and J. C. Chao, “Out-of-plane vibrations of curved non-uniform beams of constant radius”, *J. Sound Vib.* **238**:3 (2000), 443–458.
- [Lee and Perkins 1992] C. L. Lee and N. C. Perkins, “Nonlinear oscillations of suspended cables containing a two-to-one internal resonance”, *Nonlinear Dynam.* **3**:6 (1992), 465–490.
- [Lu and Perkins 1994] C. L. Lu and N. C. Perkins, “Nonlinear spatial equilibria and stability of cables under uni-axial torque and thrust”, *J. Applied Mech. (ASME)* **61**:4 (1994), 879–886.
- [Luongo and Piccardo 1996] A. Luongo and G. Piccardo, “On the influence of the torsional stiffness on non-linear galloping of suspended cables”, pp. 273–276 in *Proc. 2nd European Nonlinear Oscillations Conference* (Prague, 1996), Ústav termomechaniky, Akademie věd ČR, Prague, 1996.
- [Luongo and Piccardo 1998] A. Luongo and G. Piccardo, “Non-linear galloping of sagged cables in 1:2 internal resonance”, *J. Sound Vib.* **214**:5 (1998), 915–940.
- [Luongo et al. 1984] A. Luongo, G. Rega, and F. Vestroni, “Planar non-linear free vibrations of an elastic cable”, *Int. J. Non-Linear Mech.* **19**:1 (1984), 39–52.
- [Luongo et al. 2005] A. Luongo, D. Zulli, and G. Piccardo, “Un modello lineare di trave curva per l’analisi delle oscillazioni galoppanti di cavi sospesi”, in *Atti del XVII Congresso Nazionale AIMETA* (Florence, 2005), 2005. Available in CD-ROM.
- [McConnel and Chang 1986] K. G. McConnel and C. N. Chang, “A study of the axial-torsional coupling effect on a sagged transmission line”, *Exp. Mech.* **26**:4 (December 1986), 324–329.
- [Strømme and Hjørth-Hansen 1995] E. Strømme and E. Hjørth-Hansen, “The buffeting wind loading of structural members at an arbitrary attitude in the flow”, *J. Wind Eng. Ind. Aerod.* **56**:2-3 (1995), 267–290.
- [Tunstall 1989] M. Tunstall, “Accretion of ice and aerodynamic coefficients”, in *Proceedings of the Association des Ingénieurs Montefiore (AIM) Study Day on Galloping* (Liège, 1989), Université de Liège, 1989.
- [White et al. 1991] W. N. White, S. Venkatasubramanian, P. M. Lynch, and C. D. Huang, “The equations of motion for the torsional and bending vibrations of a stranded cable”, pp. 91–WA/APM–19 in *ASME Winter Annual Meeting*, ASME, New York, 1991.
- [Yu et al. 1993a] P. Yu, Y. M. Desai, A. H. Shah, and N. Popplewell, “Three-degree-of-freedom model for galloping, I: formulation”, *J. Eng. Mech. (ASCE)* **119**:12 (1993), 2404–2425.
- [Yu et al. 1993b] P. Yu, Y. M. Desai, A. H. Shah, and N. Popplewell, “Three-degree-of-freedom model for galloping, II: solutions”, *J. Eng. Mech. (ASCE)* **119**:12 (1993), 2426–2448.

Received 26 Jul 2006. Accepted 2 Feb 2007.

ANGELO LUONGO: luongo@ing.univaq.it
DISAT, Università degli Studi di L’Aquila, 67040 L’Aquila (AQ), Italy

DANIELE ZULLI: danzulli@ing.univaq.it
DISAT, Università degli Studi di L’Aquila, 67040 L’Aquila (AQ), Italy

GIUSEPPE PICCARDO: giuseppe.piccardo@unige.it
DICAT, Università degli Studi di Genova, Via Montallegro, 1, 16145 Genova (GE), Italy

STRESS ANALYSIS OF COMPOSITE CYLINDRICAL SHELLS WITH AN ELLIPTICAL CUTOUT

ERKAN OTERKUS, ERDOGAN MADENCI AND MICHAEL P. NEMETH

A special-purpose, semianalytical solution method for determining the stress and deformation fields in a thin, laminated-composite cylindrical shell with an elliptical cutout is presented. The analysis includes the effects of cutout size, shape, and orientation; nonuniform wall thickness; oval cross-sectional eccentricity; and loading conditions. The loading conditions include uniform tension, uniform torsion, and pure bending. The analysis approach is based on the principle of stationary potential energy and uses Lagrange multipliers to relax the kinematic admissibility requirements on the displacement representations through the use of idealized elastic edge restraints. Specifying appropriate stiffness values for the elastic extensional and rotational edge restraints (springs) allows the imposition of the kinematic boundary conditions in an indirect manner, which enables the use of a broader set of functions for representing the displacement fields. Selected results of parametric studies are presented for several geometric parameters that demonstrate that this analysis approach is a powerful means for developing design criteria for laminated-composite shells.

1. Introduction

Cutouts in cylindrical shell-type components are unavoidable in the construction of aerospace structures. This fact is significant because the structural failure of these components usually begins near the cutout due to high stress concentrations that initiate the formation of cracks. Hence, a cutout can trigger a local failure at a load level lower than the global failure load of a corresponding shell without a cutout. As a result, preliminary design sizing of a cylindrical shell with a cutout is often based on the magnitude of the stress concentrations near the cutout. Therefore, an accurate assessment of the stress concentrations in a given shell subjected to various types of loading and support conditions is essential to the development of safe and reliable designs. Moreover, validated special-purpose analysis tools that enable rapid parametric studies would be very valuable to structural designers and for development of new design criteria and design concepts.

Several analytical, numerical, and experimental studies have been conducted during the past sixty years to determine stress distributions in cylindrical shells with a cutout and subjected to various types of loadings, such as axial tension and compression, torsion, and internal and external pressure. Pioneering analytical work was conducted by [Lurie 1946; 1947] to investigate the effects of axial tension, internal pressure, and shell curvature on the stress concentrations around a circular cutout. Many years later,

Keywords: cylindrical, composite, cutout, stress.

The authors wish to dedicate this paper to the memory of Dr. James H. Starnes, Jr. of the NASA Langley Research Center. Dr. Starnes was an internationally recognized expert in aerospace structures technology and a proponent of the development of special-purpose, design-oriented analysis methods such as that presented herein.

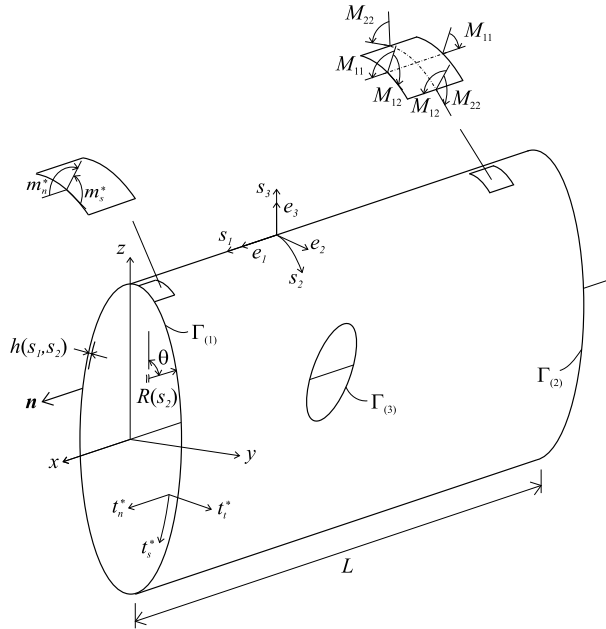


Figure 1. Geometry, coordinates systems, and applied edge tractions for an oval cylindrical shell with an elliptical cutout and nonuniform wall thickness.

analytical studies were presented by [Lekkerkerker 1966; Van Dyke 1965; Ashmarin 1966; Murthy et al. 1974; Guz et al. 2001; Van Tooren et al. 2002] that further investigated the effects of various factors on the stress concentrations around a cutout in a cylindrical shell. Similarly, experimental investigations have been conducted by [Tennyson 1968; Starnes 1972; Pierce and Chou 1973; Zirka and Chernopiskii 2003; Bull 1982], and numerical studies have been conducted by [Liang et al. 1998; Shnerenko and Godzula 2003; Storozhuk and Chernyshenko 2005]. Hicks [1964] and Ebner and Jung [1972] summarized the results obtained from several of these studies and provided extensive lists of references related to this problem. Most of these previous studies are for isotropic cylindrical shells with a circular cutout. Only a few of these studies, such as those presented by Pierce and Chou [1973] and by Murthy et al. [1974], address the effects of cutout shape (elliptical cutouts) on the stress concentrations.

Mitigation of high stress concentrations by tailoring shell wall thickness, material orthotropy and anisotropy, and cutout reinforcement is also an important consideration in the design of aerospace structures made of lightweight composite materials. Likewise, the potential for using shells of noncircular cross section are relevant to fuselage-like structures. However, only a few studies have considered these effects. For example, the influence of variation in wall thickness on the stresses in axially loaded composite cylindrical shells without a cutout has been investigated by [Li et al. 1995]. Although numerous analyses exist in the literature on the analysis of shells with circular cross sections, only a few include noncircular cross sections. Sheinman and Firer [1994] provided an analytical investigation of stresses in laminated cylindrical shells with arbitrary noncircular cross sections. More recently, Hyer and Wolford [2002] and Hyer et al. [2003] studied the effect of noncircular cross sections on damage initiation and progressive failure in composite cylinders by employing the finite element method.

The objective of the present study is to present a special-purpose analysis for a laminated-composite cylindrical shell with an elliptical cutout that can be used to investigate rapidly and parametrically the effects of shell curvature, cutout size, shape, and orientation, and ply lay-up on stress-resultant concentrations near the cutout. The analysis is applicable to thin-walled cylindrical shells with nonuniform wall thickness, noncircular (for example, oval) shell cross-section, which are subjected to tension, torsion, and bending loads as illustrated in [Figure 1](#).

To accomplish this objective, an overview of the analysis is presented first. Next, the boundary value problem is defined along with the kinematics and stress-strain relations used in the analysis. Then, the derivation of the equations governing the response and numerical procedure are described. Finally, selected numerical results for oval and circular cylindrical shells with either circular or elliptical cutouts and subjected to either tension, torsion, or pure-bending loads are presented.

2. Analysis overview

The analytical approach used herein permits the determination of the pointwise variation of displacement and stress components. It is based on the principle of stationary potential energy, but utilizes local and global functions that are not required to satisfy the kinematic boundary conditions directly. Thus, the choice of local and global functions is not limited by a particular type of kinematic boundary condition. The kinematic boundary conditions are imposed by employing the Lagrange multiplier method. Both local and global functions are used, in contrast to the traditional approach, to enhance the robustness of the analysis method. In particular, the local functions are used to capture rapidly varying stress and strain gradients and local deformations near a cutout. Toward that goal, Laurent series are used for the local functions and are expressed in terms of the mapping functions introduced by [\[Lekhnitskii 1968\]](#). Fourier series are used for the global functions and are used to capture the overall deformation and stress fields. The kinematic admissibility requirements on the local and global functions are relaxed by defining the edges of the shell such that they are supported by extensional and rotational springs. Zero-valued displacement and rotation kinematic boundary conditions are enforced in an indirect manner by specifying values for the spring stiffnesses that are large compared to the corresponding shell stiffnesses. This approach effectively yields a prescribed kinematic boundary condition in the limit as the relative stiffness of the spring becomes much greater than the corresponding shell stiffness. Similarly, values for the spring stiffnesses can be selected that correspond to a given uniform elastic restraint along an edge, similar to that provided by an end ring. This capability is important and useful, because in some test fixtures or actual structures the edge supports may not be stiff enough to simulate a fully clamped boundary condition, or flexible enough to simulate a simply supported boundary condition.

As suggested by [\[Li et al. 1995\]](#) and [\[Sheinman and Firer 1994\]](#), nonuniform variations in wall thickness of a shell which lead to nonuniform laminate stiffnesses are represented using trigonometric series. Specifically, nonuniform shell wall thickness is represented in the present study by perturbing the ply thicknesses with a function that is periodic in either the longitudinal or the circumferential direction. The variation in wall thickness is accounted for by adjusting the lamina properties, resulting in nonhomogeneous in-plane and bending stiffness matrices. The nonuniform shell curvature associated with a noncircular cross section is represented by using trigonometric series for the coordinates of an oval cross-section shell reference surface (1958). The aspect ratio, or out-of-roundness, of the cross section is

represented in the analysis using an eccentricity parameter introduced by [Romano and Kempner 1962] and later used by [Culberson and Boyd 1971; Chen and Kempner 1976]. This parameter is defined in the subsequent section, and the aspect ratio, related to the eccentricity parameter, represents the ratio of the minor axis to the major axis.

In the derivation of the equations governing the response, the total potential energy consists of the elastic strain energy of the shell, the elastic edge restraints, and the potential energy of the applied loads. The conditions that may arise from the choice of displacement approximations without any kinematic restrictions are treated as constraint equations, and the potential energy arising from constraint reactions is invoked into the total potential energy through the use of Lagrange multipliers. The equations governing the shell response are obtained by enforcing the requirement that the first variation of the total potential energy vanish. The evaluation of the area integrals appearing in the potential energy are achieved numerically using a basic quadrature method in conjunction with standard triangulation of the entire domain, as described by [Shewchuk 1996]. Solutions to the equations governing the response are obtained using a standard Gaussian elimination procedure, which yields the generalized displacement coefficients and thus, the stress and strain fields. The accuracy of the analysis depends on the number of terms used for the functional representation of the displacement fields. As the number of terms increases, the results converge to the exact solution.

3. Representation of shell geometry

The geometry of a thin-walled, noncircular, cylindrical shell of length L and with an elliptical cutout located at the shell mid-length is shown in Figure 1. The origin of the global Cartesian coordinate system, (x, y, z) , is located at an end point of the longitudinal axis of the shell. As shown in Figure 1, the x -axis coincides with the longitudinal axis of the shell. The y - and z -coordinates span the cross-sectional plane. A curvilinear coordinate system is also attached to the mid-surface of the cylindrical shell. The coordinates of points in the longitudinal, circumferential (tangential), and normal-to-the-surface (transverse) directions of the shell are denoted by (s_1, s_2, s_3) , and the corresponding unit base vectors are $\{\mathbf{e}_1, \mathbf{e}_2, \mathbf{e}_3\}$.

Following [Romano and Kempner 1958], the noncircular cross section of the cylindrical shell is defined as an oval with the coordinates y and z expressed as

$$y = R_0 \sum_{\text{modd}} a_m(\xi) \sin \frac{ms_2}{R_0}, \quad z = R_0 \sum_{\text{modd}} b_m(\xi) \cos \frac{ms_2}{R_0}, \quad (1)$$

where ξ represents the eccentricity of the oval cross section and R_0 is the equivalent radius of a circular cylindrical shell that has the same circumference as that of the oval cylindrical shell. The circumferential coordinate, s_2 , varies between 0 and $2\pi R_0$. The derivation of Equation (1) and the explicit forms of the coefficients $a_m(\xi)$ and $b_m(\xi)$ are given by [Madenci and Barut 2003].

As derived by [Romano and Kempner 1958], the coordinates y and x in Equation (1) can be related to the radius of curvature of an oval-cross-section cylindrical shell $R(s_2, \xi)$ by

$$R(s_2, \xi) = \frac{R_0}{1 + \xi \cos(2s_2/R_0)}. \quad (2)$$

Therefore, $\xi = 0$ implies no eccentricity and corresponds to a circular cross section with radius R_0 . For positive values of the eccentricity parameter ξ , the z -coordinate becomes the major axis and the y -coordinate becomes the minor axis. For negative values of ξ , the major and minor axes switch to the y - and z -axes, respectively. The range of values of the eccentricity parameter ξ is bounded by $-1 < \xi < 1$.

As shown in Figure 1, the cylindrical shell contains a cutout. The shape of this cutout is defined such that if the shell is cut along a generator and flattened into a plane, the cutout becomes an ellipse, with major and minor axes denoted by a and b , respectively. For simplicity and convenience, the cutout is referred to herein as an *elliptical* cutout. Because the domain of the analysis shown in Figure 2 corresponds to a similar flat region, a subsequent mapping of the ellipse to a unit circle is possible, which enables the use of Laurent series expansions for the local functions. Note that the special case of a *circular* cutout is given by $a = b$.

In the flat analysis domain, the minor and major axes of the ellipse are aligned with a local coordinate system, (x_1, x_2) , whose origin is located at the center of the cutout and coincides with the origin of the parameter grid (given by constant values of s_1 and s_2) that forms the curvilinear coordinates (s_1, s_2) on the cylindrical shell mid-surface. The orientation of the elliptical cutout is arbitrary with respect to the longitudinal shell axis. Hence, the orientation of the local x_1 -axis (major axis) of the cutout and the longitudinal s_1 -axis of the cylindrical shell is denoted by the angle ψ . The elliptical coordinates α and β , representing a family of confocal ellipses and hyperbolas, respectively, are utilized to obtain the stress-resultant distribution in the direction tangent to the cutout boundary. The coordinate α is equal to $\alpha_0 = \tanh^{-1}(b/a)$ on the particular ellipse that corresponds to the elliptical cutout. The other coordinate, β , varying from 0 to 2π , is known as the eccentric angle and is related to the (x_1, x_2) coordinate system by $x_1 = a \cos \beta$ and $x_2 = b \sin \beta$. The eccentric angle β is similar to the angle used for polar coordinates.

The symmetrically laminated cylindrical shells considered herein are made of K specially orthotropic layers, and each layer has an orientation angle, θ_k , that is defined with respect to the s_1 -axis. Each layer also has elastic moduli E_L and E_T , shear modulus G_{LT} , and Poisson's ratio ν_{LT} , where the subscripts L and T represent the longitudinal (fiber) and transverse principal material directions, respectively.

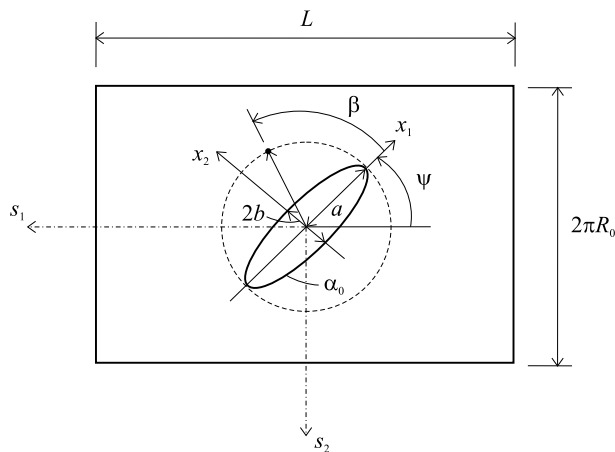


Figure 2. Computational domain of a cylindrical shell with an elliptical cutout.

As for the shell thickness variation, the nonuniform wall thickness of the shell is denoted by $h(s_1, s_2)$, and its variation is included by assuming that the thickness of each ply t_k varies as a function of the curvilinear coordinates of the form

$$t_k(s_1, s_2) = t_{k0} \left(1 - \varepsilon_1 \cos \frac{2\pi m_1 s_1}{L} - \varepsilon_2 \cos \frac{m_2 s_2}{R_0} \right), \quad (3)$$

where t_{k0} denotes the nominal thickness of the k^{th} layer in the laminate, and the parameters (m_1, m_2) and $(\varepsilon_1, \varepsilon_2)$ respectively denote the wave numbers and the amplitudes of the periodic thickness variation, in the longitudinal and circumferential directions. While the wall thickness of the shell is allowed to vary across the shell surface, the aspect ratio of the plies through the thickness is maintained. In other words, the thickness variation of each ply remains conformable to each other throughout the shell surface. A periodic thickness variation in the longitudinal direction is obtained by setting $\varepsilon_1 \neq 0$ and $\varepsilon_2 = 0$, and in the circumferential direction by $\varepsilon_1 = 0$ and $\varepsilon_2 \neq 0$. A shell with uniform thickness $t_k = t_{k0}$ is obtained by setting $\varepsilon_1 = 0$ and $\varepsilon_2 = 0$.

4. Boundary conditions and external loads

To facilitate a general imposition of prescribed boundary tractions, displacements, or rotations; the edge boundary, Γ , of the shell is decomposed into $\Gamma = \Gamma_{(1)} + \Gamma_{(2)} + \Gamma_{(3)}$. As shown in [Figure 1](#), $\Gamma_{(1)}$ and $\Gamma_{(2)}$ denote the external edge boundary of the cylindrical shell and $\Gamma_{(3)}$ represents the traction-free internal edge boundary around the cutout. The unit vector normal to an edge is represented by \mathbf{n} . Throughout this paper, a variable with the superscript $*$ is treated as a known quantity, arising from the externally applied loads or from prescribed displacements and rotations. Also, the subscripts n , s , and t denote the directions normal, tangent, and transverse (through-the-thickness) to the boundary, respectively. The details of how prescribed edge loads and displacements are imposed in the analysis are presented subsequently.

4.1. Prescribed edge loads. External loads are applied to a shell by specifying values for the positive-valued stress resultants shown in [Figure 1](#). More precisely, the membrane loads applied to the ℓ^{th} boundary segment $\Gamma_{(\ell)}$ are given by

$$N_{11} = t_n^*, \quad N_{12} = t_s^*, \quad (4)$$

where N_{11} and N_{12} are the axial and shear stress resultants, respectively, defined in the cylindrical coordinate system. Likewise, shell-wall bending loads that are applied to the ℓ^{th} boundary segment are given by

$$M_{11} = -m_n^*, \quad M_{11,1} + 2M_{12,2} = t_t^* - 2m_{s,2}^*, \quad (5)$$

where M_{11} and M_{12} are the pure bending and twisting stress resultants, respectively, defined in the cylindrical coordinate system. Moreover, the left hand side of the second equation in [Equation \(5\)](#) is the Kirchhoff shear stress resultant of classical shell theory.

As a matter of convenience, the analysis is formulated to permit in addition the specification of concentrated forces and moments that are transmitted to the ends of the shell as if through a rigid end ring, as shown in [Figure 3](#). At present, the concentrated force P_n^* , and the concentrated axial torque P_s^* are included in the analysis. The force P_n^* is simulated in the analysis by specifying a uniform distribution of the axial displacement, with the unknown magnitude Δ_n , and the torque P_s^* is simulated by specifying

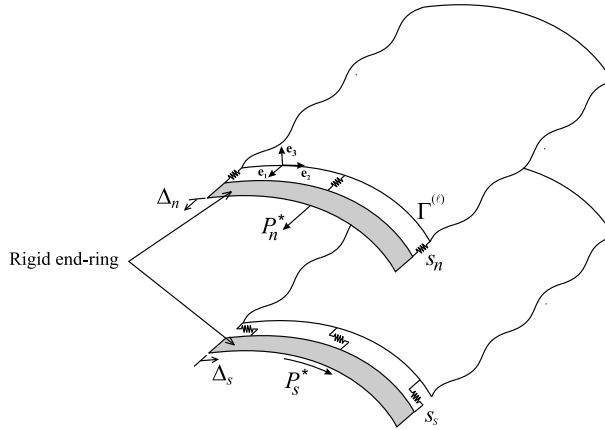


Figure 3. Application of a concentrated force through a rigid end-ring by using elastic springs along a shell edge.

a uniform distribution of the tangential displacement, with the unknown magnitude Δ_s as

$$\int_{\Gamma(\ell)} N_{11} d\Gamma = P_n^*, \quad \int_{\Gamma(\ell)} N_{12} d\Gamma = P_s^*.$$

The analytical process used to ensure that the magnitudes of Δ_n and Δ_s correspond to the specified values of P_n^* and P_s^* , respectively, is described in the following section and in [Appendix A](#).

4.2. Prescribed edge displacements and rotations. Edge displacements and rotations are applied to a shell by specifying values for the displacements and rotations shown in [Figure 4](#) that correspond to the positive-valued stress resultants shown in [Figure 1](#). In particular, the axial and tangential displacements u_n^* and u_s^* that are applied to the ℓ^{th} boundary segment $\Gamma(\ell)$ are given by

$$u_1(\mathbf{n} \cdot \mathbf{e}_1) = u_n^*, \quad u_2[(\mathbf{e}_3 \times \mathbf{n}) \cdot \mathbf{e}_2] = u_s^*.$$

Similarly, the transverse displacement u_3^* , and the rotation about an axis tangent to an edge ϑ_n^* which are applied to the ℓ^{th} boundary segment are defined by

$$u_3 = u_t^*, \quad u_{3,1}(\mathbf{n} \cdot \mathbf{e}_1) = \vartheta_n^*.$$

As mentioned previously, these prescribed displacements are enforced through the use of elastic edge restraints (springs) to relax kinematic admissibility requirements on the functions that are used to represent the displacement fields. The uniformly distributed extensional and rotational springs that are attached to the shell edges in the normal, tangential, and transverse directions and are used to enforce the kinematic boundary conditions are depicted in [Figure 4](#).

Specifying appropriate stiffness values for the springs results in full or partial restraints along the shell edges. A zero value of the spring stiffness corresponds to a traction-free edge condition. In contrast, a value of the spring stiffness that is large compared to the corresponding shell stiffness effectively corresponds to a prescribed zero-valued boundary displacement or rotation. This approach effectively yields a prescribed kinematic boundary condition in the limit as the relative stiffness of the spring becomes much

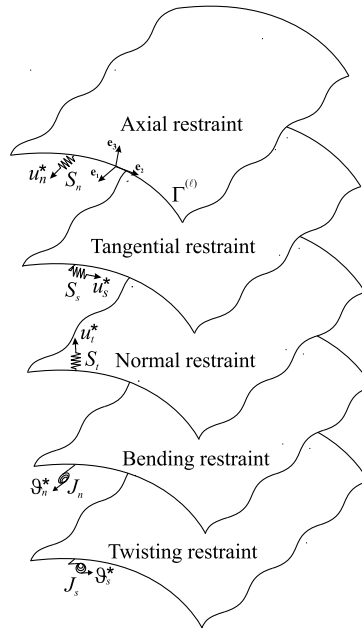


Figure 4. Types of uniformly distributed elastic spring supports that can be prescribed along the edge of a cylindrical shell.

greater than the corresponding shell stiffness. Similarly, values for the spring stiffness can be selected that correspond to a specified uniform elastic restraint along an edge, similar to that provided by a rigid end ring. This capability is important and useful, because in some test fixtures or actual structures the edge supports may not be stiff enough to simulate a fully clamped boundary condition or flexible enough to simulate a simply supported boundary condition.

As depicted in [Figure 4](#), the membrane displacements u_n and u_s , and the transverse displacement $u_t = u_3$ along the ℓ^{th} boundary segment are restrained by extensional springs with stiffness values of S_n , S_s , and S_t in the directions normal, tangential, and transverse to the boundary, respectively. In addition to the extensional springs, the edge rotations ϑ_n and ϑ_s along the ℓ^{th} boundary segment are restrained by rotational springs with stiffness values of J_n and J_s that correspond to rotation about axes tangential and normal to the edge, respectively.

Extensional springs in the directions normal and tangent to the shell edge, with stiffness values of s_n and s_s , are also used to simulate load introduction through a rigid end ring, as shown in [Figure 3](#). Specifying values for the spring stiffnesses s_n and s_s that are relatively large compared to the corresponding shell stiffnesses causes the shell edge to behave as if a rigid end ring is attached, producing the uniformly distributed displacements with the corresponding magnitudes Δ_n and Δ_s . The values for Δ_n and Δ_s that correspond to the specified concentrated loads are determined by using a penalty parameter approach. This approach causes the difference between the edge displacements of the shell and the

unknown uniform rigid end ring displacements $(u_n - \Delta_n)$ and $(u_s - \Delta_s)$ to vanish while retaining the corresponding potential energy of the applied concentrated loads P_n^* and P_s^* .

5. Kinematics and stress-strain relations

The kinematic equations used in the present study are based to a large extent on the assumptions of the Love–Kirchhoff classical thin-shell theory. Specifically, the axial, circumferential (tangential), and normal (normal to the mid-surface) displacements of a generic point of the shell are denoted by $U_1(s_1, s_2, s_3)$, $U_2(s_1, s_2, s_3)$, and $U_3(s_1, s_2, s_3)$, respectively. The corresponding displacements of a generic point of the shell mid-surface that share the same unit vector normal to the mid-surface are denoted by $u_1(s_1, s_2)$, $u_2(s_1, s_2)$, and $u_3(s_1, s_2)$, respectively. In classical shell theory, these displacements are related by

$$U_1(s_i) = u_1(s_1, s_2) - s_3\beta_1(s_1, s_2), \quad U_2(s_i) = u_2(s_1, s_2) - s_3\beta_2(s_1, s_2), \quad U_3(s_i) = u_3(s_1, s_2),$$

where $\beta_1(s_1, s_2)$ and $\beta_2(s_1, s_2)$ are the mid-surface rotations about the s_2 and s_1 axes, respectively, as

$$\beta_1(s_1, s_2) = u_{3,1}(s_1, s_2), \quad \beta_2(s_1, s_2) = u_{3,2}(s_1, s_2) - \frac{1}{R(s_2)} u_2(s_1, s_2),$$

in which a subscript after a comma denotes partial differentiation. The corresponding linear membrane-strain displacement relations and the bending-strain displacement relations are given by

$$\boldsymbol{\varepsilon} = \begin{bmatrix} \varepsilon_{11} \\ \varepsilon_{22} \\ \gamma_{12} \end{bmatrix} = \begin{bmatrix} u_{1,1} \\ \left(u_{2,2} + \frac{1}{R}u_3\right) \\ (u_{1,2} + u_{2,1}) \end{bmatrix}, \quad \boldsymbol{\kappa} = \begin{bmatrix} \kappa_{11} \\ \kappa_{22} \\ \kappa_{12} \end{bmatrix} = \begin{bmatrix} -u_{3,11} \\ -\left(u_{3,22} - \left(\frac{u_2}{R}\right)_{,2}\right) \\ -2\left(u_{3,12} - \frac{1}{R}u_{2,1}\right) \end{bmatrix}. \quad (6)$$

It is important to point out that the expression given for the change in surface twist due to deformation κ_{12} is that originally published by [Love 1888; Love 1944] for general shells, in terms of lines of principal-curvature coordinates, and derived in the book by [Timoshenko and Woinowsky-Krieger 1959] for circular cylindrical shells. As indicated by [Bushnell 1984], the expression for κ_{12} vanishes for rigid-body motions in contrast to the corresponding expression presented in Reissner’s version of Love’s first approximation shell theory [Reissner 1941; Kraus 1967; Naghdi 1962]. Equation (6) and the more general forms presented by [Bushnell 1984], are sometimes referred to as the Love–Timoshenko strain-displacement equations. Justification for this terminology is given by [Chaudhuri et al. 1986].

The stress-strain relations used in the present study are those of the classical theory of laminated plates and shells [Jones 1999], which are based on a linear through-the-thickness distribution of the strain fields. For a thin, symmetrically laminated cylindrical shell, with variable wall thickness, the relationship between the membrane and bending stress resultants and the membrane and bending strains is expressed conveniently in matrix notation by

$$\mathbf{N} = \mathbf{A}(s_1, s_2)\boldsymbol{\varepsilon}, \quad \mathbf{M} = \mathbf{D}(s_1, s_2)\boldsymbol{\kappa}. \quad (7)$$

The membrane and bending stress resultants in Equation (7) are defined as

$$\mathbf{N}^T = [N_{11} \ N_{22} \ N_{12}], \quad \mathbf{M}^T = [M_{11} \ M_{22} \ M_{12}]. \quad (8)$$

It is important to reiterate that when shell wall thickness variations are present, the membrane and bending stiffness matrices $\mathbf{A}(s_1, s_2)$ and $\mathbf{D}(s_1, s_2)$ are dependent on the curvilinear surface coordinates s_1 and s_2 .

It is convenient here to combine the relations given in Equation (7) into the matrix form

$$\mathbf{s} = \mathbf{C} \mathbf{e}, \tag{9}$$

where \mathbf{s} , \mathbf{e} , and \mathbf{C} are defined as

$$\mathbf{s}^T = [\mathbf{N}^T \quad \mathbf{M}^T], \quad \mathbf{e}^T = [\boldsymbol{\epsilon}^T \quad \boldsymbol{\kappa}^T], \quad \mathbf{C} = \mathbf{C}(s_1, s_2) = \begin{bmatrix} \mathbf{A}(s_1, s_2) & \mathbf{0} \\ \mathbf{0} & \mathbf{D}(s_1, s_2) \end{bmatrix}. \tag{10}$$

6. Equations governing the response

A general analytical approach to obtain the exact solution of the equilibrium equations for a laminated-composite cylindrical shell with variable curvature is not mathematically tractable. Therefore, a semianalytic variational approach based on the principle of stationary potential energy is used in the present study to obtain numerical results. Because elastic edge restraints are used as a means to relax the kinematic admissibility conditions on the assumed displacement functions, and because a rigid end ring capability is used to impose shell-end force resultants, the potential energy consists of the elastic strain energy of the shell and the elastic edge restraints and the potential energy of the applied loads. In particular, the potential energy is expressed symbolically by $\pi(\mathbf{q}, \Delta) = U(\mathbf{q}) + \Omega(\mathbf{q}, \Delta) + V(\mathbf{q}, \Delta)$, in which U and Ω represent the strain energy of the laminate and the elastic edge supports (springs), and V represents the potential energy due to external boundary loads. Their explicit forms are presented in Appendix A. The symbol \mathbf{q} is the vector of unknown, generalized displacement coefficients, which arises from the mathematical representation of the mid-surface displacement fields used in the variational solution process. In particular, the mid-surface displacement fields are given symbolically by $u_1(\mathbf{q})$, $u_2(\mathbf{q})$, and $u_3(\mathbf{q})$. The symbol Δ represents the vector of unknown edge displacements that arise from prescribing end loads.

Subjected to the constraint equations that arise from the use of Lagrange multipliers, the equations governing the shell response are obtained by enforcing the requirement that the first variation of the total potential energy vanish. As discussed by [McFarland et al. 1972], because the constraint equations are not functionally dependent on spatial coordinates s_1 and s_2 , the equations governing the response can be generated by modifying the total potential energy into the form

$$\pi^*(\mathbf{q}, \Delta, \boldsymbol{\lambda}) = \pi(\mathbf{q}, \Delta) + W(\mathbf{q}, \boldsymbol{\lambda}),$$

in which W is viewed as the potential energy arising from constraint reactions. In particular,

$$W(\mathbf{q}, \boldsymbol{\lambda}) = \boldsymbol{\lambda}^T \mathbf{G} \mathbf{q} = 0, \tag{11}$$

where $\boldsymbol{\lambda}$ is the unknown vector of Lagrange multipliers and \mathbf{G} is the known constraint coefficient matrix.

Substituting the specific expressions for $U(\mathbf{q})$, $\Omega(\mathbf{q}, \Delta)$, $V(\mathbf{q}, \Delta)$, and $W(\mathbf{q}, \boldsymbol{\lambda})$ that arise from approximation of the surface displacement field, and enforcing the requirement that the first variation of the modified form of the total potential energy to vanish leads to

$$\delta \pi^* = \delta \mathbf{q}^T [\mathbf{k}_{qq} \mathbf{q} + \mathbf{S}_{qq} \mathbf{q} - \mathbf{s}_{q\Delta} \Delta - \mathbf{f}^* - \mathbf{T}^* + \mathbf{G}^T \boldsymbol{\lambda}] + \delta \Delta^T [\mathbf{s}_{\Delta\Delta} \Delta - \mathbf{s}_{q\Delta}^T \mathbf{q} - \mathbf{P}^*] + \delta \boldsymbol{\lambda}^T \mathbf{G} \mathbf{q} = 0,$$

where the matrix \mathbf{k}_{qq} represents the stiffness matrix of the shell and requires evaluation of the corresponding integrand over a doubly connected region (see [Appendix A](#) for details). The spring stiffness matrices \mathbf{S}_{qq} and $s_{\Delta\Delta}$ are associated with the deformation of the shell edges and displacement of the rigid end ring, respectively. The spring stiffness matrix $s_{q\Delta}$ captures the coupling between the displacement of the shell edges and the rigid end ring. The vectors \mathbf{f}^* , \mathbf{T}^* , and \mathbf{P}^* arise from the prescribed boundary displacements, external tractions and moments, and the concentrated forces applied to a rigid end ring, respectively. For the arbitrary variations ($\delta\mathbf{q}$, $\delta\Delta$, and $\delta\lambda$), the stationary condition requires that the following equations must be satisfied:

$$\left[(\mathbf{k}_{qq} + \mathbf{S}_{qq})\mathbf{q} - s_{q\Delta}\Delta - \mathbf{f}^* - \mathbf{T}^* + \mathbf{G}^T\lambda \right] = \mathbf{0}, \quad \left[s_{\Delta\Delta}\Delta - s_{q\Delta}^T\mathbf{q} - \mathbf{P}^* \right] = \mathbf{0}, \quad \mathbf{G}\mathbf{q} = \mathbf{0}. \quad (12)$$

It is convenient to express [Equation \(12\)](#) by the single matrix equation

$$\mathbf{K}\mathbf{Q} = \mathbf{F}, \quad (13)$$

where \mathbf{K} and \mathbf{F} represent the overall system stiffness matrix and the overall load vector, respectively. These matrices have the general expanded form

$$\mathbf{K} = \begin{bmatrix} \mathbf{K}_{qq} & -s_{q\Delta} & \mathbf{G}^T \\ -s_{q\Delta}^T & s_{\Delta\Delta} & \mathbf{0}^T \\ \mathbf{G} & \mathbf{0} & 0 \end{bmatrix}, \quad \mathbf{F} = \begin{bmatrix} \mathbf{F}^* \\ \mathbf{P}^* \\ 0 \end{bmatrix},$$

in which $\mathbf{K}_{qq} = \mathbf{k}_{qq} + \mathbf{S}_{qq}$, and $\mathbf{F}^* = \mathbf{f}^* + \mathbf{T}^*$. The vector of unknowns, \mathbf{Q} , that appears in [Equation \(13\)](#) is defined as $\mathbf{Q}^T = [\mathbf{q} \ \Delta \ \lambda]$. Solving for the vector of unknowns in [Equation \(13\)](#) yields all the information needed to obtain a complete variational solution to a specific problem. The accuracy of a solution depends on the number of terms included in the expressions for the local and global functions representing the displacement fields and converges to the corresponding exact solution as the number of terms increases.

6.1. Displacement-field representation. Representation of the mid-surface displacement field is a critical step in the variational solution to the problem. By relaxing the requirements for kinematic admissibility, the mid-surface displacement fields are represented in the present study by a combination of rigid-body modes, u_{Ri} , and global and local functions, denoted by \bar{u}_i and $\bar{\bar{u}}_i$, respectively, through $u_i = u_{Ri} + \bar{u}_i + \bar{\bar{u}}_i$, where the values of the index are given by $i = 1, 2, 3$. The explicit forms of the displacement fields can be found in [Appendix B](#). The rigid-body modes account for the overall or global translation and rotation of the shell, and are selected so that they produce neither membrane strain nor changes in shell curvature and twist. These terms are included for the completeness of the kinematics of the cylindrical shell. The presence of appropriate displacement boundary conditions inherently eliminates the rigid-body motion. However, for cases where an insufficient number of kinematic boundary conditions are imposed, these rigid-body terms need to be eliminated, as discussed in detail in [Appendix C](#). Following the complex variable solution techniques used in the theory of elasticity, the local functions are expressed in terms of robust, uniformly convergent Laurent series (used for doubly connected regions) to enhance capturing of steep stress gradients and deformations near the cutout. Complete sets of trigonometric expansions are used primarily to capture the overall global response of the shell.

Here, completeness means that all the fundamental waveforms needed to construct the typical overall deformations of a shell are included in the set.

For convenience, the displacement representations are rewritten in matrix form as

$$u_{i=1,2} = \mathbf{V}_{Ri}^T \boldsymbol{\alpha}_R + \bar{\mathbf{V}}_i^T \mathbf{c}_i + \bar{\bar{\mathbf{V}}}_i^T \boldsymbol{\alpha}, \quad u_3 = \mathbf{V}_{R3}^T \boldsymbol{\alpha}_R + \bar{\mathbf{V}}_3^T \mathbf{c}_3 + \bar{\bar{\mathbf{V}}}_3^T \boldsymbol{\beta}. \quad (14)$$

An even more useful, compact form is given by

$$u_i = \mathbf{V}_i^T \mathbf{q}, \quad (15)$$

where the vector of unknown displacement coefficients, \mathbf{q} , is defined by

$$\mathbf{q}^T = [\boldsymbol{\alpha}_R^T \ \mathbf{c}_1^T \ \mathbf{c}_2^T \ \mathbf{c}_3^T \ \boldsymbol{\alpha}^T \ \boldsymbol{\beta}^T]. \quad (16)$$

In Equation (16), the vector $\boldsymbol{\alpha}_R$ contains the unknown coefficients for the rigid-body motion of the shell, and the vectors $\boldsymbol{\alpha}$ and $\boldsymbol{\beta}$ contain the real and imaginary parts of the unknown coefficients α_{nm} and β_{nm} , respectively, that are associated with the local functions. The vectors \mathbf{c}_i , where $i = 1, 2, 3$, contain the real-valued unknown coefficients $c_{i(mm)}$ associated with the global functions. The explicit forms used herein for the unknown coefficient vectors $\boldsymbol{\alpha}_R$, \mathbf{c}_i , $\boldsymbol{\alpha}$, and $\boldsymbol{\beta}$ that appear in Equation (14) along with the vector functions \mathbf{V}_i (and the corresponding subvectors \mathbf{V}_{Ri} , $\bar{\mathbf{V}}_i$, and $\bar{\bar{\mathbf{V}}}_i$) are given in Appendix B.

In addition to the general representation of the shell surface-displacement fields, similar matrix expressions are needed for the displacements and rotations of points on the shell boundary. In the present study, the boundary displacement vector \mathbf{u}_Γ is introduced that consists of the mid-surface boundary displacements in the directions normal, tangent, and transverse to a shell edge, and the mid-surface rotations about axes that are normal and tangent to a shell edge. The boundary displacements in the directions normal, tangent, and transverse to a shell edge are denoted herein by u_n , u_s , and u_t , respectively. Similarly, the mid-surface rotations about axes that are tangent and normal to a shell edge are denoted by ϑ_n and ϑ_s , respectively. In terms of the vector of unknowns defined by Equation (16), the boundary displacements \mathbf{u}_Γ and rotations are expressed in matrix form by

$$\mathbf{u}_\Gamma = \mathbf{B}\mathbf{q}, \quad \mathbf{u}_\Gamma^T = [u_n \ u_s \ u_t \ \vartheta_n]. \quad (17)$$

The matrix \mathbf{B} with known coefficients is defined as $\mathbf{B}^T = [\mathbf{u}_n^T \ \mathbf{u}_s^T \ \mathbf{u}_t^T \ \boldsymbol{\theta}_n^T]$ in which the subvectors \mathbf{u}_n^T , \mathbf{u}_s^T , \mathbf{u}_t^T , and $\boldsymbol{\theta}_n^T$ are known and defined by

$$\mathbf{u}_n^T = (\mathbf{n} \cdot \mathbf{e}_1) \mathbf{V}_1, \quad \mathbf{u}_s^T = [(\mathbf{e}_3 \times \mathbf{n}) \cdot \mathbf{e}_2] \mathbf{V}_2, \quad \mathbf{u}_t^T = \mathbf{V}_3^T, \quad \boldsymbol{\theta}_n^T = (\mathbf{n} \cdot \mathbf{e}_1) \mathbf{V}_{3,1}^T.$$

6.2. Strain- and stress-resultant field representation. After defining the shell mid-surface displacement field in terms of the generalized coordinate \mathbf{q} , the corresponding representation of the strains is obtained by substituting Equation (15) into the strain-displacement relations given in vector form by Equation (6). This substitution yields $\boldsymbol{\varepsilon} = \mathbf{L}_\varepsilon \mathbf{q}$ and $\boldsymbol{\kappa} = \mathbf{L}_\kappa \mathbf{q}$, where the strain-coefficient matrices \mathbf{L}_ε and \mathbf{L}_κ are

$$\mathbf{L}_\varepsilon = \begin{bmatrix} \mathbf{V}_{1,1}^T \\ \mathbf{V}_{2,2}^T + \frac{1}{R} \mathbf{V}_3^T \\ \mathbf{V}_{1,2}^T + \mathbf{V}_{2,1}^T \end{bmatrix}, \quad \mathbf{L}_\kappa = \begin{bmatrix} -\mathbf{V}_{3,11}^T \\ -\mathbf{V}_{3,22}^T + \frac{1}{R} \mathbf{V}_{2,2}^T + \frac{R_{,2}}{R^2} \mathbf{V}_2^T \\ -2\mathbf{V}_{3,12}^T + \frac{2}{R} \mathbf{V}_{2,1}^T \end{bmatrix}.$$

Next, the representations for $\boldsymbol{\varepsilon}$ and $\boldsymbol{\kappa}$ are substituted into Equation (9) to obtain

$$\boldsymbol{e} = \boldsymbol{L}\boldsymbol{q}, \quad \boldsymbol{L}^T = [\boldsymbol{L}_\varepsilon^T \quad \boldsymbol{L}_\kappa^T], \quad (18)$$

where \boldsymbol{L} is the overall strain-coefficient matrix .

Finally, the corresponding matrix representation of the stress resultants in terms of the generalized coordinates is obtained by substituting Equation (18) into constitutive Equation (9). The resulting vector of stress resultants is given by

$$\boldsymbol{s} = \boldsymbol{C}\boldsymbol{L}\boldsymbol{q}. \quad (19)$$

6.3. Constraint equations. In the generalized coordinate representations for u_1 and u_2 , the coefficients $c_{1(00)}$ and $c_{2(00)}$ associated with the global functions \bar{u}_1 and \bar{u}_2 in Equation (B.2) also correspond to rigid-body translation in the s_1 direction and rigid-body rotation about the s_1 axis, respectively. These two redundant rigid-body modes are eliminated by introducing constraint conditions using Lagrange multipliers. In particular, the unknown Lagrange multipliers $\lambda_{RRB(1)}$ and $\lambda_{RRB(2)}$ are associated with the redundant rigid-body modes. Also, multivaluedness of the normal direction displacement $u_3(s_1, s_2)$ that arises from the presence of logarithmic terms in the Laurent series expansion for the local function must be eliminated. The unknown Lagrange multipliers $\lambda_{SV(r)}$ and $\lambda_{SV(s)}$ are used herein to eliminate this multivaluedness. Likewise, the rigid-body modes of the cylindrical shell must be eliminated by the Lagrange multipliers $\lambda_{RB(j)}$ for $j = 1, \dots, 6$ if the specified kinematic boundary conditions are not sufficient enough to prevent them. In other words, the nonvanishing rigid-body modes must be eliminated by introducing constraint conditions prior to the stress analysis to allow the overall system stiffness matrix \boldsymbol{K} , given in Equation (13), to be nonsingular.

These requirements on the representation of the shell displacement field are enforced by using constraint equations that use Lagrange multipliers. These constraint equations are functionally independent, forming a set of linearly independent equations equal in number to the total number of Lagrange multipliers. The Lagrange multipliers can be viewed as the reactions needed to enforce the corresponding constraints. In the present study, all of these constraint conditions are included in the matrix equation given in Equation (11). The explicit forms of the vector of unknown Lagrange multipliers $\boldsymbol{\lambda}$ containing $\lambda_{RRB(1)}$ and $\lambda_{RRB(2)}$, $\lambda_{SV(r)}$, $\lambda_{SV(s)}$ and $\lambda_{RB(j)}$, for $j = 1, \dots, 6$, and the known coefficient matrix, \boldsymbol{G} , in Equation (12) are given in Appendix C.

7. Overview of validation studies

A limited series of validation studies were conducted in the present study to determine the accuracy of results obtained using the analysis method presented herein. Specifically, the studies included circular and noncircular cylindrical shells with either a circular or an elliptical cutout under uniform tension. The stress resultants around the circular and elliptical cutout for varying aspect ratios and orientations in a circular cylinder, as well as the stress concentrations arising from a circular cutout in a noncircular cylindrical shell were computed. Comparisons of the stress-resultant distributions and magnitudes in the shells were made with corresponding results obtained using an in-house finite element program developed earlier by [Madenci and Barut 1994a]. This finite element program has been validated to a large extent against previously published experimental and numerical results for stress, buckling, and post-buckling of thin-shell structures [Madenci and Barut 1994b; 1994c]. Therefore, this finite element program is

expected to serve as a reliable indicator of the accuracy of the analysis methods and results presented herein. Overall, the comparisons indicate very good agreement (less than 1% difference) between the corresponding results produced by the two analysis methods. For shells with high aspect ratio cutouts, differences of approximately 5% were obtained and found to be the result of insufficient mesh refinement in the finite element models.

8. Selected numerical results

Selected numerical results are presented in this section to demonstrate the utility of the analysis method presented herein and the potential for its use in developing design technology. These results elucidate the effects of loading condition, noncircular cross-section geometry, variation in wall thickness, cutout shape, cutout size, and cutout orientation on the intensity of stress-resultant concentrations near a cutout. Specifically, tension, torsion, and pure-bending loads are considered for $[45^\circ/-45^\circ/90^\circ/0_2^\circ/90^\circ/-45^\circ/45^\circ]_s$ quasiisotropic shells with length $L = 356$ mm and made of graphite-epoxy plies. The nominal ply thickness is $t_{k0} = 0.14$ mm, resulting in the total thickness of the shell given by $h = 2.24$ mm. The ply orientation angles are measured with respect to the longitudinal shell axis. The Young's moduli of each ply in the longitudinal, fiber direction and in the direction transverse to the fibers are specified as $E_L = 135.0$ GPa and $E_T = 13.0$ GPa, respectively. The in-plane shear modulus and Poisson's ratio of each ply are given by $G_{LT} = 6.4$ GPa and $\nu_{LT} = 0.38$.

The effects of varying the radius of curvature R_0 on the stress-resultant concentration along the contour of a circular cutout with radius $a = 25.5$ mm are shown in [Figure 5](#) for a circular cylindrical shell subjected to a uniform axial tension load. Four curves that correspond to values of $R_0/L = 0.5, 0.75, 1.0,$ and 1.25 are presented that show the tangential stress resultant $N_{\phi\phi}$, normalized by the far-field applied uniform stress resultant N_0 , as a function of position around the cutout (indicated by the *cutout angle*, ϕ). As shown in [Figure 5](#), the stress-resultant concentration is a maximum at $\phi = 90^\circ$ and 270° (at the net section of the shell) for each case and reduces from a maximum value of approximately 4.0 to a minimum value of 3.4 at the net section as the radius of curvature increases. In addition, the results show that the $N_{\phi\phi}(a, 90^\circ)$ stress-resultant concentration approaches the well-known value of 3.0 for an isotropic plate as the shell radius increases. Away from the net section, changes in the radius of curvature have a relatively small effect on the stress-resultant concentration.

The effects of varying the circular cutout radius on the stress-resultant concentration along the contour of a circular cutout is shown in [Figure 6](#) for a circular cylindrical shell with radius $R_0 = 381$ mm and subjected to a uniform axial tension load. Five curves that correspond to values of the cutout radius $a = 15, 25.5, 30, 40,$ and 50 mm are presented that also show the tangential stress resultant $N_{\phi\phi}(a, \phi)$, normalized by the far-field applied uniform stress resultant N_0 , as a function of the cutout angle ϕ . The results in [Figure 6](#) show that the stress-resultant concentration is a maximum at the net section of the shell for each case, as expected, and changes significantly from a minimum value of approximately 3.1 to a maximum value of 5.1 at the net section as the cutout radius increases — an increase of approximately 65%. The results also show that the $N_{\phi\phi}(a, 90^\circ)$ stress-resultant concentration approaches the well-known value of 3.0 for an isotropic plate as the cutout radius decreases. Away from the net section, changes in the cutout radius have a much smaller effect on the stress-resultant concentration.

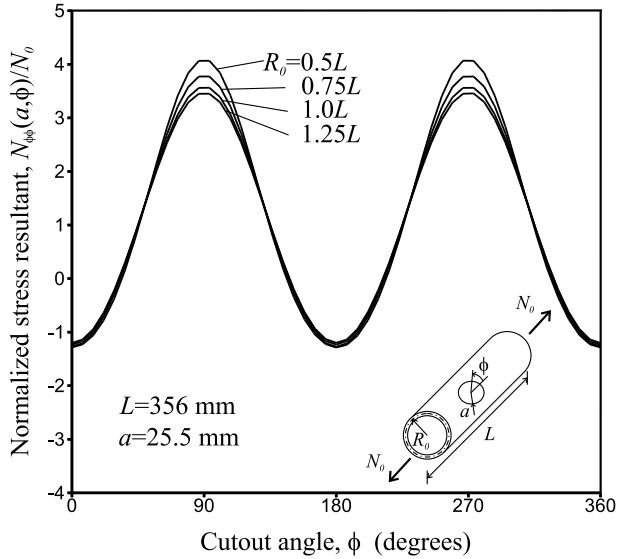


Figure 5. The effect of varying shell radius on the tangential stress resultants around a circular cutout in a quasiisotropic circular cylindrical shell subjected to a uniform tension load.

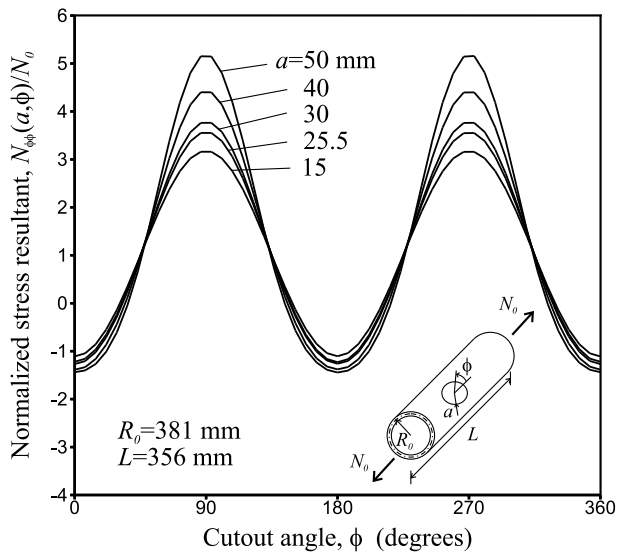


Figure 6. The effect of varying circular-cutout radius on the tangential stress resultants around a circular cutout in a quasiisotropic circular cylindrical shell subjected to a uniform tension load.

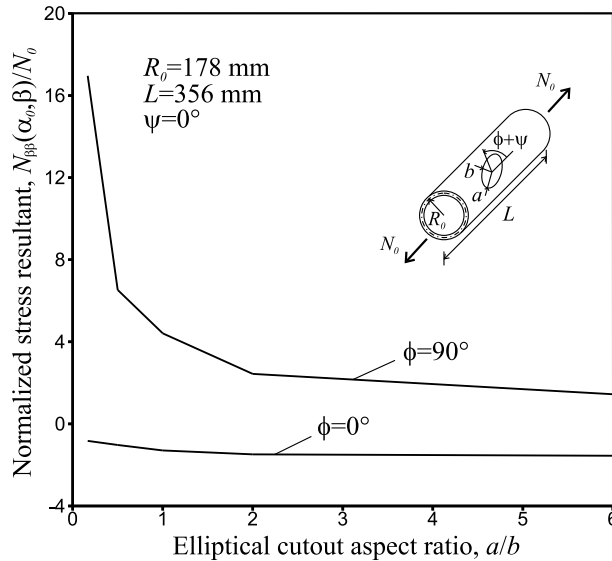


Figure 7. The effect of varying elliptical cutout aspect ratio on the tangential stress resultants around a cutout in a quasiisotropic cylindrical shell subjected to a uniform tension load.

The effect of varying the elliptical cutout aspect ratio a/b on the tangential stress-resultant distribution around the edge of a cutout in a cylindrical shell with radius $R_0 = 178$ mm and subjected to uniform tension is presented in Figure 7. The orientation of the elliptical cutout is specified by $\psi = 0^\circ$. Two curves that correspond to the locations $\phi = 0^\circ$ and 90° are presented that show the tangential stress resultant $N_{\beta\beta}(\alpha_0, \beta)$, normalized by the far-field applied uniform stress resultant N_0 , as a function of the cutout aspect ratio. As expected, the normalized stress-resultant concentration, $N_{\beta\beta}(\alpha_0, \beta)/N_0$, remains negative for all aspect ratios at $\phi = 0^\circ$, consistent with the expected Poisson effect, and the magnitudes are relatively insignificant at this location. In contrast, large stress-resultant concentrations are indicated at the net section ($\phi = 90^\circ$) that diminish from a maximum value of approximately 17.0 for a widthwise, slot-like cutout with $a = 5$ mm and $b = 30$ mm, or $a/b = 1/6$, to a minimum value of 1.4 for a lengthwise, slot-like cutout with $a = 30$ mm and $b = 5$ mm, or $a/b = 6$.

The effects of varying the orientation of a high aspect ratio, slot-like elliptical cutout on the stress-resultant concentration along the cutout contour is shown in Figure 8 for a circular cylindrical shell with radius $R_0 = 178$ mm and subjected to a uniform axial tension load. The major and minor axes of the cutout are given by $a = 30$ mm and $b = 5$ mm, respectively. The orientation of the elliptical cutout, with respect to the longitudinal shell axis, is measured by the angle ψ . Three curves that correspond to values of $\psi = 0^\circ$, 45° , and 90° are presented that show the tangential stress resultant at the cutout edge $N_{\beta\beta}$, normalized by the far-field applied uniform stress resultant N_0 , as a function of the cutout angle ϕ .

The results in Figure 8 show that the stress-resultant concentration is the least pronounced for the case of $\psi = 0^\circ$. For this case, the cutout major axis is aligned lengthwise with the shell axis and the

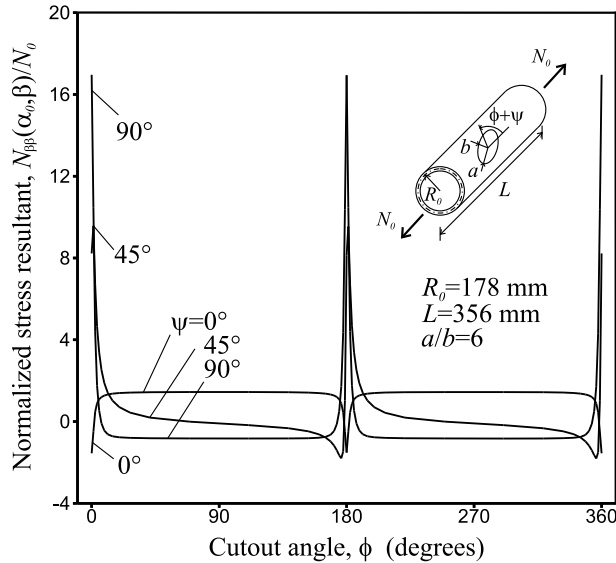


Figure 8. The effect of varying elliptical cutout orientation on the tangential stresses around the cutout in a quasiisotropic cylindrical shell subjected to a uniform tension load.

net section of the shell is the largest. The location on the cutout edge defined by $\phi = 0^\circ$ corresponds to where the edge of the cutout intersects the major axis. At this location, the edge of the cutout is in tangential compression ($N_{\beta\beta}/N_0 = -1.6$), consistent with a Poisson effect. The location defined by $\phi = 90^\circ$ corresponds to where the edge of the cutout intersects the minor axis, that is, at the net section of the shell. At this location, the edge of the cutout is in tangential tension ($N_{\beta\beta}/N_0 = 1.4$). Between approximately $\phi = 0^\circ$ and 170° and between $\phi = 190^\circ$ and 350° , the cutout width (and hence net section width) does not vary greatly. This attribute accounts for the corresponding flat regions in the $\psi = 0^\circ$ curve shown in Figure 8.

For the case of $\psi = 90^\circ$, the cutout major axis is perpendicular to the shell axis and the net section of the shell is the smallest. As before, the locations defined by $\phi = 0^\circ$ and 180° correspond to where the edge of the cutout intersects the major axis, that is, at the net section of the shell. The results in Figure 9 show that the edge of this high aspect ratio cutout has extremely high stress-resultant concentrations at these locations ($N_{\beta\beta}/N_0 = 17.0$) that have very steep gradients. Between approximately $\phi = 5^\circ$ and 175° and between $\phi = 185^\circ$ and 355° , the analysis predicts relatively benign variations in the stress-resultant concentration. The case of $\psi = 45^\circ$ exhibits stress-resultant concentrations that are, for the most part, bounded by the corresponding results for $\psi = 0^\circ$ and 90° . The analysis also predicts very high stress-resultant concentrations where the cutout edge intersects the major principal cutout axis ($N_{\beta\beta}/N_0 = 8.2$).

The effects of varying the cross-sectional eccentricity (2) of a tension loaded oval shell with a circular cutout are shown in Figure 9. The results in this figure correspond to the equivalent shell radius $R_0 = 381$ mm and a circular cutout radius given by $\alpha = 25.5$ mm. Moreover, the tangential stress-resultant concentration at the shell net section $N_{\phi\phi}(a, 90^\circ)$, normalized by the applied load N_0 , is shown as a function of the eccentricity parameter for the range of $-0.15 \leq \xi \leq 0.15$. As indicated in the figure,

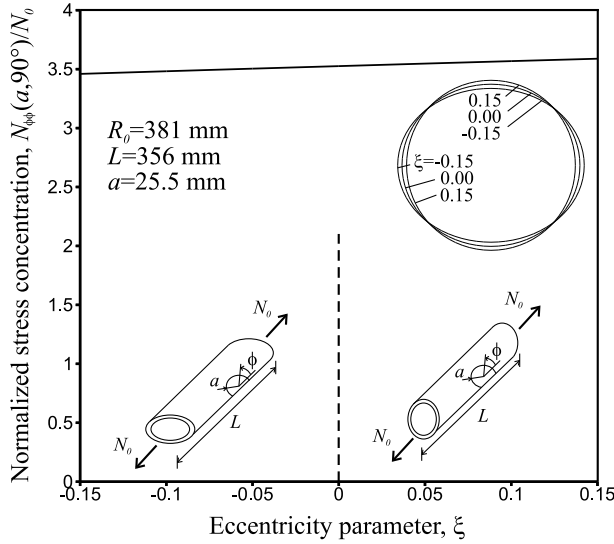


Figure 9. The effect of shell cross-sectional eccentricity on the stress-resultant concentration in an oval quasiisotropic cylindrical shell with a circular cutout and subjected to a uniform tension load.

negative and positive values of ξ correspond to cylindrical shells with the largest cross-sectional width, with parallel and perpendicular orientation, respectively. A value of $\xi = 0$ corresponds to a circular cross section and a value of $\xi = 0.15$ corresponds to a cross-sectional aspect ratio of 0.9.

The results presented in [Figure 9](#) show that the stress-resultant concentration is affected benignly by the cross-sectional eccentricity. In particular, the stress-resultant concentration increases almost linearly with increases in the eccentricity parameter from $N_{\phi\phi}(a, 90^\circ)/N_0 = 3.5$ to 3.6, which is slightly less than a 3% variation. This trend is understood by noting that the shells that correspond to negative values of ξ are flatter near the cutout than those that correspond to positive values of ξ and, as indicated by the results in [Figure 5](#), are expected to have the lower values for the stress-resultant concentrations.

The effects of longitudinal and circumferential periodic variations in wall thickness on the stress-resultant concentration at the net section of the circular cylindrical shell with radius $R_0 = 178$ mm, circular cutout radius $a = 25.5$ mm, and subjected to uniform axial tension load are shown in [Figure 10](#). Two monotonically increasing curves that correspond to values of ε_1 (with $\varepsilon_2 = 0$) and ε_2 (with $\varepsilon_1 = 0$) are presented that show the tangential stress resultant $N_{\phi\phi}(a, 90^\circ)$, normalized by the far-field applied uniform stress resultant N_0 , as a function of thickness-variation amplitudes (3) which range from 0 to 0.2. For the longitudinal thickness variation, the wave numbers used in [Equation \(3\)](#) are $m_1 = 1$ and $m_2 = 0$. Similarly, for the circumferential thickness variation, the wave numbers used in [Equation \(3\)](#) are $m_1 = 0$ and $m_2 = 1$.

The results shown in [Figure 10](#) indicate that the stress-resultant concentration at the shell net section increases as the magnitude of the thickness variation increases, for variations in either the longitudinal or circumferential direction. The maximum variation in the results is approximately 56%. Furthermore, the change in the stress-resultant concentration is slightly more pronounced for the circumferential thickness variation than for the longitudinal thickness variation. These increases are primarily due to a drastic loss

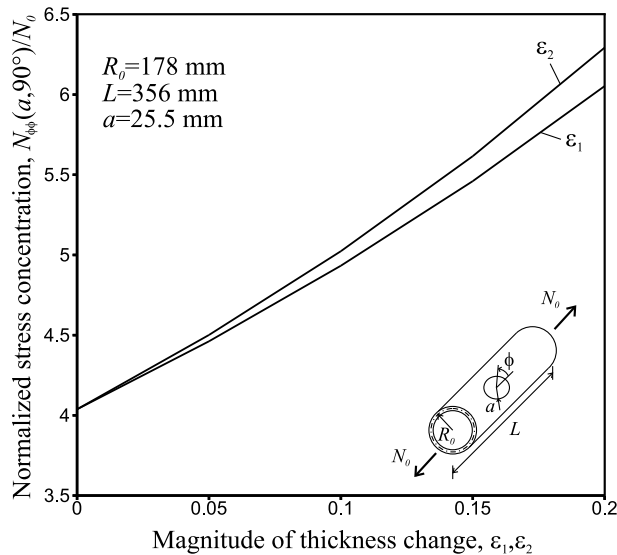


Figure 10. The effects of longitudinal ($\epsilon_1 \neq 0$ and $\epsilon_2 = 0$) and circumferential ($\epsilon_1 \neq 0$ and $\epsilon_2 = 0$) wall thickness variations on the tangential stress-resultant concentration around a circular cutout in a quasiisotropic circular cylindrical shell subjected to a uniform tension load.

of bending stiffness near the net section of the shell, as indicated by the wave numbers $m_1 = 0$ and $m_2 = 1$, where the thickness of the shell near the center of the cutout is smaller.

The effects of varying the radius of curvature R_0 on the stress-resultant concentration along the contour of a circular cutout with radius $a = 25.5$ mm is shown in Figures 11 and 12 for a circular cylindrical shell subjected to a uniform torsion load and a pure bending load, respectively. The pure-bending load corresponds to using $t_n^* = M_0 \cos(\pi/s_2)$ in Equation (4). Four curves that correspond to values of $R_0/L = 0.5, 0.75, 1.0,$ and 1.25 are presented that show the normalized values of the tangential stress resultant $N_{\phi\phi}$ as a function of position around the cutout. In Figure 11, $N_{\phi\phi}$ is normalized by the far-field applied uniform shear stress resultant, T_0 . In Figure 12, $N_{\phi\phi}$ is normalized by the far-field applied uniform bending stress resultant, M_0 .

The results in Figure 11 indicate that the stress-resultant concentration has identical maximum magnitudes at $\phi = 45^\circ, 135^\circ, 225^\circ,$ and 315° (at the net section of the shell) for each case, which corresponds to maximum diagonal tension and compression stress resultants associated with the shear stress resultants near the cutout. The magnitudes of the stress-resultant concentration for these four locations reduce from a maximum value of 6.8 to a minimum value of 5.1 as the radius of curvature increases (33% variation). Away from these four locations, changes in the radius of curvature have a smaller effect on the stress-resultant concentration. The results in Figure 12 indicate that the stress-resultant concentration for the shell subjected to the pure bending load is quite similar to that presented in Figure 5 for the corresponding tension loaded shell.

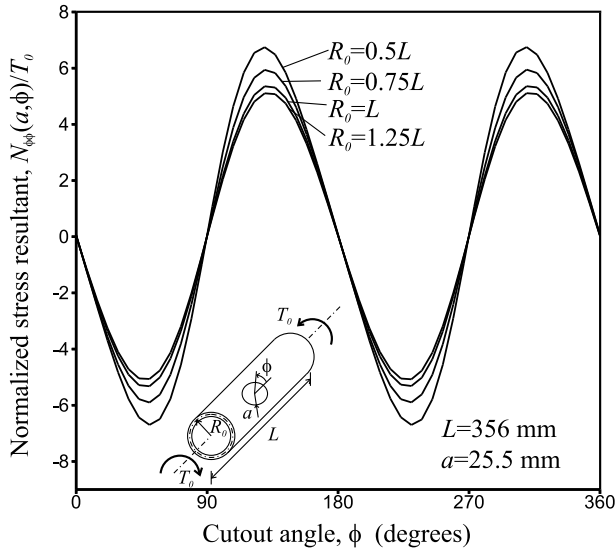


Figure 11. The effect of varying shell radius on the tangential stresses around a circular cutout in a quasiisotropic circular cylindrical shell subjected to a uniform torsion load.

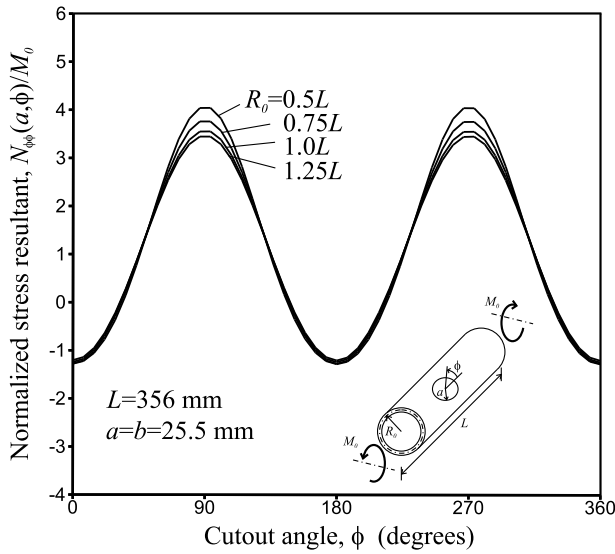


Figure 12. The effect of varying shell radius on the tangential stresses around a circular cutout in a quasiisotropic circular cylindrical shell subjected to a pure-bending load.

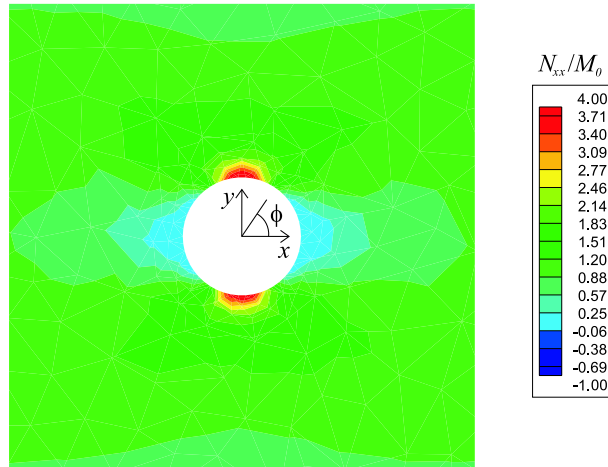


Figure 13. Stress resultant distribution near the cutout in a quasiisotropic circular cylindrical shell subjected to a pure-bending load.

Specifically, the stress-resultant concentration is a maximum at $\phi = 90^\circ$ and 270° (at the net section of the shell) for each case and reduces from a maximum value of 4.0 to a minimum value of 3.5 at the net section as the radius of curvature increases (14% variation). In addition, $N_{\phi\phi}/M_0$ approaches the well-known value of three for an isotropic plate as the shell radius increases, and away from the net section, changes in the radius of curvature have a relatively small effect on the stress-resultant concentration. A contour plot of $N_{\phi\phi}/M_0$ near the cutout is shown in Figure 13 for the case of $R_0/L = 0.5$ shown in Figure 12. The extent of the stress concentration at the shell net section ($\phi = 90^\circ$ and 270°) is clearly captured by the analysis method presented herein. The highest stress-resultant concentration is $N_{\phi\phi}(a, 90^\circ)/M_0 = 4$, and it attenuates to the value of 1.01 at a radius of about 80 mm (approximately three times the cutout radius), measured from the center of the cutout.

9. Concluding remarks

A special-purpose, semianalytical approach based on complex potential functions has been presented that can be used to efficiently and parametrically investigate the behavior of thin, noncircular cross-section cylindrical shells made of laminated-composite materials and with a cutout. In particular, the effects of radius of curvature; elliptical cutout size, aspect ratio, and orientation; oval cross-section eccentricity; wall-thickness variations; and loading conditions on the stress-resultant concentration near the cutout have been presented for a quasiisotropic shell subjected to uniform tension, uniform torsion, and pure bending. In addition, studies that were conducted to validate the analysis method have been described.

A key finding of the results obtained with this analysis method is that the maximum tangential stress-resultant concentration near a circular cutout in a tension loaded, circular, quasiisotropic shell increases by approximately 18% as the shell radius-to-length ratio decreases from 1.25 to 0.5. Likewise, increases in the maximum tangential stress-resultant concentration as large as 65% have been found to occur with a five-fold increase in cutout radius. Results have also been presented showing that extremely high

tangential stress-resultant concentrations can occur for high aspect ratio elliptical cutouts whose principal axes are not aligned with the longitudinal axis of a tension loaded shell.

Additionally, results have been presented showing that tension loaded oval shells with a circular cutout on one of the flatter sides exhibit slightly lower tangential stress-resultant concentrations than the corresponding shell with the cutout on one of the more highly curved sides. Results have also been presented that show that variations in wall thickness in either the longitudinal or circumferential direction significantly affect the stress concentration, with respect to that for the corresponding shell with a nominal thickness. The analysis also predicts that a quasiisotropic shell with a circular cutout and subjected to pure bending that yields the maximum tensile stress resultant at the longitudinal axis of the cutout behaves similarly to the corresponding tension loaded shell. The corresponding shell subjected to torsion was found to exhibit the maximum tangential stress-resultant concentrations at locations consistent with the maximum diagonal tension and compression near the cutout. Overall, the results demonstrate that the analysis approach is a powerful means for developing design criteria for laminated composite shells.

Appendix A

Strain energy of the shell. Based on classical laminated shell theory, the strain energy of the shell can be expressed as

$$U = \frac{1}{2} \int_A \mathbf{s}^T \mathbf{e} dA,$$

where A is the planform area of the shell mid-surface. Substituting the expressions for the resultant stress and strains, given in terms of the vector of unknown displacement coefficients, \mathbf{q} , by Equations (18) and (19), leads to

$$U(\mathbf{q}) = \frac{1}{2} \int_A \mathbf{q}^T (\mathbf{L}^T \mathbf{C} \mathbf{L}) \mathbf{q} dA.$$

The matrix \mathbf{L} involves the derivatives of the assumed functional displacement representations, and \mathbf{C} is the overall constitutive matrix defined by Equation (10). The expression for the strain energy is rewritten into the final form used herein as

$$U(\mathbf{q}) = \frac{1}{2} \mathbf{q}^T \mathbf{k}_{qq} \mathbf{q}, \quad \mathbf{k}_{qq} = \int_A (\mathbf{L}^T \mathbf{C} \mathbf{L}) dA.$$

The evaluation of this area integral is performed numerically by employing basic quadrature techniques. In this analysis, the quadrature points are predetermined by employing standard triangulation of the entire domain as described by [Shewchuk 1996].

Strain energy of elastic restraints. The strain energy of the elastic edge restraints (springs), Ω , is expressed as

$$\Omega = \sum_{\ell=1}^2 \left[\frac{1}{2} \sum_{\alpha=n,s,t} \int_{\Gamma(\ell)} S_{\alpha} (u_{\alpha} - u_{\alpha}^*)^2 d\Gamma + \frac{1}{2} \sum_{\alpha=n,s} \int_{\Gamma(\ell)} J_{\alpha} (\vartheta_{\alpha} - \vartheta_{\alpha}^*)^2 d\Gamma + \frac{1}{2} \sum_{\alpha=n,s} \int_{\Gamma(\ell)} s_{\alpha} (u_{\alpha} - \Delta_{\alpha})^2 d\Gamma \right]. \quad (\text{A.1})$$

As depicted in Figure 4, the boundary displacements u_n , u_s , and u_t along the ℓ^{th} boundary segment are restrained by extensional springs with the stiffness values S_n , S_s , and S_t , respectively. Likewise, the

boundary rotations ϑ_n and ϑ_s are restrained by rotational springs with the stiffness values J_n and J_s , respectively.

To apply concentrated forces along the edge of a shell and introduce edge displacements similar to those introduced by a rigid end ring or by the loading platens of a testing machine, additional springs are used to simulate the load introduction effects of a rigid end ring. In particular, rigid end ring loads are introduced into the shell using extensional springs in the directions normal and tangent to the boundary with corresponding stiffness values of s_n and s_s , as shown in [Figure 3](#). By specifying relatively large values for the spring stiffnesses s_n and s_s , the laminate edge behaves as if a rigid end ring is attached that produces the uniform displacements Δ_n and Δ_s . In contrast, a relatively small spring stiffness between the shell edge and the rigid end ring eliminates the presence of a rigid end ring.

The desired form of the elastic-restraint strain energy is obtained in terms of the unknown vector \mathbf{q} by substituting expressions for the boundary displacements and rotations, given collectively by [Equation \(17\)](#), into [Equation \(A.1\)](#). This step yields

$$\Omega = \sum_{\ell=1}^2 \left[\frac{1}{2} \sum_{\alpha=n,s,t} (\mathbf{q}^T \mathbf{S}_{\alpha\alpha}^{(\ell)} \mathbf{q} + \Omega_{u(\alpha)}^{(\ell)*} - 2\mathbf{q}^T \mathbf{f}_{\alpha}^{(\ell)*}) + \frac{1}{2} \sum_{\alpha=n,s} (\mathbf{q}^T \mathbf{J}_{\alpha\alpha}^{(\ell)} \mathbf{q} + \Omega_{\vartheta(\alpha)}^{(\ell)*} - 2\mathbf{q}^T \mathbf{r}_{\alpha}^{(\ell)*}) + \frac{1}{2} \sum_{\alpha=n,s} \left(\mathbf{q}^T \mathbf{s}_{\alpha\alpha}^{(\ell)} \mathbf{q} + \int_{\Gamma(\ell)} s_{\alpha} \Delta_{\alpha}^2 d\Gamma - 2\mathbf{q}^T \mathbf{s}_{\alpha}^{(\ell)} \Delta_{\alpha} \right) \right],$$

where the matrices $\mathbf{S}_{\alpha\alpha}^{(\ell)}$ and $\mathbf{J}_{\alpha\alpha}^{(\ell)}$ represent the stiffness contribution of the extensional and rotational springs attached to the ℓ^{th} segment of the boundary. These matrices are defined as

$$\mathbf{S}_{\alpha\alpha}^{(\ell)} = \int_{\Gamma(\ell)} S_{\alpha} \mathbf{u}_{\alpha} \mathbf{u}_{\alpha}^T d\Gamma, \quad \mathbf{J}_{\beta\beta}^{(\ell)} = \int_{\Gamma(\ell)} J_{\beta} \boldsymbol{\theta}_{\beta} \boldsymbol{\theta}_{\beta}^T d\Gamma, \quad (\alpha = n, s, t; \beta = n, s).$$

The matrix $\mathbf{s}_{\alpha\alpha}^{(\ell)}$, representing the stiffness of the springs attached to the rigid end ring, is defined as

$$\mathbf{s}_{\alpha\alpha}^{(\ell)} = \int_{\Gamma(\ell)} s_{\alpha} \mathbf{u}_{\alpha} \mathbf{u}_{\alpha}^T d\Gamma, \quad (\alpha = n, s).$$

The load vectors $\mathbf{f}_{\alpha}^{(\ell)*}$ and $\mathbf{r}_{\alpha}^{(\ell)*}$ are associated with the prescribed boundary displacements and rotations

$$\mathbf{f}_{\alpha}^{(\ell)*} = \int_{\Gamma(\ell)} S_{\alpha} u_{\alpha}^* \mathbf{u}_{\alpha} d\Gamma, \quad \mathbf{r}_{\beta}^{(\ell)*} = \int_{\Gamma(\ell)} J_{\beta} \vartheta_{\beta}^* \boldsymbol{\theta}_{\beta} d\Gamma, \quad (\alpha = n, s, t; \beta = n, s).$$

The vector $\mathbf{s}_{\alpha}^{(\ell)}$ is associated with the unknown end displacements that correspond to a given concentrated load, and is defined as

$$\mathbf{s}_{\alpha}^{(\ell)} = \int_{\Gamma(\ell)} s_{\alpha} \mathbf{u}_{\alpha} d\Gamma, \quad (\alpha = n, s).$$

The strain energies in the springs that arise from the known prescribed displacements (u_n^* , u_s^* , u_t^*) and rotations (ϑ_n^* , ϑ_s^*) are defined as

$$\Omega_{u(\alpha)}^{(\ell)*} = \int_{\Gamma(\ell)} S_{\alpha} u_{\alpha}^{*2} d\Gamma, \quad \Omega_{\vartheta(\beta)}^{(\ell)*} = \int_{\Gamma(\ell)} J_{\beta} \vartheta_{\beta}^{*2} d\Gamma, \quad (\alpha = n, s, t; \beta = n, s).$$

For convenience, the expression for the strain energy in the springs is recast in matrix form as

$$\Omega(\mathbf{q}, \Delta) = \frac{1}{2} \mathbf{q}^T \mathbf{S}_{qq} \mathbf{q} + \frac{1}{2} \Delta^T \mathbf{s}_{\Delta\Delta} \Delta - \mathbf{q}^T \mathbf{s}_{q\Delta} \Delta - \mathbf{q}^T \mathbf{f}^* + \Omega^*,$$

in which the matrices \mathbf{S}_{qq} , $\mathbf{s}_{\Delta\Delta}$, and $\mathbf{s}_{q\Delta}$ represent the stiffness of the springs associated with the deformation of the laminate, the end displacements, and their coupling, respectively. They are

$$\begin{aligned} \mathbf{S}_{qq} &= \sum_{\ell=1}^2 \sum_{\alpha=n,s,t} \mathbf{S}_{\alpha\alpha}^{(\ell)} + \sum_{\ell=1}^2 \sum_{\alpha=n,s} \mathbf{J}_{\alpha\alpha}^{(\ell)} + \sum_{\ell=1}^2 \sum_{\alpha=n,s} \mathbf{s}_{\alpha\alpha}^{(\ell)}, \\ \mathbf{s}_{\Delta\Delta} &= \text{Diag}[s_n^{(1)}, s_n^{(2)}, s_s^{(1)}, s_s^{(2)}] \times 2\pi R_0, \\ \mathbf{s}_{q\Delta} &= \begin{bmatrix} \mathbf{s}_n^{(1)} & \mathbf{s}_n^{(2)} & \mathbf{s}_s^{(1)} & \mathbf{s}_s^{(2)} \end{bmatrix}. \end{aligned}$$

The vector of unknown end displacements Δ is defined by $\Delta^T = [\Delta_n^{(1)} \ \Delta_n^{(2)} \ \Delta_s^{(1)} \ \Delta_s^{(2)}]$. The load vector arising from all prescribed boundary displacements and rotations \mathbf{f}^* , and the strain energy of all the springs due to prescribed displacements and rotations are defined as

$$\mathbf{f}^* = \frac{1}{2} \sum_{\ell=1}^2 \sum_{\alpha=n,s,t} \mathbf{f}_{\alpha}^{*(\ell)} + \frac{1}{2} \sum_{\ell=1}^2 \sum_{\alpha=n,s} \mathbf{r}_{\alpha}^{*(\ell)}, \quad \Omega^* = \frac{1}{2} \sum_{\ell=1}^2 \sum_{\alpha=n,s,t} \Omega_{u(\alpha)}^{(\ell)*} + \frac{1}{2} \sum_{\ell=1}^2 \sum_{\alpha=n,s} \Omega_{\vartheta(\alpha)}^{(\ell)*}.$$

Potential of external loads. The potential energy of the external tractions (t_n^* , t_s^* , t_t^*) and moments (m_n^* , m_s^*) acting along the ℓ^{th} boundary segment, and the concentrated loads (P_n^* , P_s^*) acting on the rigid end rings, is given in terms of the corresponding boundary displacements and rotations by

$$V = - \sum_{\ell=1}^2 \sum_{\alpha=n,s,t} \int_{\Gamma(\ell)} t_{\alpha}^* u_{\alpha} d\Gamma - \sum_{\ell=1}^2 \sum_{\alpha=n,s} \int_{\Gamma(\ell)} m_{\alpha}^* \theta_{\alpha} d\Gamma - \sum_{\ell=1}^2 \sum_{\alpha=n,s} P_{\alpha}^* \Delta_{\alpha}.$$

Substituting the expressions for the boundary displacements and rotations, given in terms of the vector \mathbf{q} , and combining terms yields $V(\mathbf{q}, \Delta) = -\mathbf{q}^T \mathbf{T}^* - \Delta^T \mathbf{P}^*$, where the vector Δ , containing the uniform end-displacements Δ_n and Δ_s of the ℓ^{th} boundary segment, is defined by $\Delta^T = [\Delta_n^{(1)} \ \Delta_n^{(2)} \ \Delta_s^{(1)} \ \Delta_s^{(2)}]$. The load vectors \mathbf{T}^* and \mathbf{P}^* are defined by

$$\mathbf{T}^{*T} = \sum_{\ell=1}^2 \sum_{\alpha=n,s,t} \int_{\Gamma(\ell)} t_{\alpha}^* \mathbf{u}_{\alpha}^T d\Gamma + \sum_{\ell=1}^2 \sum_{\alpha=n,s} \int_{\Gamma(\ell)} \theta_{\alpha}^* \boldsymbol{\theta}_{\alpha}^T d\Gamma, \quad \mathbf{P}^{*T} = \begin{bmatrix} P_n^{*(1)} & P_n^{*(2)} & P_s^{*(1)} & P_s^{*(2)} \end{bmatrix},$$

in which $P_{\alpha}^{*(\ell)}$, with $\alpha = n, s$, represents the membrane forces applied on the ℓ^{th} boundary segment through a rigid end ring.

Appendix B

Rigid-body modes. Following [Madenci and Barut 2003], the rigid-body displacements (u_{R1} , u_{R2} , u_{R3}) of a cylindrical shell, defined with respect to the curvilinear coordinates, (s_1 , s_2 , s_3), are

$$\begin{aligned} u_{R1} &= \alpha_1 - \alpha_6 y + \alpha_5 z, \\ u_{R2} &= \alpha_2 \cos \theta - \alpha_3 \sin \theta - \alpha_4 (y \sin \theta + z \cos \theta) + \alpha_5 x \sin \theta + \alpha_6 x \cos \theta, \\ u_{R3} &= \alpha_2 \sin \theta + \alpha_3 \cos \theta + \alpha_4 (y \cos \theta - z \sin \theta) - \alpha_5 x \cos \theta + \alpha_6 x \sin \theta, \end{aligned} \quad (\text{B.1})$$

where θ denotes the angle between the radius of curvature at a point on the shell surface and z -axis as shown in Figure 1.

Global functions. The global functions \bar{u}_i , that are used to capture the overall deformations away from the cutout are expressed in terms of a series expansion of orthogonal functions of the form

$$\bar{u}_i(s_1, s_2) = \sum_{m=0}^M \sum_{n=0}^m c_{i(mn)} T_m(s_1) W_n(s_2). \quad (\text{B.2})$$

The symbols $c_{i(mn)}$ are the unknown real-valued coefficients, and $T_m(s_1)$ and $W_n(s_2)$ are defined as

$$T_m(s_1) = \begin{cases} 1, & m = 0, \\ \zeta, & m = 1, \\ \sin\left[\frac{(m-1)}{2}(\zeta + 1)\right], & m > 1, \end{cases} \quad W_n(s_2(\theta)) = \begin{cases} \cos \frac{n\theta}{2}, & n \text{ even}, \\ \sin \frac{(n+1)\theta}{2}, & n \text{ odd}, \end{cases} \quad (\text{B.3})$$

in which $-1 \leq \zeta \leq 1$ and s_1 is related to ζ as $s_1 = \zeta L/2$, with L being the length of the cylinder. Note that W_n is periodical. These particular functions were chosen because they form a complete set of functions when used with Equation (B.2). Hence, they are desirable for employing in energy based semianalytic solution techniques such as the total potential energy principle that is used in this study.

Local functions. The local functions are expressed in terms of mapping functions that transform the contour of an elliptical cutout to a unit circle. These mapping functions are used to permit the use of Laurent series expansions as local functions, which is desirable because Laurent series are analytic and uniformly convergent in domains with a circular hole. As a result, the use of mapping functions significantly reduces the number of terms in the Laurent series that are needed to adequately capture steep stress and strain gradients and local deformations near a cutout. In accordance with the principle of minimum potential energy, the local functions are not required to satisfy the traction boundary conditions at the cutout boundary. Thus, the local functions $\bar{\bar{u}}_i$ are expressed in the form of Laurent series in terms

of complex functions, as

$$\bar{u}_{i=1,2} = 2 \operatorname{Re} \left[\sum_{m=1}^2 u_m^{(i=1,2)} \sum_{\substack{n=-N \\ n \neq 0}}^N \alpha_{nm} \Phi_{nm}^*(z_{\varepsilon m}) \right] H(\rho), \tag{B.4}$$

$$\bar{u}_3 = 2 \operatorname{Re} \left[\sum_{m=1}^2 \sum_{\substack{n=-N \\ n \neq 0}}^N \beta_{nm} F_{nm}^*(z_{\varepsilon m}) \right] H(\rho), \tag{B.5}$$

with $\rho = (x_1^2 + x_2^2)^{1/2}$, where the parameter N defines the extent of the complex series. In these series, α_{nm} and β_{nm} are the unknown complex coefficients that appear in Equations (14)–(16). The auxiliary function $H(\rho)$ that defines the domain of influence of the local functions is expressed as a polynomial

$$H(\rho) = \begin{cases} 1 - 10\left(\frac{\rho}{\rho_o}\right)^3 + 15\left(\frac{\rho}{\rho_o}\right)^4 - 6\left(\frac{\rho}{\rho_o}\right)^5, & 0 \leq \rho \leq \rho_o, \\ 0, & \rho > \rho_o, \end{cases}$$

such that $H(\rho_o) = H'(\rho_o) = H''(\rho_o) = 0$, where prime marks denote differentiation with respect to the variable ρ , and the parameter ρ_o denotes the radius of the region in which the local functions are effective. The purpose of choosing the auxiliary function is to prevent any possible linear dependency between the local and global functions and to restrict the influence of the local functions to a limited domain around the cutout.

The complex functions $u_m^{(1)}(z_{\varepsilon m})$ and $u_m^{(2)}(z_{\varepsilon m})$ that appear in Equation (B.4) are defined as

$$u_m^{(1)}(z_{\varepsilon m}) = \cos \psi p_m(z_{\varepsilon m}) - \sin \psi q_m(z_{\varepsilon m}), \quad u_m^{(2)}(z_{\varepsilon m}) = \sin \psi p_m(z_{\varepsilon m}) + \cos \psi q_m(z_{\varepsilon m}), \tag{B.6}$$

where the complex constants p_m and q_m are given by

$$p_m = a_{11}\mu_{\varepsilon m}^2 + a_{12} - a_{16}\mu_{\varepsilon m}, \quad q_m = a_{12}\mu_{\varepsilon m} + a_{22}/\mu_{\varepsilon m} - a_{26}.$$

In Equation (B.6), the unknown complex constants $\mu_{\varepsilon m}$ are the roots of the characteristic equation associated with membrane deformation, that is,

$$a_{11}\mu_{\varepsilon m}^4 - 2a_{16}\mu_{\varepsilon m}^3 + (2a_{26} + a_{66})\mu_{\varepsilon m}^2 - 2a_{26}\mu_{\varepsilon m} + a_{22} = 0, \tag{B.7}$$

in which the coefficients a_{ij} are the coefficients of the flexibility matrix \mathbf{a} , which is the inverse of the stiffness matrix \mathbf{A} defined by Equation (7). Both the flexibility and the stiffness matrices, \mathbf{a} and \mathbf{A} , are measured with respect to the local coordinate system (x_1, x_2) . The angle ψ represents the orientation of the local coordinate system with respect to the global coordinate system, (s_1, s_2) .

The complex potential function $\Phi_{nm}^*(z_{\varepsilon m})$, appearing in Equation (B.4) is defined as $\Phi_{nm}^*(z_{\varepsilon m}) = \xi_{\varepsilon m}^n$, in which the mapping functions $\xi_{\varepsilon m}$ map a cutout onto a unit circle. The mapping functions for an elliptical cutout, introduced by [Lekhnitskii 1968], are given by

$$\xi_{\varepsilon m} = \frac{z_{\varepsilon m} \pm \sqrt{z_{\varepsilon m}^2 - a^2 - \mu_{\varepsilon m}^2 b^2}}{a - i\mu_{\varepsilon m}^2 b}, \quad m = 1, 2, \tag{B.8}$$

where $z_{\varepsilon m} = x_1 + \mu_{\varepsilon m}x_2$, a and b are the major and minor axes of the elliptical cutout, and $i = \sqrt{-1}$. The sign of the square root term is chosen so that $|\xi_{\varepsilon m}| \geq 1$ (that is, the mapped point is guaranteed to be on or outside the unit circle).

Inverting the mapping function provides $\omega_{\varepsilon m}(\xi_{\varepsilon m})$ as

$$\begin{aligned} z_{\varepsilon m} &= \omega_{\varepsilon m}(\xi_{\varepsilon m}) = r_{\varepsilon m}\xi_{\varepsilon m} - \frac{s_{\varepsilon m}}{\xi_{\varepsilon m}}, \\ r_{\varepsilon m} &= \frac{1}{2}(a - i\mu_{\varepsilon m}b), \\ s_{\varepsilon m} &= \frac{1}{2}(a + i\mu_{\varepsilon m}b). \end{aligned} \quad (\text{B.9})$$

The unknown complex constants $\mu_{\varepsilon 1}$ and $\mu_{\varepsilon 2}$, and their complex conjugates, that is, $\mu_{\varepsilon 3} = \bar{\mu}_{\varepsilon 1}$ and $\mu_{\varepsilon 4} = \bar{\mu}_{\varepsilon 2}$, are the roots obtained from the characteristic equation associated with membrane deformation. The complex potential functions, $F_{nm}^*(z_{\kappa m})$ in Equation (B.5) are defined as

$$F_{nm}^*(z_{\kappa m}) = \begin{cases} \frac{r_{\kappa m}}{n+1}\xi_{\kappa m}^n - \frac{s_{\kappa m}}{n-1}\xi_{\kappa m}^{n-2}, & |n| > 1, \\ \frac{r_{\kappa m}}{2}\xi_{\kappa m}^2 - s_{\kappa m} \ln \xi_{\kappa m}, & n = 1, \\ r_{\kappa m} \ln \xi_{\kappa m} + \frac{s_{\kappa m}}{2}\xi_{\kappa m}^{-2}, & n = -1, \end{cases} \quad (\text{B.10})$$

in which the expressions for the mapping function $\xi_{\kappa m}$ and the constants $r_{\kappa m}$ and $s_{\kappa m}$ have the same form as the corresponding expressions for $\xi_{\varepsilon m}$, $r_{\varepsilon m}$, and $s_{\varepsilon m}$ given by Equations (B.8) and (B.9), except that the subscript ε is replaced by κ . The complex variables $z_{\kappa m}$ are defined by $z_{\kappa m} = x_1 + \mu_{\kappa m}x_2$, in which the unknown complex constants $\mu_{\kappa 1}$ and $\mu_{\kappa 2}$ and their conjugates, that is, $\mu_{\kappa 3} = \bar{\mu}_{\kappa 1}$ and $\mu_{\kappa 4} = \bar{\mu}_{\kappa 2}$, are the roots obtained from the characteristic equation associated with the bending equilibrium equation

$$D_{22}\mu_{\kappa m}^4 + 4D_{26}\mu_{\kappa m}^3 + (2D_{12} + 4D_{66})\mu_{\kappa m}^2 + 4D_{16}\mu_{\kappa m} + D_{11} = 0, \quad (\text{B.11})$$

where D_{ij} are the components of the bending stiffness matrix \mathbf{D} (Equation (7)), which is defined with respect to the local coordinate system, (x_1, x_2) .

It is important to note that the local functions in Equations (B.4) and (B.5) satisfy the in-plane and bending equilibrium equations of a homogeneous, flat laminate of uniform thickness, not a cylindrical shell. Therefore, the roots of the characteristic equations, Equations (B.7) and (B.11), serve as approximations of their exact values, which are not mathematically tractable. Because the solution procedure is based on the principle of minimum potential, their exact values are not necessarily required. However, they capture the stress concentration and local deformation near the cutout in cylindrical shells because these functions possess the inherent solution characteristics. They satisfy the equilibrium equations exactly as the radius of curvature approaches infinity and are uniformly convergent in a doubly connected region.

In the displacement representations defined by Equation (14), the vectors, α_R , c_i , α , β are defined as

$$\begin{aligned}\alpha_R^T &= [\alpha_{R1} \quad \alpha_{R2} \quad \alpha_{R3} \quad \alpha_{R4} \quad \alpha_{R5} \quad \alpha_{R6}], \\ c_i^T &= [c_{i(00)} \quad c_{i(10)} \quad c_{i(01)} \quad \dots \quad c_{i(M0)} \quad c_{i((M-1)1)} \quad \dots \quad c_{i(1(M-1))} \quad c_{i(0M)}], \\ \alpha^T &= [\alpha_{-N}^T \quad \alpha_{-N+1}^T \quad \dots \quad \alpha_{-1}^T \quad \alpha_1^T \quad \dots \quad \alpha_{N-1}^T \quad \alpha_N^T], \\ \beta^T &= [\beta_{-N}^T \quad \beta_{-N+1}^T \quad \dots \quad \beta_{-1}^T \quad \beta_1^T \quad \dots \quad \beta_{N-1}^T \quad \beta_N^T],\end{aligned}$$

in which $\gamma_n^T = [\gamma_{n1}^T \quad \gamma_{n2}^T]$, with $\gamma_{nj}^T = [\text{Re}(\gamma_{nj}), \text{Im}(\gamma_{nj})]$ for $\gamma = \alpha, \beta$.

The vector functions, $V_{i=1,2,3}$ associated with the unknown generalized coordinates q appearing in Equation (15) are defined as

$$\begin{aligned}V_1^T &= [V_{R1}^T \quad \bar{V}_1^T \quad \bar{\mathbf{0}}^T \quad \bar{\mathbf{0}}^T \quad \bar{\bar{V}}_1^T \quad \bar{\bar{\mathbf{0}}}^T], \\ V_2^T &= [V_{R2}^T \quad \bar{\mathbf{0}}^T \quad \bar{V}_2^T \quad \bar{\mathbf{0}}^T \quad \bar{\bar{V}}_2^T \quad \bar{\bar{\mathbf{0}}}^T], \\ V_3^T &= [V_{R3}^T \quad \bar{\mathbf{0}}^T \quad \bar{\mathbf{0}}^T \quad \bar{V}_3^T \quad \bar{\mathbf{0}}^T \quad \bar{\bar{V}}_3^T],\end{aligned}$$

where $\bar{\mathbf{0}}^T = [0 \dots 0]$ of order $[(M+1)(M+2)/2]$ and $\bar{\bar{\mathbf{0}}}^T = [0 \dots 0]$ of order $8N$. The vectors associated with rigid-body motion are

$$\begin{aligned}V_{R1}^T &= [1 \quad 0 \quad 0 \quad 0 \quad z \quad -y], \\ V_{R2}^T &= \left[0 \quad \frac{dy}{ds_2} \quad \frac{dz}{ds_2} \quad \left(y \frac{dz}{ds_2} - z \frac{dy}{ds_2} \right) \quad -x \frac{dz}{ds_2} \quad -x \frac{dy}{ds_2} \right], \\ V_{R3}^T &= \left[0 \quad -\frac{dz}{ds_2} \quad \frac{dy}{ds_2} \quad \left(y \frac{dy}{ds_2} + z \frac{dz}{ds_2} \right) \quad -x \frac{dy}{ds_2} \quad -x \frac{dz}{ds_2} \right].\end{aligned}$$

Similarly, the vectors associated with the global functions are

$$\bar{V}_i^T = [T_0 W_0 \quad T_1 W_0 \quad T_0 W_1 \quad T_2 W_0 \quad T_1 W_1 \quad T_0 W_2 \quad \dots \quad T_M W_0 \quad T_{M-1} W_1 \quad \dots \quad T_1 W_{M-1} \quad T_0 W_M],$$

in which the expressions for $T_i(s_1)$ and $W_i(s_2)$ are given by Equation (B.3), and

$$\begin{aligned}\bar{\bar{V}}_i^T &= [\bar{\bar{V}}_{i(-N)}^T \quad \bar{\bar{V}}_{i(-N+1)}^T \quad \dots \quad \bar{\bar{V}}_{i(-1)}^T \quad \bar{\bar{V}}_{i(1)}^T \quad \dots \quad \bar{\bar{V}}_{i(N-1)}^T \quad \bar{\bar{V}}_{i(N)}^T], \quad i = 1, 2, \\ \bar{\bar{V}}_3^T &= [\bar{\bar{V}}_{3(-N)}^T \quad \bar{\bar{V}}_{3(-N+1)}^T \quad \dots \quad \bar{\bar{V}}_{3(-1)}^T \quad \bar{\bar{V}}_{3(1)}^T \quad \dots \quad \bar{\bar{V}}_{3(N-1)}^T \quad \bar{\bar{V}}_{3(N)}^T],\end{aligned}$$

with

$$\begin{aligned}\bar{\bar{V}}_{i(n)}^T &= [\bar{\bar{V}}_{i(n1)}^T \quad \bar{\bar{V}}_{i(n2)}^T], \quad \bar{\bar{V}}_{i(nj)}^T = [2 \text{Re}[u_j^{(i)} \Phi_{nj}^*] \quad -2 \text{Im}[u_j^{(i)} \Phi_{nj}^*]], \quad (i, j = 1, 2), \\ \bar{\bar{V}}_{3(n)}^T &= [\bar{\bar{V}}_{3(n1)}^T \quad \bar{\bar{V}}_{3(n2)}^T], \quad \bar{\bar{V}}_{3(nj)}^T = [2 \text{Re}[F_{nj}^*] \quad -2 \text{Im}[F_{nj}^*]], \quad (j = 1, 2).\end{aligned}$$

Appendix C

Constraint equations. The unknown vector of Lagrange multipliers λ , and the known coefficient matrix G , in Equation (11) are defined by $\lambda^T = [\lambda_{RRB(1)} \lambda_{RRB(2)} \lambda_{SV(r)} \lambda_{SV(s)} \lambda_{RB(1)} \dots \lambda_{RB(6)}]$, and

$$G = \begin{bmatrix} \mathbf{0}_R^T & \mathbf{g}_{RRB(1)}^T & \bar{\mathbf{0}}^T & \bar{\mathbf{0}}^T & \bar{\bar{\mathbf{0}}}^T & \bar{\bar{\mathbf{0}}}^T \\ \mathbf{0}_R^T & \bar{\mathbf{0}}^T & \mathbf{g}_{RRB(2)}^T & \bar{\mathbf{0}}^T & \bar{\mathbf{0}}^T & \bar{\bar{\mathbf{0}}}^T \\ \mathbf{0}_R^T & \bar{\mathbf{0}}^T & \bar{\mathbf{0}}^T & \bar{\mathbf{0}}^T & \bar{\mathbf{0}}^T & \mathbf{g}_{SV(s)}^T \\ \mathbf{0}_R^T & \mathbf{0}_L^T & \bar{\mathbf{0}}^T & \bar{\mathbf{0}}^T & \bar{\mathbf{0}}^T & \mathbf{g}_{SV(r)}^T \\ \mathbf{g}_{RB(1)}^T & \bar{\mathbf{0}}^T & \bar{\mathbf{0}}^T & \bar{\mathbf{0}}^T & \bar{\mathbf{0}}^T & \bar{\bar{\mathbf{0}}}^T \\ \mathbf{g}_{RB(2)}^T & \bar{\mathbf{0}}^T & \bar{\mathbf{0}}^T & \bar{\mathbf{0}}^T & \bar{\mathbf{0}}^T & \bar{\bar{\mathbf{0}}}^T \\ \mathbf{g}_{RB(3)}^T & \bar{\mathbf{0}}^T & \bar{\mathbf{0}}^T & \bar{\mathbf{0}}^T & \bar{\mathbf{0}}^T & \bar{\bar{\mathbf{0}}}^T \\ \mathbf{g}_{RB(4)}^T & \bar{\mathbf{0}}^T & \bar{\mathbf{0}}^T & \bar{\mathbf{0}}^T & \bar{\mathbf{0}}^T & \bar{\bar{\mathbf{0}}}^T \\ \mathbf{g}_{RB(5)}^T & \bar{\mathbf{0}}^T & \bar{\mathbf{0}}^T & \bar{\mathbf{0}}^T & \bar{\mathbf{0}}^T & \bar{\bar{\mathbf{0}}}^T \\ \mathbf{g}_{RB(6)}^T & \bar{\mathbf{0}}^T & \bar{\mathbf{0}}^T & \bar{\mathbf{0}}^T & \bar{\mathbf{0}}^T & \bar{\bar{\mathbf{0}}}^T \end{bmatrix},$$

in which the constant coefficient vectors $\mathbf{g}_{RRB(1)}$ and $\mathbf{g}_{RRB(2)}$ are associated with redundant rigid-body modes $\mathbf{g}_{SV(r)}$ and $\mathbf{g}_{SV(s)}$, with single-valuedness of the radial displacement component, and $\mathbf{g}_{RB(j)}$ with the rigid-body modes introduced by the global functions defined in Equation (B.2). The rigid-body modes must be eliminated in the absence of a sufficient number of specified kinematic boundary conditions. These terms, as well as the vectors with zeros, are defined in the following subsections.

Redundant rigid-body modes. The coefficients $c_{1(00)}$ and $c_{2(00)}$ in Equation (B.2) for the global displacement functions produce additional rigid-body translation in the s_1 direction and rigid body rotation about the s_1 axis, respectively. Because these rigid-body modes are already represented by α_{R1} and α_{R6} in Equation (B.1), the redundant rigid-body motion arising from the presence of $c_{1(00)}$ and $c_{2(00)}$ must be eliminated in order to obtain a unique representation of the displacements. These redundant rigid-body modes are eliminated by using the constraint conditions $\lambda_{RRB(1)}c_{1(00)} = 0$, $\lambda_{RRB(2)}c_{2(00)} = 0$ in which the unknown Lagrange multipliers are denoted by $\lambda_{RRB(1)}$ and $\lambda_{RRB(2)}$. In terms of the vector of unknowns \mathbf{q} , these constraints are rewritten in vector form as

$$\lambda_{RB(1)} \begin{bmatrix} \mathbf{0}_R^T & \mathbf{g}_{RRB}^T & \bar{\mathbf{0}}^T & \bar{\mathbf{0}}^T & \bar{\bar{\mathbf{0}}}^T & \bar{\bar{\mathbf{0}}}^T \end{bmatrix} \begin{bmatrix} \alpha_R \\ \mathbf{c}_1 \\ \mathbf{c}_2 \\ \mathbf{c}_3 \\ \alpha \\ \beta \end{bmatrix} = 0, \quad \lambda_{RB(2)} \begin{bmatrix} \mathbf{0}_R^T & \bar{\mathbf{0}}^T & \mathbf{g}_{RRB}^T & \bar{\mathbf{0}}^T & \bar{\bar{\mathbf{0}}}^T & \bar{\bar{\mathbf{0}}}^T \end{bmatrix} \begin{bmatrix} \alpha_R \\ \mathbf{c}_1 \\ \mathbf{c}_2 \\ \mathbf{c}_3 \\ \alpha \\ \beta \end{bmatrix} = 0,$$

in which the vectors of zeros, $\mathbf{0}_R^T$, $\bar{\mathbf{0}}^T$, and $\bar{\bar{\mathbf{0}}}^T$, are defined by $\mathbf{0}_R^T = [0 \ 0 \ 0 \ 0 \ 0 \ 0]$, $\bar{\mathbf{0}}^T = [0 \ 0 \ \dots \ 0]$ of order $[(M+1)(M+2)/2]$, and $\bar{\bar{\mathbf{0}}}^T = [0 \ 0 \ \dots \ 0]$ of order $8N$, while the constant coefficient vector, \mathbf{g}_{RRB} , is defined as $\mathbf{g}_{RRB}^T = [1 \ 0 \ 0 \ \dots \ 0]$ of order $[(M+1)(M+2)/2]$.

Single-valuedness of the radial displacement component. The multivaluedness of the normal displacement component that arises from the presence of logarithmic terms in the local expression for the radial displacement component in Equation (B.5) must be rendered single-valued in order to obtain a unique solution. The logarithmic terms associated with complex constants β_{-1m} and β_{1m} , with $m = 1, 2$, in Equation (B.10) result in two real constants. Representing the complex variable of the Laurent series $\xi_m = \rho_m e^{i\theta_m}$, the single-valuedness requirement is enforced as

$$u_z(\xi_m = \rho_m e^{i\theta_m}) - u_z(\xi_m = \rho_m e^{i(\theta_m+2\pi)}) = 0.$$

Associated with the complex constants $\beta_{\mp 1m}$, with $m = 1, 2$, in Equation (B.10), this condition yields

$$2 \operatorname{Re} \left\{ \sum_{m=1}^2 \left\{ F_{-1m}^*(\xi_m = \rho_m e^{i\theta_m}) - F_{-1m}^*(\xi_m = \rho_m e^{i(\theta_m+2\pi)}) \right\} \beta_{-1m} \right\} = 0 \quad \text{or} \quad \operatorname{Im} \sum_{m=1}^2 [r_m \beta_{-1m}] = 0,$$

$$2 \operatorname{Re} \left\{ \sum_{m=1}^2 \left\{ F_{1m}^*(\xi_m = \rho_m e^{i\theta_m}) - F_{1m}^*(\xi_m = \rho_m e^{i(\theta_m+2\pi)}) \right\} \beta_{1m} \right\} = 0 \quad \text{or} \quad \operatorname{Im} \sum_{m=1}^2 [s_{\kappa m} \beta_{1m}] = 0.$$

In order to ensure single-valuedness, these constraints are enforced as

$$\lambda_{SV(r)} \operatorname{Im} \sum_{m=1}^2 [r_{\kappa m} \beta_{-1m}] = 0, \quad \lambda_{SV(s)} \operatorname{Im} \sum_{m=1}^2 [s_{\kappa m} \beta_{1m}] = 0,$$

in which the unknown Lagrange multipliers are denoted by $\lambda_{SV(r)}$ and $\lambda_{SV(s)}$.

In terms of the vector of unknowns \mathbf{q} , these constraint conditions can be recast in matrix form as

$$\lambda_{SV(r)} \begin{bmatrix} \mathbf{0}_R^T & \bar{\mathbf{0}}^T & \bar{\mathbf{0}}^T & \bar{\mathbf{0}}^T & \bar{\mathbf{0}}^T & \mathbf{g}_{SV(r)}^T \end{bmatrix} \begin{bmatrix} \alpha_R \\ \mathbf{c}_1 \\ \mathbf{c}_2 \\ \mathbf{c}_3 \\ \alpha \\ \beta \end{bmatrix} = 0, \quad \lambda_{SV(s)} \begin{bmatrix} \mathbf{0}_R^T & \bar{\mathbf{0}}^T & \bar{\mathbf{0}}^T & \bar{\mathbf{0}}^T & \bar{\mathbf{0}}^T & \mathbf{g}_{SV(s)}^T \end{bmatrix} \begin{bmatrix} \alpha_R \\ \mathbf{c}_1 \\ \mathbf{c}_2 \\ \mathbf{c}_3 \\ \alpha \\ \beta \end{bmatrix} = 0,$$

where the constant coefficient vectors $\mathbf{g}_{SV(r)}$ and $\mathbf{g}_{SV(s)}$ are given by

$$\mathbf{g}_{SV(j)}^T = \left[\mathbf{g}_{SV(j)(-N)}^T \quad \mathbf{g}_{SV(j)(-N+1)}^T \quad \cdots \quad \mathbf{g}_{SV(j)(-1)}^T \quad \mathbf{g}_{SV(j)(1)}^T \quad \cdots \quad \mathbf{g}_{SV(j)(N-1)}^T \quad \mathbf{g}_{SV(j)(N)}^T \right],$$

$$\mathbf{g}_{SV(r)(1)}^T = [\operatorname{Im}[r_1] \quad \operatorname{Re}[r_1] \quad \operatorname{Im}[r_2] \quad \operatorname{Re}[r_2]], \quad \mathbf{g}_{SV(r)(n \neq 1)}^T = [0 \quad 0 \quad 0 \quad 0],$$

$$\mathbf{g}_{SV(s)(1)}^T = [\operatorname{Im}[s_1] \quad \operatorname{Re}[s_1] \quad \operatorname{Im}[s_2] \quad \operatorname{Re}[s_2]], \quad \mathbf{g}_{SV(s)(n \neq 1)}^T = [0 \quad 0 \quad 0 \quad 0],$$

with $-N \leq n \leq N$.

Rigid-body modes. In the absence of kinematic boundary conditions, the rigid-body modes of the displacement field are eliminated by enforcing the constraint conditions in the form $\lambda_{RB(j)} \alpha_{R(j)} = 0$, where $j = 1, \dots, 6$ and the unknown Lagrange multipliers are denoted by $\lambda_{RB(j)}$. In terms of the vector of

unknowns \mathbf{q} , these constraints are rewritten in vector form as

$$\lambda_{RB(j)} \begin{bmatrix} \mathbf{g}_{RB(j)}^T & \bar{\mathbf{0}}^T & \bar{\mathbf{0}}^T & \bar{\mathbf{0}}^T & \bar{\mathbf{0}}^T & \bar{\mathbf{0}}^T \end{bmatrix} \begin{bmatrix} \alpha_R \\ c_1 \\ c_2 \\ c_3 \\ \alpha \\ \beta \end{bmatrix} = 0,$$

where the constant coefficient vectors $\mathbf{g}_{RB(j)}$ are defined as $\mathbf{g}_{RB(j)}^T = [\delta_{1j} \delta_{2j} \delta_{3j} \delta_{4j} \delta_{5j} \delta_{6j}]$, in which δ_{ij} is the Kronecker delta.

References

- [Ashmarin 1966] I. A. Ashmarin, "Stress concentration around a circular opening in an orthotropic cylindrical shell", *Prikl. Mat. Mekh.* **2** (1966), 44–48.
- [Bull 1982] J. W. Bull, *Stresses around large circular holes in uniform circular cylindrical shells*, vol. 17, 1982.
- [Bushnell 1984] D. Bushnell, "Computerized analysis of shells: governing equations", *Comput. Struct.* **18**:3 (1984), 471–536.
- [Chaudhuri et al. 1986] R. A. Chaudhuri, K. Balaraman, and V. X. Kunukkasseril, "Arbitrarily laminated, anisotropic cylindrical shell under internal pressure", *AIAA J.* **24**:11 (1986), 1851–1858.
- [Chen and Kempner 1976] Y. N. Chen and J. Kempner, "Buckling of oval cylindrical shells under compression and asymmetric bending", *AIAA J.* **14**:9 (1976), 1235–1240.
- [Culberson and Boyd 1971] L. D. Culberson and D. E. Boyd, "Free vibrations of freely supported oval cylinders", *AIAA J.* **9**:8 (1971), 1474–1480.
- [Ebner and Jung 1972] H. Ebner and O. Jung, "Stress concentration around holes in plates and shells", pp. 135–158 in *Contributions to the theory of aircraft structures*, Delft University Press, Delft, 1972.
- [Guz et al. 2001] A. N. Guz, I. S. Chernyshenko, and K. I. Shnerenko, "Stress concentration near openings in composite shells", *Int. Appl. Mech.* **37**:2 (2001), 139–181.
- [Hicks 1964] R. Hicks, "Stress concentrations around holes in plates and shells", pp. 3–12 in *Proceedings of the Applied Mechanics Conference*, London, 1964.
- [Hyer and Wolford 2002] M. W. Hyer and G. F. Wolford, "Progressive failure analysis of internally pressurized noncircular composite cylinders", in *43rd AIAA/ASME/ASCE/AHS/ASC Structures, Structural Dynamics, and Materials Conference* (Denver, CO), AIAA, Reston, VA, 2002, Available at <http://www.aiaa.org>. Paper No. 2002–1403.
- [Hyer et al. 2003] M. W. Hyer, G. F. Wolford, and N. F. Knight, Jr., "Damage initiation and progression in internally pressurized noncircular composite cylinders", in *44th AIAA/ASME/ASCE/AHS/ASC Structures, Structural Dynamics, and Materials Conference* (Norfolk, VA), AIAA, Reston, VA, 2003, Available at <http://www.aiaa.org>. Paper No. 2003–1594.
- [Jones 1999] R. M. Jones, *Mechanics of composite materials*, 2nd ed., Taylor and Francis, Philadelphia, PA, 1999.
- [Kraus 1967] H. Kraus, *Thin elastic shells: an introduction to the theoretical foundations and the analysis of their static and dynamic behavior*, Wiley, New York, 1967.
- [Lekhnitskii 1968] S. G. Lekhnitskii, *Anisotropic plates*, Gordon and Breach Science Publishers, New York, 1968.
- [Lekkerkerker 1966] J. G. Lekkerkerker, "Stress concentration around circular holes in cylindrical shells", pp. 283–288 in *Proceedings of the 11th International Congress of Applied Mechanics* (Munich, 1964), edited by H. Görtler, Springer, Berlin, 1966.
- [Li et al. 1995] Y. W. Li, I. Elishakoff, and J. H. Starnes, Jr., "Axial buckling of composite cylindrical shells with periodic thickness variation", *Comput. Struct.* **56**:1 (1995), 65–74.
- [Liang et al. 1998] C.-C. Liang, C.-Y. Hsu, and W. Chen, "Curvature effect on stress concentrations around circular hole in opened shallow cylindrical shell under external pressure", *Int. J. Pres. Ves. Pip.* **75**:10 (1998), 749–763.

- [Love 1888] A. E. H. Love, “The small free vibrations and deformation of a thin elastic shell”, *Philos. Tr. R. Soc. S. A* **179** (1888), 491–546.
- [Love 1944] A. E. H. Love, *A treatise on the mathematical theory of elasticity*, 4th ed., Dover, New York, 1944. [MR 6,79e](#) [Zbl 0063.03651](#)
- [Lurie 1946] A. I. Lourye, “Concentration of stresses in the vicinity of an aperture in the surface of a circular cylinder”, *Prikl. Mat. Mekh.* **10** (1946), 397–406. [MR 8,117c](#)
- [Lurie 1947] A. I. Lurie, *Statics of thin-walled elastic shells*, State Publishing House of Technical and Theoretical Literature, Moscow, 1947.
- [Madenci and Barut 1994a] E. Madenci and A. Barut, “A free-formulation-based flat shell element for non-linear analysis of thin composite structures”, *Int. J. Numer. Methods Eng.* **37**:22 (1994), 3825–3842.
- [Madenci and Barut 1994b] E. Madenci and A. Barut, “Pre- and postbuckling response of curved, thin composite panels with cutouts under compression”, *Int. J. Numer. Methods Eng.* **37**:9 (1994), 1499–1510.
- [Madenci and Barut 1994c] E. Madenci and A. Barut, “Thermal postbuckling analysis of cylindrically curved composite laminates with a hole”, *Int. J. Numer. Methods Eng.* **37**:12 (1994), 2073–2091.
- [Madenci and Barut 2003] E. Madenci and A. Barut, “The influence of geometric irregularities on the linear buckling of cylindrical shells with an elliptic cutout”, in *44th AIAA/ASME/ASCE/AHS/ASC Structures, Structural Dynamics, and Materials Conference* (Norfolk, VA), AIAA, Reston, VA, 2003. Paper No. 2003–1929.
- [McFarland et al. 1972] D. McFarland, B. L. Smith, and W. D. Bernhart, *Analysis of plates*, Spartan Books, New York, 1972.
- [Murthy et al. 1974] M. V. V. Murthy, K. P. Rao, and A. K. Rao, “On the stress problem of large elliptical cutouts and cracks in circular cylindrical shells”, *Int. J. Solids Struct.* **10**:11 (1974), 1243–1269.
- [Naghdi 1962] P. M. Naghdi, “Foundations of elastic shell theory”, Technical Report 15, Office of Naval Research, January 1962.
- [Pierce and Chou 1973] D. N. Pierce and S. I. Chou, “Stresses around elliptical holes in circular cylindrical shells”, *Exp. Mech.* **13**:11 (1973), 487–492.
- [Reissner 1941] E. Reissner, “A new derivation of the equations for the deformation of elastic shells”, *Amer. J. Math.* **63** (1941), 177–184. [MR 2,272a](#) [Zbl 0024.22803](#)
- [Romano and Kempner 1958] F. Romano and J. Kempner, “Stress and displacement analysis of simply supported non-circular cylindrical shells under lateral pressure”, PIBAL Report 415, Polytechnic Institute of Brooklyn, New York, 1958.
- [Romano and Kempner 1962] F. Romano and J. Kempner, “Stresses in short noncircular cylindrical shells under lateral pressure”, *J. Appl. Mech. (ASME)* **29** (1962), 669–674.
- [Sheinman and Firer 1994] I. Sheinman and M. Firer, “Buckling analysis of laminated cylindrical shells with arbitrary noncircular cross sections”, *AIAA J.* **32**:3 (1994), 648–654.
- [Shewchuk 1996] J. R. Shewchuk, “Triangle: engineering a 2D quality mesh generator and Delaunay triangulator”, pp. 203–222 in *Applied computational geometry: towards geometric engineering: FCRC '96 Workshop, WACG '96: selected papers* (Philadelphia, PA), edited by M. C. Lin and D. Manocha, Lecture Notes in Computer Science **1148**, Springer, New York, 1996.
- [Shnerenko and Godzula 2003] K. I. Shnerenko and V. F. Godzula, “Stress distribution in a composite cylindrical shell with a large circular opening”, *Int. Appl. Mech.* **39**:11 (2003), 1323–1327.
- [Starnes 1972] J. H. Starnes, Jr., “Effect of a circular hole on the buckling of cylindrical shells loaded by axial compression”, *AIAA J.* **10**:11 (1972), 1466–1472.
- [Storozhuk and Chernyshenko 2005] E. A. Storozhuk and I. S. Chernyshenko, “Elastoplastic deformation of flexible cylindrical shells with two circular holes under axial tension”, *Int. Appl. Mech.* **41**:5 (2005), 506–511.
- [Tennyson 1968] R. C. Tennyson, “The effects of unreinforced circular cutouts on the buckling of circular cylindrical shells under axial compression”, *J. Eng. Ind. (ASME)* **90** (1968), 541–546.
- [Timoshenko and Woinowsky-Krieger 1959] S. Timoshenko and S. Woinowsky-Krieger, *Theory of plates and shells*, 2nd ed., McGraw-Hill, New York, 1959.
- [Van Dyke 1965] P. Van Dyke, “Stresses about a circular hole in a cylindrical shell”, *AIAA J.* **3**:9 (1965), 1733–1742.

[Van Tooren et al. 2002] M. J. L. Van Tooren, I. P. M. Van Stijn, and A. Beukers, “Curvature effects on the stress distribution in sandwich cylinders with a circular cut-out”, *Compos. A Appl. Sci. Manuf.* **33**:11 (2002), 1557–1572.

[Zirka and Chernopiskii 2003] A. I. Zirka and D. I. Chernopiskii, “Stress concentration in an axially compressed cylindrical shell of medium thickness with an elliptic opening”, *Int. Appl. Mech.* **39**:11 (2003), 1335–1338.

Received 3 Feb 2006. Revised 16 Sep 2006. Accepted 29 Nov 2006.

ERKAN OTERKUS: oterkus@email.arizona.edu

Department of Aerospace and Mechanical Engineering, The University of Arizona, Tucson, AZ 85721, United States

ERDOGAN MADENCI: madenci@email.arizona.edu

Department of Aerospace and Mechanical Engineering, The University of Arizona, Tucson, AZ 85721, United States

MICHAEL P. NEMETH: *Structural Mechanics and Concepts Branch, NASA Langley Research Center, Hampton, VA 23681, United States*

HYPERSINGULAR INTEGRAL EQUATIONS FOR THE SOLUTION OF PENNY-SHAPED INTERFACE CRACK PROBLEMS

BAHATTIN KILIC AND ERDOGAN MADENCI

Based on the theory of elasticity, previous analytical solutions concerning a penny-shaped interface crack employ the derivative of the crack surface opening displacements as the primary unknowns, thus leading to singular integral equations with Cauchy-type singularity. The solutions to the resulting integral equations permit only the determination of stress intensity factors and energy release rate, and do not directly provide crack opening and sliding displacements. However, the crack opening and sliding displacements are physically more meaningful and readily validated against the finite element analysis predictions and experimental measurements. Therefore, the present study employs crack opening and sliding as primary unknowns, rather than their derivatives, and the resulting integral equations include logarithmic-, Cauchy-, and Hadamard-type singularities. The solution to these singular integral equations permits the determination of not only the complex stress intensity factors but also the crack opening displacements.

1. Introduction

During fabrication, the presence of dissimilar material interfaces is unavoidable, and they are prone to imperfections. If the interface is too strong to delaminate, the cracking occurs in the weakest of the adjoining materials. On the other hand, delamination may initiate along the interface for a sufficiently weak interface. Based on the concept of fracture mechanics, the singular character of the stresses near the crack front and the stress intensity factors are important in failure prediction.

Within the realm of the theory of elasticity both for a plane and a penny-shaped crack, there exist numerous analytical studies addressing the oscillating stress singularity and stress intensity factors at an interface crack. Extensive discussion on the treatment of an oscillatory singular stress field near the interface crack was given by [Erdogan \[1997\]](#) and recently by [Kilic et al. \[2006\]](#). The most common solution method of integral transformations includes the presence of singular stresses at the crack front by treating the derivatives of the crack opening displacements as primary unknowns, leading to a system of Cauchy-type singular integral equations. Solutions to these singular integral equations can be achieved by techniques developed by [Erdogan \[1969\]](#), [Erdogan and Gupta \[1971a; 1971b\]](#), [Miller and Keer \[1985\]](#), and [Kabir et al. \[1998\]](#) that yield the stress intensity factors.

Because of the nature of the primary unknowns in the singular integral equations, previous studies concerning interface cracks concern the calculation of the stress intensity factors or the energy release rate rather than the crack surface displacements. However, the crack surface displacements are physically more meaningful and easier to compare against experimental measurements and finite element solutions that fail to provide accurate stress intensity and energy release rate without resorting to a refined mesh

Keywords: interface, penny-shaped, crack, hypersingular.

or a special crack tip element. Furthermore, this approach is more viable for consideration of three-dimensional crack problems within the realm of mixed boundary value problems as indicated by [Kaya \[1984\]](#).

The construction of the solution to the integral equations concerning a plane crack is relatively simpler than that for a penny-shaped crack, and is discussed in detail by [Kilic et al. \[2006\]](#). For a penny-shaped interface crack between two dissimilar elastic materials that are semiinfinite in extent, [Kassir and Bregman \[1972\]](#) constructed the exact solution to the stress intensity factors utilizing analytic functions introduced by [\[Mossakovski and Rybka 1964\]](#). This problem also attracted the attention of [Erdogan \[1965\]](#), [Willis \[1972\]](#), and [Lowengrub and Sneddon \[1974\]](#). [Erdogan \[1965\]](#) obtained the singular stress field near the crack front by using the integral representation of displacement components suggested by [Harding and Sneddon \[1945\]](#) while considering the derivatives of crack surface displacements as primary unknowns in the derivation of Cauchy-type singular integral equations. However, [Willis \[1972\]](#) constructed the solution through the use of the Radon transform of the relative displacement of crack surfaces. Adopting the solution method by [Erdogan \[1965\]](#), [Lowengrub and Sneddon \[1974\]](#), [Keer et al. \[1978\]](#), and [Farris and Keer \[1985\]](#) also examined the singular character of stresses of a penny-shaped interface crack. However, the numerical evaluation of the integrals in these studies is fraught with complete regularization of the kernels by ignoring the logarithmic singularities and thus the convergence difficulty. Therefore, logarithmic singularities have to be taken into account in the numerical analysis as suggested by [Ozturk and Erdogan \[1996\]](#).

Unlike previous studies, the present study considers the crack surface displacements, rather than their derivatives, as primary unknowns in the singular integral equations. After the regularization of the kernels, the resulting integral equations include logarithmic-, Cauchy-, and Hadamard-type singularities. Solution to these singular integral equations leads to the determination of not only stress intensity factors but also crack opening displacements, which are more desirable for experimental comparisons. This approach also naturally provides the complex stress intensity factors required for the energy release rate calculation given by [Malyshev and Salganik \[1965\]](#). Within the context of solution methods available in the literature, this study for the first time presents an approach for constructing the solution of a singular integral equation in the presence of the combination of Hadamard, Cauchy, and logarithmic singularities. Although this approach provides accurate crack opening and sliding displacements, it does not remove the oscillatory singular stress field near the interface crack.

The description of the geometry and the crack configurations are shown in the next section. The solution method and the numerical analysis of the singular integral equations with the Hadamard-type singularity are described in the subsequent sections. The numerical results concern the energy release rate calculations and the crack surface displacements.

2. Problem statement

As shown in [Figure 1](#), a circular crack with radius a is situated at the interface between two material layers with thicknesses h_1 and h_2 . The crack lies on the (r, θ) plane of the cylindrical coordinate system (r, θ, z) whose origin is located at the center of the crack. The regions along the positive and negative z -directions are S_2 and S_1 , respectively. The material in each region is isotropic, elastic, and homogeneous, with shear moduli μ_1 and μ_2 , and Poisson's ratios ν_1 and ν_2 . The bounding surface of region S_2 is

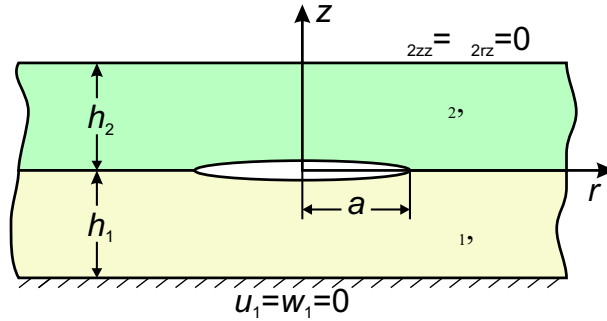


Figure 1. The circular crack geometry between two bonded dissimilar material layers.

traction free and that of S_1 is constrained from displacements. The crack surfaces are subjected to an internal pressure of p_0 . This configuration was considered previously by [Farris and Keer \[1985\]](#) while using the derivatives of the crack surface displacements as primary unknowns. It reduces to the case considered by [Goldstein and Vainshelbaum \[1976\]](#) by allowing h_1 to approach infinity.

By invoking the kinematic and stress-strain relations into the equilibrium equations in the absence of the body forces and time dependence, the displacement equilibrium equations under axisymmetric conditions for each region can be expressed as

$$\begin{aligned}
 (\kappa_i + 1) \left\{ \frac{\partial^2 u_i}{\partial r^2} + \frac{1}{r} \frac{\partial u_i}{\partial r} - \frac{1}{r^2} u_i + \frac{\partial^2 w_i}{\partial r \partial z} \right\} + (\kappa_i - 1) \left\{ \frac{\partial^2 u_i}{\partial z^2} - \frac{\partial^2 w_i}{\partial r \partial z} \right\} &= 0, \\
 (\kappa_i + 1) \left\{ \frac{\partial^2 u_i}{\partial r \partial z} + \frac{1}{r} \frac{\partial u_i}{\partial z} + \frac{\partial^2 w_i}{\partial z^2} \right\} - (\kappa_i - 1) \left\{ \frac{\partial^2 u_i}{\partial r \partial z} - \frac{\partial^2 w_i}{\partial r^2} + \frac{1}{r} \frac{\partial u_i}{\partial z} - \frac{1}{r} \frac{\partial w_i}{\partial r} \right\} &= 0,
 \end{aligned}
 \tag{1}$$

where $\kappa_i = 3 - 4\nu_i$ and u_i and w_i are the radial and vertical components of the displacement vector, respectively. The subscript $i = 1$ represents the substrate and $i = 2$ the film, as shown in [Figure 1](#). From the stress-strain relations along with kinematics, the relevant stress components in cylindrical coordinates under axisymmetric conditions can be expressed as

$$\sigma_{izz} = \frac{2\mu_i}{1 - 2\nu_i} \left\{ (1 - \nu_i) \frac{\partial w_i}{\partial z} + \nu_i \left(\frac{\partial u_i}{\partial r} + \frac{u_i}{r} \right) \right\}, \quad \sigma_{irz} = \mu_i \left(\frac{\partial u_i}{\partial z} + \frac{\partial w_i}{\partial r} \right).$$

Traction free conditions along $z = h_2$ and constrained displacement conditions along $z = -h_1$ require the imposition of conditions

$$\sigma_{zz}(r, h_2) = 0, \quad \sigma_{rz}(r, h_2) = 0, \quad u_1(r, -h_1) = 0, \quad w_1(r, -h_1) = 0, \quad 0 \leq r < \infty. \tag{2}$$

Along the interface between regions S_1 and S_2 on the plane of $z = 0$, the continuity of traction and displacement components requires the imposition of

$$\sigma_{1zz}(r, 0) = \sigma_{2zz}(r, 0), \quad \sigma_{1rz}(r, 0) = \sigma_{2rz}(r, 0), \quad 0 \leq r < \infty, \tag{3}$$

$$u_{1zz}(r, 0) = u_{2zz}(r, 0), \quad w_{1zz}(r, 0) = w_{2zz}(r, 0), \quad a \leq r < \infty. \tag{4}$$

Finally, the applied tractions on the upper and lower crack surfaces of the $z = 0^\pm$ planes are specified as

$$\sigma_{1zz}(r, 0^-) = \sigma_{2zz}(r, 0^+) = p(r), \quad \sigma_{1rz}(r, 0^-) = \sigma_{2rz}(r, 0^+) = q(r), \quad 0 \leq r < a. \quad (5)$$

The mathematical boundary value problem then reduces to the determination of the crack opening and sliding displacements, as well as the stress intensity factors and the energy release rate at the crack tip.

3. Solution procedure

The solution procedure involves the use of integral transformation techniques appropriate for mixed boundary value problems. Utilizing the integral representation of the displacement field suggested by [Harding and Sneddon \[1945\]](#) the displacement components in each region are represented by

$$u_i(r, z) = \int_0^\infty d\rho F_i(\rho, z)\rho J_1(r\rho), \quad w_i(r, z) = \int_0^\infty d\rho G_i(\rho, z)\rho J_0(r\rho), \quad (6)$$

where J_0 and J_1 are the Bessel functions of the first kind with orders 0 and 1, respectively.

Substituting these integral representations into the displacement equilibrium equations, [Equation \(1\)](#), leads to a coupled system of second-order ordinary differential equations for the auxiliary functions, $F_i(\rho, z)$ and $G_i(\rho, z)$. Their general solution form can be expressed as

$$\begin{bmatrix} F_i(\rho, z) \\ G_i(\rho, z) \end{bmatrix} = A_{i1}e^{-\rho z} \begin{bmatrix} 1 \\ 1 \end{bmatrix} + A_{i2}e^{-\rho z} \begin{bmatrix} z \\ \frac{\kappa_i}{\rho} + z \end{bmatrix} + A_{i3}e^{\rho z} \begin{bmatrix} 1 \\ -1 \end{bmatrix} + A_{i4}e^{\rho z} \begin{bmatrix} z \\ \frac{\kappa_i}{\rho} - z \end{bmatrix}, \quad (7)$$

where $A_{ij}(\rho)$ for $i = 1, 2$ and $j = 1 \dots 4$ are the unknown coefficients to be determined from the prescribed boundary conditions given by [Equations \(2\)–\(5\)](#).

Enforcing the boundary conditions specified by [Equations \(2\)](#) and [\(3\)](#) results in

$$\begin{aligned} 2\rho e^{-\rho h_2} A_{21} + (\kappa_2 + 1 + 2\rho h_2)e^{-\rho h_2} A_{22} + 2\rho e^{\rho h_2} A_{23} - (\kappa_2 + 1 - 2\rho h_2)e^{\rho h_2} A_{24} &= 0, \\ 2\rho e^{-\rho h_2} A_{21} + (\kappa_2 - 1 + 2\rho h_2)e^{-\rho h_2} A_{22} - 2\rho e^{\rho h_2} A_{23} + (\kappa_2 - 1 - 2\rho h_2)e^{\rho h_2} A_{24} &= 0, \\ e^{\rho h_1} A_{11} - h_1 e^{\rho h_1} A_{12} + e^{-\rho h_1} A_{13} - h_1 e^{-\rho h_1} A_{14} &= 0, \\ e^{\rho h_1} A_{11} + (\kappa_1/\rho - h_1)e^{\rho h_1} A_{12} - e^{-\rho h_1} A_{13} + (\kappa_1/\rho + h_1)e^{-\rho h_1} A_{14} &= 0, \\ 2\mu_2\rho A_{21} + (1 + \kappa_2)\mu_2 A_{22} + 2\mu_2\rho A_{23} - (1 + \kappa_2)\mu_2 A_{24} - 2\mu_1\rho A_{11} - (1 + \kappa_1)\mu_1 A_{12} & \\ - 2\mu_1\rho A_{13} + (1 + \kappa_1)\mu_1 A_{14} &= 0, \\ 2\mu_2\rho A_{21} + (\kappa_2 - 1)\mu_2 A_{22} - 2\mu_2\rho A_{23} + (\kappa_2 - 1)\mu_2 A_{24} - 2\mu_1\rho A_{11} - (\kappa_1 - 1)\mu_1 A_{12} & \\ + 2\mu_1\rho A_{13} - (\kappa_1 - 1)\mu_1 A_{14} &= 0. \end{aligned} \quad (8)$$

Representing the opening and sliding of the crack surfaces by unknown functions $U(r)$ and $W(r)$ as

$$u_2(r, 0^+) - u_1(r, 0^-) = U(r)H(a - r), \quad w_2(r, 0^+) - w_1(r, 0^-) = W(r)H(a - r) \quad (9)$$

ensures the continuity of the displacement components, [Equation \(4\)](#), along the interface plane of $z = 0$ and $H(\xi)$ is the Heaviside step function. In lieu of directly imposing the continuity requirement of the displacement components along the interface to simplify the algebraic manipulations, the auxiliary

functions $g_1(r)$ and $g_2(r)$ are introduced in the form

$$g_1(r) = \frac{\partial W}{\partial r} H(a - r), \quad g_2(r) = \left(\frac{\partial U}{\partial r} + \frac{U}{r} \right) H(a - r), \tag{10}$$

in which the unknown functions $U(r)$ and $W(r)$ are defined in Equation (9). Their explicit form can be obtained by substituting Equations (6) and (7) into Equation (10) as

$$g_1(r) = \int_0^\infty d\rho \rho \left[\kappa_1(A_{12} + A_{14}) - \kappa_2(A_{22} + A_{24}) + (A_{11} - A_{21} - A_{13} + A_{23})\rho \right] J_1(\rho r),$$

$$g_2(r) = \int_0^\infty d\rho \rho^2 \left[-A_{11} + A_{21} - A_{13} + A_{23} \right] J_0(\rho r).$$

Inversion of these equations by using the related Hankel transforms results in

$$G_1(\rho) = -\rho A_{21} - \kappa_2 A_{22} + \rho A_{23} - \kappa_2 A_{24} + \rho A_{11} + \kappa_1 A_{12} - \rho A_{13} + \kappa_1 A_{14},$$

$$G_2(\rho) = \rho A_{21} + \rho A_{23} - \rho A_{11} - \rho A_{13}, \tag{11}$$

in which

$$G_1(\rho) = \int_0^a ds g_1(s) s J_1(s\rho), \quad G_2(\rho) = \int_0^a ds g_2(s) s J_0(s\rho). \tag{12}$$

In matrix form, the combination of all the boundary conditions given by Equations (8) and (11) can be expressed as

$$C \mathbf{a} = \mathbf{b}, \tag{13}$$

in which the explicit forms of C , \mathbf{a} , and \mathbf{b} are given in Appendix A. The unknown coefficients A_{ij} with $i = 1, 2$ and $j = 1 \dots 4$, contained in vector \mathbf{a} can be solved for in terms of the unknown auxiliary functions $G_1(\rho)$ and $G_2(\rho)$ contained in vector \mathbf{b} in the form

$$A_{ij} = A_{ij}(G_1(\rho), G_2(\rho)). \tag{14}$$

Although the formulation presented herein only considers boundary conditions of the clamped type on region S_1 and traction free on region S_2 , it can easily be extended to include different boundary conditions such as clamped on both regions and traction free on both regions, and their combinations. Imposition of different types of boundary conditions only requires the modification of the matrix C to reflect changes in Equation (2).

The remaining unknown functions $G_1(\rho)$ and $G_2(\rho)$ are determined by enforcing the applied tractions on the crack surfaces given by Equation (5), resulting in

$$\mu_2 \int_0^\infty d\rho \rho \left[(1 + \kappa_2)(A_{24} - A_{22}) - 2\rho(A_{21} + A_{23}) \right] J_0(\rho r) = p(r),$$

$$\mu_2 \int_0^\infty d\rho \rho \left[(1 - \kappa_2)(A_{24} + A_{22}) - 2\rho(A_{21} - A_{23}) \right] J_1(\rho r) = q(r), \tag{15}$$

where the stress components are defined in region S_2 , and A_{ij} are already determined by Equation (14).

In order to avoid divergent kernels and to simplify the analysis regarding the asymptotic behavior of the kernels, both sides of Equation (15) are integrated over r while invoking Equation (12), resulting in

$$\begin{aligned} \int_0^a ds s g_1(s) \int_0^\infty d\rho H_{11}(\rho) J_1(\rho r) J_1(\rho s) + \int_0^a ds s g_2(s) \int_0^\infty d\rho H_{12}(\rho) J_1(\rho r) J_0(\rho s) \\ = \frac{1}{r} \left(\int_r p(\lambda) \lambda d\lambda + c_1 \right), \\ \int_0^a ds s g_1(s) \int_0^\infty d\rho H_{21}(\rho) (1 - J_0(\rho r)) J_1(\rho s) + \int_0^a ds s g_2(s) \int_0^\infty d\rho H_{22}(\rho) (1 - J_0(\rho r)) J_0(\rho s) \\ = \int_r q(\lambda) d\lambda + c_2, \end{aligned} \quad (16)$$

in which $H_{ij}(\rho)$, with $i, j = 1, 2$, are defined in terms of the coefficients of C^{-1} in Appendix A, and c_i represents the integration constants. As the integration variable ρ approaches infinity, the kernels $H_{ij}(\rho)$ possess the asymptotic behavior

$$\begin{aligned} \lim_{\rho \rightarrow \infty} H_{11}(\rho) = - \lim_{\rho \rightarrow \infty} H_{22}(\rho) = \gamma_{11} = \frac{\mu_1 \mu_2 (\mu_1 (1 + \kappa_2) + \mu_2 (1 + \kappa_1))}{(\mu_2 + \kappa_2 \mu_1) (\mu_1 + \kappa_1 \mu_2)}, \\ \lim_{\rho \rightarrow \infty} H_{12}(\rho) = - \lim_{\rho \rightarrow \infty} H_{21}(\rho) = \gamma_{12} = \frac{\mu_1 \mu_2 (\mu_1 (1 - \kappa_2) - \mu_2 (1 - \kappa_1))}{(\mu_2 + \kappa_2 \mu_1) (\mu_1 + \kappa_1 \mu_2)}. \end{aligned}$$

By considering the asymptotic behavior of kernels, using $\gamma = -\gamma_{12}/\gamma_{11}$ Equation (16) can be rewritten as

$$\begin{aligned} -\gamma \int_0^a ds s g_2(s) \int_0^\infty d\rho J_1(\rho r) J_0(\rho s) + \int_0^a ds s g_2(s) \int_0^\infty d\rho \frac{H_{12}(\rho) - \gamma_{12}}{\gamma_{11}} J_1(\rho r) J_0(\rho s) \\ + \int_0^a ds s g_1(s) \int_0^\infty d\rho J_1(\rho r) J_1(\rho s) + \int_0^a ds s g_1(s) \int_0^\infty d\rho \frac{H_{11}(\rho) - \gamma_{11}}{\gamma_{11}} J_1(\rho r) J_1(\rho s) \\ = \frac{1}{\gamma_{11} r} \left(\int_r p(\lambda) \lambda d\lambda + C_1 \right), \\ \gamma \int_0^a ds s g_1(s) \int_0^\infty d\rho (1 - J_0(\rho r)) J_1(\rho s) + \int_0^a ds s g_1(s) \int_0^\infty d\rho \frac{H_{21}(\rho) + \gamma_{12}}{\gamma_{11}} (1 - J_0(\rho r)) J_1(\rho s) \\ - \int_0^a ds s g_2(s) \int_0^\infty d\rho (1 - J_0(\rho r)) J_0(\rho s) + \int_0^a ds s g_2(s) \int_0^\infty d\rho \frac{H_{22}(\rho) + \gamma_{11}}{\gamma_{11}} (1 - J_0(\rho r)) J_0(\rho s) \\ = \frac{1}{\gamma_{11}} \left(\int_r q(\lambda) d\lambda + C_2 \right), \end{aligned} \quad (17)$$

After differentiating these equations term by term with respect to r , application of integration by parts to replace the unknown functions $g_1(s)$ and $g_2(s)$ with the unknown functions $W(s)$ and $U(s)$ and the

use of Equation (A.1) when appropriate leads to

$$\frac{1}{\pi} \int_0^a ds \frac{W(s)}{(s-r)^2} + \frac{1}{2\pi r} \int_0^a ds \frac{W(s)}{s-r} - \frac{1}{8\pi r^2} \int_0^a ds W(s) \ln |s-r| + \int_0^a ds W(s) K_{11}(r,s) + \int_0^a ds U(s) K_{12}(r,s) - \gamma \frac{U(r)}{r} - \gamma \frac{\partial U(r)}{\partial r} = \frac{1}{\gamma_{11}} p(r), \tag{18}$$

$$\frac{1}{\pi} \int_0^a ds \frac{U(s)}{(s-r)^2} + \frac{1}{2\pi r} \int_0^a ds \frac{U(s)}{s-r} + \frac{3}{8\pi r^2} \int_0^a ds U(s) \ln |s-r| + \int_0^a ds W(s) K_{21}(r,s) + \int_0^a ds U(s) K_{22}(r,s) + \gamma \frac{\partial W(r)}{\partial r} = \frac{1}{\gamma_{11}} q(r), \tag{19}$$

in which the kernels are defined as

$$\begin{aligned} K_{11}(r,s) &= m_{11}(r,s) - \frac{1}{\pi(s-r)^2} - \frac{1}{2\pi r(s-r)} + \frac{\ln |s-r|}{8\pi r^2} - s \int_0^\infty d\rho \frac{H_{11}(\rho) - \gamma_{11}}{\gamma_{11}} \rho^2 J_0(\rho r) J_0(\rho s), \\ K_{12}(r,s) &= s \int_0^\infty d\rho \frac{H_{12}(\rho) - \gamma_{12}}{\gamma_{11}} \rho^2 J_0(\rho r) J_1(\rho s), \\ K_{21}(r,s) &= -s \int_0^\infty d\rho \frac{H_{21}(\rho) + \gamma_{12}}{\gamma_{11}} \rho^2 J_1(\rho r) J_0(\rho s), \\ K_{22}(r,s) &= m_{22}(r,s) - \frac{1}{\pi(s-r)^2} - \frac{1}{2\pi r(s-r)} - \frac{3 \ln |s-r|}{8\pi r^2} + s \int_0^\infty d\rho \frac{H_{22}(\rho) + \gamma_{11}}{\gamma_{11}} \rho^2 J_1(\rho r) J_1(\rho s), \end{aligned} \tag{20}$$

where $m_{11}(r,s)$ and $m_{22}(r,s)$ are given in Appendix A. Multiplying Equation (19) by $i = \sqrt{-1}$ and adding to Equation (18) leads to their combination as

$$\frac{1}{\pi} \int_0^a ds \frac{f(s)}{(s-r)^2} + \frac{1}{2\pi r} \int_0^a ds \frac{f(s)}{s-r} + \frac{1}{8\pi r^2} \int_0^a ds f(s) \ln |s-r| - \frac{1}{4\pi r^2} \int_0^a ds f^*(s) \ln |s-r| + \int_0^a ds K_1(r,s) f(s) + \int_0^a ds K_2(r,s) f^*(s) + i \frac{\gamma}{2r} f(r) - i \frac{\gamma}{2r} f^*(r) + i\gamma \frac{df(r)}{dr} = \frac{p(r) + iq(r)}{\gamma_{11}}, \tag{21}$$

where the unknown complex-valued function is $f(r) = W(r) + iU(r)$, with its complex conjugate represented by f^* . The complex-valued kernels K_1 and K_2 are defined as

$$\begin{aligned} K_1(r,s) &= \frac{1}{2} \left(K_{11}(r,s) + K_{22}(r,s) - i \left[K_{12}(r,s) - K_{21}(r,s) \right] \right), \\ K_2(r,s) &= \frac{1}{2} \left(K_{11}(r,s) - K_{22}(r,s) + i \left[K_{12}(r,s) + K_{21}(r,s) \right] \right). \end{aligned}$$

In addition to the presence of Hadamard-, Cauchy-, and logarithmic-type singularities, the dominant part of the kernels $K_1(r,s)$ and $K_2(r,s)$ in Equation (21) becomes unbounded as both r and s approach zero. Kernels of this type are analogous to the generalized Cauchy-type kernels [Erdogan 1978]. The unknown function $f(r)$ can be defined as

$$f(r) = \frac{F(r)}{(a-r)^{\alpha r \beta}},$$

in which $F(r)$ is an unknown bounded function. By using the function-theoretic method of Muskhelishvili [1992] and the properties of hypersingular integral equations described by Kaya [1984], Kaya and

Erdogan [1987], Ioakimidis [1988b; 1988a; 1990], and later by Chan et al. [2003] and Kilic et al. [2006], the strength of the singularities α and β can be obtained as

$$\alpha = -\frac{1}{2} + i\omega, \quad \beta = 0, \quad \text{with} \quad \omega = \frac{1}{2\pi} \ln\left(\frac{1-\gamma}{1+\gamma}\right).$$

For an interface crack, the complex stress intensity factor that is equivalent to that of Erdogan and Gupta [1971a; 1971b] and Kassir and Bregman [1972] can be defined as

$$k_1 + ik_2 = \lim_{r \rightarrow a} (r - a)^{-\alpha^*} 2^{-\alpha} (\sigma_{zz} + i\sigma_{rz}),$$

where α^* is the complex conjugate of α . This allows the stress intensity factor to be re-expressed as

$$\frac{1}{\gamma_{11}\sqrt{1-\gamma^2}} (k_1(a) + ik_2(a)) = -2\alpha \lim_{r \rightarrow a} (r - a)^\alpha (2a)^{\alpha^*} f(r) = -2^{-2\alpha} \alpha \sqrt{a} F(a).$$

In the limiting case of both h_1 and h_2 approaching infinity, the stress intensity factor for constant pressure can be expressed analytically using the formula given by Kassir and Bregman [1972] as

$$k_1 + ik_2 = 2p_0 \sqrt{\frac{a}{\pi}} \frac{\Gamma(2 - i\omega)}{\Gamma(1/2 - i\omega)}, \tag{22}$$

in which Γ represents the gamma function. Knowing the stress intensity factors permits the evaluation of the phase angle, ψ , equivalent to that of Jensen [1998], in the form

$$\tan \psi = \frac{\text{Im}((k_1 + ik_2)h_2^{-i\omega})}{\text{Re}((k_1 + ik_2)h_2^{-i\omega})}.$$

As introduced by Erdogan and Gupta [1971a; 1971b], the energy release rate can be related to the stress intensity factors in the form

$$\mathcal{G} = \frac{\pi}{2} \frac{(\mu_1 + \kappa_1\mu_2)(\mu_2 + \kappa_2\mu_1)}{\mu_1\mu_2[(1 + \kappa_1)\mu_2 + (1 + \kappa_2)\mu_1]} (k_1^2 + k_2^2).$$

4. Numerical analysis of integral equations

By introducing $r = a(x + 1)/2$, $s = a(t + 1)/2$, for $-1 \leq (x, t) \leq 1$, the integro-differential equation, Equation (21), is normalized as

$$\begin{aligned} & \frac{2}{\pi a} \int_{-1}^1 dt \frac{g(t)}{(t-x)^2} + \frac{1}{2\pi r} \int_{-1}^1 dt \frac{g(t)}{t-x} + \frac{a}{16\pi r^2} \int_{-1}^1 dt g(t) \ln|t-x| - \frac{a}{8\pi r^2} \int_{-1}^1 dt f^*(t) \ln|t-x| \\ & + \int_{-1}^1 dt M_1(x, t)g(t) + \int_{-1}^1 dt M_2(x, t)g^*(t) + i\frac{\gamma}{2r}g(x) - i\frac{\gamma}{2r}g^*(x) + i\frac{2\gamma}{a} \frac{dg(x)}{dx} = \frac{p(r) + iq(r)}{\gamma_{11}}, \end{aligned} \tag{23}$$

where $g(x) = f(a(x + 1)/2)$ and M_1 and M_2 are defined as

$$M_1(x, t) = \frac{1}{2} \left(M_{11}(x, t) + M_{22}(x, t) - i \frac{a}{2} [K_{12}(r, s) - K_{21}(r, s)] \right),$$

$$M_2(x, t) = \frac{1}{2} \left(M_{11}(x, t) - M_{22}(x, t) + i \frac{a}{2} [K_{12}(r, s) + K_{21}(r, s)] \right),$$

where

$$M_{11}(x, t) = \frac{a}{2} m_{11}(r, s) - \frac{2}{\pi a(t-x)^2} - \frac{1}{2\pi r(t-x)} + \frac{a \ln |t-x|}{16\pi r^2} - \frac{as}{2} \int_0^\infty d\rho \frac{H_{11}(\rho) - \gamma_{11}}{\gamma_{11}} \rho^2 J_0(\rho r) J_0(\rho s),$$

$$M_{22}(x, t) = \frac{a}{2} m_{22}(r, s) - \frac{2}{\pi a(t-x)^2} - \frac{1}{2\pi r(t-x)} - \frac{3a \ln |t-x|}{16\pi r^2} + \frac{as}{2} \int_0^\infty d\rho \frac{H_{22}(\rho) + \gamma_{11}}{\gamma_{11}} \rho^2 J_1(\rho r) J_1(\rho s).$$

Furthermore, the normalized unknown function $g(x)$ can be rewritten as

$$g(x) = \frac{G(x)}{(1-x)^\alpha}, \tag{24}$$

where the unknown auxiliary function $G(x)$ is bounded.

The kernels $M_1(x, t)$ and $M_2(x, t)$ appearing in Equation (23) involve the computation of infinite integrals. These integrals are evaluated by using the modified form of Filon’s numerical scheme in order to account for the oscillations arising from the Bessel functions of the first kind. This integration algorithm is outlined in Appendix B. The complexity of the kernels in Equation (23) requires that the singular integral equations be solved numerically. The solution procedure involves the reduction of the integro-differential equations with Hadamard-, Cauchy-, and logarithmic-type singularities to a system of linear algebraic equations using the collocation technique introduced by Miller and Keer [1985] and later extended by Quan [1991] to include the generalized Cauchy kernel, and by Kabir et al. [1998] to include Hadamard- and logarithmic-type singularities.

In this technique, the quadrature interval $[-1, 1]$ is partitioned into a series of subintervals. The integration points, t_k , at the ends and midpoint of each subinterval are shown in Figure 2. The collocation points x_n are defined at the midpoint of two consecutive integration points.

The unknown function $G(t)$ in Equation (24) is approximated over each subinterval $t_{2k-1} \leq t \leq t_{2k+1}$, for $k = 1, \dots, N$, by quadratic Lagrange interpolation polynomials, which are given as

$$G(t) \approx \left[\frac{(t - t_{2k})^2}{h_k^2} - \frac{(t - t_{2k})}{h_k} \right] \frac{G_{2k-1}}{2} + \left[1 - \frac{(t - t_{2k})^2}{h_k^2} \right] G_{2k} + \left[\frac{(t - t_{2k})^2}{h_k^2} + \frac{(t - t_{2k})}{h_k} \right] \frac{G_{2k+1}}{2},$$

where $G_k = G(t_k)$ and $h_k = (t_{2k+1} - t_{2k-1})/2$.

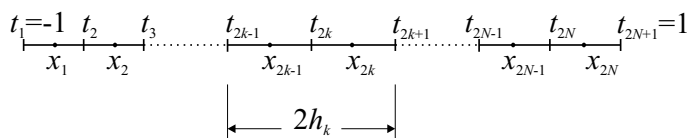


Figure 2. Discretization of the quadrature interval.

Approximation of the unknown function $G(x)$ permits the discretization of Equation (23) as

$$\sum_{m=1}^{2N+1} \left[\frac{2}{\pi a} w_m^H(x_n) G_m + \frac{1}{2\pi r_n} w_m^C(x_n) G_m + \frac{a}{16\pi r_n^2} w_m^L(x_n) G_m - \frac{a}{8\pi r_n^2} w_m^{L*}(x_n) G_m^* + M_1(x_n, t_m) v_m G_m + M_1(x_n, t_m) v_m^* G_m^* \right] + \sum_{j=1}^3 \left[i \frac{\gamma}{2r_n(1-x_n)^\alpha} (B_j G_{I+j} - B_j G_{I+j}^*) + i \frac{2\gamma}{a(1-x_n)^{1+\alpha}} B_j G_{I+j} \right] + i \frac{2\gamma}{a(1-x_n)^\alpha} \sum_{j=1}^M D_j(h_n) G_{L+j} = \frac{1}{\gamma_{11}} (p(x_n) + iq(x_n)), \quad (25)$$

where N is the number of subintervals for the unknown function $G(x)$ and $r_n = a(x_n + 1)/2$. The singular weight functions, $w_m^H(x)$, $w_m^C(x)$, $w_m^L(x)$, and v_m , as well as I and B_j , are given by Kabir et al. [1998] and L and D_j are defined by Kilic et al. [2006]. The variable with a superscript * denotes its complex conjugate.

Because this discretization results in a number of unknowns G_m , which are one more than the number of equations, an additional constraint equation becomes necessary in order to achieve a unique solution to Equation (25). However, the nature of this solution method does not yield any additional constraint equations based on the physics of the problem. Therefore, the necessary equation is introduced in an artificial way in order to achieve a unique solution, as suggested by Kabir et al. [1998] and Kilic et al. [2006]. It is obtained by multiplying the integro-differential equation given by (23) by $r^2(1 - x^2)^{3/2}$ and integrating over x between -1 and 1 . After changing the order of integrations, performing the appropriate algebraic manipulations leads to the normal and discretized forms

$$\int_{-1}^1 dt K_{1c}(t)g(t) + K_{2c}(t)g^*(t) = \tilde{g}, \quad \sum_{m=1}^{2N+1} K_{1c}(t_m)v_m G_m + K_{2c}(t_m)v_m^* G_m^* = \tilde{g}.$$

The details of the algebraic manipulations, as well as the definitions of \tilde{g} , $K_{1c}(t)$, and $K_{2c}(t)$, are given in Appendix C.

Furthermore, the examination of the kernels reveals that they approach zero as $t \rightarrow -1$ ($s \rightarrow 0$) for $x \neq -1$ ($r \neq 0$). Therefore, $G_1 = G(-1)$ disappears as $t \rightarrow -1$, for $x \neq -1$, making the first column equal to zero in the construction of the algebraic equations formed by Equation (25); thus leading to a singular coefficient matrix. To make the system of equations nonsingular, the first row of the coefficient matrix is replaced by imposing the conditions of zero radial displacement and zero slope of transverse displacement at the center of the crack, that is,

$$\text{Im}[g(t = -1)] = 0, \quad \text{Re}\left[\frac{\partial g(t = -1)}{\partial t}\right] = 0.$$

The discrete form of the singular integral equation and constraint equation can be cast into the form $A_{nm}G_m = g_m$ for $m, n = 1, \dots, 2N + 1$, where the unknown vector has form $\mathbf{G}^T = \{G_1, G_2, \dots, G_{2N+1}\}$.

N	k_1	k_2
3	0.630	-0.0929
5	0.634	-0.0979
10	0.635	-0.0992
20	0.635	-0.0995
30	0.635	-0.0996

Table 1. Convergence of stress intensity factors.

5. Numerical results

To establish the number of subintervals associated with the unknown functions, the problem of a penny-shaped crack at the interface of two semi-infinite dissimilar materials under unit pressure is considered. Material properties are the same as those given by Kassir and Bregman [1972], and Young’s modulus and Poisson’s ratio have numerical values of 3×10^7 psi and 0.3 for the material at the upper half and 10^7 psi and 0.22 for material at the lower half. The analytical solution using Equation (22) can be computed as $k_1 + ik_2 = 0.635 - 0.0996i$. The convergence of the stress intensity factors as a function of number of integration points is presented in Table 1. As demonstrated in this table, the numerical technique used in this study gives 3-digit accuracy, as compared to analytical solution using only 30 integration points. Therefore, in the solution of the integral equations, the number of subintervals associated with the unknown function is chosen to be 100. The material properties used in this analysis are the same as those given by Farris and Keer [1985] and Wan et al. [2003], and their values are presented in Table 2. In this table, the aluminum layer of 7075-T6 Al represents the rigid substrate, and the polymeric materials represent the film.

The validity of the results of the present analysis was established by comparing the crack opening and sliding displacements with the finite element predictions. Finite element analysis was conducted using PLANE42 elements of the commercially available package ANSYS®. The PLANE42 element can be used as an axisymmetric element with four nodes, having two degrees of freedom at each node. In the finite element discretization, the radius of the material layer is 20 times that of the crack radius in order to represent infinite length in radial direction. The finite element mesh has 50 equally spaced nodes in the radial direction along the crack surface. The elements surrounding the crack tip are of traditional elements without special treatment of the singularity at the crack tip.

Material	Modulus (MPa)	Poisson’s Ratio
7075-T6 Al Alloy	7.1705×10^4	0.33
Polymeric Material	4.0×10^3	0.35
Solithane 113	3.447	0.499
PMMA	2.758	0.495

Table 2. Mechanical properties of materials.

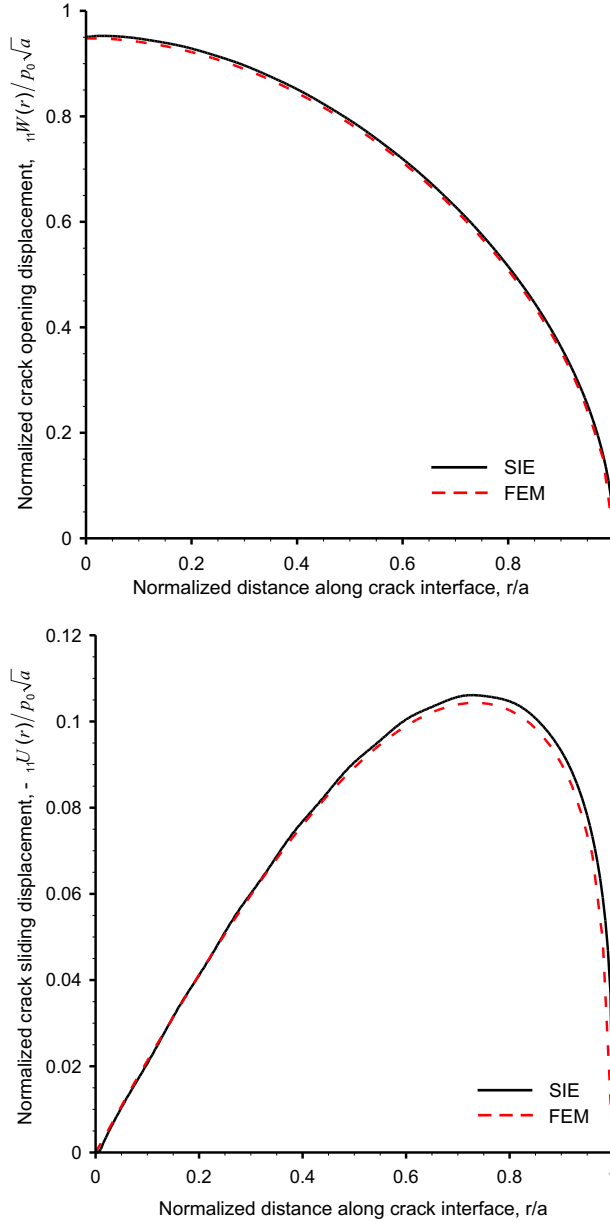


Figure 3. Crack opening (top) and sliding (bottom) displacement between 7075-T6 Al substrate and polymeric film for $h_2/h_1 = 1$.

In the validation of the present analysis against the finite element predictions, the film thickness is taken to be equal to that of the substrate, $h_2/h_1 = 1$, and the crack length is equal to that of the thin film thickness, $h_2/a = 1$. As shown in [Figure 3](#), predictions of the present analysis are in remarkable agreement with the finite element results. To capture the effects of thin film thickness on the fracture parameters, the ratio of thin film thickness to crack radius h_2/a is varied ranging from 0.4 to 4.

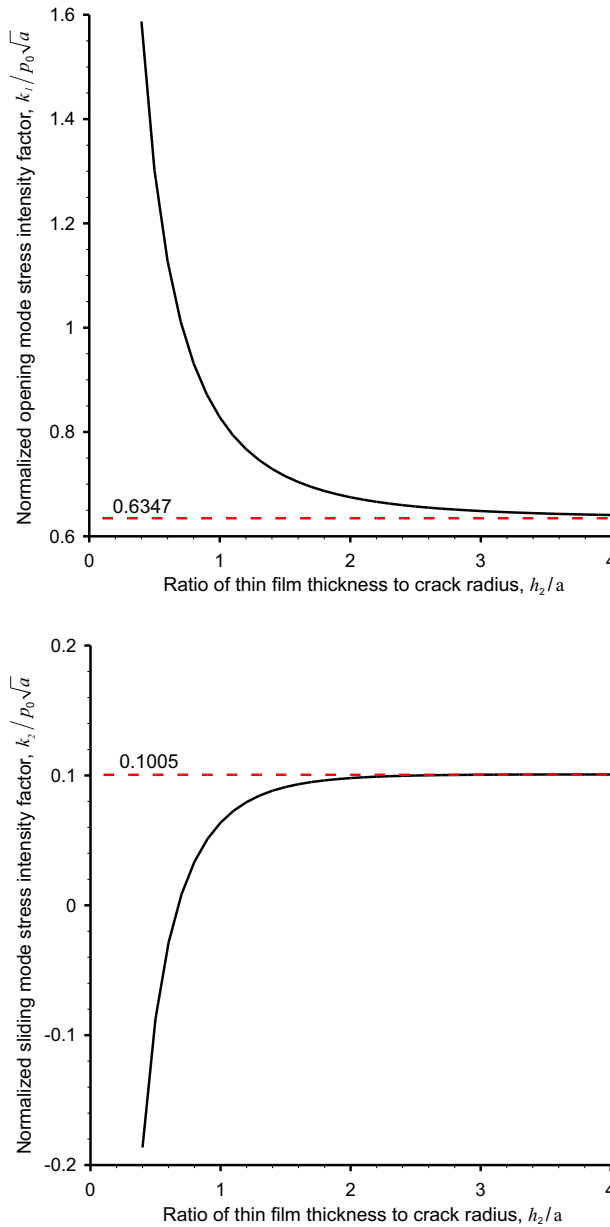


Figure 4. Opening (top) and sliding (bottom) mode stress intensity factor for a crack between 7075-T6 Al substrate and polymeric film for $h_2/h_1 = 1$.

As observed in Figures 4–5, the energy release rate and stress intensity factors for the opening and sliding modes increase as the ratio of h_2/a decreases. The complex stress intensity factor approaches the limiting value given by Kassir and Bregman [1972] as the ratio of h_2/a increases. The central deflection as a function of the ratio h_2/a is shown in Figure 6.

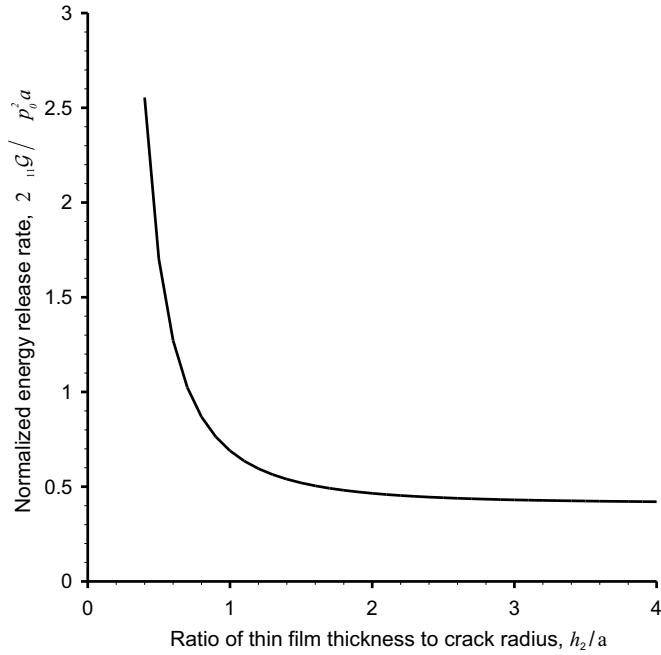


Figure 5. Energy release rate at a crack front between 7075-T6 Al substrate and polymeric film for $h_2/h_1 = 1$.

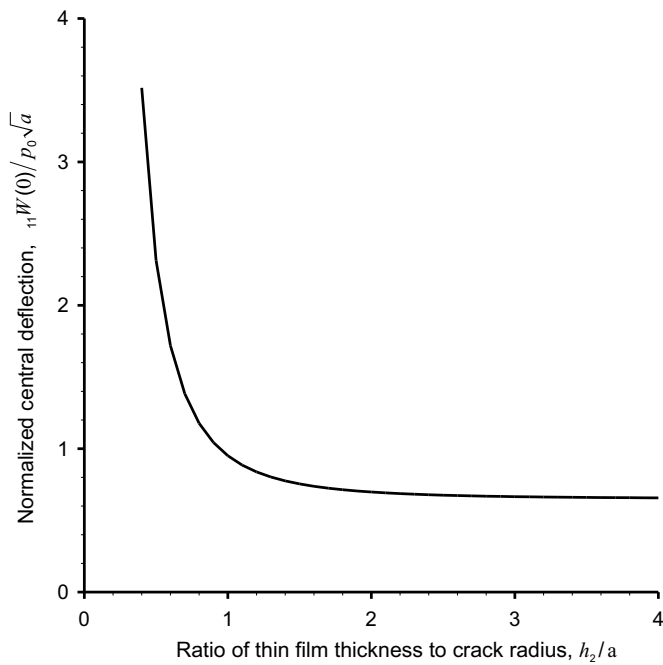


Figure 6. Central deflection of a crack between 7075-T6 Al substrate and polymeric film for $h_2/h_1 = 1$.

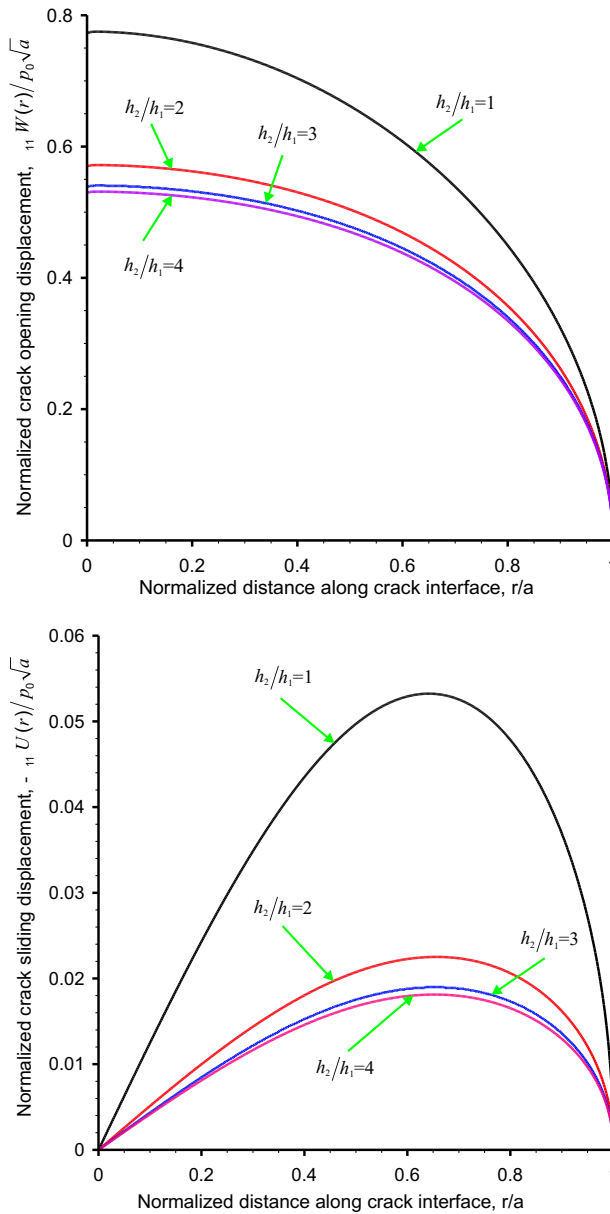


Figure 7. Crack opening (top) and sliding (bottom) displacement between Solithane 113 and PMMA material layers.

If the adhesive between the two material layers has a comparable modulus, it should be explicitly included in the analysis. The present analysis can be used to model such a material system. To illustrate this capability, the adherend material PMMA is attached to a rigid substrate using the adhesive material Solithane 113. The results are presented for four different adherend-to-adhesive thickness ratios

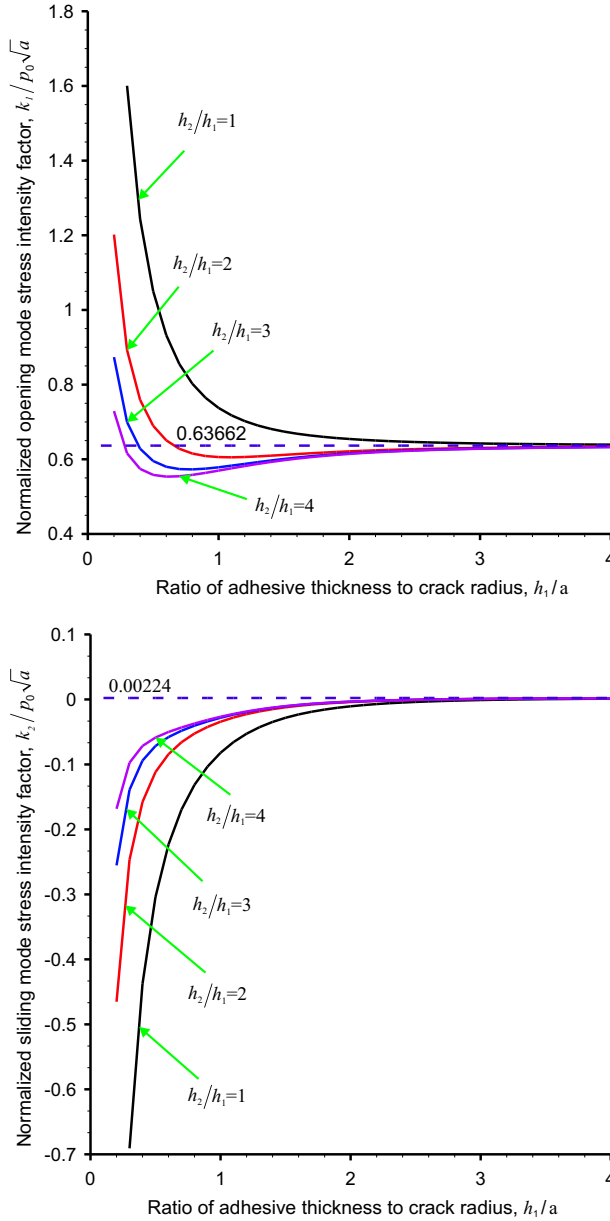


Figure 8. Opening (top) and sliding (bottom) mode stress intensity factor for a crack between Solithane 113 and PMMA material layers.

of $h_2/h_1 = 1$ and 4 by an increment of 1. The crack opening and sliding displacements are shown in Figure 7. The stress intensity factors and energy release rate increase as h_1/a decreases for $h_2/h_1 = 1$, as presented in Figures 8–9. However, for $h_2/h_1 = 4$, the stress intensity factor for the opening mode and energy release rate have a minimum at $h_1/a \approx 0.75$, as also pointed out by Farris and Keer [1985], but the stress intensity factor for the sliding mode increases as h_1/a decreases. Similar behavior is observed for

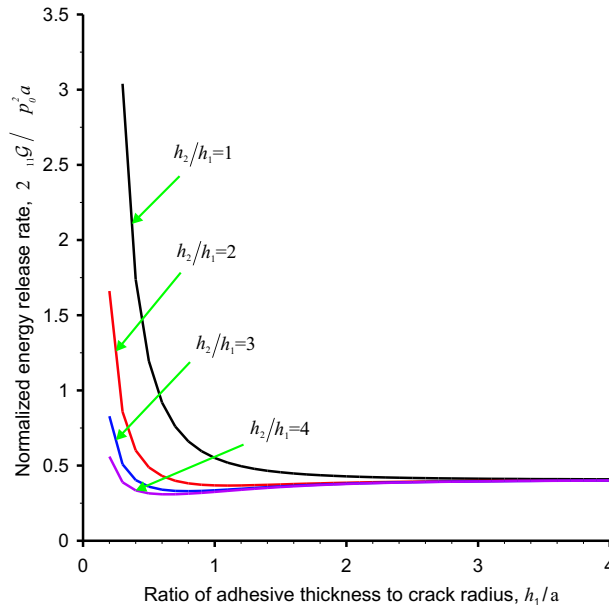


Figure 9. Energy release rate at a crack front between Solithane 113 and PMMA material layers.

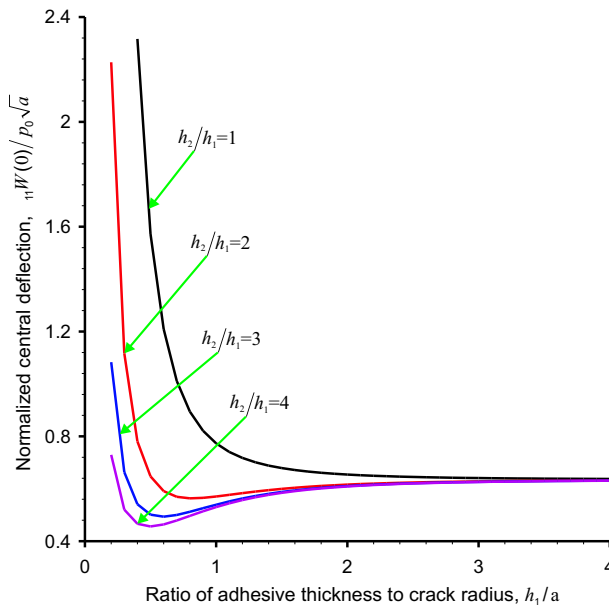


Figure 10. Central deflection of a crack between Solithane 113 and PMMA material layers.

$h_2/h_1 = 2$ and $h_2/h_1 = 3$. As the h_1/a ratio increases, the complex stress intensity factor approaches that given by Kassir and Bregman [1972]. The crack opening displacements at the center are also presented in Figure 10.

6. Conclusions

By using the linear theory of elasticity and applying the appropriate mixed boundary conditions, the interface penny-shaped crack problem is reduced to a boundary-value problem. The formulation of this boundary-value problem leads to a singular integral equation of the Hadamard-, Cauchy-, and logarithmic-type, which is solved numerically to directly obtain the crack opening and sliding displacements, as well as the stress intensity factors and energy release rate. Numerical results are validated by comparing against the crack opening and sliding displacements obtained from the finite element analysis. The limiting value of the complex stress intensity factor for which both the substrate and film thicknesses approach infinity is also in agreement with the analytical benchmark solution. The present analysis can be used to investigate the interface toughness between not only the film and rigid substrate but also the film and adhesive, which have comparable magnitudes of elastic moduli. Within the context of solution methods available in the literature, this study, for the first time, presents an approach for constructing the solution of a singular integral equation in the presence of a combination of Hadamard, Cauchy, and logarithmic singularities.

Appendix A

The matrix C in Equation (13) is given by

$$\begin{bmatrix}
 -\rho & -\kappa_2 & \rho & -\kappa_2 & \rho & \kappa_1 & -\rho & \kappa_1 \\
 \rho & 0 & \rho & 0 & -\rho & 0 & -\rho & 0 \\
 2\mu_2\rho & (1+\kappa_2)\mu_2 & 2\mu_2\rho & -(1+\kappa_2)\mu_2 & -2\mu_1\rho & -(1+\kappa_1)\mu_1 & -2\mu_1\rho & (1+\kappa_1)\mu_1 \\
 2\mu_2\rho & (\kappa_2-1)\mu_2 & -2\mu_2\rho & (\kappa_2-1)\mu_2 & -2\mu_1\rho & -(\kappa_1-1)\mu_1 & 2\mu_1\rho & -(\kappa_1-1)\mu_1 \\
 0 & 0 & 0 & 0 & e^{\rho h_1} & -h_1 e^{\rho h_1} & e^{-\rho h_1} & -h_1 e^{-\rho h_1} \\
 0 & 0 & 0 & 0 & e^{\rho h_1} & \left(\frac{\kappa_1}{\rho} - h_1\right)e^{\rho h_1} & -e^{-\rho h_1} & \left(\frac{\kappa_1}{\rho} + h_1\right)e^{-\rho h_1} \\
 2\rho e^{-\rho h_2} & (\kappa_2+1+2\rho h_2)e^{-\rho h_2} & 2\rho e^{\rho h_2} & -(\kappa_2+1-2\rho h_2)e^{\rho h_2} & 0 & 0 & 0 & 0 \\
 2\rho e^{-\rho h_2} & (\kappa_2-1+2\rho h_2)e^{-\rho h_2} & -2\rho e^{\rho h_2} & (\kappa_2-1-2\rho h_2)e^{\rho h_2} & 0 & 0 & 0 & 0
 \end{bmatrix}$$

The vectors a and b , also from Equation (11), are given by $a^T = [A_{21} \ A_{22} \ A_{23} \ A_{24} \ A_{11} \ A_{12} \ A_{13} \ A_{14}]$, and $b^T = [G_1(\rho) \ G_2(\rho) \ 0 \ 0 \ 0 \ 0 \ 0 \ 0]$, where superscript T represents the transpose. The kernels appearing in infinite integrals in Equation (16) are expressed as

$$\begin{aligned}
 H_{11}(\rho) &= \mu_2[(1 + \kappa_2)(B_{41} - B_{21}) - 2\rho(B_{11} + B_{31})], \\
 H_{12}(\rho) &= \mu_2[(1 + \kappa_2)(B_{42} - B_{22}) - 2\rho(B_{12} + B_{32})], \\
 H_{21}(\rho) &= \mu_2[(1 - \kappa_2)(B_{41} + B_{21}) - 2\rho(B_{11} - B_{31})], \\
 H_{22}(\rho) &= \mu_2[(1 - \kappa_2)(B_{42} + B_{22}) - 2\rho(B_{12} - B_{32})],
 \end{aligned}$$

where the coefficients $B_{ij} = C_{ij}^{-1}$.

The closed-form evaluation of certain integrals that are used in Equations (17)–(19) are

$$\begin{aligned} \int_0^\infty d\rho J_1(\rho r) J_1(\rho s) &= \frac{2}{\pi} \begin{cases} \frac{1}{s} [K(s/r) - E(s/r)], & s < r, \\ \frac{1}{r} [K(r/s) - E(r/s)], & s > r, \end{cases} \\ \int_0^\infty d\rho J_0(\rho r) J_0(\rho s) &= \frac{2}{\pi} \begin{cases} \frac{1}{r} K(s/r), & s < r, \\ \frac{1}{s} K(r/s), & s > r, \end{cases} \\ s \int_0^\infty d\rho \rho J_m(\rho r) J_m(\rho s) &= \delta(r - s), \end{aligned} \tag{A.1}$$

where $\delta(r)$ is the Dirac delta function. The complete elliptic integrals of the first and second kind, K and E , respectively, are defined by

$$K(m) = \int_0^{\pi/2} \frac{d\theta}{\sqrt{1 - m^2 \sin^2 \theta}}, \quad E(m) = \int_0^{\pi/2} d\theta \sqrt{1 - m^2 \sin^2 \theta}, \tag{A.2}$$

where $-1 \leq m \leq 1$. The functions $m_{11}(r, s)$ and $m_{22}(r, s)$ appearing in Equation (20) are defined as

$$m_{11}(r, s) = \begin{cases} \frac{2s(2r^2 E(s/r) + (s^2 - r^2)K(s/r))}{\pi r(s^2 - r^2)^2}, & s < r, \\ \frac{4s^2 E(r/s) - 2(s^2 - r^2)K(r/s)}{\pi(s^2 - r^2)^2}, & s > r, \end{cases} \quad m_{22}(r, s) = \begin{cases} \frac{2((s^2 + r^2)E(s/r) + (s^2 - r^2)K(s/r))}{\pi(s^2 - r^2)^2}, & s < r, \\ \frac{2s((s^2 + r^2)E(r/s) - (s^2 - r^2)K(r/s))}{\pi r(s^2 - r^2)^2}, & s > r, \end{cases}$$

in which K and E are the complete first and second kind elliptic integrals, respectively, and their explicit forms are given by Equation (A.2).

Appendix B

The approximate evaluation of the integrals of type $I(r, s, t; a, b) = \int_a^b dx f(x)\chi_1(rx)\chi_2(sx)\chi_3(tx)$, in which χ_i , with $i = 1, 2, 3$, are functions that possibly have oscillatory behavior (for example, Bessel functions) and $f(x)$ being smooth in the interval $[a, b]$ can be achieved by

$$I(r, s, t; a, b) = \sum_{j=1}^N I_j(r, s, t; x_{2j-1}, x_{2j+1}), \tag{B.1}$$

in which N is the number of subintervals in the interval $[a, b]$. Although it is not necessary for the subintervals to have the same abscissa, the subinterval lengths are taken as equal for simplicity, leading to equal integration intervals $x_{2j-1} - x_{2j+1} = (b - a)/N$. I_j is defined as

$$I_j(r, s, t; x_{2j-1}, x_{2j+1}) = \int_{x_{2j-1}}^{x_{2j+1}} dx f(x)\chi_1(rx)\chi_2(sx)\chi_3(tx). \tag{B.2}$$

Over the subinterval $[x_{2j-1}, x_{2j+1}]$, this integral can be approximated as $I_j(r, s, t; x_{2j-1}, x_{2j+1}) = w_{2j-1} f(x_{2j-1}) + w_{2j} f(x_{2j}) + w_{2j+1} f(x_{2j+1})$, where w_{2j-1} , w_{2j} , and w_{2j+1} are the integration weights. They are determined by assuming a quadratic variation of the product of the functions χ_i , with $i = 1, 2, 3$,

in the interval $[x_{2j-1}, x_{2j+1}]$ with $n = 0, 1, 2$ such that

$$\int_{x_{2j-1}}^{x_{2j+1}} dx x^n \chi_1(rx) \chi_2(sx) \chi_3(tx) = x_{2j-1}^n w_{2j-1} + x_{2j}^n w_{2j} + x_{2j+1}^n w_{2j+1} = R_n. \tag{B.3}$$

In matrix form, these equations are rewritten as

$$\begin{bmatrix} 1 & 1 & 1 \\ x_{2j-1} & x_{2j} & x_{2j+1} \\ x_{2j-1}^2 & x_{2j}^2 & x_{2j+1}^2 \end{bmatrix} \begin{bmatrix} w_{2j-1} \\ w_{2j} \\ w_{2j+1} \end{bmatrix} = \begin{bmatrix} R_0 \\ R_1 \\ R_2 \end{bmatrix}, \tag{B.4}$$

from which the weights are computed after the evaluation of the expressions for $R_n(r, s, t; x_{2j-1}, x_{2j+1})$. This is achieved by defining the variable $x = az + x_{2j}$, with $a = (x_{2j+1} - x_{2j-1})/2$, and by approximating the functions χ_i , with $i = 1, 2, 3$, in the integrals in Equation (B.2) using the Chebyshev polynomials of the first kind as

$$\chi_i(p(az + x_{2j})) = \sum_{m=0}^{M_i} b_m T_m(z), \quad \text{with } p \in \{r, s, t\}, \tag{B.5}$$

in which M_i , with $i = 1, 2, 3$, is the highest degree of Chebyshev polynomial used in the approximation and the coefficients are given by

$$b_m = \frac{c}{M_i} \left(\chi_i(p(az_0 + x_{2j})) + (-1)^m \chi_i(p(az_{M_i} + x_{2j})) + 2 \sum_{k=1}^{M_i-1} \chi_i(p(az_k + x_{2j})) \cos \frac{mk\pi}{M_i} \right),$$

in which $z_k = \cos(k\pi/M_i)$, $c = 1$ for $m = 1, \dots, M_i - 1$ and $c = 1/2$ for $m = 0, M_i$. Substitution from Equation (B.5) into Equation (B.3) with $n = 0, 1, 2$ results in

$$R_n = a \sum_{p=0}^{M_1} \sum_{r=0}^{M_2} \sum_{s=0}^{M_3} b_{1p} b_{2r} b_{3s} \int_{-1}^1 dz (az + x_{2j})^n T_p(z) T_r(z) T_s(z),$$

This expression permits the explicit evaluation of R_n with the identities [Balkan 1995]

$$\begin{aligned} \int_{-1}^1 dz T_p(z) T_r(z) T_s(z) &= F(p, r, s, 1), \\ \int_{-1}^1 dz z T_p(z) T_r(z) T_s(z) &= \frac{F(p, r, s, 2)}{2}, \\ \int_{-1}^1 dz z^2 T_p(z) T_r(z) T_s(z) &= \frac{F(p, r, s, 3) + F(p, r, s, 1)}{4}, \end{aligned}$$

in which

$$F(p, r, s, n) = \frac{1}{2} \left(\frac{s+n}{(s+n)^2 - (p+r)^2} + \frac{n-s}{(n-s)^2 - (p+r)^2} + \frac{s+n}{(s+n)^2 - (p-r)^2} + \frac{n-s}{(n-s)^2 - (p-r)^2} \right)$$

for $p + r + s + n = \text{odd}$, and zero otherwise.

Substituting for R_n and numerically inverting the system of Equation (B.4) leads to the integration weights. Finally, the approximate value of the integrals is calculated from Equation (B.1). The accuracy

of the integration algorithm is demonstrated by considering the infinite integral $I = \int_0^\infty dx x e^{-x^2} J_0^2(x)$, with the exact solution of $I = e^{-1/2} I_0(1/2)/2 = 0.3225176352245750$, in which I_0 is the modified Bessel function of the second kind. Its numerical evaluation, with $N = 100$ and $M_i = 8$, with $i = 1, 2, 3$, for $a = 0$ and $b = 10$, and letting $f(x) = 1$, $\chi_1(x) = x e^{-x^2}$ and $\chi_2(x) = \chi_3(x) = J_0(x)$, leads to a value of 0.3225176352245752.

Appendix C

The numerical scheme used to solve a hypersingular integral equation requires an additional constraint equation to achieve a unique solution. However, the nature of the problem does not provide any constraint conditions, as opposed to formulations of the Cauchy type. Furthermore, Equation (23) has a unique solution without any additional constraint equation. Thus, a constraint equation is introduced by multiplying Equation (23), with $r^2(1 - x^2)^{3/2}$, and integrating over x as

$$\begin{aligned} & \frac{2}{\pi a} \int_{-1}^1 dt g(t) \int_{-1}^1 dx \frac{r^2(1 - x^2)^{3/2}}{(t - x)^2} + \frac{1}{2\pi} \int_{-1}^1 dt g(t) \int_{-1}^1 dx \frac{r(1 - x^2)^{3/2}}{t - x} \\ & + \frac{a}{16\pi} \int_{-1}^1 dt g(t) \int_{-1}^1 dx \ln |t - x| (1 - x^2)^{3/2} - \frac{a}{8\pi} \int_{-1}^1 dt f^*(t) \int_{-1}^1 dx \ln |t - x| (1 - x^2)^{3/2} \\ & + \int_{-1}^1 dt g(t) \int_{-1}^1 dx M_1(x, t) r^2(1 - x^2)^{3/2} + \int_{-1}^1 dt g^*(t) \int_{-1}^1 dx M_2(x, t) r^2(1 - x^2)^{3/2} \\ & + i \frac{\gamma}{2} \int_{-1}^1 dx g(x) r(1 - x^2)^{3/2} - i \frac{\gamma}{2} \int_{-1}^1 dx g^*(x) r(1 - x^2)^{3/2} \\ & + i \frac{2\gamma}{a} \int_{-1}^1 dx \frac{dg(x)}{dx} r^2(1 - x^2)^{3/2} = \int_{-1}^1 dx \frac{p(r) + iq(r)}{\gamma_{11}} r^2(1 - x^2)^{3/2}. \quad (C.1) \end{aligned}$$

This equation can be further simplified by using the results for the definite integrals of Hadamard and Cauchy types given by Kaya [1984], and the definite integrals of logarithmic type as

$$\begin{aligned} \int_{-1}^1 dt \frac{t^n \sqrt{1 - t^2}}{(t - x)^2} &= \sum_{k=1}^{n+1} k b_k x^{k-1}, & \int_{-1}^1 dt \frac{t^n \sqrt{1 - t^2}}{t - x} &= \sum_{k=0}^{n+1} b_k x^k, \\ \frac{1}{\pi} \int_{-1}^1 dt \sqrt{1 - t^2} \ln |t - x| &= \frac{x^2}{2} - \frac{1}{4}(1 + 2 \ln 2), \\ \frac{1}{\pi} \int_{-1}^1 dt t^2 \sqrt{1 - t^2} \ln |t - x| &= \frac{x^4}{4} - \frac{x^2}{4} + \frac{1}{32}(1 - 4 \ln 2), \end{aligned}$$

where

$$b_k = \frac{\sqrt{\pi}}{2} \frac{\Gamma((n - k)/2)}{\Gamma((n - k + 3)/2)}$$

for $n - k = \text{odd}$, and zero otherwise. Finally, this equation can be put into the concise form

$$\int_{-1}^1 dt K_{1c}(t)g(t) + K_{2c}(t)g^*(t) = \tilde{g},$$

$$K_{1c}(t) = \frac{a}{512}(-3(83 + \ln 16) - 1728t - 552t^2 + 2176t^3 + 1400t^4) + i\frac{3}{4}a\gamma(1+t)(-1+2t+3t^2)\sqrt{1-t^2} + \int_{-1}^1 dx M_1(x, t)r^2(1-x^2)^{3/2}, \quad (\text{C.2})$$

$$K_{2c}(t) = \frac{a}{256}(3(3 + \log 16) + 8t^2(-3+t^2)) - i\frac{a\gamma}{4}(1+t)(1-t^2)^{3/2} + \int_{-1}^1 dx M_2(x, t)r^2(1-x^2)^{3/2},$$

$$\tilde{g} = \int_{-1}^1 dx \frac{p(r) + iq(r)}{\gamma_{11}} r^2(1-x^2)^{3/2}.$$

Note that the multiplying factor, $r^2(1-x^2)^{3/2}$ is used because it permits simplification of Equation (C.1) by using known definite integrals, which leads to the accurate evaluation of constraint equation. Integration by parts is used to remove the derivative of the unknown function. Integrals appearing in Equation (C.2) can be evaluated accurately using Chebyshev polynomials of second kind [Abramowitz and Stegun 1964].

References

- [Abramowitz and Stegun 1964] M. Abramowitz and I. A. Stegun, *Handbook of mathematical functions with formulas, graphs, and mathematical tables*, vol. 55, National Bureau of Standards Applied Mathematics Series, U.S. Government Printing Office, Washington, DC, 1964. [MR 29 #4914](#) [Zbl 0171.38503](#)
- [Balkan 1995] H. Balkan, *Thin layer with circular debonding over a substrate under either axisymmetric compression or thermal loading*, Ph.D. thesis, University of Arizona, Tucson, AZ, 1995.
- [Chan et al. 2003] Y.-S. Chan, A. C. Fannjiang, and G. H. Paulino, “Integral equations with hypersingular kernels: theory and applications to fracture mechanics”, *Int. J. Eng. Sci.* **41**:7 (2003), 683–720. [MR 2004a:45004](#)
- [Erdogan 1965] F. Erdogan, “Stress distribution in bonded dissimilar materials containing circular or ring-shaped cavities”, *J. Appl. Mech. (ASME)* **87** (1965), 829–836.
- [Erdogan 1969] F. Erdogan, “Approximate solutions of systems of singular integral equations”, *SIAM J. Appl. Math.* **17**:6 (1969), 1041–1059. [MR 41 #5909](#) [Zbl 0187.12404](#)
- [Erdogan 1978] F. Erdogan, “Mixed boundary value problems in mechanics”, pp. 1–86 in *Mechanics today*, vol. 4, edited by S. Nemat-Nasser, Pergamon, New York, 1978.
- [Erdogan 1997] F. Erdogan, “Fracture mechanics of interfaces”, pp. 3–36 in *Proceedings of the First International Conference on Damage and Failure of Interfaces* (Vienna), edited by H.-P. Rossmanith, A. A. Balkema, Rotterdam, 1997.
- [Erdogan and Gupta 1971a] F. Erdogan and G. D. Gupta, “Layered composites with an interface flaw”, *Int. J. Solids Struct.* **7**:8 (1971), 1089–1107.
- [Erdogan and Gupta 1971b] F. Erdogan and G. D. Gupta, “The stress analysis of multi-layered composites with a flaw”, *Int. J. Solids Struct.* **7**:1 (1971), 39–61.
- [Farris and Keer 1985] T. N. Farris and L. M. Keer, “Williams’ blister test analyzed as an interface crack problem”, *Int. J. Fract.* **27**:2 (1985), 91–103.
- [Goldstein and Vainshelbaum 1976] R. W. Goldstein and V. M. Vainshelbaum, “Axisymmetric problem of a crack at the interface of layers in a multi-layered medium”, *Int. J. Eng. Sci.* **14**:4 (1976), 335–352.
- [Harding and Sneddon 1945] J. W. Harding and I. N. Sneddon, “The elastic stress produced by the indentation of the plane surface of a semi-infinite elastic body by a rigid punch”, *Proc. Camb. Philos. Soc.* **41** (1945), 16–26. [MR 6,251e](#) [Zbl 0060.42001](#)

- [Ioakimidis 1988a] N. I. Ioakimidis, “The hypersingular integrodifferential equation of a straight crack along the interface of two bonded isotropic elastic half-planes”, *Int. J. Fract.* **38**:4 (1988), R75–R79.
- [Ioakimidis 1988b] N. I. Ioakimidis, “Mangler-type principal value integrals in hypersingular integral equations for crack problems in plane elasticity”, *Eng. Fract. Mech.* **31**:5 (1988), 895–898.
- [Ioakimidis 1990] N. I. Ioakimidis, “Generalized Mangler-type principal value integrals with an application to fracture mechanics”, *J. Comput. Appl. Math.* **30**:2 (1990), 227–234. MR 91d:26003 Zbl 0698.73074
- [Jensen 1998] H. M. Jensen, “Analysis of mode mixity in blister tests”, *Int. J. Fract.* **94**:1 (1998), 79–88.
- [Kabir et al. 1998] H. Kabir, E. Madenci, and A. Ortega, “Numerical solution of integral equations with logarithmic-, Cauchy- and Hadamard-type singularities”, *Int. J. Numer. Methods Eng.* **41**:4 (1998), 617–638. Zbl 0905.65127
- [Kassir and Bregman 1972] M. K. Kassir and A. M. Bregman, “The stress-intensity factor for a penny-shaped crack between two dissimilar materials”, *J. Appl. Mech. (ASME)* **39** (1972), 308–310. Trans. ASME 94, Series E.
- [Kaya 1984] A. C. Kaya, *Application of integral equations with strong singularities in fracture mechanics*, Ph.D. thesis, Lehigh University, Bethlehem, PA, 1984.
- [Kaya and Erdogan 1987] A. C. Kaya and F. Erdogan, “On the solution of integral equations with strongly singular kernels”, *Quart. Appl. Math.* **45**:1 (1987), 105–122. MR 88e:45012 Zbl 0631.65139
- [Keer et al. 1978] L. K. Keer, S. H. Chen, and M. Comninou, “The interface penny-shaped crack reconsidered”, *Int. J. Eng. Sci.* **16**:10 (1978), 765–772. MR 80d:73111 Zbl 0381.73087
- [Kilic et al. 2006] B. Kilic, E. Madenci, and R. Mahajan, “Energy release rate and crack surface contact zone by hypersingular integral equations”, *Int. J. Solids Struct.* **43**:5 (2006), 1159–1188.
- [Lowengrub and Sneddon 1974] M. Lowengrub and I. N. Sneddon, “The effect of internal pressure on a penny-shaped crack at the interface of two bonded dissimilar elastic half-spaces”, *Int. J. Eng. Sci.* **12**:5 (1974), 387–396.
- [Malyshev and Salganik 1965] B. M. Malyshev and R. L. Salganik, “The strength of adhesive joints using the theory of cracks”, *Int. J. Fract. Mech.* **1**:2 (1965), 114–128.
- [Miller and Keer 1985] G. R. Miller and L. M. Keer, “A numerical technique for the solution of singular integral equations of the second kind”, *Quart. Appl. Math.* **42**:4 (1985), 455–465. MR 87c:65165a Zbl 0593.65094
- [Mossakovski and Rybka 1964] V. I. Mossakovski and M. T. Rybka, “Obobshchenie kriteriia Griffithsa–Sneddona na sluchai neodnorodnogo telas”, *Prikl. Mat. Mekh.* **28** (1964), 1061–1069. In Russian; translation in *J. Appl. Math. Mech.* **28**:6 (1964), 1277–1286. Zbl 0141.42504
- [Muskhelishvili 1992] N. I. Muskhelishvili, *Singular integral equations*, 2nd ed., Dover, New York, 1992. MR 94a:45001 Zbl 0174.16201
- [Ozturk and Erdogan 1996] M. Ozturk and F. Erdogan, “Axisymmetric crack problem in bonded materials with a graded interfacial region”, *Int. J. Solids Struct.* **33**:2 (1996), 193–219.
- [Quan 1991] M. A. Quan, *Analysis of a finite interface crack emitting from the junction of three sectors*, Ph.D. thesis, University of California, Los Angeles, 1991.
- [Wan et al. 2003] K.-T. Wan, S. Guo, and D. A. Dillard, “A theoretical and numerical study of a thin clamped circular film under an external load in the presence of a tensile residual stress”, *Thin Solid Films* **425**:1 (2003), 150–162.
- [Willis 1972] J. R. Willis, “The penny-shaped crack on an interface”, *Q. J. Mech. Appl. Math.* **25**:3 (1972), 367–385.

Received 21 Feb 2006. Revised 25 Sep 2006. Accepted 29 Nov 2006.

BAHATTIN KILIC: bkilic@email.arizona.edu

Department of Aerospace and Mechanical Engineering, The University of Arizona, Tucson, AZ 85721, United States

ERDOGAN MADENCI: madenci@email.arizona.edu

Department of Aerospace and Mechanical Engineering, The University of Arizona, Tucson, AZ 85721, United States

WAVELET SPECTRAL ELEMENT FOR WAVE PROPAGATION STUDIES IN PRESSURE LOADED AXISYMMETRIC CYLINDERS

MIRA MITRA AND S. GOPALAKRISHNAN

We study transient wave propagation in a pressure loaded isotropic cylinder under axisymmetric conditions. A 2-D wavelet based spectral finite element (WSFE) is developed to model the cylinder with radial and axial displacements. The method involves a Daubechies compactly supported scaling function approximation in the temporal dimension and one spatial (axial direction) dimension. This reduces the governing partial differential wave equation into a set of variable coefficient ODEs, which are then solved using Bessel's function approximation. This spectral method captures the exact inertial distribution and thus results in large computational savings compared to the conventional finite element (FE) formulation. In addition, the use of localized basis functions in the present formulation circumvents several serious limitations of the previous FFT based techniques. Here, the proposed method is used to study radial and axial wave propagation in cylinders with different configurations. The analysis is performed in both time and frequency domains. The time domain responses are validated with 2-D FE results.

1. Introduction

Wave propagation analysis in cylindrical structures is of much relevance for its applications to problems like health monitoring of fluid carrying pipes, excavation casings, and so on [Yin and Yue 2002; El-Raheb 2005]. Recently, with the advent of carbon nanotubes, researchers have been working towards dynamic and wave propagation analyses [Mahan 2002; Wang et al. 2005] of hollow cylindrical shells resembling the carbon nanotube configuration.

Wave propagation problems deal with high frequency excitations and the FE modeling is not computationally viable here as the element size has to be comparable to wavelengths, which are very small at higher frequencies. This results in large system size, and thus alternative numerical schemes [Bao et al. 1999; Godinho et al. 2003; 2004] are generally developed, which are highly accurate in numerical differentiation and also computationally efficient. The FFT based Spectral Finite Element (FSFE) [Doyle 1999] is one such technique specially formulated for wave propagation analysis, and it follows the FE procedure in the transformed frequency domain. In FSFE for 2-D problems, the nodal displacements are related to the nodal forces through a frequency-wavenumber dependent dynamic stiffness matrix. It captures the mass distribution accurately and hence makes it possible to derive the exact elemental matrix. Thus in the absence of discontinuities, a single element is sufficient to model the 2-D structure of any length but unbounded along one spatial dimension.

The main drawback of FSFE is that it cannot handle waveguides of short lengths. This is because the periodicity assumption in the time approximation results in wrap-around for smaller time windows, which totally distorts the response. In addition, for 2-D problems, FSFE are essentially semi-infinite, that

Keywords: wave propagation, wavelets, spectral finite element, axisymmetry.

is, bounded in only one direction. Thus the effect of one spatial boundary cannot be captured and this is attributed to the global nature of the basis functions of the Fourier series approximation of the spatial dimension. However, in Wavelet based Spectral Finite Element (WSFE) [Mitra and Gopalakrishnan 2005], use of localized Daubechies [1992] compactly supported wavelets as basis functions removes the wrap-around problem and can efficiently model undamped structures of finite length. For 2-D problems WSFE [Mitra and Gopalakrishnan 2006c; 2006b] can accurately model structures of finite dimensions. This is again due to the use of localized Daubechies scaling functions as the basis for approximation of spatial dimension.

The governing differential equations for axisymmetric structures have variable coefficients. Thus the 2-D WSFE formulation for these problems is different from that for WSFE for plates [Mitra and Gopalakrishnan 2006c; 2006b]. Here, unlike plates, the reduced ODEs obtained after transformations of the PDEs are variable coefficient equations which have Bessel's function as their solution. Hence, the shape functions are obtained in terms of Bessel's functions. The formulation of the elemental dynamic stiffness matrix from these shape functions is very similar to that in FE.

As in the case of 2-D FSFE, the frequency dependent wave characteristics corresponding to each spatial (axial) wavenumber, can be extracted from our WSFE formulation. However, unlike FSFE, the wavenumbers will be accurate only up to a certain fraction of the Nyquist frequency [Mitra and Gopalakrishnan 2006a]. In addition, here the governing PDE involves variable coefficients as a function of the radius and hence the spectrum relations are derived for a certain radius following a similar procedure as for the WSFE method for plates. Thus the frequency dependent spectrum relation obtained for such axisymmetric problems varies for both axial wavenumbers and the radius.

The paper is organized as follows. Section 2 elaborates the reduction of PDEs to ODEs, Section 3 contains the frequency domain analysis and Section 4 the spectral finite element formulation. Numerical results for time and frequency domains for different cylinder configurations are presented in Section 5. The simulated responses are validated with 2-D FE analysis. The paper ends with important conclusions.

2. Reductions of wave equations to ODEs

The steps followed in 2-D WSFE for an axisymmetric cylinder are as follows. Here, first the Daubechies scaling functions are used for approximation in time and this reduces the governing PDEs with variable coefficients into a set of coupled PDEs in spatial dimensions. The wavelet extrapolation technique proposed by Williams and Amaratunga [1997] is used for adapting wavelets in the finite domain and the imposition of initial conditions. The coupled transformed PDEs are decoupled through eigenvalue analysis. Though the eigen analysis involved is time consuming, this can be computed and stored as it is not dependent on the particular problem. Next, each of these decoupled PDEs are further reduced to a set of coupled ODEs by using the same Daubechies scaling functions for approximation in the spatial dimension. Unlike the temporal approximation, here, the scaling function coefficients lying outside the finite domain are not extrapolated but obtained through periodic extension for unrestrained (free) axial edges. In this paper, the formulation and examples are presented only for unrestrained axial boundary conditions. However, other boundary conditions such as fixed-fixed or free-fixed can also be imposed through a restrain matrix [Mitra and Gopalakrishnan 2006c]. Each set of these ODEs is coupled, and here decoupling can only be done for unrestrained boundary conditions. As said earlier, these decoupled ODEs have coefficients

that vary with the radius. Here, the Bessel function solution is used as interpolating functions and the elemental dynamic stiffness matrix is obtained using these functions. The above mentioned steps are discussed in detail in the following subsections.

2.1. Governing differential equations. The governing differential equations for a hollow cylindrical structure are generally written in cylindrical coordinate system (r, θ, z) , which denotes the radial, circumferential and axial directions. The displacement components are u, v and w in the radial, circumferential and axial directions. For the axisymmetric condition, the circumferential displacement v and the variations of the other two displacements with respect to θ are not considered in the modeling. Thus the equations of motion for an axisymmetric isotropic hollow cylinder contain only displacements u, w with variations along r, z (see Figure 1) and time t , and can be written as

$$\begin{aligned}
 (\lambda + 2\mu)\nabla_0^2\Delta &= \rho\frac{\partial^2\Delta}{\partial t^2}, \\
 c_d^2\nabla_0^2\Delta &= \frac{\partial^2\Delta}{\partial t^2}, \quad c_d^2 = (\lambda + 2\mu)/\rho,
 \end{aligned}
 \tag{1}$$

$$\begin{aligned}
 \mu\nabla_1^2\mathcal{U}_\theta &= \rho\frac{\partial^2\mathcal{U}_\theta}{\partial t^2}, \\
 c_s^2\nabla_1^2\mathcal{U}_\theta &= \frac{\partial^2\mathcal{U}_\theta}{\partial t^2}, \quad c_s^2 = \mu/\rho,
 \end{aligned}
 \tag{2}$$

where ∇_n^2 , for subscripts $n = 0$ and 1 , is defined by

$$\nabla_n^2 \equiv \frac{\partial^2}{\partial r^2} + \frac{1}{r}\frac{\partial}{\partial r} - \frac{n^2}{r^2} + \frac{\partial^2}{\partial z^2}.$$

The variables Δ and \mathcal{U}_θ are dilation and rotation vectors reduced for axisymmetric motions as

$$\Delta = \frac{1}{r}\frac{\partial(ru)}{\partial r} + \frac{\partial w}{\partial z}, \quad \mathcal{U}_\theta = \frac{\partial u}{\partial z} - \frac{\partial w}{\partial r},
 \tag{3}$$

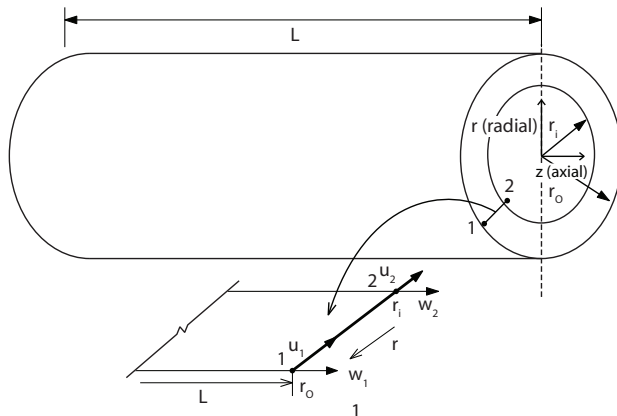


Figure 1. Axisymmetric element with nodal displacements and forces.

and λ, μ are the Lamé’s constants and ρ is the mass density. From Equations (3), the displacements can be written in decoupled form as

$$\nabla_1^2 u = \frac{\partial \Delta}{\partial r} + \frac{\partial \mathcal{U}_\theta}{\partial z}, \quad \nabla_0^2 w = \frac{\partial \Delta}{\partial z} - \frac{1}{r} \frac{\partial (r \mathcal{U}_\theta)}{\partial r}. \tag{4}$$

The associated boundary conditions are

$$\sigma_r = \lambda \Delta + 2\mu \frac{\partial u}{\partial r}, \quad \sigma_z = \mu \frac{\partial u}{\partial z} + \frac{\partial w}{\partial r}, \tag{5}$$

where σ_r and σ_z are the radial and axial forces acting on the surface of the cylinder along the z direction.

2.2. Daubechies compactly supported wavelets. A concise review of orthogonal basis of Daubechies wavelets Daubechies 1992 is provided. The wavelets $\psi_{j,k}(t)$ form compactly supported orthonormal basis for $L^2(\mathbb{R})$. The wavelets and the associated scaling functions $\varphi_{j,k}(t)$ are obtained by translation and dilation of single functions $\psi(t)$ and $\varphi(t)$:

$$\psi_{j,k}(t) = 2^{j/2} \psi(2^j t - k), \quad \varphi_{j,k}(t) = 2^{j/2} \varphi(2^j t - k), \quad j, k \in \mathbb{Z}.$$

The scaling functions $\varphi(t)$ are derived from the dilation or scaling equation,

$$\varphi(t) = \sum_k a_k \varphi(2t - k),$$

and the wavelet function $\psi(t)$ is obtained as

$$\psi(t) = \sum_k (-1)^k a_{1-k} \varphi(2t - k).$$

The a_k are the filter coefficients and are fixed for specific wavelet or scaling function basis. For compactly supported wavelets only a finite number of a_k are nonzero. The filter coefficients a_k are derived by imposing certain constraints on the scaling functions which are as follows. (1) The area under scaling function is normalized to one. (2) The scaling function $\varphi(t)$ and its translates are orthonormal. (3) The wavelet function $\psi(t)$ has M vanishing moments. The number of vanishing moments M denotes the order N of the Daubechies wavelet, where $N = 2M$.

Let $P_j(f)(t)$ be the approximation of a function $f(t)$ in $L^2(\mathbb{R})$ using $\varphi_{j,k}(t)$ as a basis, at a certain level (resolution) j . Then

$$P_j(f)(t) = \sum_k c_{j,k} \varphi_{j,k}(t), \quad k \in \mathbb{Z},$$

where the $c_{j,k}$ are the approximation coefficients.

2.3. Temporal approximation. The first step of formulation of WSFE is the reduction of each of the two governing differential equations (1) and (2) with variables Δ and \mathcal{U}_θ , to a set of PDEs in spatial dimensions by Daubechies scaling function based transformation in time. The procedure has been discussed earlier in [Mitra and Gopalakrishnan 2005; 2006c] for WSFE formulation for beams and plates, respectively and is described here in brief for completeness. Let $\Delta(r, z, t)$ be discretized at n points in the time window $[0, t_f]$. Let $\tau = 0, 1, \dots, n - 1$ be the sampling points; then

$$t = \Delta t \tau,$$

where Δt is the time interval between two sampling points. The function $\Delta(r, z, t)$ can be approximated by the scaling function $\varphi(\tau)$ at an arbitrary scale as

$$\Delta(r, z, t) = \Delta(r, z, \tau) = \sum_k \Delta_k(r, z) \varphi(\tau - k), \quad k \in \mathbb{Z},$$

where the $\Delta_k(r, z)$ (written Δ_k hereafter) are the approximation coefficients at spatial coordinates r and z and (1) can be written as

$$\sum_k c_d^2 \left(\frac{\partial^2}{\partial r^2} + \frac{1}{r} \frac{\partial}{\partial r} + \frac{\partial^2}{\partial z^2} \right) \Delta_k \varphi(\tau - k) = \frac{1}{\Delta t^2} \sum_k \Delta_k \varphi''(\tau - k). \tag{6}$$

Taking the inner product of both sides with the translates of scaling functions $\varphi(\tau - j)$, where $j = 0, 1, \dots, n - 1$ and using their orthogonal properties, we get n simultaneous PDEs:

$$c_d^2 \left(\frac{\partial^2}{\partial r^2} + \frac{1}{r} \frac{\partial}{\partial r} + \frac{\partial^2}{\partial z^2} \right) \Delta_j = \frac{1}{\Delta t^2} \sum_{k=j-N+2}^{j+N-2} \Omega_{j-k}^2 \Delta_k, \quad j = 0, 1, \dots, n-1, \tag{7}$$

where N is the order of the Daubechies wavelet and the Ω_{j-k}^2 are the connection coefficients, defined by

$$\Omega_{j-k}^2 = \int \varphi''(\tau - k) \varphi(\tau - j) d\tau. \tag{8}$$

Similarly, for the first-order derivative, the Ω_{j-k}^1 are defined by

$$\Omega_{j-k}^1 = \int \varphi'(\tau - k) \varphi(\tau - j) d\tau.$$

For compactly supported wavelets, $\Omega_{j-k}^1, \Omega_{j-k}^2$ are nonzero only in the interval $k = j - N + 2$ to $k = j + N - 2$. The detail for evaluation of connection coefficients for different derivative orders is given in [Beylkin 1992].

It can be observed from the PDEs given by (7) that certain coefficients Δ_j near the vicinity of the boundaries ($j = 0$ and $j = n - 1$) lie outside the time window $[0, t_f]$ defined by $j = 0, 1, \dots, n - 1$. These coefficients must be treated properly for finite domain analysis. Here, a wavelet based extrapolation scheme [Williams and Amaratunga 1997] is implemented for the solution of boundary value problems. This approach allows treatment of finite length data and uses polynomials to extrapolate the coefficients lying outside the finite domain either from interior coefficients or initial/boundary values. The method is particularly suitable for approximation in time, because of the ease of imposing initial values. The method converts the PDEs (7) to a set of coupled PDEs:

$$c_d^2 \left(\frac{\partial^2}{\partial r^2} + \frac{1}{r} \frac{\partial}{\partial r} + \frac{\partial^2}{\partial z^2} \right) \{ \Delta_j \} = [\Gamma^1]^2 \{ \Delta_j \}, \tag{9}$$

where Γ^1 is the first order connection coefficient matrix obtained after using the wavelet extrapolation technique. It should be mentioned here that though the connection coefficients matrix, Γ^2 , for the second order derivative can be obtained independently, here it is written as $[\Gamma^1]^2$ as it helps to impose the

initial conditions [Mitra and Gopalakrishnan 2005]. These coupled PDEs are decoupled using eigenvalue analysis, via

$$\Gamma^1 = \Phi \Pi \Phi^{-1},$$

where Π is the diagonal eigenvalue matrix and Φ is the eigenvectors matrix of Γ^1 . Let the eigenvalues be $i\gamma_j$, with $i = \sqrt{-1}$. The decoupled PDEs corresponding to Equations (9) are

$$c_d^2 \left(\frac{\partial^2}{\partial r^2} + \frac{1}{r} \frac{\partial}{\partial r} + \frac{\partial^2}{\partial z^2} \right) \widehat{\Delta}_j = -\gamma_j^2 \widehat{\Delta}_j \quad j = 0, 1, \dots, n-1, \tag{10}$$

where $\widehat{\Delta}_j$ is

$$\widehat{\Delta}_j = \Phi^{-1} \Delta_j.$$

Following the same steps, the final transformed form of (2) is

$$c_s^2 \left(\frac{\partial^2}{\partial r^2} + \frac{1}{r} \frac{\partial}{\partial r} - \frac{1}{r^2} + \frac{\partial^2}{\partial z^2} \right) \widehat{U}_{\theta j} = -\gamma_j^2 \widehat{U}_{\theta j} \quad j = 0, 1, \dots, n-1. \tag{11}$$

Similarly, the transformed form of the decoupled displacement equations (4) and force boundary conditions (5) can be written as

$$\nabla_1^2 \widehat{u}_j = \frac{\partial \widehat{\Delta}_j}{\partial r} + \frac{\partial \widehat{U}_{\theta j}}{\partial z}, \quad \nabla_0^2 \widehat{w}_j = \frac{\partial \widehat{\Delta}_j}{\partial z} - \frac{1}{r} \frac{\partial (r \widehat{U}_{\theta j})}{\partial r}, \tag{12}$$

$$\widehat{\sigma}_{rj} = \lambda \widehat{\Delta}_j + 2\mu \frac{\partial \widehat{u}_j}{\partial r}, \quad \widehat{\sigma}_{zj} = \mu \frac{\partial \widehat{u}_j}{\partial z} + \frac{\partial \widehat{w}_j}{\partial r}, \tag{13}$$

where $\widehat{\sigma}_{rj}$ and $\widehat{\sigma}_{zj}$ are the transformed forces $\sigma_r(r, z, t)$ and $\sigma_z(r, z, t)$ respectively.

2.4. Spatial approximation. As stated earlier, the next step involved is to further reduce each of the transformed and decoupled PDEs given by Equations (10) and (11) for $j = 0, 1, \dots, n-1$ to a set of coupled ODEs using the Daubechies scaling function approximation in the axial (z) direction. Similar to time approximation, the transformed variable $\widehat{\Delta}_j$ is discretized at m points in the spatial window $[0, L_z]$, where L_z is the length in z direction. Let $\zeta = 0, 1, \dots, m-1$ be the sampling points; then

$$z = \Delta z \zeta,$$

where Δz is the spatial interval between two sampling points. The function $\widehat{\Delta}_j(r, z)$ can be approximated by the scaling function $\varphi(\zeta)$ at an arbitrary scale as

$$\widehat{\Delta}_j(r, z) = \widehat{\Delta}_j(r, \zeta) = \sum_k \widehat{\Delta}_{lj}(r) \varphi(\zeta - l), \quad l \in \mathbb{Z},$$

where the $\widehat{\Delta}_{lj}(r, z)$ (written $\widehat{\Delta}_{lj}$ hereafter) are the approximation coefficients. Thus (10) can be written as

$$c_d^2 \left(\frac{d^2}{dr^2} + \frac{1}{r} \frac{d}{dr} \right) \widehat{\Delta}_{lj} \varphi(\zeta - l) + c_d^2 \frac{1}{\Delta z^2} \widehat{\Delta}_{lj} \varphi''(\zeta - l) = -\gamma_j^2 \widehat{\Delta}_{lj} \varphi(\zeta - l). \tag{14}$$

Taking the inner product on both sides of (14) with the translates of scaling functions $\varphi(\zeta - i)$, where $i = 0, 1, \dots, m - 1$ and using their orthogonal properties, we get m simultaneous ODEs:

$$c_d^2 \left(\frac{d^2}{dr^2} + \frac{1}{r} \frac{d}{dr} \right) \widehat{\Delta}_{ij} + c_d^2 \frac{1}{\Delta z^2} \sum_{l=i-N+2}^{i+N-2} \widehat{\Delta}_{ij} \Omega_{i-l}^2 = -\gamma_j^2 \widehat{\Delta}_{ij}, \quad i = 0, 1, \dots, m - 1, \quad (15)$$

where N is the order of the Daubechies wavelet and Ω_{i-l}^2 is the connection coefficient for second order derivative defined in Equations (8).

It can be seen from the ODEs given by (15), that, similar to time approximation, even here, certain coefficients $\widehat{\Delta}_{ij}$ near the vicinity of the boundaries ($i = 0$ and $i = m - 1$) lie outside the spatial window $[0, L_z]$ defined by $i = 0, 1, \dots, m - 1$. These coefficients must be treated properly for finite domain analysis. Here, however, unlike in the time approximation, these coefficients are obtained through periodic extension, but only for free lateral edges, while other boundary conditions can be imposed quite differently using a restrain matrix [Patton and Marks 1996; Chen et al. 1996]. The unrestrained (free-free) boundary conditions may also be imposed in a similar way using restrain matrix but it has been seen from the numerical experiments that the use of a periodic extension gives accurate results. In addition, it allows decoupling of the ODEs using eigenvalue analysis and thus reduces the computational cost. Here, after expressing the unknown coefficients lying outside the finite domain in terms of the inner coefficients considering periodic extension, the ODEs given by (15) can be written as a matrix equation of the form

$$c_d^2 \left(\frac{d^2}{dr^2} + \frac{1}{r} \frac{d}{dr} \right) \{\widehat{\Delta}_{ij}\} + c_d^2 [\Lambda^1]^2 \{\widehat{\Delta}_{ij}\} = -\gamma_j^2 \{\widehat{\Delta}_{ij}\}, \quad (16)$$

where $[\Lambda^1]$ is the first order connection coefficient matrix obtained after periodic extension, and it is of the form

$$[\Lambda^1] = \frac{1}{\Delta Y} \begin{bmatrix} \Omega_0^1 & \Omega_{-1}^1 & \dots & \Omega_{-N+2}^1 & \dots & \Omega_{N-2}^1 & \dots & \Omega_1^1 \\ \Omega_1^1 & \Omega_0^1 & \dots & \Omega_{-N+3}^1 & \dots & 0 & \dots & \Omega_2^1 \\ \vdots & \vdots & & \vdots & & \vdots & & \vdots \\ \Omega_{-1}^1 & \Omega_{-2}^1 & \dots & 0 & \dots & \Omega_{N-3}^1 & \dots & \Omega_0^1 \end{bmatrix}.$$

The coupled ODEs given by (16) are decoupled using eigenvalue analysis similar to that done in time approximation as

$$\Lambda^1 = \Psi \Upsilon \Psi^{-1},$$

where Υ is the diagonal eigenvalue matrix and Ψ is the eigenvectors matrix of Λ^1 . It should be mentioned here that matrix Λ^1 has a circulant form and its eigen parameters are known analytically [Davis 1963]. Let the eigenvalues be $i\beta_i$, then the decoupled ODEs corresponding to Equations (16) are

$$c_d^2 \left(\frac{d^2}{dr^2} + \frac{1}{r} \frac{d}{dr} - \beta_i^2 \right) \widetilde{\Delta}_{ij} = -\gamma_j^2 \widetilde{\Delta}_{ij}, \quad i = 0, 1, \dots, m - 1, \quad (17)$$

where $\widetilde{\Delta}_{ij} = \Psi^{-1} \widehat{\Delta}_{ij}$. Following similar steps, the final transformed form of (11) is given by

$$c_s^2 \left(\frac{d^2}{dr^2} + \frac{1}{r} \frac{d}{dr} - \frac{1}{r^2} - \beta_i^2 \right) \widetilde{\mathcal{U}}_{\theta ij} = -\gamma_j^2 \widetilde{\mathcal{U}}_{\theta ij}. \quad (18)$$

Similarly, the decoupled displacement equations (12) and boundary conditions (13) can be written as

$$\left(\frac{d^2}{dr^2} + \frac{1}{r} \frac{d}{dr} - \frac{1}{r^2} - \beta_i^2\right) \tilde{u}_{ij} = \frac{d\tilde{\Delta}_{ij}}{dr} - i\beta\tilde{U}_{\theta ij}, \quad (19)$$

$$\left(\frac{d^2}{dr^2} + \frac{1}{r} \frac{d}{dr} - \beta_i^2\right) \tilde{w}_{ij} = -i\beta_i \tilde{\Delta}_{ij} - \frac{1}{r} \frac{d(r\tilde{U}_{\theta ij})}{dr}, \quad (20)$$

$$\tilde{\sigma}_{rij} = \lambda \tilde{\Delta}_{ij} + 2\mu \frac{d\tilde{u}_{ij}}{dr}, \quad (21)$$

$$\tilde{\sigma}_{zij} = -i\beta_i \mu \tilde{u}_{ij} + \frac{d\tilde{w}_{ij}}{dr}. \quad (22)$$

The transformed and decoupled ODEs given by (17), (18) and (19)–(22) are used in the next two sections for frequency domain analysis and spectral finite element formulation.

3. Computation of wavenumbers

For wavenumber computation, the transformed differential equations (17) and (18) in terms of variables $\tilde{\Delta}_{ij}$ and $\tilde{U}_{\theta ij}$ are to be expressed in terms of transformed displacements \tilde{u}_{ij} and \tilde{w}_{ij} using the relations given by Equations (3). Here, these transformed ODEs have coefficients that are functions of radius r unlike the governing equations for plate. That is, the wavenumber can be derived using a homogeneous assumption at a certain radius r . At a certain radius r , the solutions of the ODEs for \tilde{u}_{ij} and \tilde{w}_{ij} are of the form

$$\tilde{u}_{ij} = \sum_{k=1}^6 \bar{u}_{ij} e^{-ikr}, \quad \tilde{w}_{ij} = \sum_{k=1}^6 \bar{w}_{ij} e^{-ikr}, \quad (23)$$

where k is the wavenumber in the radial r direction and \bar{u}_{ij} , \bar{w}_{ij} are functions of r . Hereafter, the subscripts i and j are dropped for simplified notation and all the following equations are valid for $j = 0, 1, \dots, n-1$ and $i = 0, 1, \dots, m-1$. By substituting (23) in the transformed ODEs obtained from Equations (17) and (18), the two polynomial equations in k become

$$\begin{aligned} (ic_d^2 k^3 - (2c_d^2 k^2/r) + i(\beta^2 c_d^2 - c_d^2/r - \gamma^2)k + (-3c_d^2/r^3 - c_d^2 \beta^2/r + \gamma^2/r))\bar{u} \\ + (-ic_d^2 \beta k^2 + (c_d^2 \beta/r)k + (ic_d^2 \beta^3 - i\beta \gamma^2))\bar{w} = 0, \\ (-ic_s^2 \beta k^2 + (-c_s^2 \beta/r)k - i(c_s^2/r^2 - c_s^2 \beta^2 + \gamma^2)\beta)\bar{u} + (-ic_s^2 k^3 + (c_s^2/r)k^2 - i(c_s^2/r + c_s^2 \beta^2 - \gamma^2)k)\bar{w} = 0. \end{aligned}$$

They can be solved to obtain the wavenumbers k for the spectrum relation, that is, the wavenumber-frequency relations at a certain radius r and axial wavenumber β . The solution can be performed easily by posing the problem as a Polynomial Eigenvalue Problem (PEP) similar to that done for FSFE formulation of a 2-D anisotropic plate in [Chakraborty and Gopalakrishnan 2005]. The PEP for this problem is of the form

$$\mathbf{A}_3 k^3 + \mathbf{A}_2 k^2 + \mathbf{A}_1 k + \mathbf{A}_0 = 0,$$

where \mathbf{A}_3 , \mathbf{A}_2 , \mathbf{A}_1 and \mathbf{A}_0 are 2×2 matrices. It should be restated here that the spectrum relations obtained from WSFE formulation are accurate up to a certain fraction of the Nyquist frequency f_{Nyq} . This fraction p_N depends on the order N of the Daubechies scaling function used [Mitra and Gopalakrishnan 2006a].

4. Spectral finite element formulation

The degrees of freedom associated with the element formulation are shown in [Figure 1](#). The element has two degrees of freedom per node, which are \tilde{u} and \tilde{w} . The two sets of decoupled ODEs given by [Equations \(17\) and \(18\)](#) and the displacement relations [Equations \(19\) and \(20\)](#) are to be solved for \tilde{u} and \tilde{w} . The actual solutions $u(r, z, t)$ and $w(r, z, t)$ are obtained using inverse wavelet transform twice for temporal and spatial (axial) dimensions. For the finite length data, the wavelet transform and its inverse can be obtained using a transformation matrix given by [\[Williams and Amaratunga 1994\]](#).

Here, the Bessel's functions are used for the solution of the transformed governing equation given by [Equations \(17\) and \(18\)](#). The solutions for $\tilde{\Delta}$ and $\tilde{\Omega}_\theta$ are obtained as

$$\tilde{\Delta}(r) = C_1 J_0(k_e r) + C_2 Y_0(k_e r), \quad \tilde{\Omega}_\theta(r) = C_3 J_1(k_s r) + C_4 Y_1(k_s r), \quad (24)$$

where $k_e^2 = (\gamma^2/c_d^2 - \beta^2)$, $k_s^2 = (\gamma^2/c_s^2 - \beta^2)$ and C_1, C_2, C_3, C_4 are constants. J_n and Y_n are Bessel's functions of first and second kinds.

Substituting [\(24\)](#) in [\(19\)](#), [\(20\)](#) and solving for \tilde{u} and \tilde{w} gives (see [\[Heimann and Kolsky 1966\]](#))

$$\begin{aligned} \tilde{u}(r) &= -k_e (C_1 J_1(k_e r) + C_2 Y_1(k_e r)) - i\beta (C_3 J_1(k_s r) + C_4 Y_1(k_s r)), \\ \tilde{w}(r) &= -i\beta (C_1 J_0(k_e r) + C_2 Y_0(k_e r)) - k_s (C_3 J_0(k_s r) + C_4 Y_0(k_s r)). \end{aligned} \quad (25)$$

These solutions provide the interpolating functions for forming the elemental dynamic stiffness matrix. The unknown constants $\{\mathbf{a}\} = \{C_1, C_2, C_3, C_4\}$ can be determined from the transformed nodal displacements $\tilde{u}(r)$, $\tilde{w}(r)$ at inner ($r = r_i$) and outer ($r = r_o$) radii. The nodal displacement vector is $\{\tilde{\mathbf{u}}^e\} = \{\tilde{u}_1, \tilde{w}_1, \tilde{u}_2, \tilde{w}_2\}$, where $\tilde{u}_1 = \tilde{u}(r_i)$, $\tilde{w}_1 = \tilde{w}(r_i)$, $\tilde{u}_2 = \tilde{u}(r_o)$ and $\tilde{w}_2 = \tilde{w}(r_o)$. Thus we can relate nodal displacements and unknown constants from [Equations \(25\)](#) as

$$\{\tilde{\mathbf{u}}^e\} = [\mathbf{B}]\{\mathbf{a}\}. \quad (26)$$

Substituting [\(25\)](#) into the transformed force boundary conditions [\(21\)](#) and [\(22\)](#), we obtain

$$\begin{aligned} \tilde{\sigma}_r(r) &= (-\{(\lambda + 2\mu)k_e^2 - \lambda\beta^2\}J_0(k_e r) + 2\mu k_e^2 J_1(k_e r)/(k_e r))C_1 \\ &\quad + (-\{(\lambda + 2\mu)k_e^2 - \lambda\beta^2\}Y_0(k_e r) + 2\mu k_e^2 Y_1(k_e r)/(k_e r))C_2 \\ &\quad + 2i\mu k_s \beta (J_0(k_s r) - J_1(k_s r)/(k_s r))C_3 + 2i\mu k_s \beta (Y_0(k_s r) - Y_1(k_s r)/(k_s r))C_4 \end{aligned} \quad (27)$$

and

$$\tilde{\sigma}_z(r) = -2i\mu\beta k_e (J_1(k_e r)C_1 + Y_1(k_e r)) - \mu(k_s^2 - \beta^2)(J_1(k_s r)C_3 + Y_1(k_s r)C_4). \quad (28)$$

From these equations, we relate the nodal force vector $\{\mathbf{F}^e\} = \{\tilde{\sigma}_{r1}, \tilde{\sigma}_{z1}, \tilde{\sigma}_{r2}, \tilde{\sigma}_{z2}\}$ to the constants $\{\mathbf{a}\}$ as

$$\{\tilde{\mathbf{F}}^e\} = [\mathbf{C}]\{\mathbf{a}\}, \quad (29)$$

where $\tilde{\sigma}_{r1} = \tilde{\sigma}_r(r_i)$, $\tilde{\sigma}_{z1} = \tilde{\sigma}_z(r_i)$, $\tilde{\sigma}_{r2} = \tilde{\sigma}_r(r_o)$ and $\tilde{\sigma}_{z2} = \tilde{\sigma}_z(r_o)$. Finally, from [\(26\)](#) and [\(29\)](#), a relation between transformed nodal forces and displacements is obtained:

$$\{\tilde{\mathbf{F}}^e\} = [\mathbf{C}][\mathbf{B}]^{-1}\{\tilde{\mathbf{u}}^e\} = [\tilde{\mathbf{K}}^e]\{\tilde{\mathbf{u}}^e\},$$

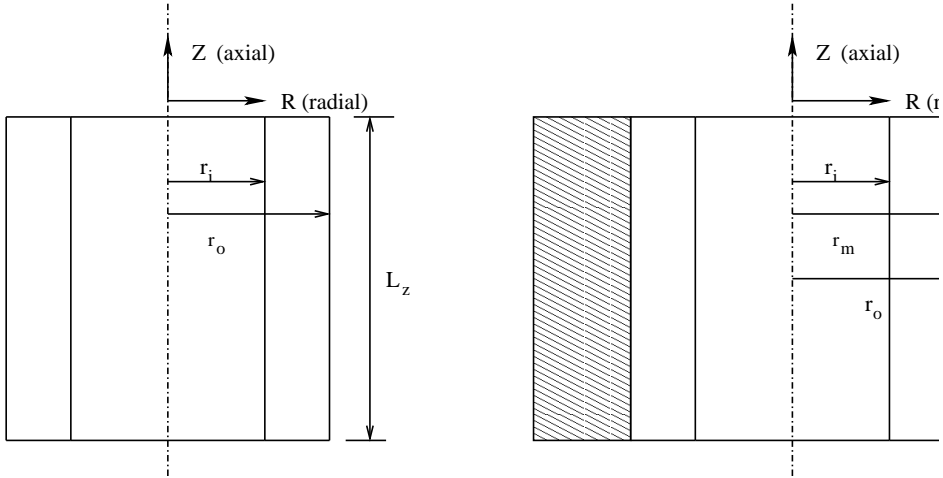


Figure 2. Aluminum (left) and aluminum-steel (right) hollow cylinders.

where $[\tilde{\mathbf{K}}^e]$ is the exact elemental dynamic stiffness matrix. These elemental dynamic stiffness matrices can be assembled in a similar way as in conventional FE to obtain the global stiffness matrix for the analysis of more complex structures.

5. Numerical experiments

In this section, the developed 2-D WSFE is used to analyze axisymmetric radial and axial wave propagations in isotropic cylinders due to broadband impulse excitation. First, the simulations are performed for an aluminum hollow cylinder free at both ends and internal and/or external pressure acting in radial/axial directions. The cylinder has an inner radius $r = r_i$, outer radius $r = r_o$ and the axial length is L_z , as shown in [Figure 2](#), left. The loading conditions are shown in [Figure 3](#). Examples are also presented

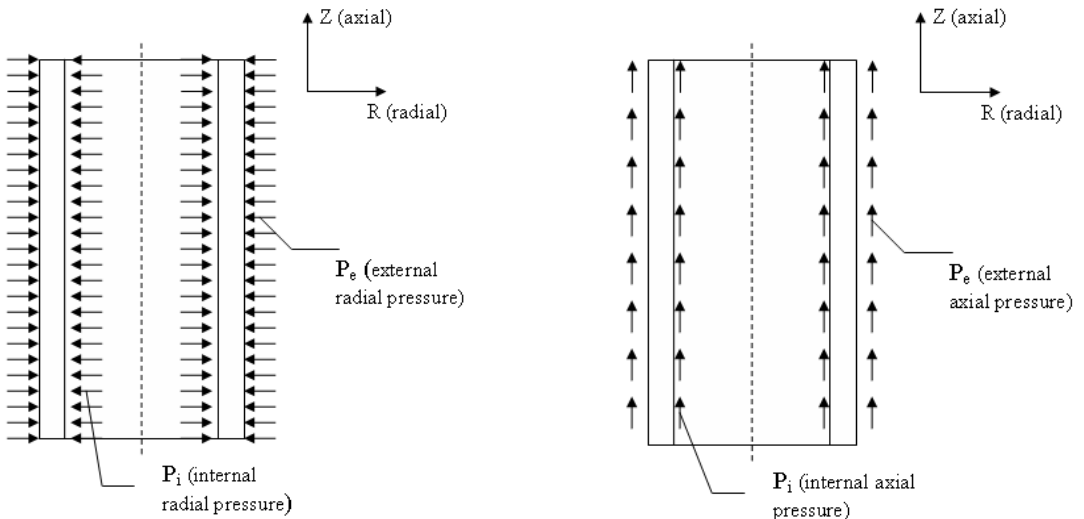


Figure 3. Radial (left) and axial (right) internal and external pressure.

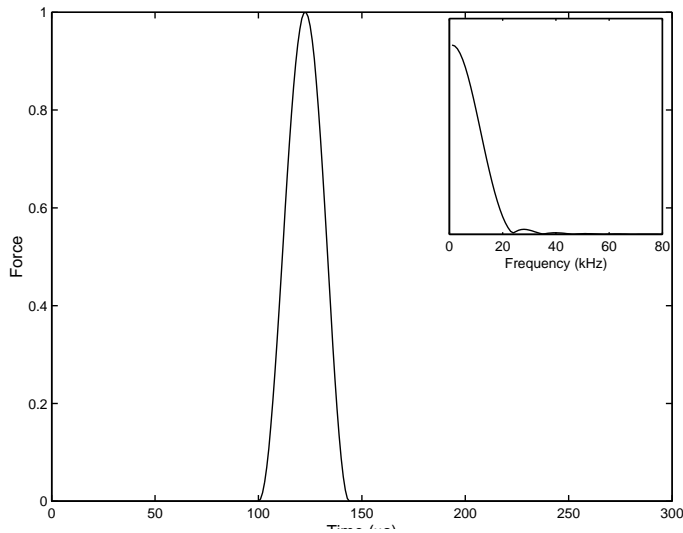


Figure 4. Impulse load in time and frequency (inset) domain.

where instead of uniform pressure, the radial/axial load acting along the axial direction has a pulse-like spatial (axial) distribution. Next, a more complex structure is considered for analysis, a cylinder made of a bimaterial, aluminum-steel (Figure 2, right). The material properties adopted for the aluminum and steel cylinders are: Young’s modulus, $E_a = 70$ GPa and $E_s = 200$ GPa; mass densities, $\rho_a = 2700$ kg/m³ and $\rho_s = 7860$ kg/m³; Poisson’s ratio, $\nu = 0.3$.

In all these results, the impulse load applied has unit amplitude and the time duration is $50 \mu s$, with a frequency content 44 kHz. The load is shown in the time and frequency domains in Figure 4.

The 2-D WSFE model is formulated with the Daubechies scaling function of order $N = 22$ for the temporal approximations and $N = 4$ for the spatial one. The time sampling rate $\Delta t = 2 \mu s$, unless otherwise mentioned, while the spatial sampling rate Δz is varied depending on L_z . As mentioned earlier, for the aluminum cylinder, only one 2-D WSFE is used to simulate the responses, independent of its dimensions. However, for the bimaterial cylinder in Figure 2, right, two elements are required for modeling, due to the discontinuity present in the problem.

5.1. Wavenumber computation. The spectrum relations for an aluminum hollow cylinder with $r_i = 0.02$ m and $r_o = 0.03$ m at different radii r obtained from the wavenumber computation discussed earlier are plotted in Figure 5. The three panels of the figure show the real or propagating part of the wavenumbers for $r = 0.02, 0.025$ and 0.03 m. These wavenumbers have significant imaginary parts which imply that the waves are inhomogeneous in nature, in other words, they attenuate while they propagate. As the radius is moved from inner to outer radius, the cut-off frequency which is the frequency at which the wavenumber is zero is also driven outward to a higher frequency. The wavenumbers are plotted for an axial wavenumber of $\beta = 50$ and are obtained with $\Delta t = 4 \mu s$ (Nyquist frequency of 125 kHz). However, as mentioned in [Mitra and Gopalakrishnan 2006a], WSFE predicts accurate wavenumbers only up to a certain fraction p_N of the Nyquist frequency f_{nyq} . This fraction depends only on the order of Daubechies scaling function N , and is approximately equal to 0.6 for $N = 22$. Thus, in Figure 5, the

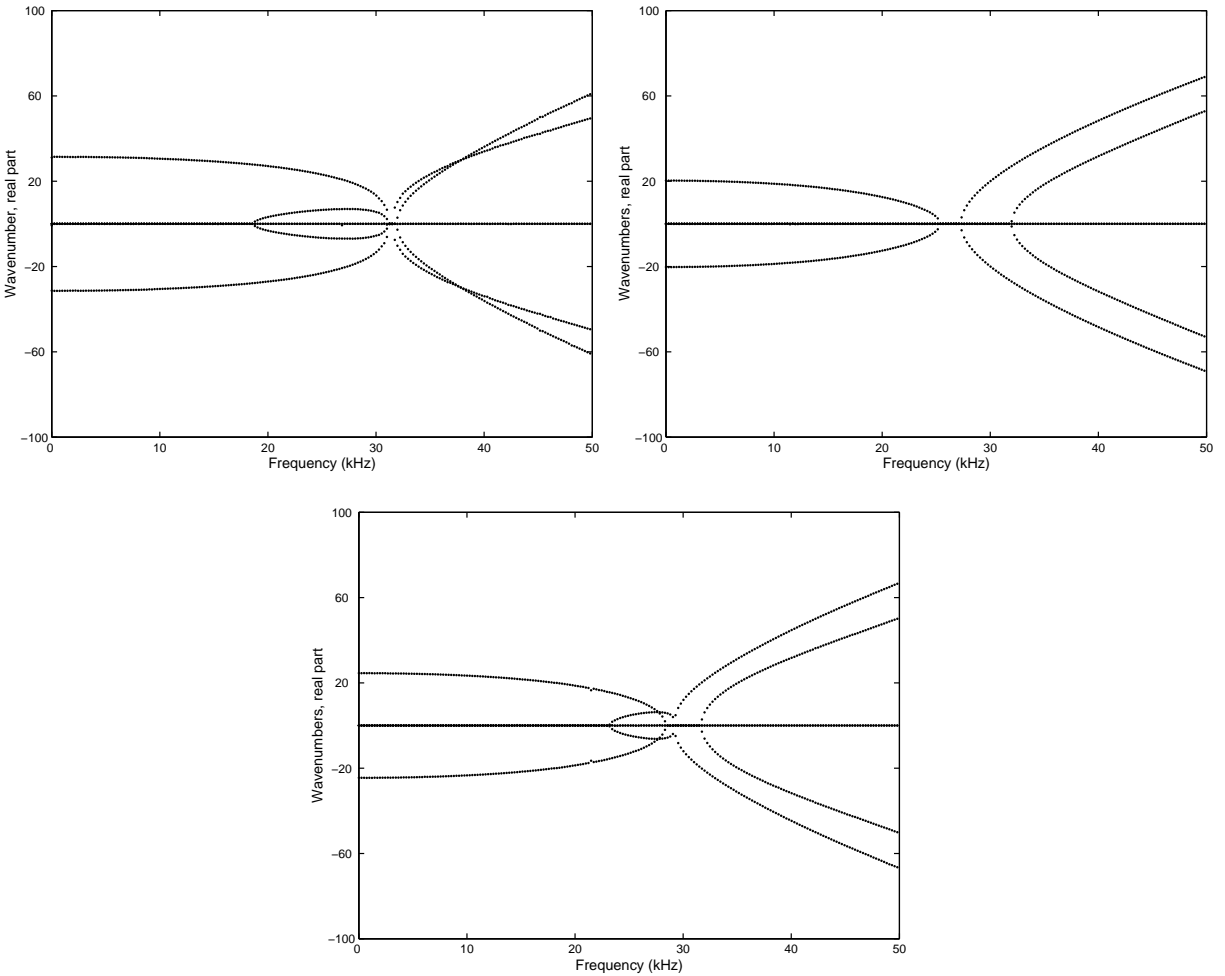


Figure 5. Real parts of wavenumbers at $r = r_i$ (top left), $r = \frac{1}{2}(r_i + r_o)$ (bottom) and $r = r_o$ (top right).

spectrum relations are plotted only up to 60 kHz, which is less than the allowable frequency range of $f_N = p_N f_{Nyq} = 75$ kHz.

5.2. Time domain analysis. Here, first the responses obtained using the formulated element are validated with 2-D FE analysis. [Figure 6](#) compares the radial velocities for an aluminum cylinder with $r_i = 0.05$ m, $r_o = 0.1$ m and $L_z = 2.0$ m (see [Figure 2](#), left) with 2-D FE results, showing the radial velocities at the midpoint (at $L_z/2$ from the free ends) and at inner $r = r_i$ and outer radii $r = r_o$ respectively. The applied load is the unit impulse, as shown in [Figure 4](#). It is applied as a uniform pressure P_i ([Figure 3](#), left) in the radial direction along the inner surface ($r = r_i$). As an example, such internal pressure can be encountered in fluid carrying pipes and other cylindrical pressure vessels. The 2-D FE results are obtained using ANSYS 10.0, with a mesh consisting of 10220 four-noded quadrilateral axisymmetric elements (PLANE42). Newmarks' scheme with time step $2 \mu s$ is used for time integration. A further

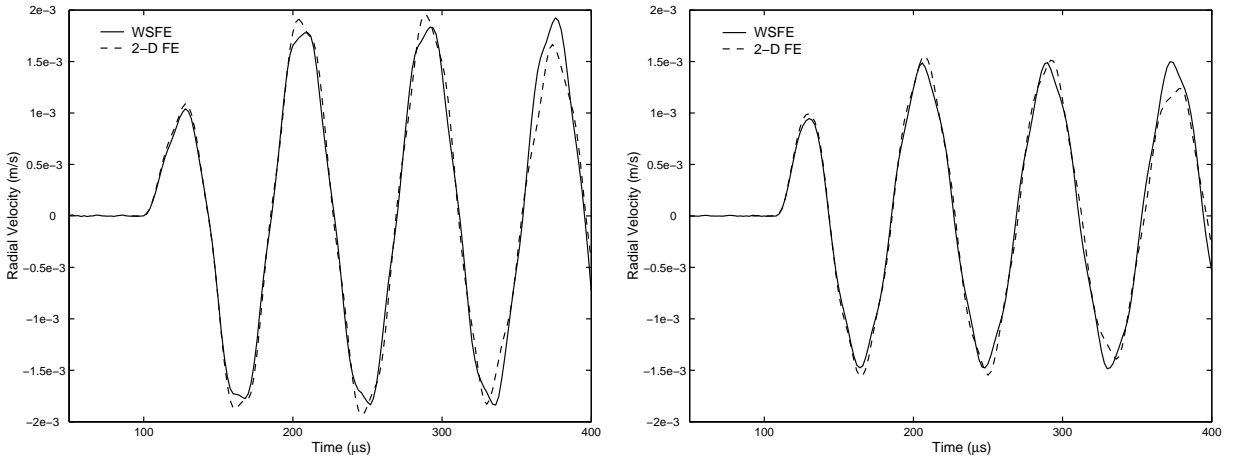


Figure 6. Radial velocities at midpoint along the axial direction at $r = r_i$ (left) and $r = r_o$ (right), due to internal radial pressure.

refinement of the FE mesh does not give significant difference in results. WSFE for this example is formulated with $N = 22$, time interval $\Delta t = 2 \mu s$ and time window $T_w = 512 \mu s$. Unlike FSFE, here the accuracy of the simulation is independent of the time window T_w because the present method is free from the wrap-around problem. Here T_w is chosen as required for observation. The number of discretization steps in the axial direction is $m = 128$ and thus the spatial sampling rate is $\Delta z = 0.0039$ m. Here only one WSFE is used for modeling as it was mentioned earlier, that is in absence of any discontinuities, only one WSFE is capable of modeling the entire structure irrespective of its dimensions. In the case of FSFE, the axial dimension is considered to be infinite or unbounded. It can be observed from these plots that the WSFE results match well with the corresponding 2-D FE results. Similar axial velocity responses

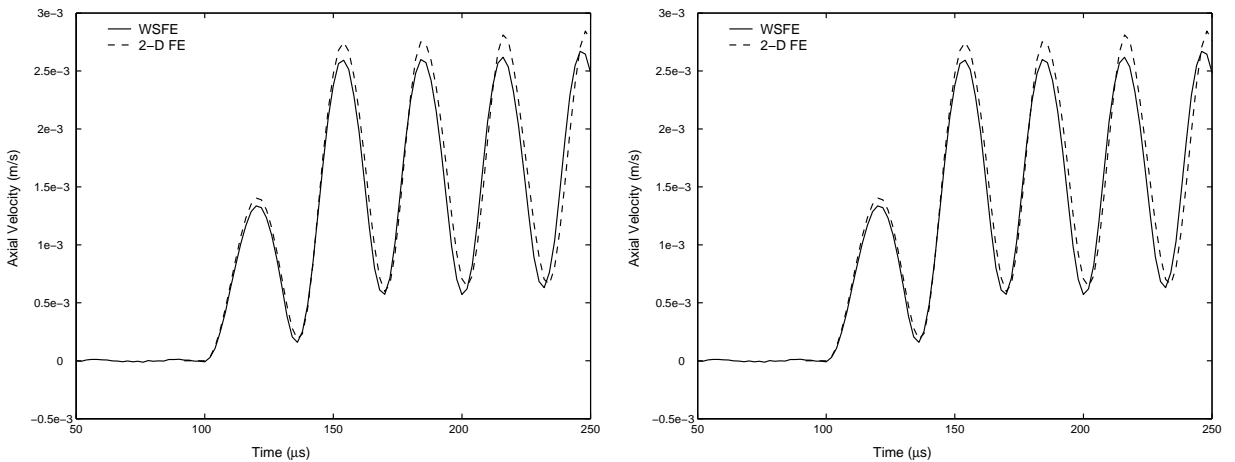


Figure 7. Axial velocities at midpoint along the axial direction at $r = r_i$ (left) and $r = r_o$ (right), due to internal axial pressure.

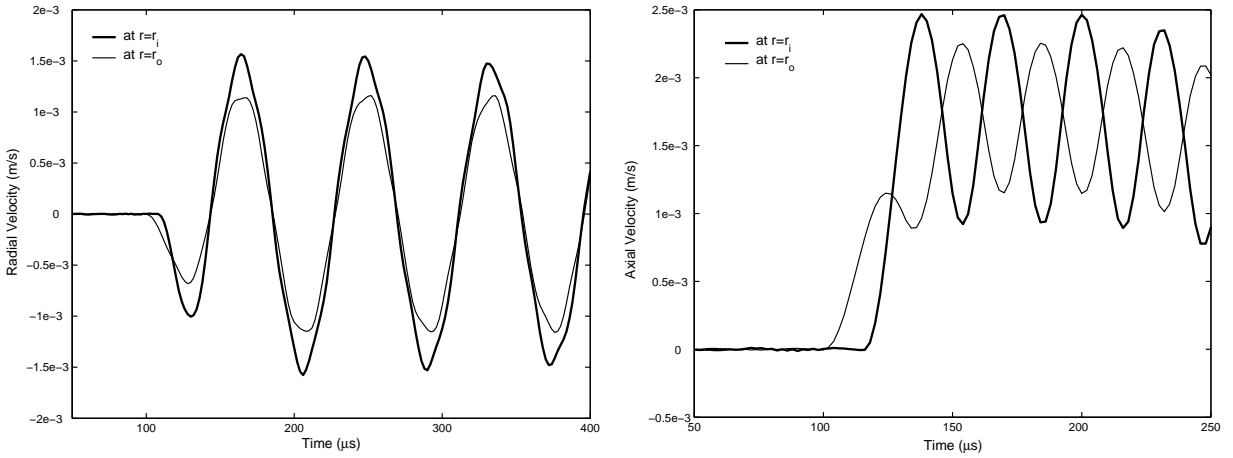


Figure 8. Radial (left) and axial (right) velocities at midpoint along the axial direction due to external radial and axial pressures respectively.

are plotted in [Figure 7](#) under the same loading conditions as before, except that here they are applied in axial direction ([Figure 3](#), right). The figure shows the axial velocities at $r = r_i$ and $r = r_o$ at distances $L_z/2$ from the free ends. Even here, the responses are validated with 2-D FE results and it can be seen that the responses compare very well. The modeling parameters for WSFE and the FE mesh are kept the same as in the previous case of radial velocities. Similar radial and axial velocities of the cylinder described above are plotted in [Figure 8](#). However, here an external pressure P_e is considered instead of internal pressure as in previous example. This example is done to simulate the loading condition in a cylindrical excavation casing. The velocities are measured at midpoint at $L_z/2$ from the free end along the axial (z) direction at both inner $r = r_i$ and outer $r = r_o$ surfaces. [Figure 9](#) plot similar radial and axial velocities, with the difference that the loading condition consists of both internal (P_i) and external (P_e) pressures.

Next, WSFE is used to model a relatively complex structure of bimaterial, aluminum-steel cylinder. The configuration is shown in [Figure 2](#), right, where the inner cylinder is composed of aluminum and is surrounded by a concentric steel cylinder. The innermost radius is $r_i = 0.05$ m, the radius of the interface is $r_m = 0.09$ m and the outermost radius is $r_o = 0.1$ m. The length of the cylinder is $L_z = 2.0$ m and the impulse load (see (30)) is applied uniformly at the inner surface $r = r_i$ as an internal pressure in the radial/axial directions. As stated earlier, two WSFEs are required to model the structure because of the presence of discontinuity. WSFE modeling involves $m = 64$ spatial sampling points. [Figure 10](#) plots the radial and axial velocities measured at the midpoint ($L_z/2$) and $r = r_i$. The responses are also compared with those of an aluminum cylinder of the same dimensions. The amplitude of the incident wave for the aluminum cylinder is much more than that of the aluminum-steel cylinder as expected as the latter has a much higher stiffness. Comparisons are also provided with 2-D FE results for the aluminum-steel cylinder. The FE mesh and the Newmark's time integration scheme is the same as in the previous example. It can be seen that the response matches well with the FE results for both radial and axial wave

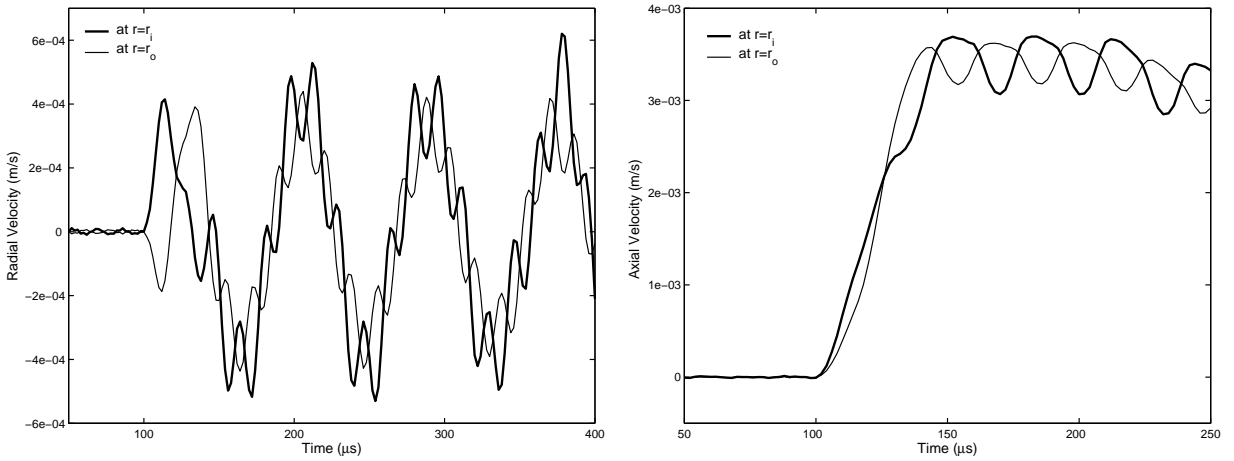


Figure 9. Radial (left) and axial (right) velocities at midpoint along the axial direction due to external and internal pressure in the radial and axial directions respectively.

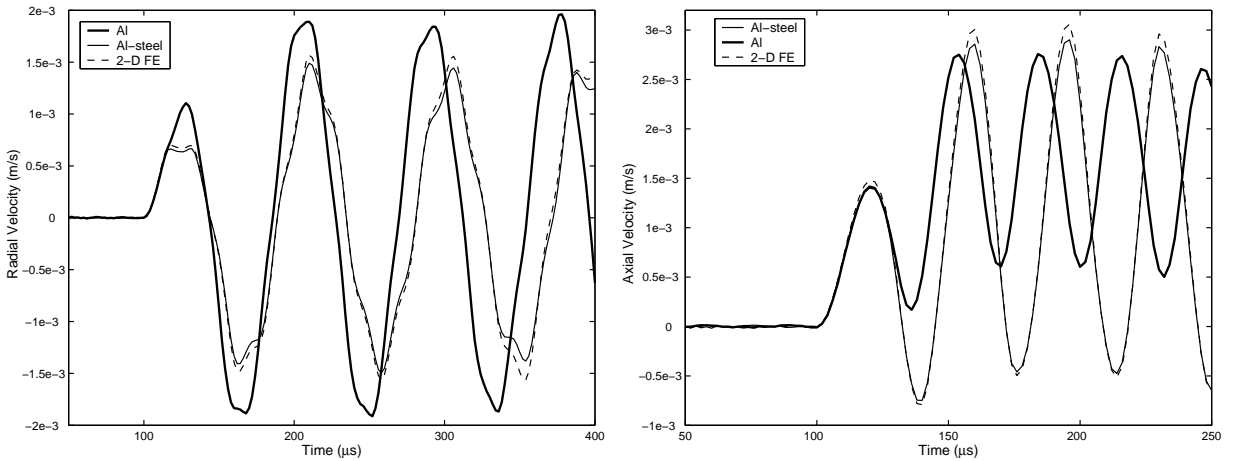


Figure 10. Radial (left) and axial (right) velocities in bimaterial Al-steel cylinder at midpoint along axial direction at $r = r_i$.

propagations. This numerical experiment is done with the purpose of emphasizing the efficiency of the proposed technique for modeling rather complex structures.

Next, instead of internal pressure, we apply an impulse load at the outer surface ($r = r_o$), with a pulse-like distribution along the axial direction, given by

$$F(z) = e^{-(z/\alpha)^2}, \tag{30}$$

where α is a constant and can be varied to change the pulse width in the z direction. Figure 11 compares the radial velocities in a hollow aluminum cylinder (with $r_i = 0.05$ m, $r_o = 0.1$ m and $L_z = 0.5$ m: see Figure 2, left) with 2-D FE results. The unit impulse load shown in Figure 4 is applied in the radial

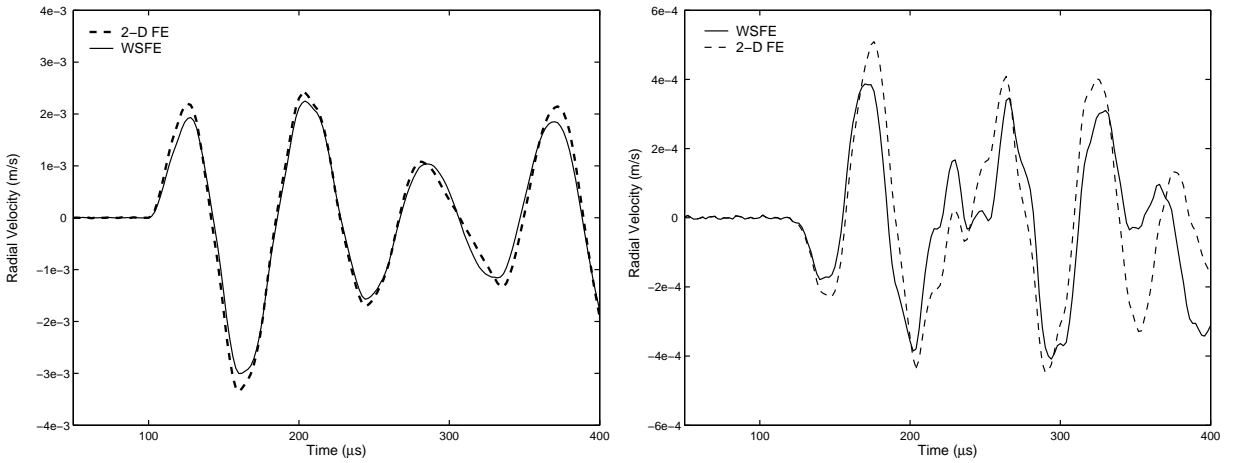


Figure 11. Radial velocities at midpoint (left) and quarter-point (right) along axial direction at $r = r_o$.

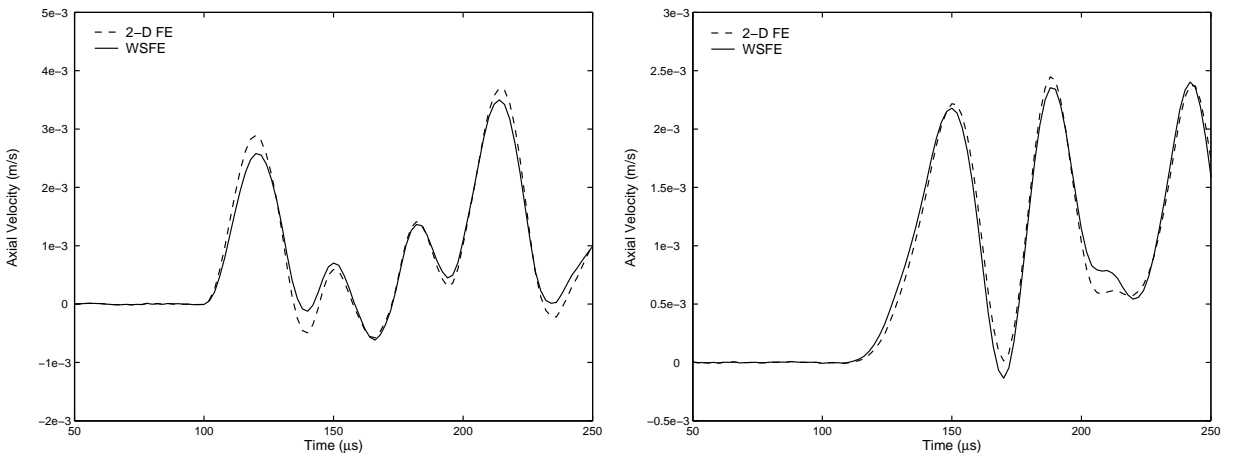
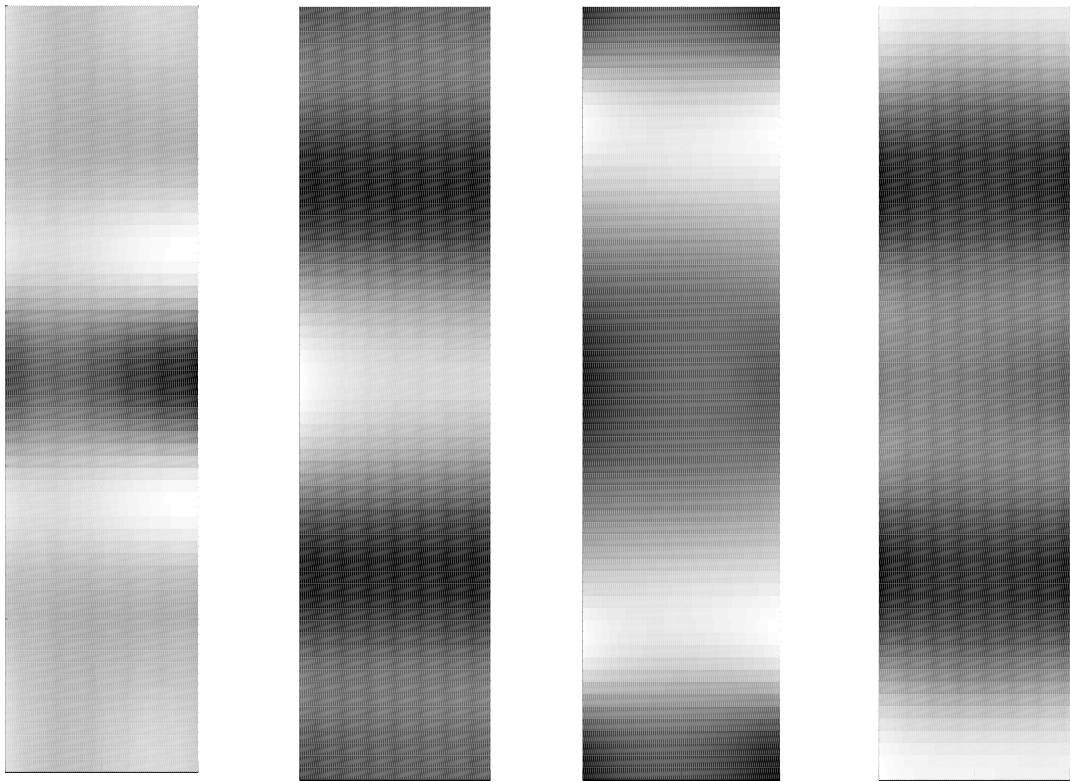


Figure 12. Axial velocities at midpoint (left) and quarter-point (right) along axial direction at $r = r_o$.

direction at $r = r_o$ and its distribution along the axial direction is given by (30) with $\alpha = 0.05$. The responses are simulated using a single WSFE with $m = 64$ sampling points in axial direction and thus spatial sampling rate is $\Delta z = 0.0078$ m. The 2-D FE analysis is done with ANSYS 10.0, with 2540, 4-noded quadrilateral axisymmetric elements (PLANE42) mesh. Time integration is performed with Newmarks scheme with time step $2 \mu\text{s}$. Figure 11 shows the radial velocities at $r = r_o$, half-way ($L_z/2$) and a quarter of the way ($L_z/4$) from the free ends. It can be seen that the responses obtained using the present method compares well with FE simulations. However, the difference between the results obtained from FE and WSFE simulations is more for the responses measured at the quarter-point and presented in Figure 11, right. A more refined mesh for FE analysis may give better correlation, but we



(a) $T = 150 \mu s$ (b) $T = 200 \mu s$ (c) $T = 250 \mu s$ (d) $T = 300 \mu s$

Figure 13. Snapshots of radial wave velocities. Vertical coordinate: axial direction, from 0 to 0.5 m; horizontal coordinate: radial direction, from 0.05 to 0.1 m.

have not used it in order to avoid the computational cost and because the comparisons are very good in all the other cases (Figure 11, left, and Figure 12). The latter figure plots the axial velocities when the load is applied in the axial direction. Even here, the results matches very well with those obtained from the FE analysis.

Figure 13 presents the snapshots of the radial velocities presented in Figure 11. Here, the thickness of the cylinder being more, the radial (and axial) variations of the radial wave velocities can be studied. The snapshots in Figure 13 are taken at $T = 150, 200, 250$ and $300 \mu s$, the impulse load having been applied at $100 \mu s$ with the peak unit amplitude at $125 \mu s$ (Figure 4). The figure shows the pattern of propagation of radial waves in both axial and radial directions due to the loading as described before for Figure 11. Such snapshots help to obtain the wave velocities at any spatial location at a given instance of time. For example, the snapshot at $T = 150 \mu s$ shows that at this time the incident radial wave has propagated along the axial direction and also the position of occurrence of maximum velocity can be obtained. At later times, say, $T = 300 \mu s$, the profile of wave propagation includes waves resulting from reflections at the boundaries. Similar interpretations can be given for the other snapshots. Note that the velocities

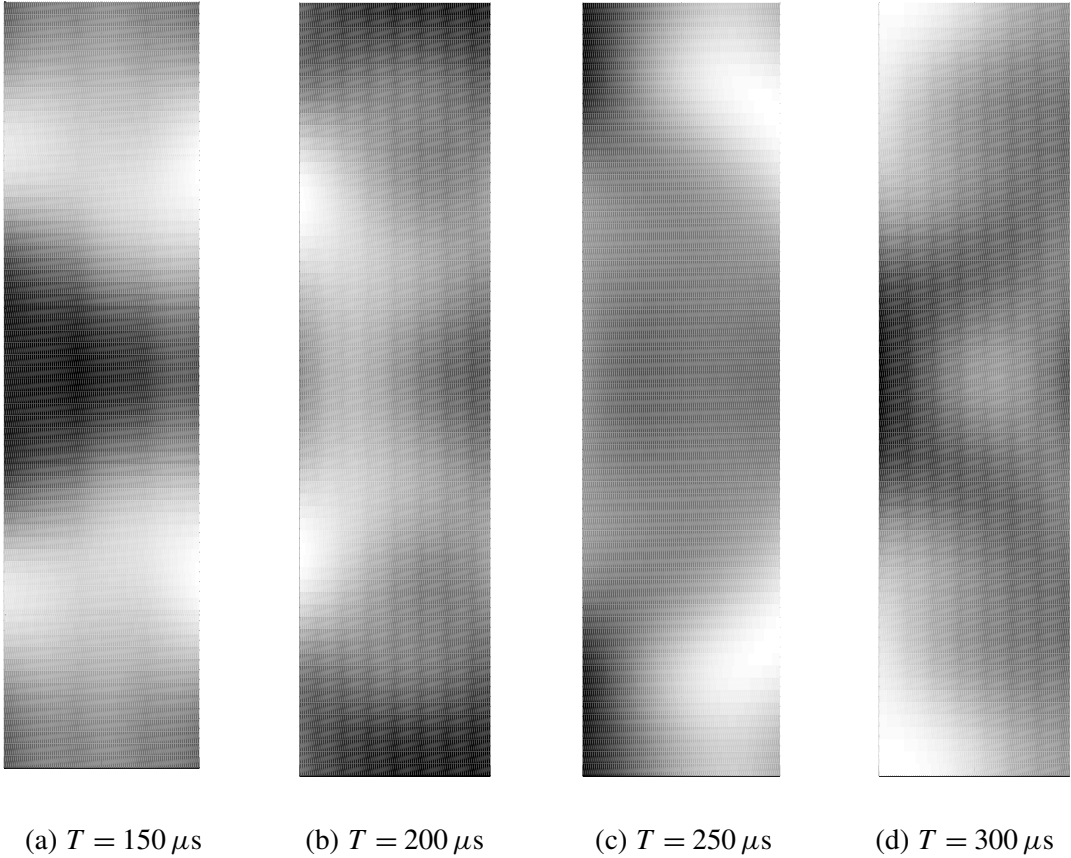


Figure 14. Snapshots of axial wave velocities. Vertical coordinate: axial direction, from 0 to 0.5 m; horizontal coordinate: radial direction, from 0.05 to 0.1 m.

at all the sampling points along the axial direction and at any points on the radial direction R required for the snapshots are obtained from a single simulation.

Snapshots for axial velocities due to loads applied in the axial direction are plotted in [Figure 14](#). The loading conditions, structural properties and modeling parameters are as before. Again, snapshots at $T = 150, 200, 250$ and $300 \mu s$ are shown.

6. Conclusions

Here, a 2-D wavelet spectral element is developed for wave propagation analysis in isotropic axisymmetric cylinders. The conventional FE technique for such transient high frequency dynamics is not computationally viable and the spectral finite element method provides an efficient alternative. The use of localized Daubechies compactly supported wavelets as basis functions helps to overcome several important drawbacks of the prevalent FFT based spectral finite element method while retains the advantages of computational efficiency, simultaneous time and frequency domains analysis. Firstly, WSFE method can accurately model finite dimension structures unlike FSFE, which can only model 2-D structures

unbounded in one direction. Next, WSFE is free from wrap around problems associated with FSFE due to its periodicity assumption in temporal approximation. Consequently, FSFE, unlike WSFE cannot handle undamped finite length structures and even in presence of damping, larger time window is needed to remove distortions arising from wrap-around.

In this paper, radial and axial wave propagations in hollow isotropic cylinders of finite dimensions are studied in time and frequency domains. The time domain responses are validated with 2-D axisymmetric FE analysis and good comparison is observed. Next, the radial and axial distributions of the wave velocities are studied in cylinder of different configurations. Finally, the wave propagation analysis in a bimaterial cylinder is performed to show the ease of the proposed modeling technique in modeling more complicated structures.

References

- [Bao et al. 1999] X. L. Bao, P. K. Raju, and H. Uberall, “Circumferential waves on an immersed, fluid filled elastic cylindrical shell”, *J. Acoust. Soc. Am.* **105**:5 (1999), 2704–2709.
- [Beylkin 1992] G. Beylkin, “On the representation of operators in bases of compactly supported wavelets”, *SIAM J. Numer. Anal.* **29**:6 (1992), 1716–1740.
- [Chakraborty and Gopalakrishnan 2005] A. Chakraborty and S. Gopalakrishnan, “A spectrally formulated plate element for wave propagation analysis in anisotropic material”, *Comput. Methods Appl. Mech. Eng.* **194**:42-44 (2005), 4425–4446.
- [Chen et al. 1996] M. Q. Chen, C. Hwang, and Y. P. Shih, “The computation of wavelet-Galerkin approximation on a bounded interval”, *Int. J. Numer. Methods Eng.* **39**:17 (1996), 2921–2944.
- [Daubechies 1992] I. Daubechies, *Ten lectures on wavelets*, CBMS-NSF series in applied mathematics, SIAM, Philadelphia, 1992.
- [Davis 1963] P. J. Davis, *Interpolation and approximation*, Blaisdell, New York, 1963.
- [Doyle 1999] J. F. Doyle, *Wave propagation in structures*, Springer, New York, 1999.
- [El-Raheb 2005] M. El-Raheb, “Transient waves in an inhomogeneous hollow infinite cylinder”, *Int. J. Solids Struct.* **42**:20 (2005), 5356–5376.
- [Godinho et al. 2003] L. M. C. Godinho, A. Tadeu, and F. Branco, “Wave scattering by infinite cylindrical shell structures submerged in a fluid medium”, *Wave Motion* **38**:2 (2003), 131–149.
- [Godinho et al. 2004] L. M. C. Godinho, A. Tadeu, and F. Branco, “Dynamic analysis of submerged fluid-filled pipelines subjected to a point pressure load”, *J. Sound Vib.* **271**:1–2 (2004), 257–277.
- [Heimann and Kolsky 1966] J. H. Heimann and H. Kolsky, “The propagation of elastic waves in thin cylindrical shells”, *J. Mech. Phys. Solids* **14**:3 (1966), 121–130.
- [Mahan 2002] G. D. Mahan, “Oscillations of a thin hollow cylinder: carbon nanotubes”, *Phys. Rev. B* **65**:23 (2002), 235402–235409.
- [Mitra and Gopalakrishnan 2005] M. Mitra and S. Gopalakrishnan, “Spectrally formulated wavelet finite element for wave propagation and impact force identification in connected 1-D waveguides”, *Int. J. Solids Struct.* **42**:16-17 (2005), 4695–4721.
- [Mitra and Gopalakrishnan 2006a] M. Mitra and S. Gopalakrishnan, “Extraction of wave characteristics from wavelet based spectral finite element formulation”, *Mech. Syst. Signal Process.* **20**:8 (2006), 2046–2079.
- [Mitra and Gopalakrishnan 2006b] M. Mitra and S. Gopalakrishnan, “Wavelet based 2-D spectral finite element for wave propagation analysis in isotropic plates”, *CMES—Comp. Model. Eng. Sc.* **15**:1 (2006), 49–67.
- [Mitra and Gopalakrishnan 2006c] M. Mitra and S. Gopalakrishnan, “Wavelet based 2-D spectral finite element formulation for wave propagation analysis in isotropic plates”, *Comput. Model. Eng. Sci.* **15**:1 (2006), 49–68.
- [Patton and Marks 1996] R. D. Patton and P. C. Marks, “One dimensional finite elements based on the Daubechies family of wavelets”, *AIAA J.* **34**:8 (1996), 1696–1698.

- [Wang et al. 2005] C. Y. Wang, C. Q. Ru, and A. Mioduchowski, “Axisymmetric and beam-like vibrations of multi-wall carbon nanotubes”, *Phys. Rev. B* **72** (2005), 75414–75424.
- [Williams and Amaratunga 1994] J. R. Williams and K. Amaratunga, “Introduction to wavelets in engineering”, *Int. J. Numer. Methods Eng.* **37**:14 (1994), 2365–2388.
- [Williams and Amaratunga 1997] J. R. Williams and K. Amaratunga, “A discrete wavelet transform without edge effects using wavelet extrapolation”, *J. Fourier Anal. Appl.* **3**:4 (1997), 435–449.
- [Yin and Yue 2002] X. Yin and Z. Yue, “Transient plane-strain response of multilayered elastic cylinders to axisymmetric impulse”, *J. Appl. Mech. (Trans. ASME)* **69**:6 (2002), 825–835.

Received 27 Jun 2006. Accepted 15 Sep 2006.

MIRA MITRA: mira@aero.iisc.ernet.in

Department of Aerospace Engineering, Indian Institute of Science, Bangalore 560 012, India

<http://www.aero.iisc.ernet.in/~mira>

S. GOPALAKRISHNAN: krishnan@aero.iisc.ernet.in

Department of Aerospace Engineering, Indian Institute of Science, Bangalore 560 012, India

STATISTICAL STRENGTH OF TWISTED FIBER BUNDLES WITH LOAD SHARING CONTROLLED BY FRICTIONAL LENGTH SCALES

PANKAJ K. PORWAL, IRENE J. BEYERLEIN AND STUART LEIGH PHOENIX

We develop Monte Carlo simulation and theory to study the statistical strength characteristics of twisted fiber bundles. These consist of fibers that follow a Weibull distribution for strength with shape parameter ρ , and are arranged in an ideal helical structure with surface helix angle α_s . Fiber interactions are considered in terms of frictional forces that control stress recovery along broken fibers away from the breaks. A twist-modified global load sharing (TM-GLS) rule is developed for stress redistribution from fibers that are slipping and thus only partially loaded near the breaks. Expressions for the radial pressure distribution in the yarn and corresponding lengths of frictional zones in broken fibers in the various layers are derived considering the discrete nature of the fibers in the bundle. Three different characteristic length scales of strength development for a twisted bundle are proposed, which depend on friction coefficient, f , and surface twist angle, α_s . These are δ_c^{\min} , δ_c^{avg} , or δ_c^{\max} , arising from the consideration of the minimum, average, or maximum stress recovery length among the fibers in the bundle along its axis. We show that the normalized strengths of a twisted bundle with length equal to any one of these characteristic lengths approximately follow a Gaussian distribution. Compared to a TM-ELS (twist-modified equal load sharing) bundle, the TM-GLS bundle has improved strength because through friction a broken fiber can recover its stress within the bundle length. We also show that the relationship between the normalized bundle strength and α_s depends on the characteristic length scale used: for δ_c^{\min} the normalized strength drops quickly with α_s ; for δ_c^{avg} it decreases as well, but at a slower rate; and for δ_c^{\max} the normalized strength first attains a maximum at an optimal value of α_s before ultimately decreasing with α_s . Finally, we compare the simulation results for optimal twist angle with experimental data in the literature and get excellent agreement.

1. Introduction

Twisted fibrous structures, such as ropes and cables made from ultrastrong fibers like Kevlar[®], Spectra[®], Dyneema[®], and Vectran[®], are now used in a wide range of applications requiring not only very high tensile strength and stiffness but also flexibility in bending. Novel applications are emerging from commercialization of fibers like M5[®] (DuPont) and synthetic spider silk [Lazaris et al. 2002; Huemmerich et al. 2004]. Still others in development are based on aligned and twisted carbon nanotube bundles

Keywords: twisted fiber bundle or yarn, Monte Carlo simulation, statistical strength, global load sharing, characteristic length scales, friction effects, pressure development.

The authors would like to gratefully acknowledge the support of the Science- and Technology-based Distinguished Student Award provided to graduate student Pankaj K. Porwal by Los Alamos National Laboratory. IJB and PKP would like to thank the Fluid Dynamics Group (T-3) management and administration for their support. This work has been supported in part under the “Institute for Future Space Transport”, a NASA University Institute funded under Cooperative Agreement NCC3-994. This research was conducted using the resources of the Cornell Theory Center, which receives funding from Cornell University, New York State, federal agencies, foundations, and corporate partners.

[Andrews et al. 1999; Vigolo et al. 2000; Jiang et al. 2002; Ko et al. 2003; Ericson et al. 2004; Zhang et al. 2004]. These novel applications include, but are not limited to, linear structures (for example, suspension ropes in bridges, parachute lines, tire cords, and the futuristic concept of the *space elevator*), and two-dimensional fabric-based structures (for example, body armor in the form of ballistic vests, blankets, and panels in automobiles and aircrafts). In many of these critical applications, survival of the user depends upon the optimal functioning of the twisted structure, and in such cases reliable strength predictions are crucial.

The most common model geometry for a twisted fiber bundle or yarn is the ideal helical structure [Hearle et al. 1969], in which the fibers are arranged in concentric layers following helical paths with the same angular orientation. The outermost layer has the highest helix angle (that is, the surface helix angle α_s) and layers deeper into the bundle have progressively lower helix angles down to the center fiber which is straight. Furthermore, fibers in this ideal structure have no initial strains or buckling, which requires that fibers in different concentric layers have lengths equal to the helical path lengths of their particular layer. In practise, achieving this uniformity in a long yarn that has been twisted in an automated manufacturing process, requires the phenomenon of *migration*. During migration fibers, traveling along the yarn length, radially move from one layer to another over length scales that are long compared to both the yarn diameter and the characteristic length of stress transfer near fiber breaks. When such an ideal helical structure is under an external tensile load, the fiber strains are largest along the yarn axis and smallest in the outermost layer.

1.1. Optimal strength of yarn. Earlier works predicting the strength of ideal yarns have focused mostly on staple yarn structures where fibers are of a given finite length and deterministic strength. For a given coefficient of interfiber friction and surface twist angle the strength of the yarn, also deterministic, is governed by the first fiber to fail, this being the center fiber. Additional strain increments cause a cascade of fiber failures propagating outwards until the complete collapse.

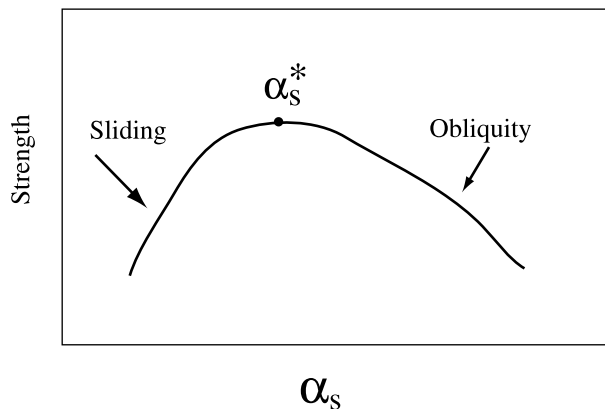


Figure 1. Staple yarn strength versus surface helix angle. Optimal helix angle exists due to the strengthening effects of yarn pressure and interfiber friction, and to the weakening effects of fiber obliquity as the surface helix angle is increased.

Twisting of a yarn produces both strengthening and weakening influences. This is illustrated in [Figure 1](#), which is a plot of yarn strength versus surface helix angle. At low helix angles, as the surface helix angle increases the radial pressure in the yarn also increases causing more rapid stress recovery along fibers near breaks leading to overall strengthening of the yarn. At higher twist angles, obliquity effects in the fibers become dominant, since the fiber stress component contributing to the strength is proportional to the square of the cosine of the helix angle of the fiber path. Overall the sum of all stress components decreases as the surface helix angle is increased. Because of these two competing effects there exists a twist level, called optimal twist, where the maximum yarn strength is achieved. The optimal twist level and the maximum strength also depend on various constituent properties. For an excellent summary of the earlier theoretical and experimental works, we refer the readers to [\[Hearle et al. 1969\]](#).

1.2. Weibull fiber strength. High-performance fibers like Kevlar, Spectra, and even CNTs [\[Barber et al. 2005\]](#) exhibit statistical variation in their strength or strain to failure, which is typically described by a statistical distribution also involving length effects. Due to this variation, failure of the parent yarn is a stochastic process dictated by the stress field and sampling of fiber strengths along the yarn. This complex failure process imparts statistical variation and size effects to yarn strength.

The Weibull distribution is commonly used to describe the statistical variation in fiber strength giving the probability of failure of a fiber at stress level σ as

$$F(\sigma) = 1 - \exp \left\{ - \left(\frac{\sigma}{\sigma_{\delta_0}} \right)^\rho \right\},$$

where σ_{δ_0} and ρ are Weibull scale and shape parameters. Note that the scale parameter σ_{δ_0} corresponds to length δ_0 of the fiber (corresponding to a standard gauge length used in tension tests). For an arbitrary fiber length δ the scale parameter can be modified as [\[Phoenix and Beyerlein 2000\]](#)

$$\sigma_\delta = \left(\frac{\delta_0}{\delta} \right)^{1/\rho} \sigma_{\delta_0}, \quad (1)$$

and the probability of failure at stress level σ corresponding to fiber length δ is given by

$$F(\sigma) = 1 - \exp \left\{ - \frac{\delta}{\delta_0} \left(\frac{\sigma}{\sigma_{\delta_0}} \right)^\rho \right\}. \quad (2)$$

1.3. Load sharing among broken fibers. When a fiber breaks, the load that it previously carried is redistributed among the intact fibers. Historically, several idealized load sharing rules, for example, equal load sharing (ELS), global load sharing (GLS), and local load sharing (LLS), have been developed for parallel (untwisted) bundles.

In ELS the load from a broken fiber is lost along the full fiber length between the clamps and is redistributed equally among the intact fibers. In GLS the load from a broken fiber is locally lost at the break but is gradually recovered over length l_f away from the break through interfiber frictional shear forces. The full length of the recovery region is $2l_f$ and is called the recovery zone. At any cross-section intersecting the recovery zone of a break, the difference between the fiber stress before the break occurred and that actually supported by the fiber in presence of the break is distributed equally among the intact, nonslipping fibers in that cross-section. In LLS the lost load from a broken fiber is locally redistributed among its nearest neighbors according to various possible rules.

In a twisted yarn the primary factors in the construction of the load sharing rule are sliding interfiber friction near fiber breaks and the length scales they introduce as well as fiber obliquity due to twist. These are affected by surface helix angle, radial position in the yarn, and yarn tension. Attempts to account for some of the above features have appeared in the literature. Pan [1993] developed an orientation efficiency factor that he applied to Daniels' ELS bundle strength. Otherwise the ELS rule applied to all the fibers in the bundle. Pan et al. [1998] and Rao and Farris [2000] performed some experiments to show the existence of optimal strength and size effects in the yarns. On the other hand, Phoenix [1979] modeled twisted fiber bundle with Weibull fibers incorporating slack effects resulting from incomplete migration but ignored friction.

Recently Porwal et al. [2006] developed a Monte Carlo simulation model for the failure of a twisted bundle to assess the accuracy of two simplified analytical models, one based on geometrical averaging and the other on statistical averaging. The simulation model made use of a new load sharing rule, called twist-modified equal load sharing (TM-ELS), which is an extension of the ELS rule and accounts for the effects of twist but ignores friction. Under TM-ELS equilibrium is satisfied only in the yarn axis direction. The Monte Carlo simulation model as well as the two analytical theories resulted in the yarn strength being normally distributed. Very good agreement was found between the two theories and the simulation results for a wide range of yarn surface helix angles and variability in fiber strength as measured by the Weibull shape parameter. Favorable comparison was also achieved between the results of Porwal et al. [2006] and Phoenix [1979]. Finally Porwal et al. [2006] considered the issue of interfiber friction; its effect on fiber stress transfer and ultimately on the strength of a long yarn was treated in a simplified way in a chain-of-bundles model. Other more recent attempts in this category, including work on impregnated yarns, are by Naik et al. [2001] where they estimated strength of impregnated yarn using effective shear traction and fiber obliquity factor.

In the current work a probability model for the strength of a twisted bundle with an ideal helical structure is developed, which accounts for statistical Weibull fiber strength and frictional effects. To do so, we first develop a new load sharing rule, called the twist modified global load sharing (TM-GLS) rule. Specifically, TM-GLS is an extension of GLS similar to the extension of ELS to obtain TM-ELS as in [Porwal et al. 2006], applied over small yarn division.

1.4. Characteristic length for the bundle. The aim of the current work is to compare TM-ELS and TM-GLS simulations and observe the effects of friction on the bundle strength distribution and also the size effects. Such extension from TM-ELS to TM-GLS is nontrivial because it involves not only accounting for a radial pressure distribution in the context of a changing fiber stress distribution as fibers fail, but also an extension from two dimensions (a cross-sectional plane) to three dimensions, where the third dimension is a characteristic frictional length. For an individual fiber, the characteristic length is usually defined as the fiber length over which slipping occurs around a break [Phoenix and Beyerlein 2000]. This length will vary from fiber to fiber depending on its helix angle and frictional forces on its surface. To simulate the strength of a bundle it is necessary to choose a bundle length that effectively captures the characteristic stress transfer lengths of the constituent fibers. To this end we examine three specific choices of the bundle simulation lengths in this work and find that it has a strong influence on the capacity of the individual fibers in the yarn to develop the maximum stress determined by yarn extension as well

as to have multiple breaks along its length. For only one of these choices the bundle stress achieves a maximum.

2. Modeling approach

We consider the same yarn geometry as used in the previous work by [Porwal et al. \[2006\]](#) and thus only review the main points. In this work we do not consider effects such as twisting caused by the yarn tensile load or torque caused by the yarn tensile strain. The twisted bundle has n fibers, which are concentrically packed in l layers as shown in [Figure 2](#). Fibers form concentric layers with the assumption that if there is a large enough void in the concentric layer for a fiber, then it is occupied by the fiber. The layers are numbered $1, \dots, k, \dots, l$. The midpoint of layer k is located at a radius r_k from the yarn axis and is given by $r_k \approx (k - 1)d_f$, where d_f is fiber diameter. Also the helix angle α_k of the fibers in layer k is given as

$$\alpha_k = \tan^{-1} \frac{r_k \tan \alpha_s}{R},$$

where $R = r_l$ is the yarn radius and α_s is the helix angle of the outermost layer l . The number of concentrically accommodated fibers in layer k is given by

$$n_k \approx \left\lfloor \frac{2\pi(k - 1)d_f}{d_f} \right\rfloor \approx \lfloor 2\pi(k - 1) \rfloor \approx 2\pi(k - 1), \quad \text{for } k > 1 \text{ and } n_1 = 1,$$

where $\lfloor \cdot \rfloor$ is the floor function. Note that n_k does not depend on d_f and $n = n_1 + \dots + n_l$ is the total number of fibers in the yarn.

2.1. Development of tension from free ends. The distinct feature of a GLS bundle is the gradual recovery of stress in a fiber away from breaks. Consider a fiber section of length L between two breaks in layer k . If fP_k is the frictional force per unit area on the lateral surface of a sliding fiber element in this section ([Figure 3](#)), where f is the coefficient of friction and P_k is the interfiber contact pressure on layer k acting normal to the fiber surface, then from the equilibrium along the fiber length we have $dT'_k(\pi d_f^2/4) = fP_k\pi d_f dx$. The tensile stress in the fiber in terms of distance x along the fiber axis from

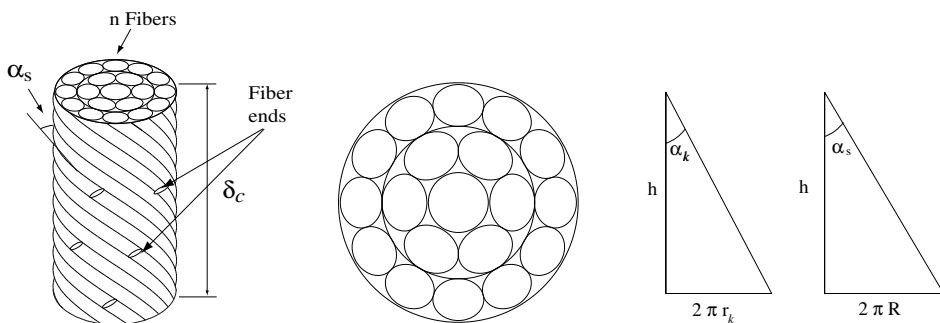


Figure 2. Yarn geometry: (left) yarn segment, (middle) concentric packing, (right) layer helix angles, where h is the height of one turn of twist.

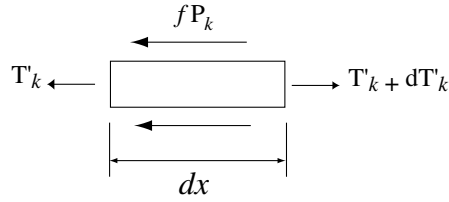


Figure 3. Development of tension in the fiber near a break in layer k .

a break is given by

$$\frac{dT'_k}{dx} = \frac{4fP_k}{d_f}, \quad \text{for } 0 \leq x \leq l_{f_k}, \tag{3}$$

where $l_{f_k} \leq L/2$ is the length of the friction zone on either end of the fiber. Using the boundary condition $T'_k = 0$ at $x = 0$, Equation (3) integrates to

$$T'_k(x) = \frac{4fP_k}{d_f}x, \quad \text{for } 0 \leq x \leq l_{f_k}. \tag{4}$$

From Equation (4) the maximum tensile stress T_k in a fiber, first attained at $x = l_{f_k}$, is given by

$$T_k = \frac{4fP_k}{d_f}l_{f_k}. \tag{5}$$

The fiber is called a nonslipping fiber if the stress given by Equation (5) is equal to the stress determined by yarn extension, neglecting Poisson’s effect [Hearle et al. 1969], that is,

$$T_k = E_f \epsilon_y \cos^2(\alpha_k), \tag{6}$$

where ϵ_y and E_f are the yarn strain and fiber Young’s modulus, respectively. In this case there are two distinct friction zones in a fiber at the ends with the tensile stresses linearly increasing from 0 to T_k . Over the middle portion of length $L - 2l_{f_k}$ the tensile stress remains equal to T_k , which is considered effectively gripped as depicted in Figure 4 with a solid line. For such a fiber the average tensile stress can be written as

$$\bar{T}_k = \frac{1}{L} \left(2l_{f_k} \frac{T_k}{2} + T_k(L - 2l_{f_k}) \right) = T_k \left(1 - \frac{l_{f_k}}{L} \right). \tag{7}$$

Otherwise, for the slipping fiber, the maximum developed tensile stress from Equation (4) will be just $2fP_kL/d_f$ for $l_{f_k} = L/2$. In this case two friction zones of length $L/2$, as depicted by the dashed line in Figure 4, are symmetrically placed about the center with zero stress at the ends and maximum stress, $2fP_kL/d_f$, in the middle. The average stress in this case thus will be

$$\bar{T}_k = \frac{fP_k}{d_f}L. \tag{8}$$

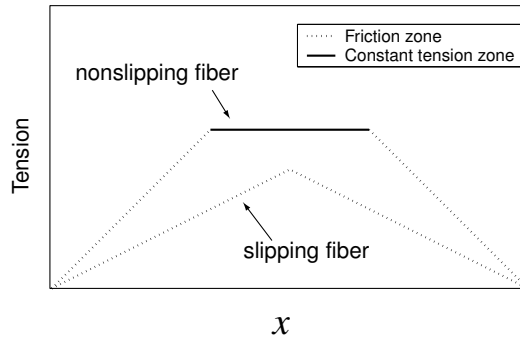


Figure 4. Tensile stress profiles in the fibers.

2.2. Pressure calculations. In this section we develop an expression for interfiber contact pressure as a function of radial distance in a yarn cross-section considering the discrete nature of the fibers in the yarn. We begin by considering the pressure developed by a single fiber helically wrapped around a cylinder under tension.

2.2.1. Pressure developed by an individual fiber. When a fiber under constant tension T is wound around a cylinder in a circular loop a nominal contact pressure P is experienced by both the fiber and cylinder given by

$$P = \frac{dT}{r} = \frac{d_f T}{r}, \tag{9}$$

where r is the radius of cylinder and d is the nominal contact width along the fiber. To simplify the pressure calculation we assume that the fiber has a square cross-section with side d_f so that $d = d_f$.

In the case of a twisted bundle, the above expression needs to be modified to account for the helical path of the fiber (Figure 5). This can be easily done by replacing r in the denominator of Equation (9)

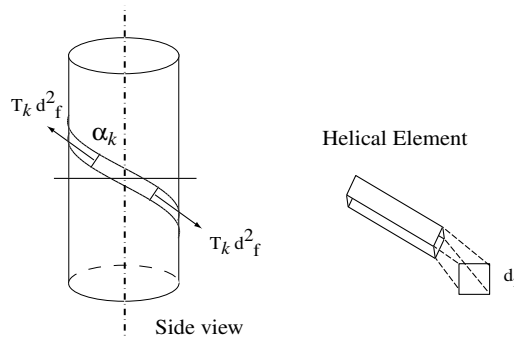


Figure 5. Pressure developed by a helically wound fiber in the k -th layer (left). The fiber cross-section is assumed to be square for the purpose of calculating pressure (right).

by the local radius of curvature, which is $r_k/\sin^2 \alpha_k$. Thus the pressure developed becomes

$$P_{k,k} = \frac{d_f T_k \sin^2(\alpha_k)}{r_k}. \tag{10}$$

This pressure acts normal to the lateral surface of the fiber and is assumed to be constant across the entire cross-section of the fiber. It is clear from Equation (10) that as the helix angle increases, the pressure developed by the fiber increases.

The above expression for pressure assumes that the stress in the fiber is constant along the length of the fiber. However, this is not the case in an actual yarn. To account for the effect of varying stress in the fiber we use an average stress \bar{T}_k over the length of the fiber to calculate the average pressure, that is,

$$\bar{P}_{k,k} = \frac{d_f \bar{T}_k \sin^2(\alpha_k)}{r_k}, \tag{11}$$

where \bar{T}_k is given by either Equation (7) or (8). Henceforth the average pressure is simply called the pressure.

2.2.2. Pressure variation in the yarn. For layer k within the yarn the total pressure \bar{P}_k is sum of its own pressure, Equation (11), and the pressure from layers outside it. To ease the calculation of the pressure in layer k we assume that the fibers inside and outside of this layer are homogeneous isotropic cylinders. Thus, the pressure is given by

$$\bar{P}_k = \bar{P}_{k,k} + \bar{P}_{k,o} = \sum_{j=k}^l \bar{P}_{j,j}, \tag{12}$$

where $\bar{P}_{k,o} = \sum_{j=k+1}^l \bar{P}_{j,j}$ is the contribution to the pressure from layers outside the k -th layer.

Note that calculation of the pressure using discrete fibers allows us to account for individual fiber failures. This, however, is beyond the scope of this work and left for a future study.

2.3. Lengths of friction zones in fiber. We consider the two cases corresponding to the two fiber stress profiles in Figure 4.

Case 1: nonslipping fiber. This case considers the nonslipping fiber in Figure 4. If the pressure in layer k is \bar{P}_k , then Equation (5) would become

$$T_k = \frac{4f\bar{P}_k}{d_f} l_{f_k}. \tag{13}$$

From Equations (12) and (13) we obtain

$$T_k = \frac{4f}{d_f} (\bar{P}_{k,k} + \bar{P}_{k,o}) l_{f_k}, \tag{14}$$

and using Equations (6), (7), (11) and (14) we get

$$\frac{d_f \cos^2(\alpha_k)}{4f} = \left[\frac{d_f \cos^2(\alpha_k) \sin^2(\alpha_k)}{r_k} \left(1 - \frac{l_{f_k}}{L}\right) + \frac{\bar{P}_{k,o}}{E_f \epsilon_y} \right] l_{f_k}. \tag{15}$$

Defining C_k and B_k as

$$C_k = \frac{d_f \cos^2(\alpha_k) \sin^2(\alpha_k)}{r_k}, \quad B_k = \frac{d_f \cos^2(\alpha_k)}{4f},$$

we can solve Equation (15) to obtain l_{f_k} as

$$l_{f_k} = \frac{(C_k + \bar{P}_{k,o}/E_f \epsilon_y) - \sqrt{(C_k + \bar{P}_{k,o}/E_f \epsilon_y)^2 - 4C_k B_k/L}}{2C_k/L}$$

$$= \frac{L}{2} \left\{ \left(1 + \frac{\bar{P}_{k,o}}{C_k E_f \epsilon_y} \right) - \sqrt{\left(1 + \frac{\bar{P}_{k,o}}{C_k E_f \epsilon_y} \right)^2 - \frac{r_k}{f L \sin^2(\alpha_k)}} \right\}. \quad (16)$$

Here we consider only the negative solution because the positive solution gives $l_{f_k} > L/2$.

Case 2: slipping fiber. For the case of the slipping fiber in Figure 4, Equations (8), (11), and (12) yield

$$\bar{P}_{k,k} = \frac{f \bar{P}_k L \sin^2(\alpha_k)}{r_k} = \frac{f(\bar{P}_{k,k} + \bar{P}_{k,o})L \sin^2(\alpha_k)}{r_k},$$

giving

$$\bar{P}_{k,k} = \frac{\bar{P}_{k,o}}{\frac{r_k}{f L \sin^2(\alpha_k)} - 1}. \quad (17)$$

Since the layers cannot make a negative pressure contribution, the denominator of the Equation (17) must be positive, that is,

$$\frac{r_k}{f L \sin^2(\alpha_k)} > 1.$$

This requirement is opposite the condition required for the validity of Equation (16), which is

$$\frac{r_k}{f L \sin^2(\alpha_k)} < \left(1 + \frac{\bar{P}_{k,o}}{C_k E_f \epsilon_y} \right)^2 \quad \text{or} \quad \frac{r_k}{f L \sin^2(\alpha_k)} < 1^+,$$

where 1^+ is any quantity > 1 . The friction zone length for this case will be $l_{f_k} = L/2$.

Note that for the l -th layer, which is the outermost layer, $\bar{P}_{l,o} = 0$ by definition. Furthermore, if case 2 is true, then it is a degenerate case 2 because no pressure development means zero tension in the fibers. This leads to $\bar{P}_l = 0$ and so on for all other layers and by our assumptions thus far the fibers will simply unravel. To overcome this difficulty we can assume some nonzero external pressure $P_o > 0$ as Sullivan [1942] did. Also note that in an actual yarn, fibers do not stay in one particular layer over the whole yarn length, but they rather move from layer to layer through the process called migration. Consequently, despite having several breaks, a surface fiber can be well anchored over much of its length thus allowing tension and hence pressure to develop.

2.4. Characteristic lengths of bundle for strength calculation. Here we define three different characteristic length scales based on constituent material and yarn geometrical properties, which are crucial to strength development in the yarn with each one involving a different failure mechanism. The axial length of the yarn that will develop the maximum tension (as determined by yarn extension) from a single break

in the cross-section passing through the middle of the yarn length in layer k is $2l_{f_k} \cos \alpha_k$. Three length scales δ_c^{\max} , δ_c^{\min} , and δ_c^{avg} can be computed from this length

$$\delta_c^{\max} = \max_k \{2l_{f_k} \cos \alpha_k\}, \quad \delta_c^{\min} = \min_k \{2l_{f_k} \cos \alpha_k\}, \quad \delta_c^{\text{avg}} = \sum_{k=1}^l w_k 2l_{f_k} \cos \alpha_k.$$

The last definition uses a weight function w_k , a suitable choice of which is the fraction of fibers in each layer, that is, $w_k = n_k/n$. Taking $\delta_c = \delta_c^{\max}$ all fiber layers can reach maximum tension if a break develops in the cross-section passing through the middle of the yarn length. In other words, through the frictional stresses, the axial tension is recovered far from the break point to the level that the fiber can sustain redistributed stress. In the case of $\delta_c = \delta_c^{\min}$, only the layer with the minimum length of friction zone projected along the yarn axis can develop maximum tension along their broken fibers. So in this case frictional stresses are largely unutilized. For $\delta_c = \delta_c^{\text{avg}}$, only some of the broken fibers can develop maximum tension, utilizing frictional stresses moderately.

2.5. TM-GLS and Monte Carlo simulation algorithm. In the Monte Carlo simulation model we consider a characteristic length δ_c of the yarn. Since it is not feasible to redistribute the load at each cross-sectional plane, we divide this characteristic length into a predetermined number n_{div} of divisions of much shorter length $\delta = \delta_c/n_{\text{div}}$. Because of the helical paths of the fibers, the fiber elements in layer k actually have longer lengths $\delta_k = \delta/\cos \alpha_k$, which also differs from layer to layer. We then assign a random strength $X_{f,i}^{\text{div}}$ to each fiber element in the yarn characteristic length, where i is fiber number and div is the division number that ranges from 1 to n_{div} . These strengths are assigned according to a Weibull distribution whose shape parameter is ρ and the scale parameter is referenced to length δ_k for layer k according to Equation (2) with $\delta = \delta_k$.

The TM-GLS redistribution scheme evolves iteratively using the following discrete steps as we increase the external load, keeping in mind that after any particular step a given fiber may have one or more breaks:

- (i) In a particular step t the axial stresses of the fiber elements are first calculated and then compared to the assigned fiber element strengths $X_{f,i}^{\text{div}}$.
- (ii) From this comparison any fiber element whose axial stress exceeds its assigned strength is considered failing in this step in which case its load becomes zero. The stresses in all other elements along this fiber that are in the stress recovery zone of this newly broken element are then calculated according to

$$T_{f,i}^s = \frac{4f}{d_f} \bar{P}_k c \delta_k, \quad \text{if } \frac{4f}{d_f} \bar{P}_k c \delta_k \leq T_{f,i},$$

where $T_{f,i}$ is the stress in the individual fiber i as determined by yarn extension and integer c is the distance of a particular element from the broken element in terms of number of elements, that is, for the broken fiber element $c = 0$ and for subsequent neighboring elements $c = 1, 2, \dots$ on either side of the newly broken element. When there are breaks on both sides of an unbroken element, then c must be modified to be the smaller of two values obtained by counting from each of the broken elements. The elements just described are slipping elements in the recovery zone of some broken

element and thus have stresses less than $T_{f,i}$. Thus, they are actually shedding stresses that are then resolved along the yarn axis.

- (iii) These resolved components are then redistributed equally to the stress components (resolved along the yarn axis) of the fiber elements not shedding their stresses, and then the stresses of these elements acting along their own respective axes are recalculated.
- (iv) The stresses in the recovery zones of newly broken elements are then set equal to the stresses determined in Section 2.5 (ii).

Our general scheme is to model the failure process in discrete steps $t = 0, 1, \dots$ in the following way. (To simplify the notation we suppress the superscript div in $T_{f,i}^{s(\text{div})}$). At step t we denote the stress in fiber element i acting along its own axis (not the yarn axis) as $T_{f,i}^{(t)}$ as in (i) above. $T_{f,i}^{(t)}$ is considered to be composed of two components: the first is the stress carried by the fiber element $T_{f,i}^{\epsilon(t)}$ due to the applied load as if all the fibers are intact, while the second is the sum of the additional stress portions inherited from the fiber elements shedding their stresses $T_{f,i}^r(t)$ in that division. Summing these for fiber element i within a particular yarn division we have

$$T_{f,i}^{(t)} = \begin{cases} T_{f,i}^{s(t)}, & \text{if fiber is shedding its stress,} \\ T_{f,i}^{\epsilon(t)} + T_{f,i}^r(t), & \text{otherwise.} \end{cases}$$

From Equation (6) for fiber element i we have $T_{f,i}^{\epsilon(t)} = E_f \epsilon_y^{(t)} \cos^2 \alpha_{f,i}$. At each step we recalculate $T_{f,i}$ according to

$$T_{f,i}^{(t+1)} = \begin{cases} T_{f,i}^{s(t+1)}, & \text{if fiber is shedding its stress,} \\ T_{f,i}^{\epsilon(t+1)} + T_{f,i}^r(t) + \frac{\sum_{j=1}^{n_b} (T_{f,b(j)}^{(t)} - T_{f,b(j)}^{s(t+1)}) \cos \alpha_{f,b(j)}}{(n - N_b) \cos \alpha_{f,i}}, & \text{otherwise,} \end{cases}$$

where $b(j)$ is the index number of j -th fiber element shedding its load, n_b is the number of additional fiber elements shedding their loads when going from step t to $t + 1$, and N_b is the total number of fiber elements shedding their loads at $t + 1$. In this equation we see a stress enhancement effect in the benefactor fiber (along its axis) that results when it has a larger helix angle as compared to the fiber that failed.

We note that t does not necessarily correspond to an increment in the applied loading; the index t is increased either (a) when we increase the external load level, or (b) when at a given external load level the redistribution of stresses leads to failure of more fibers.

At any step t the applied stress is in equilibrium with internal stresses developed by the fiber elements in each division, so the stress carried by the yarn is given by

$$\sigma^{(t)} = \frac{\sum_{i=1}^n T_{f,i}^{(t)} \cos(\alpha_{f,i})}{\sum_{i=1}^n 1 / \cos \alpha_{f,i}}$$

and the strength of the yarn would be $\max_t \{\sigma^{(t)}\}$. We note one fundamental difference between TM-GLS and GLS. In the latter once a fiber element falls in the friction zone, its stress remains constant during further external load increments; so it can not fail. In the former, however, stresses in slipping fiber elements may increase due to the ever increasing yarn pressures and frictional forces.

3. Results and discussion

We normalize the bundle strength and failure behavior quantities with σ_{δ_c} , the Weibull scale parameter corresponding to the yarn characteristic length δ_c . Since there are no stiffness variations in the fibers and no interfiber slack effects inherited from the migration, the actual fiber Young's modulus and Weibull scale parameter for fiber strength are normalized out of the calculation. Note that σ_{δ_c} depends on δ_c and ρ through Equation (1). In the simulations the key parameter ρ is varied from 2 to 10. This range is typical of commercially available high-performance fibers such as Toray carbon T1000G, Kevlar, Spectra, Zylon, with diameters on the order of 4 to 25 μm . Another key parameter is the interfiber friction coefficient f which affects δ_c (see Figure 9). We consider the values $f = 0.1$ and 0.3, which are representative of the above mentioned fibers. All of the following simulations are for $\delta_c = \delta_c^{\text{min}}$ unless stated otherwise. We also vary the surface twist angle over $0^\circ < \alpha_s < 25^\circ$. The normalized value of external pressure is assumed to be $\bar{P}_{l,0}/E_f\epsilon_y = 0.001$ or 0.1% of the fiber stress in an untwisted yarn, which is a small fraction of the pressure typically generated even for small twist angles as seen later. The fiber diameter is taken as $d_f = 10 \mu\text{m}$ and the length of fiber in the simulation is $L = 20 \text{ cm}$. Typically this length is longer than the fiber characteristic length at very small twist because of the initial external constraining pressure.

3.1. Convergence study. We first study the convergence of μ/σ_{δ_c} for important simulation parameters such as the number of replications n_s , number of divisions n_{div} , and magnitude of stress increment ΔT . To achieve sufficient accuracy in the simulations we determine acceptable values of these parameters in an iterative manner. First we fix $n_{\text{div}} = 50$ and $\Delta T = E_f\Delta\epsilon$, where $\Delta\epsilon = 0.001$ is much smaller than the Weibull scale parameter for fiber failure strain, and find the value of n_s for which we get convergence. Figure 6 (left) shows a plot of the normalized mean μ/σ_{δ_c} versus number of replications. We find very good convergence for n_s beyond 200. Next we fix $n_s = 500$ and $n_{\text{div}} = 50$ and study μ/σ_{δ_c} versus strain increment, $\Delta\epsilon$, that is, $\Delta T = E_f\Delta\epsilon$. Figure 6 (right) shows the resulting convergence for decreasing

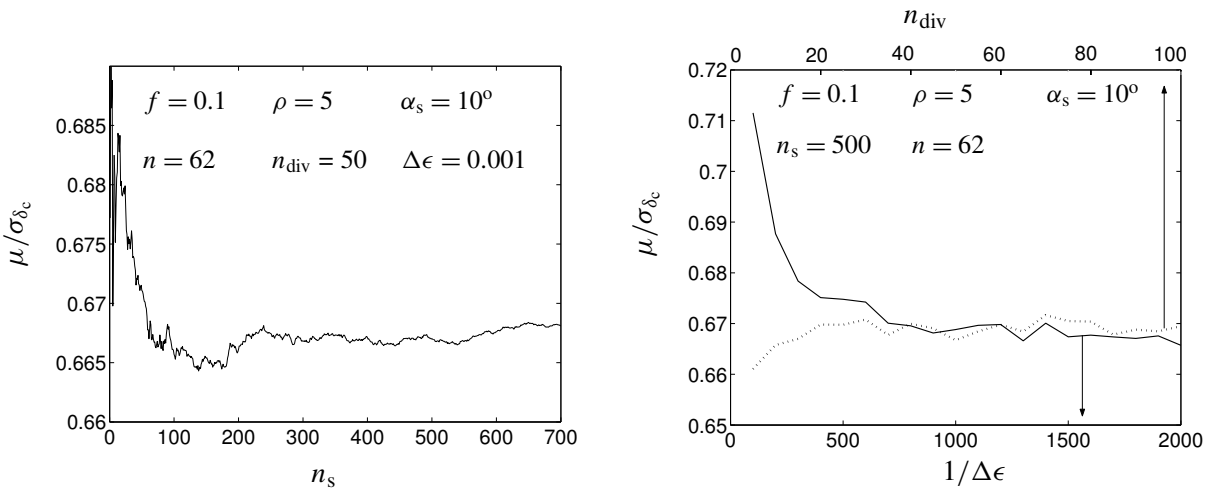


Figure 6. Convergence of normalized mean, μ/σ_{δ_c} , versus (left) number of runs, n_s , and (right) number of divisions, n_{div} , and strain increment, $\Delta\epsilon$.

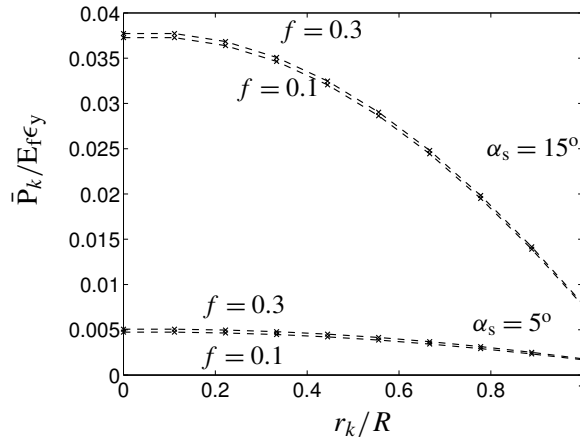


Figure 7. Normalized pressure, $\bar{P}_k/E_f\epsilon_y$, versus normalized radial distance, r_k/R . Here $l = 10$ and $n = 279$.

$\Delta\epsilon$. We also fix $n_s = 500$ and $\Delta\epsilon = 0.001$ and consider the convergence of μ/σ_{δ_c} in n_{div} , also shown in Figure 6 (right). Thus we choose $n_s = 500$, $n_{div} = 50$ and $\Delta\epsilon = 0.001$ for our simulations.

3.2. Pressure development, fiber friction zone and yarn characteristic lengths. Figure 7 shows the change in normalized pressure with normalized radial distance from the center of the yarn. The pressure increases as radius decreases to the center of the yarn, whereby the pressure contributions of the outer layers accumulate. The calculation in Figure 7 considers all the fibers to be intact. For this reason there is little difference in pressure distribution for the different friction coefficients $f = 0.1$ and 0.3 (for both $\alpha_s = 5^\circ$ and 15°). Fibers that fail carry reduced stresses over the characteristic fiber and yarn lengths leading to an overall decrease in pressure magnitude from that shown in Figure 7. Friction will also

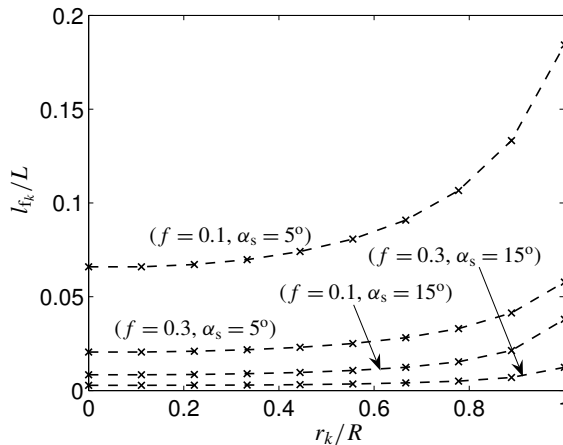


Figure 8. Normalized friction length, l_{f_k}/L , versus normalized yarn radius, r_k/R . Here $l = 10$ and $n = 279$.

come into play after a significant number of fiber breaks have accumulated in the yarn. In Figure 7 we note a huge gain in pressure with increase in α_s . This happens because of the effect of sine-squared of the helix angle in the numerator of Equation (10).

Figure 8 shows plots of the friction zone length versus radial distance from the center of the yarn. As anticipated, the friction length increases from the center to the outer surface irrespective of f and α_s . For a fixed α_s the length of the fiber friction zone decreases with increasing f and for a fixed f it decreases with increasing α_s . As is the case for the pressure distribution in the yarn, the α_s has a stronger effect than f on the fiber friction zone length.

The marker points in Figures 7 and 8 correspond to the values at the centers of the concentric layers and dashed lines are there to show the trend.

Figure 9 shows the decrease in the three characteristic length scales, which we consider in this work, with α_s for $f = 0.1$. The reduction occurs because the friction lengths decrease with an increase in α_s . As expected, $\delta_c^{\max} > \delta_c^{\text{avg}} > \delta_c^{\min}$ for all α_s . Also, we see the same trend for other values of coefficient of friction.

3.3. Stress strain curves. Figure 10 shows sample stress strain curves corresponding to different values of the Weibull shape parameter, ρ , and surface helix angle, α_s . The simulation assumes a stress-controlled tensile experiment. The lower, isolated marker points indicate sudden collapse of the yarn. We define the strain ϵ_y in Figure 10 as the strain in the intact virtual central fiber of the yarn. Therefore the slope of these curves is a reasonable approximation of yarn elastic stiffness. The linearity of all the curves until sudden failure suggests a macroscopic brittle-like behavior. For a fixed α_s the slope increases with an increase in ρ , whereas in the case when ρ is fixed the slope decreases with an increase in α_s . Also

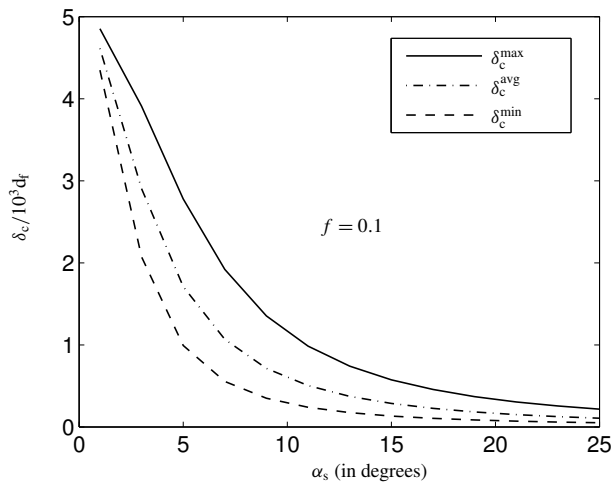


Figure 9. Normalized characteristic length scale for strength development $\delta_c / 10^3 d_f$ versus surface helix angle α_s . $l = 10, n = 279$.

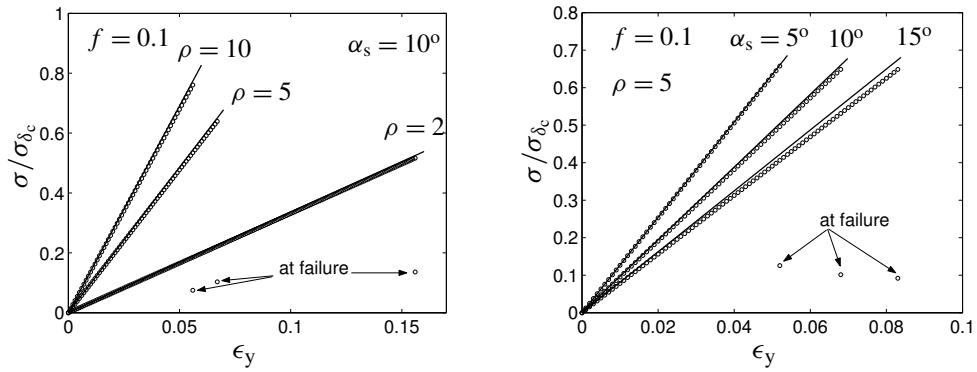


Figure 10. Stress strain curves for twisted yarn for various parameters values as shown in the figures. Solid lines are theoretical curves and marker points indicate simulation curves.

shown in Figure 10 are the theoretical curves given by

$$\frac{\sigma}{\sigma_{\delta_c}} = \frac{E_f \epsilon_y \cos^2 \bar{\alpha}}{\sigma_{\delta_c}} = \frac{E_f \epsilon_y \cos^2 \bar{\alpha}}{\sigma_{\delta}} \left(\frac{\delta}{\delta_c} \right)^{1/\rho},$$

where it is assumed that all the fibers have the same helix angle $\bar{\alpha}$ given by

$$\bar{\alpha} = \cos^{-1} \left(\frac{\sum_{k=1}^l n_k \cos \alpha_k}{n} \right).$$

We achieve very good agreement between the theoretical and simulation curves, except for large values of α_s , where localized failure mechanisms might come into play. These plots correspond to a single realizations of a yarn test and thus conclusions cannot be drawn regarding the relative strengths and strains to failure for different values of ρ and α_s because the yarn realizations exhibit variability from one to another.

3.4. Cumulative probability distribution, mean and standard deviation. Figure 11 shows the cumulative probability distribution functions, G , resulting from the Monte Carlo simulations for $\alpha_s = 10^\circ$ and $\rho = 2, 5, \text{ and } 10$ on normal probability paper. The nearly straight lines indicate that the strength is approximately normally distributed.

Figure 12 and 13 plot the normalized mean strength, $\mu/\sigma_{\delta_c^{\min}}$, and standard deviation, $\sqrt{n} \gamma/\sigma_{\delta_c^{\min}}$, versus surface helix angle, α_s , for $n = 62$ and 279 , and $\rho = 2, 5, \text{ and } 10$ (for $f = 0.1$ and 0.3). In these calculations we use δ_c^{\min} as the yarn characteristic length. Significantly, the curves for the two values of friction coefficients, that is, $f = 0.1$ and 0.3 coincide with each other when normalized with respect to $\sigma_{\delta_c^{\min}}$. For comparison, we also show the results from the earlier work [Porwal et al. 2006] on TM-ELS. The TM-GLS and TM-ELS curves generally exhibit the same behavior for δ_c^{\min} . The TM-GLS curves, however, show some improvement in the strength due the presence of frictional forces. As in the TM-ELS bundle, the TM-GLS bundles also exhibit a size effect. The strength is slightly lower for a larger bundle with $n = 279$ fibers than for smaller one with $n = 62$. No particular pattern in the standard

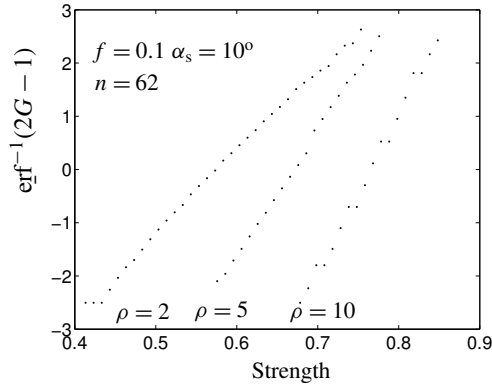


Figure 11. Cumulative probability distribution function on normal probability paper ($n_s = 10000$).

deviation is seen apart from the fact that it decreases with an increase in ρ corresponding to a decrease in fiber strength variability. Further study is required to exactly understand the size effects and the standard deviation in the strength of these twisted yarns.

3.5. Effect of length scale on strength development and existence of optimal twist angle.

Figure 14 clearly indicates the importance of the choice of δ_c , by comparing the mean strength of the yarns with surface twist α_s for different choices of simulation lengths, δ_c^{\max} , δ_c^{\min} , or δ_c^{avg} . When mean bundle strength is simply normalized by μ_1 , the mean bundle strength at $\alpha_s = 1^\circ$, it increases with surface twist angle α_s , up to $\alpha_s = 25^\circ$. However, normalizing by μ_1 is not completely correct because it does not account for the size effect in the strength of the individual fibers. The scale parameter of the individual fibers increases, as δ_c decreases, according to

$$\sigma_{\delta_c} = \left(\frac{\delta_0}{\delta_c}\right)^{1/\rho} \sigma_{\delta_0}.$$

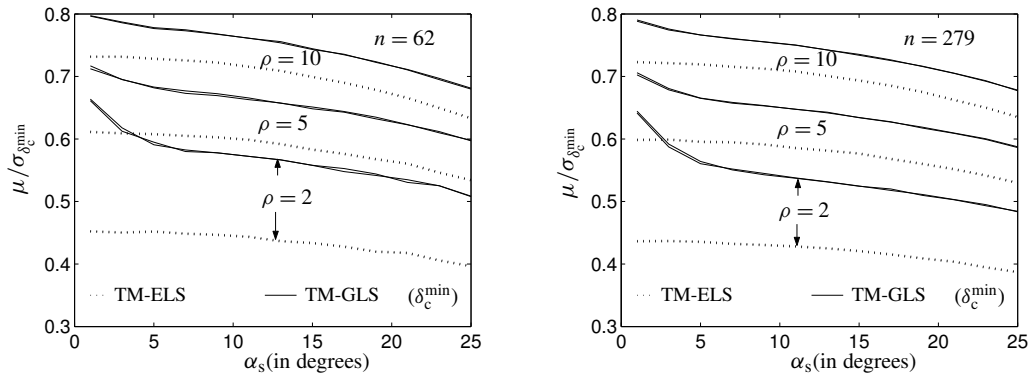


Figure 12. Normalized mean, $\mu/\sigma_{\delta_c^{\min}}$, versus surface helix angle, α_s . The TM-GLS results are for $f = 0.1$ and 0.3 . TM-ELS results are from [Porwal et al. 2006].

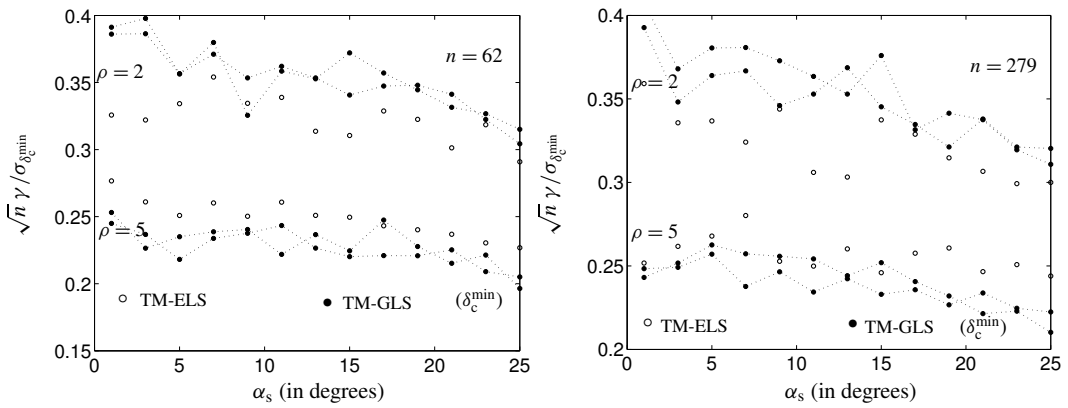


Figure 13. Normalized standard deviation $\sqrt{n} \gamma / \sigma_{\delta_c^{\min}}$ versus surface helix angle α_s . The TM-GLS results are for $f = 0.1$ and 0.3 . TM-ELS results are from [Porwal et al. 2006].

This more appropriate normalization will account for the changing length of the bundle in simulation. Significantly, the yarn strength achieves a maximum for δ_c^{\max} but not the other two length scales. This same result occurs with other parameter sets as well. The other two length scales limit the role played by the frictional stresses and therefore are not wise choices for modeling and simulation of yarn failure.

The inset figure in Figure 14 plots normalized bundle strength (S/S_0 , where S_0 is the bundle strength when $\alpha_s = 0^\circ$) versus surface twist angle using data extracted from experimental results of Rao and Farris [2000]. The optimal helix angle predicted by our model ($\alpha_s \approx 7^\circ$) is in excellent agreement with

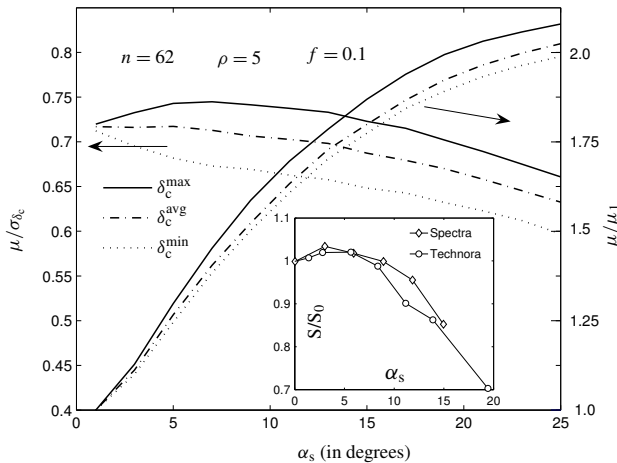


Figure 14. Normalized mean bundle strength μ / σ_{δ_c} and μ / μ_1 versus surface helix angle α_s for different length scales. Here μ_1 is the value at $\alpha_s = 1^\circ$. Inset figure (S/S_0 versus α_s) is plotted using data from [Rao and Farris 2000], where S_0 is the yarn strength when $\alpha_s = 0^\circ$.

experimental results of [Rao and Farris \[2000\]](#) despite the fact that the idealized yarn geometry of our model is different from the yarn produced by their twisting process. The magnitudes of the strengths are apparently different because the normalizations used are different. Further, the experimental strength decreases at relatively higher rate than theoretical value because of the inefficiencies due to incomplete migration at higher twist angle, which is assumed to be complete in our model.

4. Conclusions

We have made a fundamental improvement in the twisted bundle strength model by incorporating effects of friction and pressure development. We have defined and shown that the choice of the characteristic length scale and normalization parameter are crucial in simulating the strength behavior, particularly as a function of the surface helix angle ([Figure 14](#)). Monte Carlo simulation is employed to show that the bundle strength approximately follows a normal distribution. Further, the TM-GLS bundle strength exhibits a peak when δ_c^{\max} and $\sigma_{\delta_c}^{\max}$ are selected as the characteristic length scale and normalization parameter, respectively. In this case, broken fibers in any layer are allowed to develop stress via frictional forces to the maximum level determined by yarn extension and therefore potentially break again elsewhere along their length.

References

- [Andrews et al. 1999] R. Andrews, D. Jacques, A. M. Rao, T. Rantell, F. Derbyshire, Y. Chen, J. Chen, and R. C. Haddon, “[Nanotube composite carbon fibers](#)”, *Appl. Phys. Lett.* **75**:9 (1999), 1329–1331.
- [Barber et al. 2005] A. H. Barber, I. Kaplan-Ashiri, S. R. Cohen, R. Tenne, and H. D. Wagner, “[Stochastic strength of nanotubes: an appraisal of available data](#)”, *Compos. Sci. Technol.* **65**:15-16 (2005), 2380–2384.
- [Ericson et al. 2004] L. M. Ericson, H. Fan, H. Peng, V. A. Davis, W. Zhou, J. Sulpizio, Y. Wang, R. Booker, J. Vavro, C. Guthy, A. N. G. Parra-Vasquez, M. J. Kim, S. Ramesh, R. K. Saini, C. Kittrell, G. Lavin, H. Schmidt, W. W. Adams, W. E. Billups, M. Pasquali, W.-F. Hwang, R. H. Hauge, J. E. Fischer, and R. E. Smalley, “[Macroscopic, neat, single-walled carbon nanotube fibers](#)”, *Science* **305**:5689 (2004), 1447–1450.
- [Hearle et al. 1969] J. W. S. Hearle, P. Grosberg, and S. Vacker, *Structural mechanics of fibers, yarns, and fabrics*, vol. 1, Wiley-Interscience, 1969.
- [Huemmerich et al. 2004] D. Huemmerich, T. Scheibel, F. Vollrath, S. Cohen, U. Gat, and S. Ittah, “[Novel assembly properties of recombinant spider dragline silk proteins](#)”, *Curr. Biol.* **14**:22 (2004), 2070–2074.
- [Jiang et al. 2002] K. Jiang, Q. Li, and S. Fan, “[Nanotechnology: spinning continuous carbon nanotube yarns](#)”, *Nature* **419**:6909 (2002), 801–801.
- [Ko et al. 2003] F. Ko, Y. Gogotsi, A. Ali, N. Naguib, H. Ye, G. L. Yang, C. Li, and P. Willis, “[Electrospinning of continuous carbon nanotube-filled nanofiber yarns](#)”, *Adv. Mater.* **15**:14 (2003), 1161–1165.
- [Lazaris et al. 2002] A. Lazaris, S. Arcidiacono, Y. Huang, J.-F. Zhou, F. Duguay, N. Chretien, E. A. Welsh, J. W. Soares, and C. N. Karatzas, “[Spider silk fibers spun from soluble recombinant silk produced in mammalian cells](#)”, *Science* **295**:5554 (2002), 472–476.
- [Naik et al. 2001] N. K. Naik, I. Mudzingwa, and M. N. Singh, “[Effect of twisting on tensile failure of impregnated yarns with broken filaments](#)”, *J. Compos. Technol. Res.* **23**:3 (2001), 225–234.
- [Pan 1993] N. Pan, “[Prediction of statistical strengths of twisted fibre structure](#)”, *J. Mater. Sci.* **28**:22 (1993), 6107–61114.
- [Pan et al. 1998] N. Pan, H. C. Chen, J. Thompson, M. K. Inglesby, and S. H. Zeronian, “[Investigation on the strength-size relationship in fibrous structures including composites](#)”, *J. Mater. Sci.* **33**:10 (1998), 2667–2672.
- [Phoenix 1979] S. L. Phoenix, “[Statistical theory for the strength of twisted fiber bundles with applications to yarns and cables](#)”, *Text. Res. J.* **49**:7 (1979), 407–423.

- [Phoenix and Beyerlein 2000] S. L. Phoenix and I. J. Beyerlein, “Statistical strength theory for fibrous composite materials”, Chapter 1.19, pp. 559–640 in *Comprehensive composite materials*, vol. 1, edited by A. Kelly et al., Pergamon/Elsevier, 2000.
- [Porwal et al. 2006] P. K. Porwal, I. J. Beyerlein, and S. L. Phoenix, “Statistical strength of a twisted fiber bundle: an extension of Daniels equal-load-sharing parallel bundle theory”, *J. Mech. Mater. Struct.* **1**:8 (2006), 1425–1447.
- [Rao and Farris 2000] Y. Rao and R. J. Farris, “A modeling and experimental study of the influence of twist on the mechanical properties of high-performance fiber yarns”, *J. Appl. Polym. Sci.* **77**:9 (2000), 1938–1949.
- [Sullivan 1942] R. R. Sullivan, “A theoretical approach to the problem of yarn strength”, *J. Appl. Phys.* **13**:3 (1942), 157–167.
- [Vigolo et al. 2000] B. Vigolo, A. Pénicaud, C. Coulon, C. Sauder, R. Pailler, C. Journet, P. Bernier, and P. Poulin, “Macroscopic fibers and ribbons of oriented carbon nanotubes”, *Science* **290**:5495 (2000), 1331–1334.
- [Zhang et al. 2004] M. Zhang, K. R. Atkinson, and R. H. Baughman, “Multifunctional carbon nanotube yarns by downsizing an ancient technology”, *Science* **306**:5700 (2004), 1358–1361.

Received 6 Jul 2006. Revised 6 Jun 2006. Accepted 20 Feb 2007.

PANKAJ K. PORWAL: pkp2@cornell.edu

Department of Theoretical and Applied Mechanics, Cornell University, Ithaca, NY 14853
<http://www.tam.cornell.edu/~pkp2/>

IRENE J. BEYERLEIN: irene@lanl.gov

Theoretical Division, Los Alamos National Laboratory, Los Alamos, NM 87545

STUART LEIGH PHOENIX: slp6@cornell.edu

Department of Theoretical and Applied Mechanics, Cornell University, Ithaca, NY 14853
<http://www.tam.cornell.edu/Phoenix1.html>

SUBMISSION GUIDELINES

ORIGINALITY

Authors may submit manuscripts in PDF format on-line. Submission of a manuscript acknowledges that the manuscript is *original and has neither previously, nor simultaneously, in whole or in part, been submitted elsewhere*. Information regarding the preparation of manuscripts is provided below. Correspondence by email is requested for convenience and speed. For further information, write to:

[Marie-Louise Steele](#)
Division of Mechanics and Computation
Durand Building, Room 262
Stanford University
Stanford CA 94305

LANGUAGE

Manuscripts must be in English. A brief abstract of about 150 words or less must be included. The abstract should be self-contained and not make any reference to the bibliography. Also required are keywords and subject classification for the article, and, for each author, postal address, affiliation (if appropriate), and email address if available. A home-page URL is optional.

FORMAT

Authors are encouraged to use L^AT_EX and the standard article class, but submissions in other varieties of T_EX, and, exceptionally in other formats, are acceptable. Electronic submissions are strongly encouraged in PDF format only; after the refereeing process we will ask you to submit all source material.

REFERENCES

Bibliographical references should be listed alphabetically at the end of the paper and include the title of the article. All references in the bibliography should be cited in the text. The use of B_IB_TE_X is preferred but not required. Tags will be converted to the house format (see a current issue for examples), however, in the manuscript, the citation should be by first author's last name and year of publication, e.g. "as shown by Kramer, et al. (1994)". Links will be provided to all literature with known web locations and authors are encouraged to provide their own links on top of the ones provided by the editorial process.

FIGURES

Figures prepared electronically should be submitted in Encapsulated PostScript (EPS) or in a form that can be converted to EPS, such as GnuPlot, Maple, or Mathematica. Many drawing tools such as Adobe Illustrator and Aldus FreeHand can produce EPS output. Figures containing bitmaps should be generated at the highest possible resolution. If there is doubt whether a particular figure is in an acceptable format, the authors should check with production by sending an email to:

production@mathscipub.org

Each figure should be captioned and numbered so that it can float. Small figures occupying no more than three lines of vertical space can be kept in the text ("the curve looks like this:"). It is acceptable to submit a manuscript with all figures at the end, if their placement is specified in the text by means of comments such as "Place Figure 1 here". The same considerations apply to tables.

WHITE SPACE

Forced line breaks or page breaks should not be inserted in the document. There is no point in your trying to optimize line and page breaks in the original manuscript. The manuscript will be reformatted to use the journal's preferred fonts and layout.

PROOFS

Page proofs will be made available to authors (or to the designated corresponding author) at a web site in PDF format. Failure to acknowledge the receipt of proofs or to return corrections within the requested deadline may cause publication to be postponed.

Journal of Mechanics of Materials and Structures

Volume 2, N^o 4 April 2007

- Asymptotic analysis and reflection photoelasticity for the study of transient crack propagation in graded materials** N. JAIN AND A. SHUKLA 595
- Asymptotic homogenization model for three-dimensional network reinforced composite structures** K. S. CHALLAGULLA, A. GEORGIADIS AND A. L. KALAMKAROV 613
- Thermal stress analysis of functionally graded composites with temperature-dependent material properties** H. K. CHING AND J. K. CHEN 633
- Finite element modeling of a layered, multiphase magnetoelectroelastic cylinder subjected to an axisymmetric temperature distribution** N. GANESAN, A. KUMARAVEL AND R. SETHURAMAN 655
- A linear curved-beam model for the analysis of galloping in suspended cables** A. LUONGO, D. ZULLI AND G. PICCARDO 675
- Stress analysis of composite cylindrical shells with an elliptical cutout** E. OTERKUS, E. MADENCI AND M. P. NEMETH 695
- Hypersingular integral equations for the solution of penny-shaped interface crack problems** B. KILIC AND E. MADENCI 729
- Wavelet spectral element for wave propagation studies in pressure loaded axisymmetric cylinders** M. MITRA AND S. GOPALAKRISHNAN 753
- Statistical strength of twisted fiber bundles with load sharing controlled by frictional length scales** P. K. PORWAL, I. J. BEYERLEIN AND S. LEIGH PHOENIX 773